# TURBULENT MIXING OF OPPOSING FLOWS INSIDE CHIMNEY STRUCTURE OF POOL TYPE RESEARCH REACTOR

***By***

**SAMIRAN SENGUPTA**

(ENGG01200804003)

Bhabha Atomic Research Centre, Mumbai

*A thesis submitted to the*

*Board of Studies in Engineering Sciences*

*In partial fulfilment of requirements*

*for the Degree of*

**DOCTOR OF PHILOSOPHY**

***of***

**HOMI BHABHA NATIONAL INSTITUTE**

**February, 2017**

# Homi Bhabha National Institute

## Recommendations of the Viva Voce Committee

As members of the Viva Voce Committee, we certify that we have read the dissertation prepared by **Samiran Sengupta** entitled **"Turbulent Mixing of Opposing Flows inside Chimney Structure of Pool type Research Reactor"** and recommend that it may be accepted as fulfilling the thesis requirement for the award of Degree of Doctor of Philosophy.

| | | |
|---|---|---|
| **Chairman - Prof. S. Banerjee** for. | (A.K. Dureja) A.D., HBNI | **Date:** 03/02/17 |
| **Guide / Convener - Prof. P. K. Vijayan** | | **Date:** 3/2/17 |
| **Co-guide - Prof. R. K. Singh** | | **Date:** 03/02/2017 |
| **Examiner - Prof. Kannan N. Iyer** | | **Date:** 03/02/2017 |
| **Member - Prof. G. K. Dey** | Gautam Kumar Dey | **Date:** 03/02/2017 |
| **Member - Prof.(Smt.) S. B. Roy** | | **Date:** 3. 2. 2017. |
| **Member - Prof. N. K. Maheswari** | Naresh kr. Maheshwari | **Date:** 3/2/17 |

Final approval and acceptance of this thesis is contingent upon the candidate's submission of the final copies of the thesis to HBNI.

I/We hereby certify that I/we have read this thesis prepared under my/our direction and recommend that it may be accepted as fulfilling the thesis requirement.

**Date:**

**Place: Mumbai**

**(Prof. R. K. Singh)**
**Co-guide**

**(Prof. P. K. Vijayan)**
**Guide**

# STATEMENT BY AUTHOR

This dissertation has been submitted in partial fulfillment of requirements for an advanced degree at Homi Bhabha National Institute (HBNI) and is deposited in the Library to be made available to borrowers under rules of the HBNI.

Brief quotations from this dissertation are allowable without special permission, provided that accurate acknowledgement of source is made. Requests for permission for extended quotation from or reproduction of this manuscript in whole or in part may be granted by the Competent Authority of HBNI when in his or her judgment the proposed use of the material is in the interests of scholarship. In all other instances, however, permission must be obtained from the author.

SSengupta

(Samiran Sengupta)

# DECLARATION

I, hereby declare that the investigation presented in the thesis has been carried out by me. The work is original and has not been submitted earlier as a whole or in part for a degree / diploma at this or any other Institution / University.

S Sengupta

(Samiran Sengupta)

# List of Publications arising from the thesis

## Journal

1. *"A numerical study of flow and mixing characteristics inside the chimney structure of a pool type research reactor"*, Samiran Sengupta, P. K. Vijayan, K. Sasidharan, V. K. Raina, Annals of Nuclear Energy, 2013, Vol .78, pp.167–180.

2. *"Numerical simulation of turbulent mixing inside scaled down model of a square chimney for a pool type research reactor"*, Samiran Sengupta, P. K. Vijayan, R. K. Singh, A. Bhatnagar, V. K. Raina, Studies in Chemical Process Technology, American Society of Science and Engineering, 2013, Vol. 1, pp. 8–23.

3. *"Numerical simulation of turbulent flow mixing inside a square chimney structure of a research reactor"*, Samiran Sengupta, P. K. Vijayan, R. K. Singh, A. Bhatnagar, V. K. Raina, Kerntechnik, 2013, Vol. 78, pp. 400–410.

4. *"PIV investigations on the turbulent mixing of two opposing flows inside a scaled chimney model of a research reactor",* Samiran Sengupta, Majid H. Khan, Vijay K. Veluri, P. K. Vijayan, Amit Agrawal, S. Bhattacharya, Experimental Thermal and Fluid Science, 2015, Vol. 63, pp. 115–132.

5. *"Experimental investigations on turbulent mixing of hot upward flow and cold downward flow inside a chimney model of a nuclear reactor",* Samiran Sengupta, Aniruddha Ghosh, C. Sengupta, P. K. Vijayan, S. Bhattacharya, R. C. Sharma, Nuclear Engineering and Design, 2016, Vol. 297, pp.291–311.

## Conferences

1. *"Design of a scaled test facility to simulate turbulent mixing inside the chimney of a pool type research reactor"*, Samiran Sengupta, P. K. Vijayan, S. B. Chafle and K. Sasidharan, 37th National and 4th International Conference on Fluid Mechanics and Fluid Power, ISBN: 978-81-910571-1-9, FMFP10-NE-02. IIT Madras, 2010

2. *"CFD simulation of turbulent mixing of two opposing flow inside the model of a chimney"*, Samiran Sengupta, P. K. Vijayan, K. Sasidharan, V. K Raina, $4^{th}$ National Conference on Nuclear Reactor Technology, Mumbai, 2011

3. *"Turbulent mixing inside the chimney model of a pool type research reactor"*, Samiran Sengupta, P. K. Vijayan, K. Sasidharan, V. K Raina, $19^{th}$ International Conference on Nuclear Engineering, ICONE19 –43613, Japan, 2011

4. *"Turbulent mixing of hot upward flow and cold downward flow inside the chimney of a pool type research reactor"*, Samiran Sengupta, P. K. Vijayan, K. Sasidharan, V. K. Raina, $21^{st}$ International Conference in Reactor Technology (SMiRT 21), Div-III: Paper ID-458, New Delhi, 2011.

5. *"Effect of chimney height and nozzle inclination on stagnation depth of chimney structure for a pool type research reactor",* Samiran Sengupta, P. K. Vijayan, S. B. Chafle, A. Bhatnagar, V. K. Raina, $20^{th}$ International Conference on Nuclear Engineering, ICONEPOWER2012 –54179, 2012.

6. *"Experimental flow test facility to study the turbulent mixing inside the chimney model of a pool type research reactor",* Samiran Sengupta, P. K. Vijayan, A. Bhatnagar, V. K. Raina, $39^{th}$ National Conference on Fluid Mechanics and Fluid Power, FMFP2012-34, SVNIT, Gujrat, 2012

7. *"Turbulent mixing of two opposing jets inside square chimney model of a pool type research reactor",* Samiran Sengupta, P. K. Vijayan, R. K. Singh, A. Bhatnagar, $22^{nd}$ National and $11^{th}$ ISHMT-ASME heat and mass transfer, HMTC1300174, IIT Kharagpur, 2013

SSengupta

(Samiran Sengupta)

# DEDICATIONS

*To*

***My Beloved Family***

Dipanwita

Anirban

Ananya

and

My Parents

# ACKNOWLEDGEMENTS

I wish to acknowledge and express my heartfelt gratitude for the support rendered to me by my guide Prof. P.K. Vijayan, Former Director Reactor Design & Development Group, BARC. His support and words, not to mention his dedication to imparting knowledge and guiding towards solutions, thereby making me feel like being a true researcher. I am also thankful to my co-guide Prof. R. K. Singh, Former Associate Director RDDG, BARC, for advising me and augmenting my knowledge for the work.

I express my sincere gratitude to Prof. Amit Agrawal, IIT Bombay for providing the PIV Laboratory facilities for this study. I am also thankful to Shri Majid Hassan Khan for helping me to carry out the PIV experiment.

I take this opportunity to express my sincere gratitude to the Chairman and members of the Doctoral committee. The internal reviews by the Doctoral committee chaired by Prof. S. Banerjee were extremely helpful for directing this research to a successful and logical end. I thank eminent members of the Doctoral committee Prof. G. K. Dey, Prof. Smt. S. B. Roy and Prof. N. K. Maheshwari for their kind advice and suggestions to improve the quality of the work.

I am also grateful to my external examiners Prof. Kannan Iyer, IIT Bombay and Prof. Simon Walker, Imperial College London for their critical comments and in-depth review of my thesis. Going through their reviews has led me to looking at the things from an altogether different perspective. This has reflected in the thesis as well at appropriate junctures.

I also want to express my profound gratitude to Shri V. K. Raina, Former Director Reactor Group, Shri K. Sasidharan, Former Head RRDPD, Shri G. Bhardwaj, Former Head RRMD for the inspiration and support for taking up the research work.

I express deep sense of gratitude to Shri R. C. Sharma, Former Director Reactor Group, Shri Anil Bhatnagar, Former Head RDDPD and Shri. Sujay Bhattacharya, Associate Director Reactor Group & Head RRDPD for their valuable guidance and continuous help. I am also thankful to Shri Shaji Mammen, Project Manager HFRR for his kind co-operation for this work. I also want to thank all the staff of Reactor Group and specifically Shri C. Sengupta, Shri C. Prabhakar, Shri Aniruddha Ghosh, Shri U. D Patil, Shri K. Chakraborty and Shri R. S. Kale for providing necessary support.

I am also thankful to Shri Deb Mukhopadhyay, Shri Brindaban Ghosh of Reactor Safety Division and Shri P. Venkat of Computer Division for their continuous help throughout this work.

Last but not the least I want to thank my family & friends. I could not achieve this without their love and support.

# CONTENTS


| Chapter No. | Topic | Page |
|---|---|---|
| **Acknowledgements** | | viii |
| **Abstract** | | xiii |
| **List of Figures** | | xv |
| **List of Tables** | | xxi |
| **Nomenclature** | | xxiii |
| **Chapter 1** | **Problem Definition – Scope & Objectives** | **1** |
| 1.1 | Introduction | 1 |
| 1.2 | Problem definition | 4 |
| 1.3 | Objectives | 10 |
| 1.4 | Organisation of thesis | 11 |
| **Chapter 2** | **Literature Survey** | **13** |
| 2.1 | Introduction | 13 |
| 2.2 | Mixing in T-junction, oblique pipe, X-junction and opposing jets | 17 |
| 2.2.1 | Dynamics of fluid mixing in T-junction | 18 |
| 2.2.2 | Turbulent mixing of hot water jet from an oblique pipe | 35 |
| 2.2.3 | Turbulent mixing in cross pipe using LES | 36 |
| 2.2.4 | Mixing of two fluids in an X-junction | 37 |
| 2.2.5 | Mixing of opposing jets | 38 |
| 2.2.5.1 | Laminar mixing of opposing jets | 39 |
| 2.2.5.2 | DNS simulation of confined jets from opposing feeder pipes | 47 |
| 2.2.5.3 | Turbulent mixing of opposing jets | 49 |
| 2.2.5.4 | Mixing of multiple opposing jets | 53 |
| 2.2.5.5 | Stagnation point offset due to impingement of opposing jets | 55 |
| 2.3 | Closure of literature review | 58 |
| 2.4 | Scope of present work | 69 |

**Chapter 3 Numerical Simulation of Prototype Chimney** **71**
3.1 Introduction 71
3.2 Flow mixing inside prototype chimney geometry 71
3.3 Validation for applicability of PHOENICS 77
3.4. Numerical simulation for 45º prototype chimney 85
3.4.1 Nodalisation and boundary conditions 86
3.4.2 Results and Discussion 89
3.4.2.1 Effect of bypass flow ratio on velocity distribution 89
3.4.2.2 Effect of bypass flow ratio on temperature distribution 99
3.4.2.3 Effect of chimney height 101
3.4.2.4 Effect of temperature difference 103
3.5 Effect of nozzle inclination for Prototype 106
3.5.1 Numerical discritisation 106
3.5.2 Results and Discussion 109
3.6 Closure 122

**Chapter 4 Scaling Philosophy** **123**
4.1 Introduction 123
4.2 Governing Equations 124
4.2.1 Assumptions 124
4.2.2 Non-dimensionalisation 126
4.3 Similitude Criteria 130
4.3.1 Simulation of Reynolds number ($Re_D$) 132
4.3.2 Simulation of Richardson number (Ri) 133
4.3.3 Simulation of Prandtl number (Pr) 135
4.3.4 Simulation of Peclet number (Pe) 136
4.4 Closure 136

**Chapter 5 Testing of Scaling Philosophy** **139**
5.1 Introduction 139
5.2 Hydrodynamic model 139
5.3 Boundary conditions 141
5.4 Results and Discussion 142
5.4.1 Effect of Core Flow on velocity distribution 151
5.4.2 Effect of Core Flow on temperature distribution 153

5.4.3 Non-dimensionalisation 153
5.4.4 Effect of chimney height 155
5.4.5 Effect of nozzle inclination 157
5.4.5.1 Nozzle inclination - 35º 157
5.4.5.2 Nozzle inclination - 25º 174
5.5 Comparison between numerical results of model and prototype 180
5.6 Closure 184

**Chapter 6 Experimental Validation in Flow Test Facility 189**
6.1 Introduction 189
6.2 Experimental loop 192
6.2.1 Process water system 194
6.2.2 Chilled water system 195
6.2.3 Instrumentation 196
6.3 Experimental procedure 200
6.4 Experimental results and discussion 203
6.4.1 Effect of bypass flow ratio 203
6.4.2 Effect of core flow 212
6.4.3 Effect of temperature 224
6.4.4 Effect of chimney height 227
6.5 Comparison between Experiment and Numerical results 234
6.6 Closure 240

**Chapter 7 Experimental Validation using PIV technique 243**
7.1 Introduction 243
7.2 Experimental setup 244
7.3 Particle Image Velocimetry system 247
7.4 Experimental procedure 250
7.5 Experimental results 252
7.5.1 Core flow – 1800 kg/hr 253
7.5.2 Core flow – 3600 kg/hr 256
7.6 Comparison with Numerical results 259
7.7 Closure 263

**Chapter 8 Conclusions and Suggestions for Future work** **265**
8.1 Contribution and Research findings 265
8.2 Conclusions 268
8.3 Scope for future work 270

**Appendix A** **271**
A.1 Principles of PIV technique 272
A.2 Components of PIV system 274
A.3 PIV images 276

**References** **279**

# ABSTRACT

Pool type research reactor often gets preference for production of radioisotopes as well as carrying out various irradiation experiments, due to its simpler design with easy accessibility from the core top. Due to limitation of the pool water height for clear visibility of the reactor core from the pool top for fuel and isotope handling operation, upward flow through the core becomes the necessity for pool type reactors having higher power density. As reactor core top is open, radioactive coolant has a tendency to reach towards the pool top due to inertia and buoyancy leading to increase in radiation level at the pool top. Since, pool top activity level should be limited during normal operation; these reactors often use an open chimney structure at the reactor core outlet.

This chimney structure facilitates guiding of the radioactive water from the reactor core towards the side outlet nozzles and simultaneously drawing water from the reactor pool through the chimney top in the downward direction. This downward flow through the chimney is compensated by providing additional core bypass flow to the reactor pool. A dynamic balance between the two opposing flows – hot water from core outlet (upward flow) and cold water from pool (the downward core bypass flow), suitable nozzle inclination and height of the chimney are required to prevent the radioactive water mixing with the bulk pool water. Though, open chimney structures have been used by some nuclear research reactors (HANARO, ETRR-2 and OPAL), very few studies are reported which identify the major parameters responsible for the fluid dynamics inside the chimney structure. The focus of the study is to identify various parameters which affect the turbulent mixing inside the chimney structure and also to specify those parameters which ensure that the radioactive coolant from the reactor core is well within the chimney region so that radiation level in the pool top is maintained below the specified limits.

Various parameters such as upward core flow, bypass flow ratio, chimney height and its nozzle inclination were identified and their effects on the velocity and temperature distributions inside three-dimensional chimney structures were studied using CFD code

PHOENICS. The effect of temperature difference between upward core flow and downward bypass flow was also analysed. The location where the upward velocity becomes zero is defined as the "stagnation height". Analyses were carried out and the stagnation heights were predicted for chimney structures considering different bypass flow conditions of the reactor. Experiments were also carried out on scaled models to validate the results of the numerical simulations.

Scaling philosophy was arrived by non-dimensionalising the basic conservation equations of mass, momentum and energy for the mixing phenomenon and preserving the relevant dimensionless numbers (such as Reynolds number, Richardson number, Prandtl number, Peclet number, height to diameter ratio and bypass flow ratio) in the prototype and in the model. Since it was not practically feasible to exactly simulate all the dimensionless numbers in the model as in the prototype, the effects due to variation in dimensionless numbers were also studied.

An experimental set up (2:9 scaled model) was established and experiments were carried out for a range of Reynolds number and bypass flow ratios. Tests were performed to establish the effect of buoyancy on the mixing behaviour. The flow visualization results were compared for validating the results obtained from the CFD simulations. Measured temperature variation along the centre line of the chimney was also compared. Correlations were developed for predicting the temperature profile, stagnation height, vortex spread height and pool temperature front height for various flow conditions through the chimney structure. For quantitative measurement of velocity field, a smaller setup (1:18 scaled model) was designed for acquiring the velocity field using Particle Image Velocimetry (PIV) technique. The measured velocity distribution in the dimensionless form was compared with the computational results obtained for the prototype and the scaled model (2:9) in order to validate the scaling philosophy as well as the CFD code predictions.

# LIST OF FIGURES


| Fig. No. | Topic | Page |
|---|---|---|
| 1.1 | Schematic diagram of open pool type reactor cooled by downward flow | 2 |
| 1.2 | Schematic diagram of open pool type reactor cooled by upward flow | 3 |
| 1.3 | Reactor pool block of HFRR with internal structures | 5 |
| 1.4 | Simplified process flow diagram of primary coolant system of HFRR | 6 |
| 1.5 | Arrangement of chimney structure with major dimension | 7 |
| 1.6 | Flow mixing behavior inside the chimney structure | 10 |
| 2.1 | Chimney structures of some pool type research reactors | 14 |
| 2.2 | Chimney model scheme of ETRR-2 (El- Morshdy, 2007) | 15 |
| 2.3 | Flow maps for various bypass flow rates (El-Morshdy, 2007) | 16 |
| 2..4 | Flow mixing in a T-junction | 18 |
| 2.5 | Vortical structures caused by a jet in cross flow (Fric and Roshko, 1994) | 21 |
| 2.6 | Mixing in T-junction with rectangular cross section (Hirota et al., 2006) | 23 |
| 2.7 | T-junction experiment in WALTON facility (Ogawa et al., 2005) | 24 |
| 2.8 | Mixing of cold main flow with a hot branch flow in a Tee junction (Hosseini, Yuki and Hashizume, 2008) | 26 |
| 2.9 | Isothermal mixing of streams in horizontal T-junction (Walker et al., 2009) | 29 |
| 2.10 | Vattenfall T-junction test facility (Elevation view) (Frank et al., 2010) | 33 |
| 2.11 | Mixing of jets from an oblique pipe to cross flow stream (Dang et al., 2008) | 35 |
| 2.12 | Turbulent mixing in cross pipe junction (Webb and Waanders, 2006) | 37 |
| 2.13 | Mixing of two fluids in an X-junction (Vicente et al., 2008) | 38 |
| 2.14 | Geometry and Flow pattern of impingement mixer (Wood et al., 1991) | 40 |
| 2.15 | Two dimensional confined laminar opposing equal jets (Hosseinalipour and Mujumdar, 1997a) | 41 |
| 2.16 | Geometry and results of impingement jet contactor (Unger et al., 1998) | 43 |
| 2.17 | Geometric configuration and flow regime (Devahastin, Mujumdar, 2002) | 45 |
| 2.18 | Half domain for 2-D mixing of opposing jets (Wang et al., 2005) | 46 |
| 2.19 | Mixing in a confined impinging jet reactor (Schwertfirm et al., 2007) | 48 |
| 2.20 | Geometric flow configuration and computational domain for 2-D opposing turbulent jets (Hosseinalipour and Mujumdar,1995) | 50 |

| | | |
|---|---|---|
| 2.21 | Stream lines for 2-D opposing turbulent jets (Hosseinalipour, and Mujumdar, 1995) | 51 |
| 2.22 | Three dimensional mixing of opposing jets (Wang and Mujumdar, 2005) | 52 |
| 2.23 | Mixing of two opposing jets (Wang and Mujumdar, 2007) | 54 |
| 2.24 | Mixing in two pairs of opposing jets jets (Wang and Mujumdar, 2007) | 55 |
| 2.25 | Geometry of CIJR and flow patterns at various Re (Li et al., 2014) | 57 |
| 2.26 | Mixing of unconfined opposed jets (Li et al., 2010) | 58 |
| 3.1 | Schematic diagram of flow mixing inside the chimney structure | 72 |
| 3.2 | Half domain model for 3-D mixing of opposing jets | 78 |
| 3.3 | Nodalisation scheme | 79 |
| 3.4 | Comparison of velocity distribution | 80 |
| 3.5 | Comparison of concentration distribution | 81 |
| 3.6 | T-junction test section for cross flow experiment (Naik-Nimbalkar, 2010) | 83 |
| 3.7 | Comparison of normalised velocity and temperature distribution between experimental data and numerical results | 84 |
| 3.8 | Isometric view of computational model | 86 |
| 3.9 | Mesh prepared in PHOENICS | 87 |
| 3.10 | Velocity distribution with R = 0.0 (H/D = 5) | 90 |
| 3.11 | Upward velocity ($v_y$) plots in x-z plane at y = 1.5D, 2D, 4D, 5D (R = 0.00) | 92 |
| 3.12 | Velocity distribution with R = 0.05 (H/D = 5) | 94 |
| 3.13 | Upward velocity ($v_y$) plots in x-z plane at y = 1.5D, 2D, 3D, 5D (R = 0.05) | 95 |
| 3.14 | Velocity distribution with R = 0.15 (H/D = 5) | 97 |
| 3.15 | Velocity ($v_y$) contour plots in x-z plane at y=1.5D, 1.75D, 2D, 5D (R=0.15) | 98 |
| 3.16 | Centre line velocity variation along the height of chimney (H/D = 5) | 99 |
| 3.17 | Temperature contours (H/D = 5) | 100 |
| 3.18 | Centre line temperature variation along the height of chimney (H/D = 5) | 101 |
| 3.19 | Effect of H/D ratio on centre line velocity variation along the height | 102 |
| 3.20 | Effect of H/D ratio on centre line temperature variation along the height | 103 |
| 3.21 | Effect of temperature differential on centre line velocity variation (H/D = 5) | 104 |
| 3.22 | Effect of temperature differential on centre line velocity variation (H/D = 4) | 104 |
| 3.23 | Effect of temperature differential on centre line velocity variation (H/D = 6) | 105 |
| 3.24 | Effect of height and temperature differential on stagnation height | 105 |
| 3.25 | Effect of height on dimensionless temperature front height | 106 |

| | | |
|---|---|---|
| 3.26 | Computational domain and mesh (H= 2.25 m, θ=35°) | 107 |
| 3.27 | Geometry of chimney structures with various height and nozzle inclination | 108 |
| 3.28 | Velocity distribution with 25° nozzle inclination for height 2.25 m (R =0.0) | 110 |
| 3.29 | Velocity distribution with 35° nozzle inclination for height 2.25 m (R =0.0) | 110 |
| 3.30 | Velocity vector plot ( y=0.0 to 2.25 m, θ= 25°, H= 2.25 m, R=0.0) | 111 |
| 3.31 | Velocity vector plot ( y=0.0 to 2.25 m, θ= 35°, H= 2.25 m, R=0.0) | 111 |
| 3.32 | Velocity distribution with 25° nozzle inclination for height 2.25 m (R=0.15) | 112 |
| 3.33 | Velocity distribution with 35° nozzle inclination for height 2.25 m (R=0.15) | 112 |
| 3.34 | Velocity vector plot (y=0.0 to 2.25 m, , θ= 25°, H=2.25 m, R=0.15) | 113 |
| 3.35 | Velocity vector plot (y=0.0 to 2.25 m, , θ= 35°, H=2.25 m, R=0.15) | 113 |
| 3.36 | Variation of stagnation height with nozzle inclination (H= 2.25 m) | 114 |
| 3.37 | Variation of stagnation height with nozzle inclination (H=2.7 m) | 115 |
| 3.38 | Temperature contour plot with 25° nozzle inclination (H= 2.25 m, R=0.05) | 116 |
| 3.39 | Temperature contour plot with 35° nozzle inclination (H=2.25 m, R=0.05) | 116 |
| 3.40 | Temperature contour plot with 25° nozzle inclination (H= 2.25 m, R=0.15) | 117 |
| 3.41 | Temperature contour plot with 35° nozzle inclination (H= 2.25 m, R=0.15) | 118 |
| 3.42 | Variation of temperature front height with nozzle inclination (H=2.25 m) | 118 |
| 3.43 | Variation of pool temperature front depth with nozzle inclination (H=2.7 m) | 119 |
| 3.44 | Variation of dimensionless stagnation height (H/D= 5) | 120 |
| 3.45 | Variation of dimensionless stagnation height (H/D= 6) | 120 |
| 3.46 | Variation of dimensionless temperature front height (H/D=5, H/D=6) | 121 |
| 4.1 | Geometry of the chimney model | 123 |
| 5.1 | Computational model | 140 |
| 5.2 | Mesh for computation | 141 |
| 5.3 | Velocity distribution (R = 0.0) | 144 |
| 5.4 | Velocity distribution (R = 0.05) | 145 |
| 5.5 | Velocity distribution (R = 0.10) | 146 |
| 5.6 | Velocity distribution (R = 0.15) | 147 |
| 5.7 | Centre line velocity distribution along y-direction | 148 |
| 5.8 | Temperature distribution (R = 0.05) | 149 |
| 5.9 | Temperature distribution (R = 0.10) | 150 |
| 5.10 | Temperature distribution (R = 0.15) | 150 |
| 5.11 | Centre line temperature distribution along y-direction | 151 |

5.12 Centre line velocity distribution along y-direction (upward flow=16.67 kg/s) 152
5.13 Centre line velocity distribution along y-direction (upward flow=25 kg/s) 152
5.14 Effect of flow on centre line temperature distribution 153
5.15 Dimensionless centre line velocity distribution 154
5.16 Dimensionless centre line temperature distribution 155
5.17 Effect of chimney height and flow on centre line velocity distribution 156
5.18 Effect of chimney height and flow on centre line temperature distribution 156
5.19 Mesh used for computation domain (θ=35°, H=0.6 m) 157
5.20 Velocity distribution for core flow of 12.5 kg/s (R=0.0, θ=35°, H=0.6 m) 160
5.21 Velocity vector in central chimney ($W_{in}$=12.5 kg/s, R=0.0, θ=35°, H=0.6m) 161
5.22 Velocity distribution for core flow of 12.5 kg/s (R=0.05, θ=35°, H=0.6 m) 162
5.23 Velocity vector in central chimney ($W_{in}$=12.5 kg/s, R=0.05, θ=35°) 162
5.24 Velocity distribution for core flow of 12.5 kg/s (R=0.10, θ=35°, H=0.6 m) 163
5.25 Velocity vector in central chimney ($W_{in}$=12.5 kg/s, R=0.10, θ=35°) 164
5.26 Velocity distribution for core flow of 12.5 kg/s (R=0.15, θ=35°, H=0.6 m) 164
5.27 Velocity vector in central chimney ($W_{in}$=12.5 kg/s, R=0.15, θ=35°) 165
5.28 Centre line upward velocity variation with chimney height ($Re_D$= 2.25×10$^5$) 166
5.29 Temperature contours - core flow 12.5 kg/s (R=0.05, 0.10, 0.15) 168
5.30 Centre line temperature variation with chimney height ($Re_D$ = 2.25×10$^5$) 168
5.31 Centre line upward velocity variation ($Re_D$ = 3×10$^5$, 3.75×10$^5$, 4.5×10$^5$) 169
5.32 Centre line temperature variation ($Re_D$ = 3×10$^5$, 3.75×10$^5$, 4.5×10$^5$) 170
5.33 Dimensionless velocity variation with dimensionless height (θ=35°) 171
5.34 Dimensionless temperature variation with dimensionless height (θ=35°) 172
5.35 Dimensionless stagnation height variation with $Re_D$ (θ=35°) 173
5.36 Dimensionless pool temperature front height variation with $Re_D$ (θ=35°) 173
5.37 Computational domain (H = 0.5 m, inclination θ = 25°) 174
5.38 Centre line velocity variation (θ=25°, $Re_D$ = 3×10$^5$, 3.75×10$^5$, 4.5×10$^5$) 176
5.39 Centre line temperature variation (θ=25°,$Re_D$ = 3×10$^5$, 3.75×10$^5$, 4.5×10$^5$) 177
5.40 Dimensionless velocity variation with dimensionless height (θ=25°) 178
5.41 Dimensionless temperature variation with dimensionless height (θ=25°) 178
5.42 Dimensionless stagnation height variation with Reynolds number $Re_D$ (θ=25°, H/D=5, 6 and ΔT = 9, 0ºC) 179
5.43 Variation of dimensionless height of pool temperature front with $Re_D$ (θ=25°, H/D = 5,6) 180

| | | |
|---|---|---|
| 5.44 | Variation of dimensionless upward velocity for model and prototype (θ=25°, 35°,45°) | 181 |
| 5.45 | Variation of dimensionless temperature profile for model and prototype (θ=25°, 35°,45°) | 183 |
| 5.46 | Variation of dimensionless stagnation height for model and prototype (θ=25°, 35°,45°) | 185 |
| 5.47 | Variation of dimensionless height of pool temperature front for model and prototype (θ=25°, 35°,45°) | 186 |
| 6.1 | Schematic diagram of mixing behaviour in side chimney and tank | 189 |
| 6.2 | Details of Process water tank along with internals | 191 |
| 6.3 | Details of the Experimental Setup | 193 |
| 6.4 | Simplified Process & Instrument diagram of experimental facility | 196 |
| 6.5 | Stagnation height ($h_S$) and Vortex spread height ($h_V$) | 202 |
| 6.6 | Experimental results ($W_{in}$=500 lpm, $W_b$=75 lpm) | 205 |
| 6.7 | Experimental results ($W_{in}$=500 lpm, $W_b$=50 lpm) | 207 |
| 6.8 | Experimental results ($W_{in}$=500 lpm, $W_b$=25 lpm) | 209 |
| 6.9 | Experimental results ($W_{in}$=500 lpm, $W_b$=0 lpm) | 211 |
| 6.10 | Experimental results ($W_{in}$=1000 lpm, $W_b$=150 lpm) | 214 |
| 6.11 | Experimental results ($W_{in}$=1000 lpm, $W_b$=100 lpm) | 215 |
| 6.12 | Experimental results ($W_{in}$=1000 lpm, $W_b$=50 lpm) | 216 |
| 6.13 | Experimental results ($W_{in}$=1000 lpm, $W_b$=0 lpm) | 217 |
| 6.14 | Experimental results ($W_{in}$=1500 lpm, $W_b$=225 lpm) | 220 |
| 6.15 | Experimental results ($W_{in}$=1500 lpm, $W_b$=150 lpm) | 221 |
| 6.16 | Experimental results ($W_{in}$=1500 lpm, $W_b$=75 lpm) | 222 |
| 6.17 | Experimental results ($W_{in}$=1500 lpm, $W_b$=0 lpm) | 223 |
| 6.18 | Effect of temperature and core flow on temperature profile | 226 |
| 6.19 | Effect of core flow on temperature profile for chimney (H=0.6 m) | 228 |
| 6.20 | Effect of chimney height and Reynolds number on temperature profile | 231 |
| 6.21 | Photographed images (H = 0.6 m) | 232 |
| 6.22 | Variation of Stagnation height and Vortex spread height with $Re_D$ | 233 |
| 6.23 | Comparison of stagnation height - experiments and numerical simulations | 235 |
| 6.24 | Temperature profile - experiment and numerical results (H = 0.5 m) | 236 |
| 6.25 | Comparison between experiment and numerical simulation (H = 0.6 m) | 236 |
| 6.26 | Effect of temperature difference on mixing ($W_{in}$=1000 lpm, H/D=6) | 237 |
| 6.27 | Effect of temperature difference on mixing ($W_{in}$=1500 lpm, H/D=6) | 238 |

| | | |
|---|---|---|
| 6.28 | Effect of temperature difference on mixing ($W_{in}$=500 lpm, H/D=6) | 239 |
| 7.1 | Geometry of the chimney model | 243 |
| 7.2 | Simplified Process flow diagram of experimental setup for PIV | 245 |
| 7.3 | Experimental set up | 246 |
| 7.4 | Front view of set up showing rotameters and regulating ball valves | 247 |
| 7.5 | Experimental set up showing Laser head mounted on the top and Camera from the front side of the chimney | 248 |
| 7.6 | Velocity vector plots from PIV data ($W_{in}$=1800 kg/hr, $Re_D$=20000) | 254 |
| 7.7 | Upward centre line velocity variation from PIV data ($W_{in}$=1800 kg/hr, $Re_D$=20000) | 256 |
| 7.8 | Velocity vector plots from PIV data ($W_{in}$=3600 kg/hr, $Re_D$=40000) | 257 |
| 7.9 | Upward centre line velocity variation from PIV data ($W_{in}$=3600 kg/hr, $Re_D$=40000) | 258 |
| 7.10 | Dimensionless centre line velocity variation from PIV data ($Re_D$=20000, 40000) | 259 |
| 7.11 | Experimental data Vs. Computation results (R=0.0) | 260 |
| 7.12 | Experimental data Vs. Computation results (R=0.05) | 260 |
| 7.13 | Experimental data Vs. Computation results (R=0.10) | 261 |
| 7.14 | Experimental data Vs. Computation results (R=0.15) | 261 |
| 7.15 | Dimensionless stagnation height - Experimental data Vs. Computation results | 263 |
| A.1 | Sketch of a typical PIV system | 271 |
| A.2 | Sketch of successive processes of the PIV system | 273 |
| A.3 | Light sheet formation using cylindrical and spherical lens for PIV | 275 |
| A.4 | Captured images (Top images – Laser A, Bottom images – Laser B) | 277 |
| A.5 | Image captured showing seeding particles | 277 |

# LIST OF TABLES


| Table No. | Topic | Page |
|---|---|---|
| 2.1 | Summary of literature | 65 |
| 3.1 | Experimental conditions for simulation (Naik-Nimbalkar et al., 2010) | 82 |
| 3.2 | Variation of $h_S/D$ with inclination and bypass flow ratio for H/D=5 | 119 |
| 3.3 | Variation of $h_S/D$ with inclination and bypass flow ratio for H/D=6 | 121 |
| 4.1 | Details of prototype and scaled down model | 130 |
| 4.2 | Reynolds number simulation | 132 |
| 4.3 | Heater power requirement for Reynolds number simulation | 133 |
| 4.4 | Richardson number simulation with height H=2.7 m (Model H=0.6 m) | 134 |
| 4.5 | Heater power requirement for Richardson number simulation | 135 |
| 4.6 | Test Matrix - Comparison of prototype and model parameters (H/D = 6) | 137 |
| 4.7 | Test Matrix - Comparison of prototype and model parameters (H/D = 5) | 138 |
| 5.1 | Values of constants for turbulence model | 140 |
| 5.2 | Dimensionless numbers for chimney model with 35° nozzle inclination | 158 |
| 5.3 | Dimensionless numbers for chimney model with 25° nozzle inclination | 175 |
| 6.1 | Instrument details and Accuracy of the measured values | 199 |
| 6.2 | Test cases for the model chimney (H = 500 mm) | 203 |
| 6.3 | Dimensionless pool temperature front height ($h_T^*=h_T/D$) | 229 |
| 6.4 | Correlation for dimensionless temperature profile | 230 |
| 6.5 | Dimensionless vortex spread height ($h_V/D$) and stagnation height ($h_S/D$) | 234 |
| 7.1 | Comparison of prototype chimney and scaled down model | 244 |
| 7.2 | Test cases for the experiments | 252 |

## NOMENCLATURE

| | |
|---|---|
| A | area of square cross section of chimney (m$^2$) |
| C | concentration (%) |
| $c_p$ | specific heat of liquid (J/kg/K) |
| D | side of the central square chimney (m) |
| $G_b$ | production rate of turbulent kinetic energy by gravitational force (W/m$^3$) |
| Gr | Grashof number [$g\beta(T_{in}-T_p)H^3/\nu^2$] |
| g | gravitational acceleration (m/s$^2$) |
| H | height of chimney (m) |
| H* | height to side ratio (H/D) |
| $h_S$ | stagnation height (m) |
| $h_T$ | pool temperature front height (m) |
| $h_V$ | votex spread height (m) |
| $h_S$* | dimensionless stagnation height ($h_S$/D) |
| $h_T$* | dimensionless pool temperature front height ($h_T$/D) |
| $h_V$* | dimensionless vortex spread height ($h_V$/D) |
| k | fluid thermal conductivity (W/m/K) |
| $l_m$ | mixing length (m) |
| P | dimensionless pressure of fluid ($p/\rho/U_{in}^2$) |
| Pe | Peclet number ($Re_D$.Pr) |
| Pr | Prandtl number ($C_p\mu/k$) |
| $P_k$ | production rate of turbulent kinetic energy by shear force (W/m$^3$) |
| p | pressure of fluid (Pa) |
| R | bypass flow ratio ($W_b/W_{in}$) |
| $Re_b$ | Reynolds mumber based on bypass flow ($\rho U_b D/\mu$) |
| $Re_D$ | Reynolds number ($\rho U_{in} D/\mu$) |
| Ri | Richardson number [$g\beta(T_{in}-T_p)H/U_{in}^2$] |
| $S_d$ | stagnation depth (m) |
| T | temperature (ºC) |
| T* | dimensionless temperature $(T-T_c)/(T_h-T_c)$ |
| $T_h$ | hot water (core flow) inlet temperature (ºC) |
| $T_c$ | cold water (bypass flow) inlet temperature (ºC) |
| $U_b$ | average fluid velocity at top inlet of chimney (m/s) |

$U_{in}$ average fluid velocity at bottom inlet of chimney (m/s)

$U_\tau$ resultant friction velocity (m/s)

$V_x$ dimensionless velocity in x direction ($v_x/U_{in}$)

$V_y$ dimensionless velocity in y direction ($v_y/U_{in}$)

$V_z$ dimensionless velocity in z direction ($v_z/U_{in}$)

$v_x$ fluid velocity in x direction (m/s)

$v_y$ fluid velocity in y direction (m/s)

$v_z$ fluid velocity in z direction (m/s)

W mass flow rate (kg/s)

x co-ordinate axes (m)

y co-ordinate axes (m)

Y dimensionless y distance (y/D)

z co-ordinate axes (m)

## Symbols

$\alpha$ thermal diffusivity ($k/\rho c_p$)

$\Delta$ difference (dimensionless)

$\varepsilon$ turbulence energy dissipation rate (W)

*k* turbulent kinetic energy (J)

$\mu$ viscosity ($Ns/m^2$)

$\nu_t$ turbulent viscosity ($m^2/s$)

$\rho$ fluid density ($kg/m^3$)

## Subscripts

b bypass

c cold

h hot

in inlet to chimney

p pool water

S stagnation

T temperature front

V vortex spread

x, y, z co-ordinates

# Chapter 1

# Problem Definition – Scope & Objectives

## 1.1 Introduction

Turbulent mixing has various applications in industry such as chemical reaction, mixing in pipelines and combustion processes. The mixing of two or more fluid streams is common in many power, chemical process or environmental applications. Mixing is also important in many manufacturing operations for the chemical, biochemical and pharmaceutical industries. Mixing also plays an important role in nuclear reactor applications specifically in multi-rod bundles between inter connected subchannels. Another application in nuclear reactors is ECCS injection, where thermal load is dependent on the mixing behaviour of hot fluid with the cold fluid and local temperature fluctuations. This load is determined for carrying out the stress and fatigue analysis for various components such as surge and spray lines, safety injection lines, several branch lines & nozzles.

In nuclear research reactor applications also turbulent mixing is used for spraying water in the emergency spray header on the top of the core; formation of hot water layer on the top of the pool; mixing of core outlet water into the pool etc. For open pool type research reactors with low power, core cooling is achieved through downward forced flow, where pool water is sucked through the core by pumps. Core outlet water being radioactive is passed through delay tanks for providing sufficient decay of the radioactive nuclides & through heat exchangers to transfer heat and finally gets mixed into the pool after completing a closed loop (Fig. 1.1). However, when reactor power increases leading to larger power density, the available pressure head of pool height (which is restricted due to concern of fuel and isotope handling) cannot provide sufficient downward flow for cooling of the core. In case the coolant velocity through the reactor core is increased to augment the heat transfer capability, the pressure drop across the core increases. Since reactor pool is open to atmosphere and the water level above the core is usually kept less than 10 m to facilitate handling of fuel and irradiation assemblies, the core inlet pressure is about 1 bar(g). Moreover, the reactor core being compact with plate type fuel having narrow gap (about 2-3 mm) between fuel bearing plates, pressure drop across the core is about 2 bar. This causes core outlet pressure to fall below atmospheric pressure to that extent that cavitation might take place and hence is not acceptable.

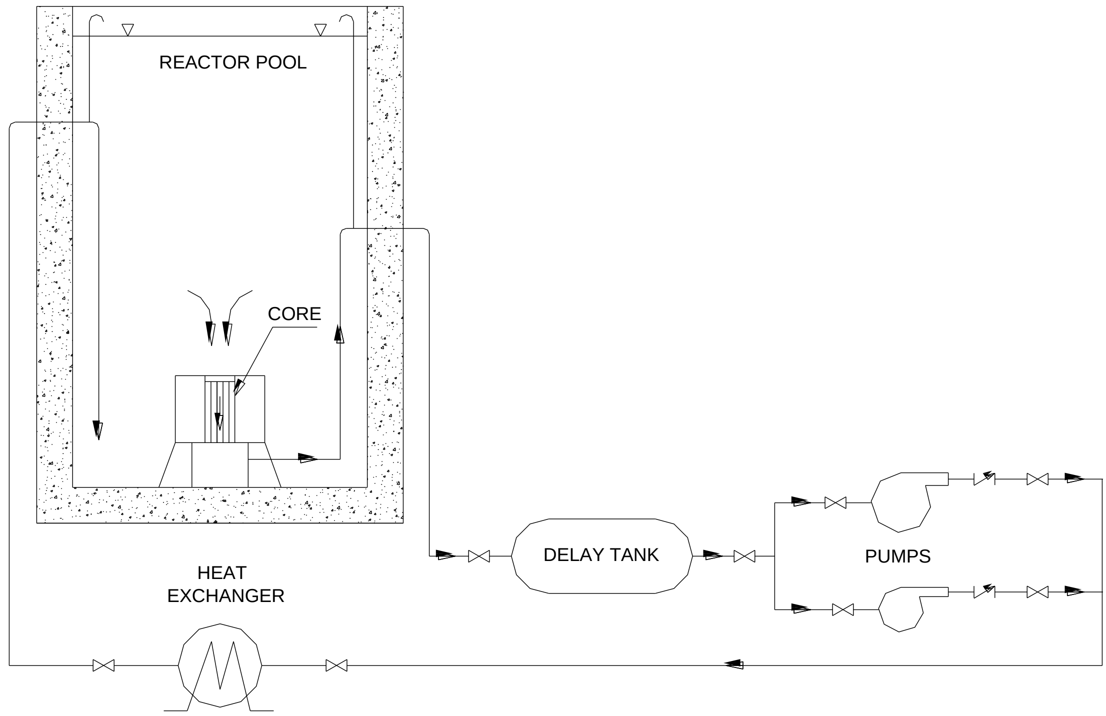


Fig. 1.1: Schematic diagram of open pool type reactor cooled by downward flow

This difficulty can be circumvented by changing the direction of flow to upward through the core, so that required higher pressure at the inlet of the core can be provided at the bottom of the core by pump developed pressure. But, this leads to the problem of mixing core outlet water directly into the pool, which causes concern of the radioactive nuclides getting mixed with pool water causing higher radiation field at the pool top and makes the area inaccessible during normal operation of the reactor. To avoid this mixing of radio-nuclides of core outlet water directly into the pool, a chimney structure is provided on the top of the core in some reactors. This allows to guide the core outlet water to the outlet nozzles so that radioactive water can be sent through delay tank to decay down the radio-nuclides (mainly $N^{16}$) and then through heat exchanger for transferring heat and finally sent back to the core (Fig. 1.2). A part of this flow before sending to the core is mixed into the pool, which is sucked into the chimney from the top. This helps in reducing the hot upward jet of core outlet water entering into the pool.

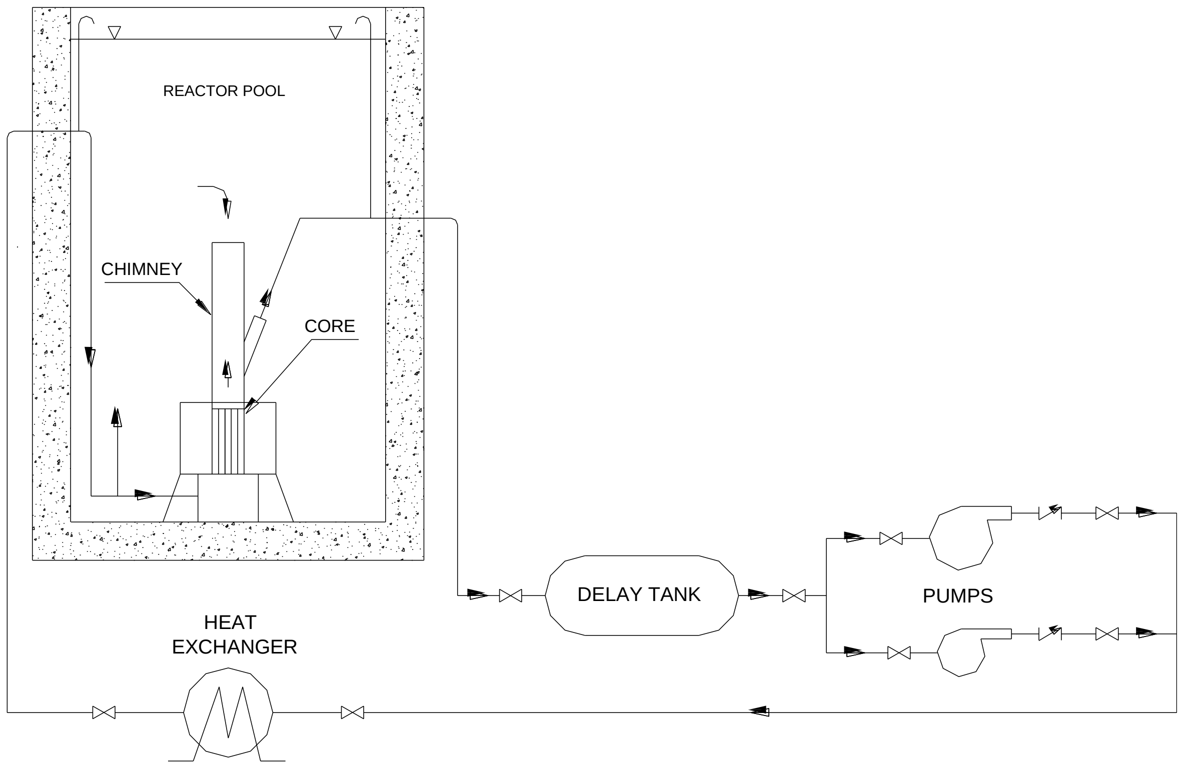


Fig. 1.2: Schematic diagram of open pool type reactor cooled by upward flow

Though this concept has been used in many research reactors (e.g., HANARO in Korea, ETRR-2 in Egypt, ANSTO RRR in Australia and OSIRIS in France), due to large variation of chimney structures and also boundary conditions of flow parameters, detailed three dimensional studies of mixing inside the chimney have not been reported in literature. The present work considers this problem of turbulent mixing of upward flowing hot fluid and downward flowing cold fluid inside the chimney of open pool type research reactors.

## 1.2 Problem definition

Open pool type research reactors are often preferred for production of isotopes and irradiation experiments, due to its simple design and easy accessibility from the reactor pool top. With increasing demand for higher neutron flux, reactor power density increases and higher velocity of coolant flow through the core is required to remove the heat from the reactor core. This requires larger driving pressure differential across the reactor core. However, due to limitation of the pool height for clear visibility of the reactor core from the pool top (to facilitate handling of fuel and radioisotopes), upward flow through the core becomes the only choice for this type of reactors. The pressure at the bottom of the reactor core can be increased by this way to provide the required pressure differential to overcome the resistance of the core.

However, there is a specific disadvantage of selecting upward flow through the core. After passing through the core, the coolant becomes radioactive due to formation of $N^{16}$, $O^{19}$, $Na^{24}$, $Ar^{41}$ etc., by nuclear reactions with neutrons present in the core. Since the reactor core top is kept open for facilitating fuel and isotope handling, the radioactive coolant which is flowing in the upward direction has a tendency to reach the pool top due to its inertia and also due to buoyancy (because of hotter core outlet water than pool water). This leads to an increase in radiation level at the pool top. Since, pool top activity level should be limited during normal operation; these reactors often use an open chimney structure at the reactor core outlet in order to prevent radioactive coolant reaching the pool top. The chimney design facilitates guiding of the radioactive water from the reactor core towards the side outlet nozzles and simultaneously allows sucking of water from the reactor pool through the chimney top opening. A typical example is High Flux Research Reactor (HFRR) being developed at BARC. An isometric view of reactor pool block indicating the arrangement of the chimney structure on the top of the reactor core is shown in Fig. 1.3.

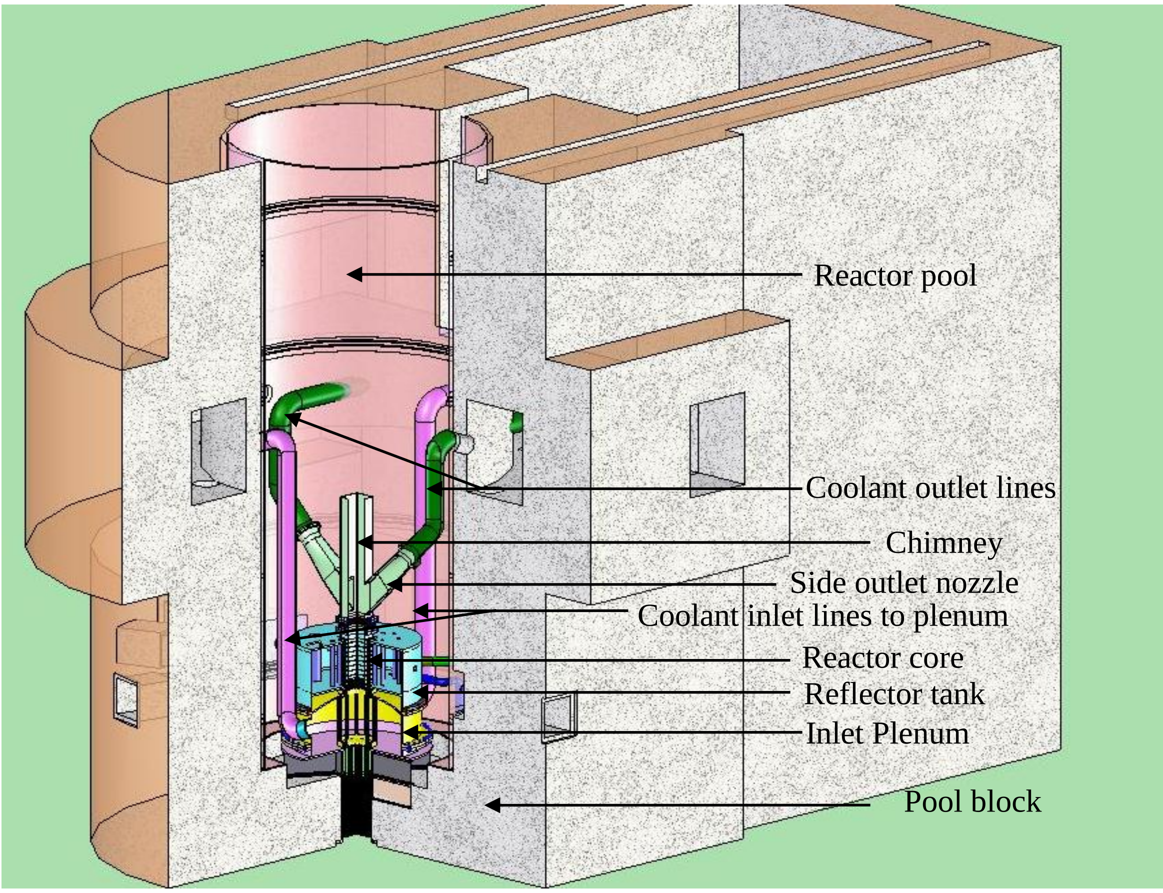


Fig. 1.3: Reactor pool block of HFRR with internal structures

A simplified flow diagram of the primary coolant system of the HFRR is shown in Fig. 1.4. The reactor core is cooled by forced upward flow through the fuel assemblies. The hot water from core outlet is guided through a chimney and is drawn by a set of primary coolant pumps through the two side outlet nozzles of the chimney. The core outlet water being radioactive is passed through delay tanks to decay down the activity level mainly caused by $N^{16}$ radio-nuclides. Subsequently primary coolant water is sent through the heat exchangers where heat is transferred to the secondary coolant. Cold primary coolant water from the outlet of the heat exchangers is fed back to the inlet plenum at the bottom of the reactor core.

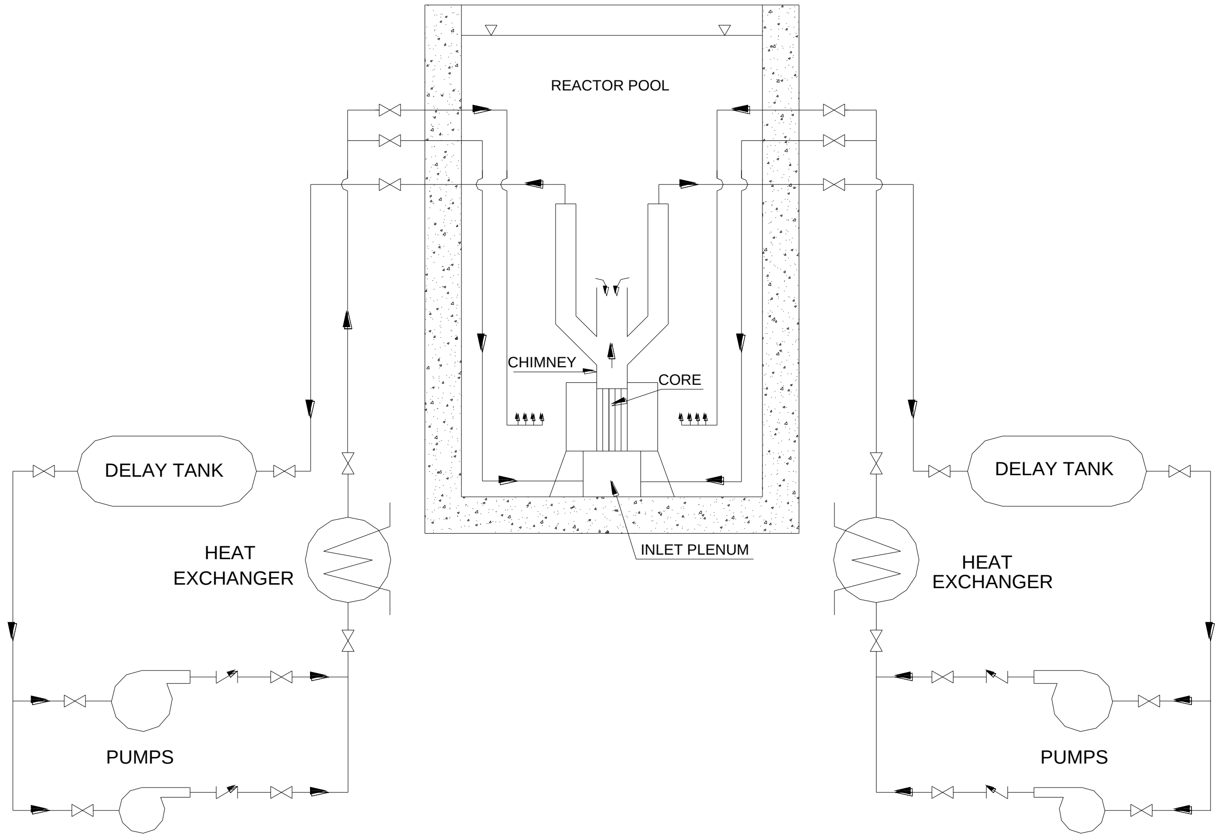


Fig. 1.4: Simplified process flow diagram of primary coolant system of HFRR

Since core outlet water has become radioactive due to neutron activation of coolant water inside the reactor core, it is not desirable to mix core outlet water with the pool water. This is achieved by providing a chimney at the core outlet. Figure 1.5 shows the structural arrangement of chimney with major dimension proposed for HFRR. For clarity piping is not shown in the figure. Because of high velocity (about 4 m/s) of hot water at the core outlet, it tries to reach to the top of the pool through the top opening of the chimney. In order to prevent this upward flow crossing the top opening of the chimney; a downward flow from the pool through the top opening of the chimney is desirable. Both the upward

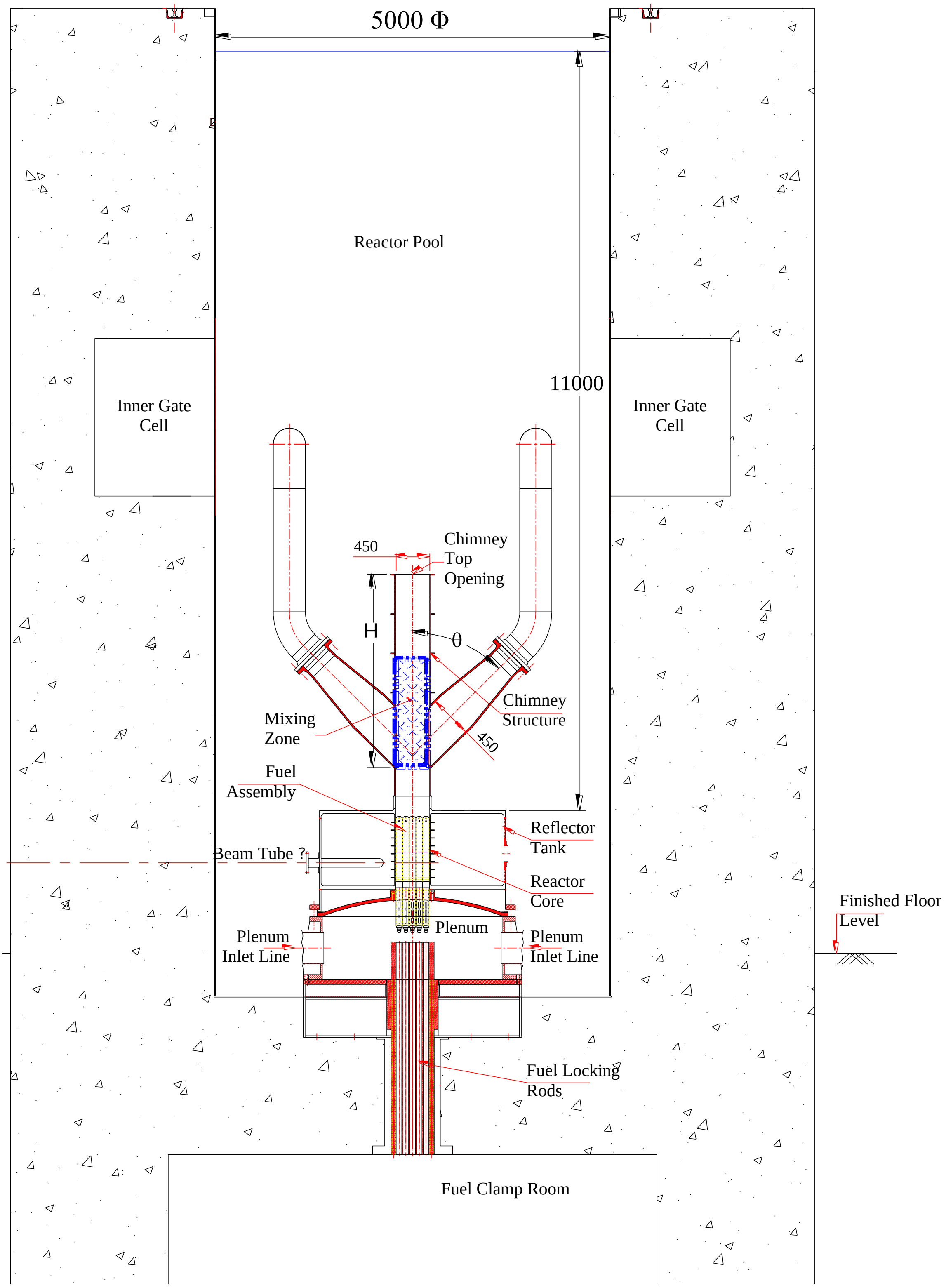


Fig. 1.5: Arrangement of chimney structure with major dimension

flow from the core outlet and the downward flow from the pool mix together inside the chimney (expected mixing zone shown in Fig. 1.5). The combined flow is sucked out through the side nozzles of the chimney with the help of the primary coolant pumps. The downward flow into the chimney from the pool is compensated by providing a core bypass flow discharged to the pool.

Similar to normal operating condition, mixing of hot water from the core and cold water from the pool takes place inside the chimney even after shut down of the reactor for a period of about 2 hours. However, during this period, only 10% of the normal flow is maintained by auxiliary coolant pumps to transfer the decay heat produced by the decay of radioactive fission products. Since the flow velocity is reduced to 10% of the normal flow, the upward strong current decreases and the activation level of core outlet water also decreases due to lower neutron population in the core during this period.

During reactor operation at full power, water activity in the reactor core is about $10^6$Bq/ml because of $N^{16}$ production. Activity in the reactor pool water is about $10^3$Bq/ml due to build up of $Na^{24}$, $Mg^{27}$ and $Al^{28}$ (mainly because of the bypass flow joining the pool water). All these nuclear reactions require neutrons of high energy as explained in the following section. During normal reactor operation with full power, no leakage from core to reactor pool is acceptable because of very high activity ($10^6$Bq/ml) of core outlet water. However, after reactor shut down, high energy neutrons will not be available and within 2 minutes the water activity inside core will reduce to$10^3$Bq/ml which is equivalent to pool water activity due to presence of long lived radionuclides (i.e., $Na^{24}$, $Mg^{27}$ and $Al^{28}$). Downward flow is still continued from reactor pool to chimney by forced cooling using shutdown pumps. Natural circulation valve is opened after 2 hours and by that time the activity level of pool water and water inside reactor core is of similar order (<1000

Bq/ml). Hence upward flow from chimney to reactor pool will not cause higher radiation field in pool top.

$N^{16}$formation requires neutrons having energies above 10.24 MeV. It decays to $O^{16}$ with a half-life of 7.1 s emitting gammas of energies 6.13 MeV and 7.1 MeV. The reaction governing this activation is $O^{16}(n,p)N^{16}$.

$Na^{24}$ is produced due to the interaction of fast neutrons ($\geq$ 3.74 MeV) with aluminum atoms. It decays to $Mg^{24}$ with a half-life of about 15 hours by emitting a beta ($\beta$) particle of 1.4 MeV energy and two photons of energies 1.37 MeV and 2.75 MeV. The reaction governing this activation is $Al^{27}(n,\alpha)Na^{24}$.

$Mg^{27}$is also produced due to the interaction of fast neutrons ($\geq$ 2.25 MeV) with aluminum atoms. It decays back to $Al^{27}$ with a half-life of 9.5 min., emitting a beta ($\beta$) and a gamma of energies about 1.7 MeV and 1 MeV respectively. The reaction governing this activation is $Al^{27}(n,p)Mg^{27}$.

$Al^{28}$is produced due to the interaction of thermal energy neutrons with aluminum atoms. It decays to $Si^{28}$with a half-life of about 2.25 min emitting a beta particle ($\beta$) and a gamma of energies 2.86 MeV and 1.78 MeV respectively. The reaction responsible for this activation is $Al^{27}(n,\gamma)Al^{28}$.

Long term shut down cooling is ensured by natural circulation flow through the core by opening the natural circulation valves (NCVs) provided at the core inlet lines before joining the inlet plenum. During this period, only upward flow takes place within the chimney. Since activation level of water in the core has decayed down significantly by this time and the upward velocity is also small, mixing of core outlet water in pool is not a matter of concern during this period.

Therefore, the most severe condition of concern is the mixing of radioactive core outlet water with pool water during the normal operating condition, which is considered further for the simulation in the project work.

### 1.3 Objectives

The present work aims at studying the complex flow behaviour of coolant water inside the chimney of a research reactor, located on the top of the reactor core. A sketch showing the expected flow mixing behavior inside the chimney which is the major interest of our study is shown in Fig 1.6. The stagnation point, where the upward velocity becomes zero and the stagnation height ($h_s$) is also shown in the sketch. The distance of stagnation point from the chimney bottom reference is defined as the stagnation height.

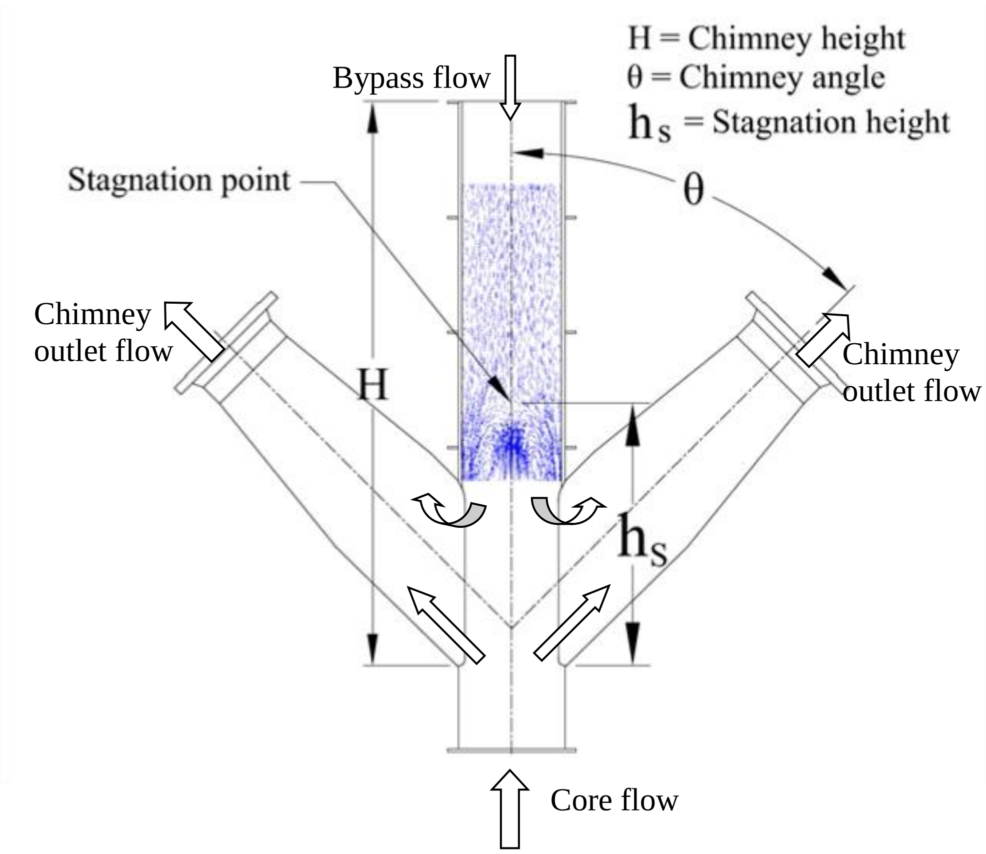


Fig. 1.6: Flow mixing behavior inside the chimney structure

The mixing behaviour in the chimney region needs to be characterised to ensure that there is no flow out from the chimney to the reactor pool. Moreover, the spread of the radioactive water within the chimney (of height about 3 m and cross section 0.45 m × 0.45 m) and radioactivity decaying effect due to delay caused during upward movement (due to low velocity) are also important parameters to affect the radiation field at the pool top. Hence the velocity distribution in the chimney region is important.

The behaviour of water coolant inside the chimney being complex in nature, this is proposed to be studied using CFD codes to realistically simulate the turbulent mixing. CFD codes are considered to be robust for single phase flow conditions. However, validation of CFD codes for nuclear applications is lacking for the study presented here where the hydro-dynamics of the mixing phenomenon inside the confined chimney structure is very much dependent on the flow behaviour inside the reactor pool. The flow distribution across the cross section at the top entry region of the chimney is decided by dynamic balancing depending on the bypass flow sent to the reactor pool as well as the thermal mixing occurring between the pool water and the core outlet water. The major objectives of this present study are to investigate the mixing of the upward and downward flows inside the chimney structure and to characterise its behaviour for

(i) various bypass flow ratios

(ii) different inclination angles between the central chimney and the outlet nozzle

(iii) change in chimney height

(iv) isothermal conditions of opposing flow

(v) upward flow as hot fluid and downward flow as cold fluid.

## 1.4 Organisation of thesis

The thesis is organized in nine chapters.

i) Chapter 1 gives the general introduction, the problem definition, scope and objectives of the study.

ii) Literature survey is given in Chapter 2.

iii) Numerical simulation of turbulent mixing inside the prototype chimney structure is given in Chapter 3.

iv) Scaling philosophy is described in Chapter 4.

v) In Chapter 5, the scaling philosophy is tested by comparing the numerical results of the model and that of the prototype for various angles, heights of the chimney and flow conditions.

vi) The experimental validation of the computational results is presented in Chapter 6. Experimental setup, instrumentation and experimental procedure are described. Finally Experiments conducted and the results obtained are compared with numerical simulation results.

vii) In Chapter 7, experimental study using PIV set up is described. The velocity field predicted from the experiments is compared with numerical results for validation of the CFD code.

viii) Summary, conclusions and suggestions for future work are presented in Chapter 8.

Additional background material associated with the present work is provided in Appendix.

# Chapter 2

# Literature Survey

## 2.1 Introduction

Turbulent mixing of upward flowing hot fluid and downward flowing cold fluid inside the chimney of pool type research reactors is a complex phenomenon. Provision of open chimney structure is used at the reactor core outlet to prevent mixing of radioactive coolant from the core with the bulk pool water by some nuclear research reactors - HANARO (Kim et al., 1996) in Korea; ETRR-2 (Abou Mandour et al., 2007) in Egypt; ANSTO RRR (Doval and Mazufri, 2002) in Australia and OSIRIS (Nuclear Energy Directorate Division, CEA, 2002) in France. The open chimney structures of some of these reactors found in the literature are shown in Fig. 2.1. Due to the complex flow behaviour, wide variation of chimney structures and boundary conditions, detailed three dimensional studies have not been reported. No literature is available to correlate parameters such as bypass flow ratio, temperature difference between the opposing flows, inclination between central chimney & outlet nozzle as well as the chimney height etc., which may affect the mixing behaviour.

El-Morshdy (2007) had made an analytical study considering steady, incompressible, irrotational flow to predict the stagnation depth for the core chimney of the Egyptian research reactor (ETRR-2). The limitation of the model does not allow more realistic simulation of complex fluid flow behavior with turbulence inside the chimney. ETRR-2 core chimney was modelled with simplified assumptions of potential flow considering two dimensional geometry of the chimney. The potential flow equations were discretized using finite difference technique for the entire domain.

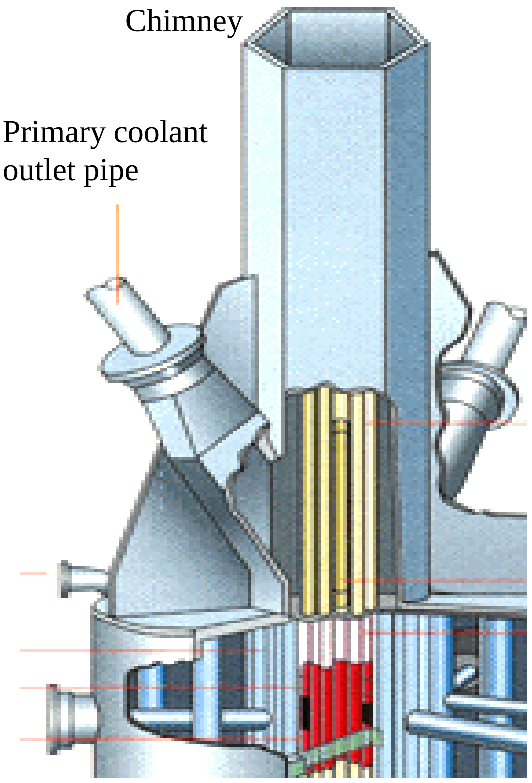


HANARO (Kim et al., 1996)


ETRR-2 (Abou Mandour et al., 2007)

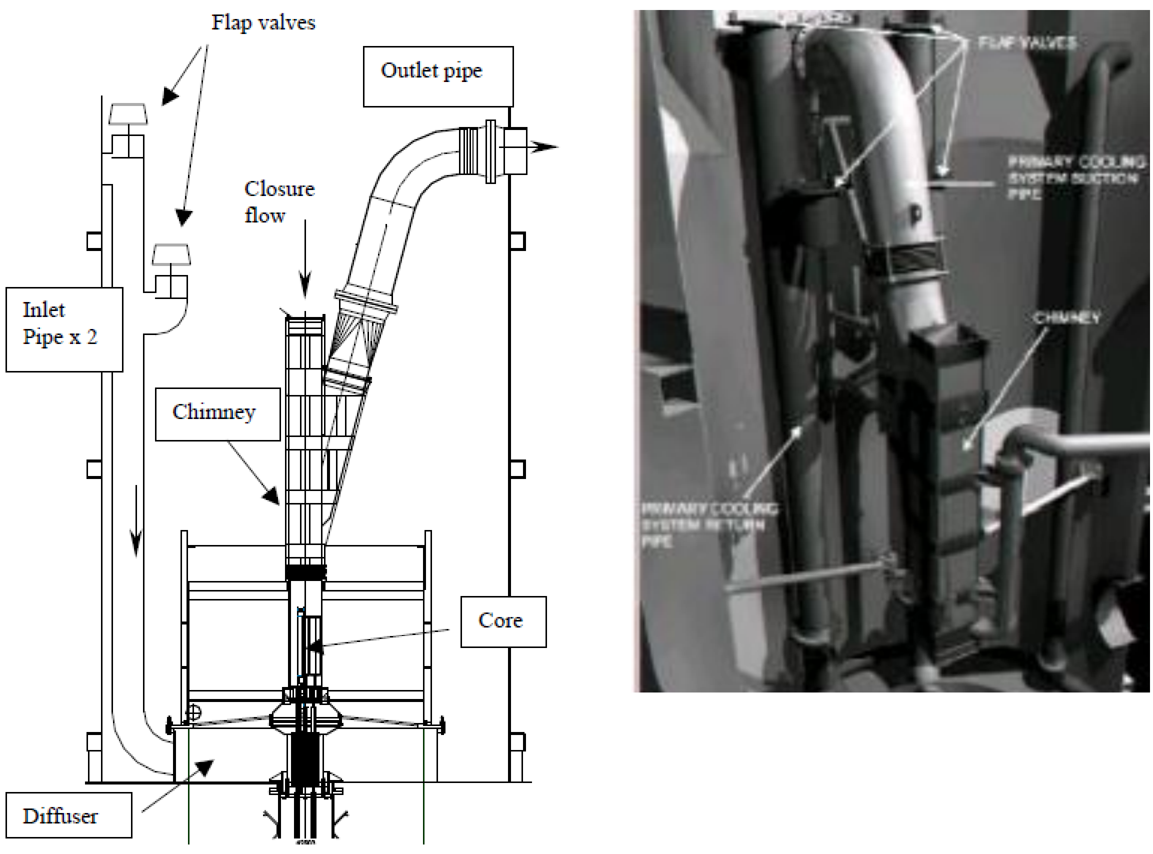


ANSTO RRR (Doval and Mazufri, 2002)

Fig. 2.1: Chimney structures of some pool type research reactors

A FORTRAN program was developed for solution of these equations using iterative process till convergence was achieved. Core flow was kept constant at about 1900 $m^3$/hr and core bypass flow ($Q_c$) was varied from 0 to 70 $m^3$/hr. Chimney model scheme considered for the solution is shown in Fig. 2.2. The entire domain was divided into five regions (R1 to R5) considering the chimney to have two major parts. The lower chimney had a rectangular cross-section (438 mm × 489 mm) and height (L1) of about 1200 mm. The upper chimney had 1000 mm long (L2) inner opening which allows the passage of core flow and bypass flow towards the exit. The Exit section had a width of W2 (438 mm). The upper chimney part (R4) above the lower chimney had a length and width of L3 and W1 (438 mm) respectively. Core bypass flow is drawn inside the chimney through the top opening of this region. Boundary conditions considered are given below.

i) Vertical wall surface : $v_x = 0$ ii) Horizontal wall surface : $v_y = 0$

iii) Bottom inlet : $v_y = U_{in}$ iv) Top outlet : $v_y = U_{out}$

v) Chimney top : $v_x = 0$

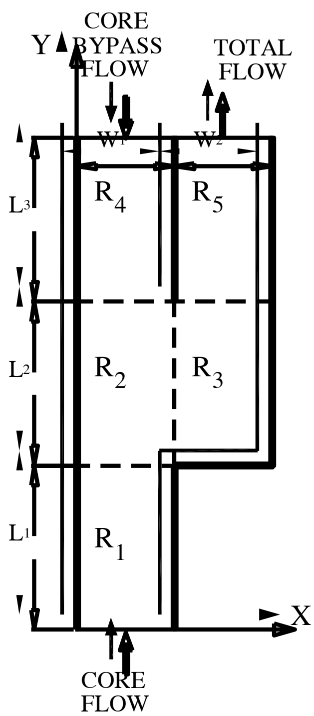


Fig. 2.2: Chimney model scheme of ETRR-2 (El- Morshdy, 2007)

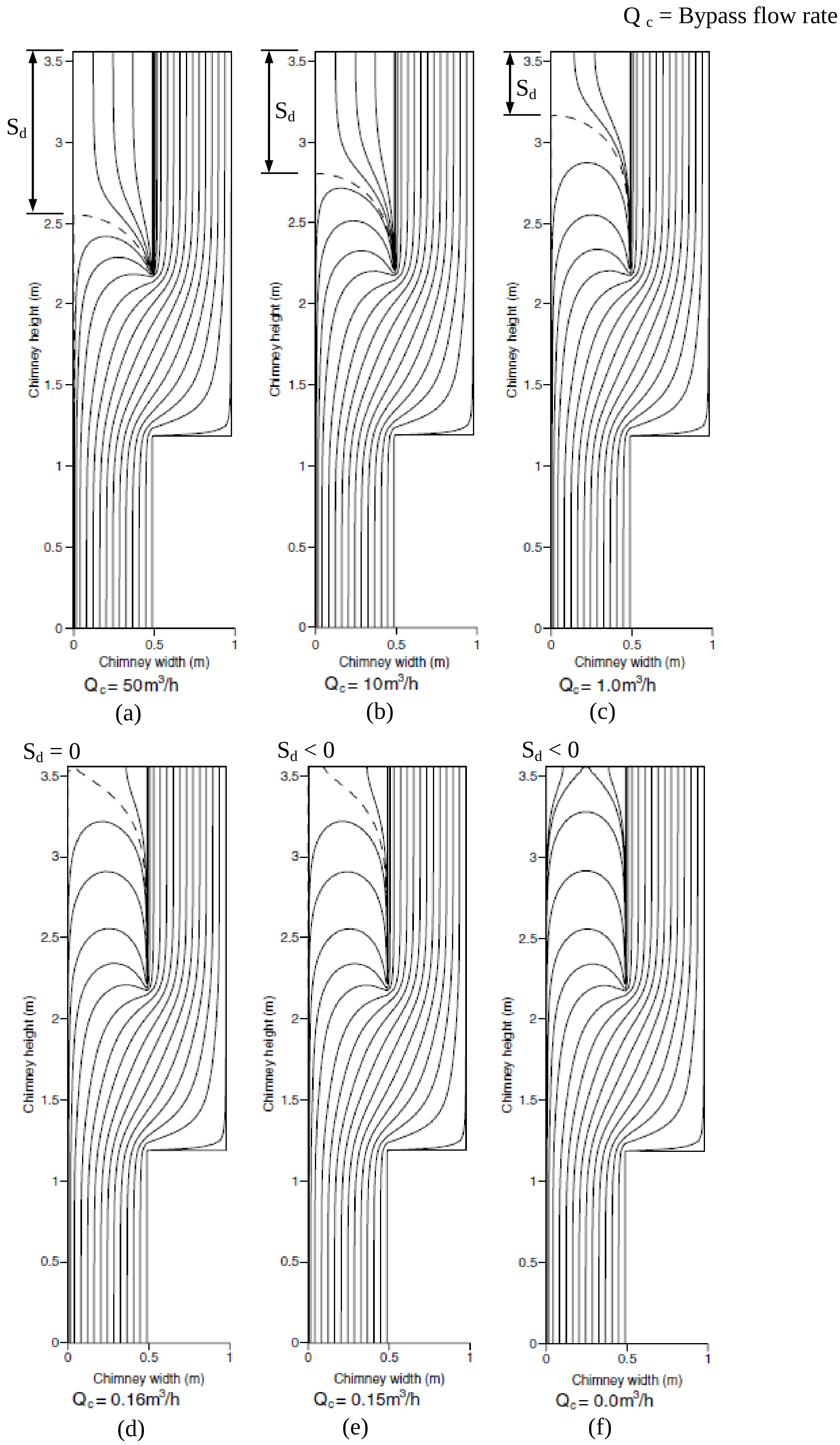


Fig. 2.3: Flow maps for various bypass flow rates (El-Morshdy, 2007)

The resulting stream line contours obtained by El-Morshdy (2007) is shown in Fig. 2.3. The dashed line shows the stagnation line corresponding to stream function equals to zero. The distance from the upper-most point of the stagnation line to the chimney top opening edge is defined as the stagnation depth ($S_d$). The stream lines below the stagnation line has an upward flow direction while the stream lines above the stagnation line has a downward flow direction. Figures 2.3a, b and c show the results for bypass flow of 50, 10 and 1 $m^3/h$ respectively. The stagnation depth ($S_d$) for these three cases are shown in the figures. It is observed that stagnation depth decreases with decrease in bypass flow rates. When bypass flow is reduced to 0.16 $m^3/h$, stagnation depth becomes zero as shown in Fig. 2.3d. It is observed that a part of the core flow reaches the open chimney top and mixes with pool bulk water (as shown in Fig. 2.3e and f) when core bypass flow is less than or equal to 0.16 $m^3/h$ and stagnation depth is found to be negative. It was recommended to keep the stagnation depth from top about 1 m (which is adequate to prevent the radioactive water from rising to the pool top and minimizing the exposure rate at pool surface) which corresponds to a nominal core bypass flow of 50 $m^3/hr$ (i.e., about 2.6% of the core flow). Based on the sharp decrease in stagnation depth for core bypass flow below 10 $m^3/h$, it was recommended to operate the reactor with minimum 10 $m^3/h$ (0.5% of core flow) of core bypass flow.

Since the mixing of upward hot fluid and downward cold fluid inside the chimney is relevant to the mixing of fluid streams in T-junction, oblique pipe, cross pipe and X-junction and opposing jets, those literatures are reviewed in the following sections.

## 2.2 Mixing in T-junction, oblique pipe, cross pipe, X-junction and opposing jets

Turbulent mixing of fluid streams in pipelines without chemical reaction has various applications and has been studied numerically and experimentally by various researchers.

Studies of mixing in T-junction, Oblique pipe, Cross pipe, X-junction, opposing jets etc., reported in literature and their areas of application can be broadly classified in two categories i) Study of passive scalar transport between fluid streams (e.g. study of potable water distribution systems, where water from different sources is mixed. Similarly, study of the dispersion of disinfectant or polluting substances). ii) Study of heat transfer characteristics due to mixing of hot and cold fluid streams (e.g. thermal fatigue assessment of reactor components due to local cycling of stresses on the adjacent pipe wall). They are presented in the following sections.

### 2.2.1 Dynamics of fluid mixing in T-junction

Mixing of fluids in pipeline through a T-junction is frequently encountered in combustion reaction processes, nuclear reactors and chemical process industries (Maruyama et al., 1981; Kim, 1985; Tosun 1987; Stroka and Forney, 1989). Quantification of mixing in terms of tracer concentration distribution was reported and process optimisation was expressed via empirical means by these researchers. A typical case of flow mixing in T-junction is shown in Fig. 2.4.

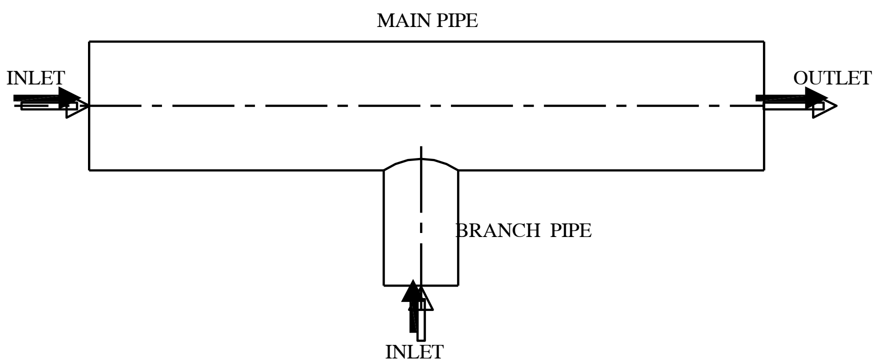


Fig. 2.4: Flow mixing in a T-junction

Mathematical model was established by Chen et al. (1990) to assess the composition and temperature field downstream from a T-junction where two natural gas streams of different temperatures meet. Diameters of main pipe and branch pipe were considered to be 0.508 m and 0.102 m respectively. Main flow rate and branch flow rate were $1.19 \times 10^5$ and $3.89 \times 10^2$ $m^3/h$ respectively. Pressure and temperature of main flow were 31 bar and 280.56 K respectively. For branch flow, they were 31 bar and 283.33 K respectively. The results were compared with computational fluid dynamics simulation using k-ε turbulence model. Jet centre temperature and species concentration was reported to be in good agreement. Further the mathematical modeling of mixing induced in T-junction (Chen et al., 1991) was tested by comparing tracer concentration distribution across the main pipe to the experimental observations reported by Forney and his co-workers (Forney and Kwon, 1979; Forney and Lee, 1982; Stroka and Forney, 1989). In this model, a tracer was injected as a side stream into a main flow containing no tracer. Both flow streams entered the T-junction at the same temperature and pressure. Jet to main flow velocity ratio was varied from 0.05 to 7 to cover flow conditions leading to a free jet (a jet stream staying clear of the main pipe wall) and a wall jet (a jet stream staying in contact with the main pipe wall). Model predictions were found to be in fairly good agreement with experimental observations.

Gas mixing was experimentally characterized by measuring the temperature distribution downstream of a T-junction under turbulent flow conditions by Tang et al. (1993). The test section of T-junction was made of acrylic plastic with thermal conductivity (0.19 W/m/K). Ambient air was sent by a compressor through the main pipe and velocity was varied from 3.52 m/s to 29.5 m/s to cover a range of Reynolds number of the main flow (8380 to 79000). Air from a compressed cylinder was fed to the side pipe and its temperature was maintained 7-10 ºC more than the ambient air by using temperature controlled heating system. Velocity of air in the side pipe was varied from 2.0 to 20.62 m/s to cover a range of Reynolds number for the side flow (1200 to 12200). Inner diameter of the main pipe and side pipe in T-junction was 38.1 mm and 9.5 mm respectively. The temperature measurements were accomplished using type E subminiature thermocouples with an outer diameter of 0.254 mm to minimize potential disturbances to the flow field. This type of thermocouple has an exposed junction and a response time of 2 s in air which is adequate for steady state flow experiments. Measured temperature profiles were compared with numerical solutions obtained considering the two equation κ-ε turbulence model using FLUENT. Turbulent transport processes were characterized by six system parameters: $C_\mu = 0.09$, $C_1 = 1.44$, $C_2 = 1.92$, $\sigma_\kappa = 1.0$, $\sigma_\varepsilon = 1.3$, $\sigma_h = 0.7$. Here all the five parameters were assumed the values determined by Launder and Spalding (1974) except the value of $\sigma_h$, i.e., the turbulent Prandtl number, $Pr_t$ which was assigned a value of ~ 1. Uniform velocity and temperature profiles were assumed at both the inlets. The "Wall function" approach was assumed at the interface between the wall and fluid. Regarding the boundary condition of the main pipe wall, thermal conductivity of pipe wall and external heat transfer coefficient involving natural convection from a horizontal cylinder was specified. Qualitative agreement between the experiment and numerical prediction was observed. However, the rate of convective heat transfer from the gas stream to the main pipe wall occurring at the T-junctions was underestimated.

Flow structures resulting from the interaction of turbulent jet issuing transversely into a uniform stream were described with the help of flow visualization and hot-wire anemometry by Fric and Roshko (1994). Jet to cross flow velocity ratios from 2 to 10 were investigated at cross flow Reynolds numbers from 3800 to 11400. Four types of coherent structures were identified due to interactions between the jet and the crossflow as shown in Fig. 2.5. They were (i) the jet shear-layer vortices (ii) the horse-shoe vortices (iii) the counter-rotating vortex pair and (iv) the wake vortices. The horse shoe vortices form upstream of the jet exit, wrapping around the exiting jet column. The jet shear layer consists of the ring vortices in the jet boundary. The wake structures from downstream of the jet column persist and convect far downstream of the exit nozzle. The jet column transitions to the counter-rotating vortex pair, the dominant vertical structure of the transverse jet after the jet has turned in the crossflow direction. The mixing of round jet normal to uniform cross flow was also studied by Smith and Mungal (1998). The Reynolds number based on the jet exit diameter and exit velocity was varied from 8400 to 41500. Jet to cross velocity ratios was varied from 5 to 25. Planar laser induced fluorescence (PLIF) of acetone vapour was used to acquire quantitative two dimensional images of the concentration field.

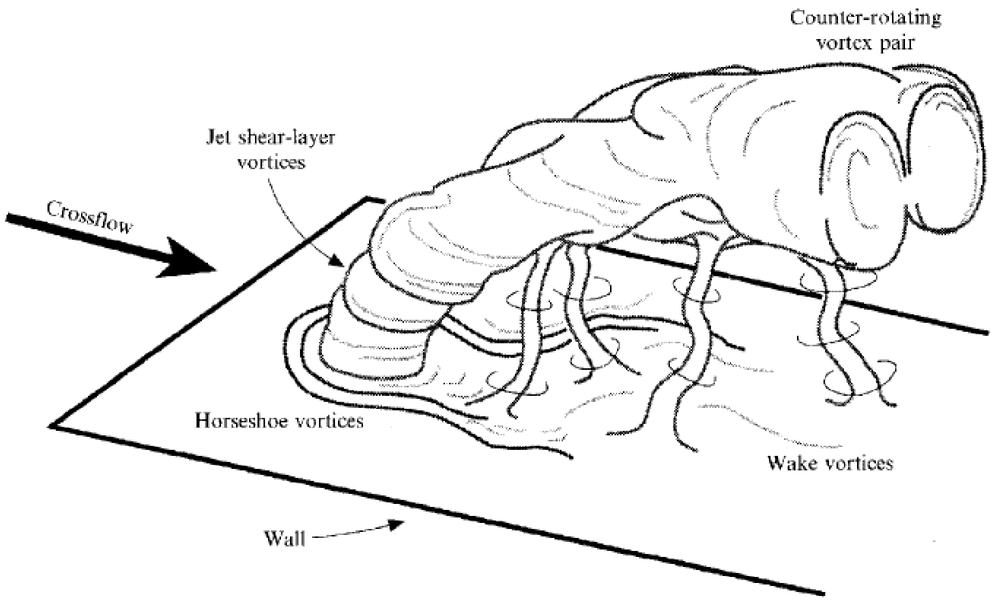


Fig. 2.5: Vortical structures caused by a jet in cross flow (Fric and Roshko, 1994)

Mixing of two gases in a T-junction mixer were investigated by Kok and Vander Wal (1996). The flow field was analysed using κ-ε turbulence model by computer code FLOW3D. Main flow pipe diameter was 100 mm and the branch pipe diameter was 10 mm / 26 mm. Air was blown by a fan to the inlet of the main pipe line. The branch inlet was fed with nitrogen flow. The average oxygen concentration which represented the air fraction was measured by an analyzer. A separate experiment was carried out to measure the velocity profile using laser Doppler velocimetry where water was used as the fluid. The results obtained from the numerical simulations were in good agreement with the experiments.

Experimental study on turbulent mixing of hot and cold air in a T-junction with rectangular cross section was studied and characteristics of velocity and temperature fields due to mixing were predicted by Hirota et al. (2006) for three velocity ratios 0.5, 1 and 2 between the branch flow and the main flow. The mechanism of turbulent heat transfer was reported by Hirota et al. (2010). Schematic diagram of the test channel is shown in Fig. 2.6. The main channel of height (H = 60 mm) and width (2A = 120 mm) joined the branch channel at right angle to form a T-junction. The cross section of the branch channel was 120 mm (2A) × 30 mm (B) as shown in the sketch. The experiments were conducted keeping the Reynolds number (=$U_o d_h/\nu$, where $d_h$ is the hydraulic diameter of the main channel) of the main channel flow before mixing at $1.5 \times 10^4$. Velocity distributions were measured using a PIV system. Temperature distributions were measured using thermocouples. Simultaneous measurements of the fluctuating velocity and temperature were conducted by combining LDV and cold wire thermometer. The bulk temperature of main flow $T_c$ and that of the branch flow $T_h$ were set at 12ºC and 60 ºC respectively. The bulk velocity of the branch flow is set at the same value as that of the main flow. The branch flow was seeded with oil mist and the images visualized by a laser sheet were captured by the digital high speed video camera at a rate of 250 frames/s. The interface of two flows were found to deform quite irregularly and mushroom like discrete longitudinal eddies were observed along the interface of two flows. It was reported that the vertical oscillation of the interface is caused by the stream wise velocity component and the mushroom like eddies are caused by the vertical fluctuating velocity.

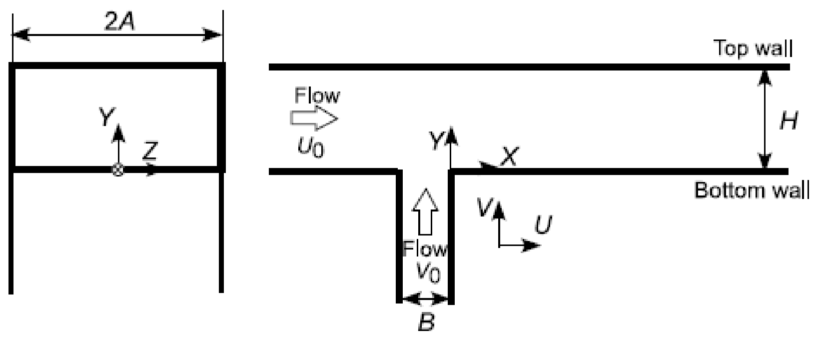


Fig. 2.6: Mixing in T-junction with rectangular cross section (Hirota et al., 2006)

Influence of upstream elbow in the main pipe was studied by Ogawa et al. (2005) on fluid (water) mixing in T-pipe junction at long cycle fluctuation (WALTON) facility. Both the main pipe and the branch pipe were in the horizontal plane as shown in Fig. 2.7. Temperature distribution in the mixing Tee was measured by a movable thermocouple tree and velocity field was measured by high speed PIV. The flow pattern was classified into three patterns; (i) wall jet (ii) deflecting jet and (iii) impinging jet according to momentum ratio between two pipes. Water velocity in branch pipe in the experiment was 1.0 m/s. Velocity of main pipe was varied to 0.23, 0.46 and 1.46 m/s to have momentum ratio of 0.2, 0.8 and 8.1 respectively. Upstream buffer tanks were provided to straighten the flow at the inlets of main pipe and branch pipe. Each type of flow pattern with upstream elbow was distinguished using the following criteria of momentum ratio $M_R$ and compared with the results for the straight pipe case (Igarashi et al., 2003). Various types of flow patterns observed were shown in Fig. 2.7c.

| Type of Jets | Straight pipe | With 90º bend upstream |
|---|---|---|
| Wall jet | $M_R > 1.35$ | $M_R > 2.0$ |
| Deflecting jet | $0.35 < M_R < 1.35$ | $0.52 < M_R < 2.0$ |
| Impinging jet | $M_R < 0.35$ | $M_R < 0.52$ |

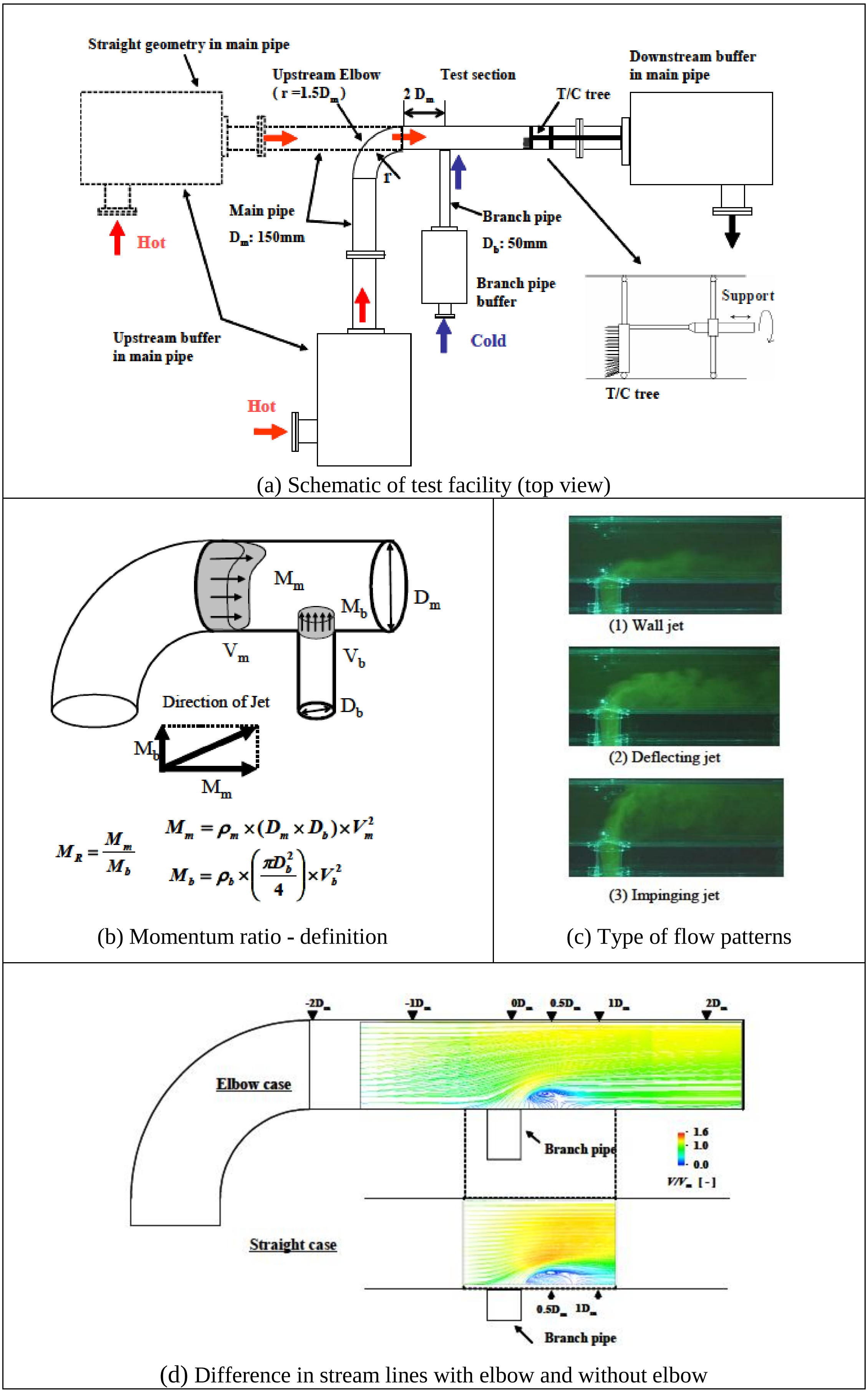


(a) Schematic of test facility (top view)

(b) Momentum ratio - definition

(c) Type of flow patterns

(d) Difference in stream lines with elbow and without elbow

Fig. 2.7: T-junction experiment in WALTON facility (Ogawa et al., 2005)

The temperature difference was varied from 15 to 50ºC. The measurements were carried out under steady state condition. The flow rates and the temperatures at the inlets of main and branch pipes were kept constant. It was observed that the temperature difference had nearly no effect on normalized temperature distribution and frequency characteristics as long as the buoyancy force was negligible. The influence of buoyancy force was found negligible when water velocity in the main pipe is more than 0.1 m/s (Igarashi et al., 2002). Temperature fluctuation intensity near the wall was found more in case of presence of elbow in main pipe than that for straight pipe case under wall jet condition. Biased velocity profile at the elbow outlet was found to cause boundary line to shift more towards the main pipe flow as compared to the straight case as shown in Fig. 2.7d.

Another experiment of mixing in a Tee junction with a 90° bend upstream was carried to by Hosseini, Yuki and Hashizume (2008) where the main pipe runs vertically upward in the test section as shown in Fig. 2.8 and the branch pipe is connected to the main pipe at right angle to form the tee junction. Both the main pipe and branch pipes were made of 3 mm thick acrylic circular pipes. The main flow was straightened by a straightener tank, a reducer and a long main pipe ($13D_m$) before the 90º bend. The branch pipe was also quite long ($60D_b$) to ensure fully developed flow before the mixing area. Water was used as the working fluid. A heat exchanger and a heating tank were used to control the inlet temperature of both main flow and branch flow. Heating tank used gas and electric heaters to send hot water through the branch pipe. The temperature and velocity measurements showed that the 90° bend at upstream had a strong effect on the fluid mixing mechanism.

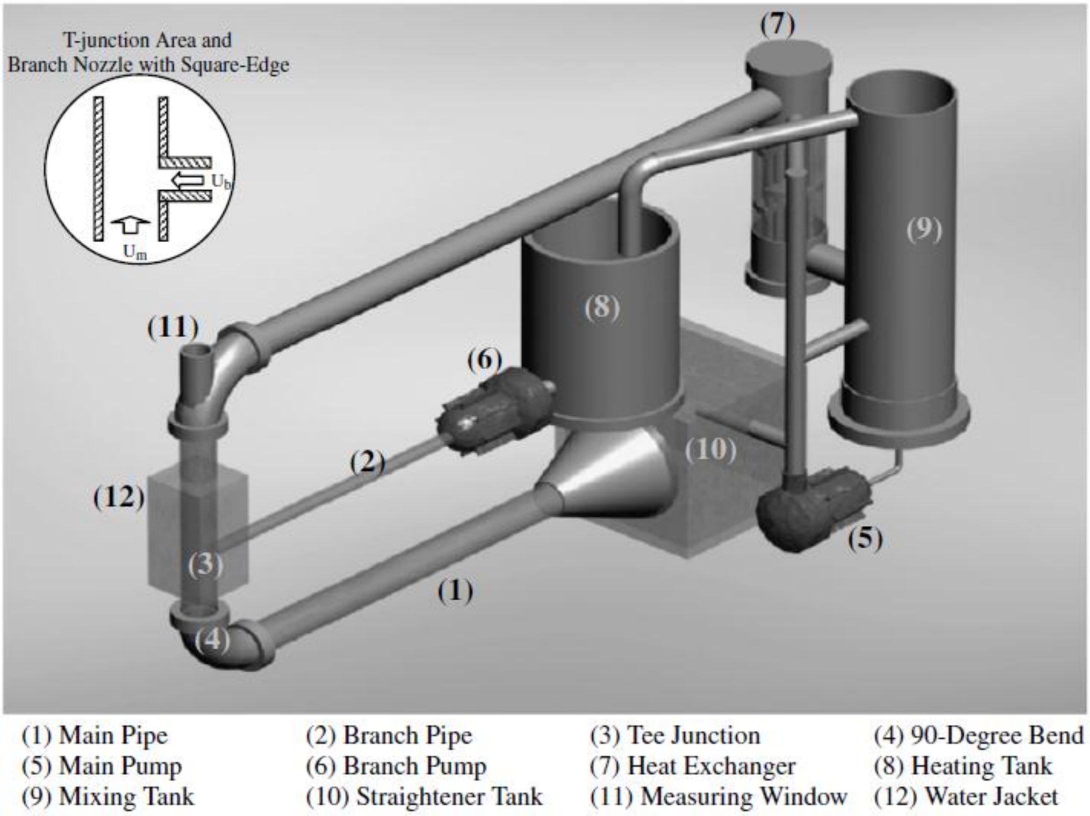


Fig. 2.8: Mixing of cold main flow with a hot branch flow in a Tee junction (Hosseini, Yuki and Hashizume, 2008)

The particle image velocimetry (PIV) technique was used to visualise the flow characteristics in the Tee junction area. Laser sheet thickness was 1-3 mm and its energy level was 200 mJ. Tracers made from nylon powder (80 µm diameter and 1.03 gm/cc density) were used. Camera had a frame rate of 30 fps. In each shot 99 images were captured continually. Total five shots were taken to evaluate the flow fields. Thermocouples were installed 1 mm from the wall to measure fluid temperature. It was observed that velocity and temperature fluctuations near the wall decreased by increasing the momentum ratio between the main flow and the branch flow (keeping both the flow rates constant). This was achieved by decreasing the branch pipe diameter. Results showed that at high Reynolds number (33000-150000), mixing phenomenon was controlled by the mechanism of large eddy. It was indicated that the momentum ratio between the main flow and branch flow of the Tee junction played an important role for the classification of the fluid mixing mechanism. Based on the mean velocity distributions and velocity fluctuations, the behaviour of the branch jet was categorized into four types of turbulent jets; sorted from highest to the smallest momentum ratios: i) the wall jet ii) the re-attached jet iii) the turn jet and iv) the impinging jet. The effect of upstream bend on the types of turbulent jets was specified as given hereunder.

| Type of Jets | without bend | With 90º bend upstream |
|---|---|---|
| Wall jet | $M_R > 4$ | $M_R > 90$ |
| Re-attached jet | $1.35 < M_R < 4$ | $20 < MR < 90$ |
| Turn jet | $0.35 < M_R < 1.35$ | $2.5 < M_R < 20$ |
| Impinging jet | $M_R < 0.35$ | $M_R < 2.5$ |

Experiments on turbulent mixing in a horizontal T-junction geometry considering isothermal mixing of two fluid streams were carried out by Walker et al. (2009). Instead of temperature as transport scalar, the concentration of dissolved salts was measured using conductivity sensors to predict the mixing behaviour. It was assumed that the temperature and the tracer salt concentration behaved in similar way. The experiments were carried out in T-junction with 51 mm inner diameter pipes made from acrylic glass as shown in Fig. 2.9a. Both the branches were oriented horizontally. Tap water was flowing in the main branch and demineralised water was flowing through the side branch. The conductivity difference between the tap water and desalinated water was used as the parameter characterizing the changing concentration during the mixing process. The water was supplied through honeycomb section (length 60 mm and each cell diameter 3.5 mm) to straighten the flow before it reaches the inlet of T-junction. The electrical conductivity of the fluid is used as a parameter characterizing the concentration of salts dissolved in the tap water. A set of three wire mesh sensors with 16 x16 measuring points in each of them were used to record the instantaneous conductivity distributions downstream of the T-junction. To minimize the presence of these wire mesh sensors, only the results of the first upstream sensor were used for estimation of the distribution of the mixing scalar. The signals from the other two sensors were used for velocity measurements. The position of the first sensor was changed to nine different axial planes downstream of the T-junction (X/D=1.0 to 6.1). The distance between the measuring planes of two sensors remained constant (15.5 mm). Experiments were carried out by varying the flow rate in the main and the branch pipes. The distribution of the time averaged mixing scalar was reported for four different velocity ratios ($V_{branch}$ / $V_{main}$ =0.40, 0.71, 1.00 and 1.67). Reynolds number range was from 8770 to 43860 depending on the average water velocity at the exit of the mixing pipe. In the experiments, four characteristic flow regions were identified in the vicinity of the T-junction as shown in Fig. 2.9(b). The extension of these regions depends on the velocity ratio. The first zone is characterized by almost pure tap water (mean transport scalar value ≈ 1) with low RMS values. The magnitude of relative concentration fluctuations is characterized by the RMS value of the mixing scalar (Generally high RMS values are observed in the regions with a high concentration gradient). In this first zone, most of the mass flow is originating from main branch and thus higher axial velocities are expected in this zone. The second zone consists of mixture with mean transport scalar values between 0.25 and 0.75 as well as very high RMS values. Adjacent to this region with strong mixing activities, there is an area featuring small RMS values similar to the first zone. The fluid in this sickle-shaped zone is almost pure demineralised water (DI). The fourth zone is located on the side of the side branch pipe. It is composed by the two vortices forming the recirculation region. This is due to resulting wake structure produced by the intruding side flow. Since the momentum of side flow has no component in the main flow direction as it enters the T-junction, it causes a retardation of the main flow and results in this vortex structure.

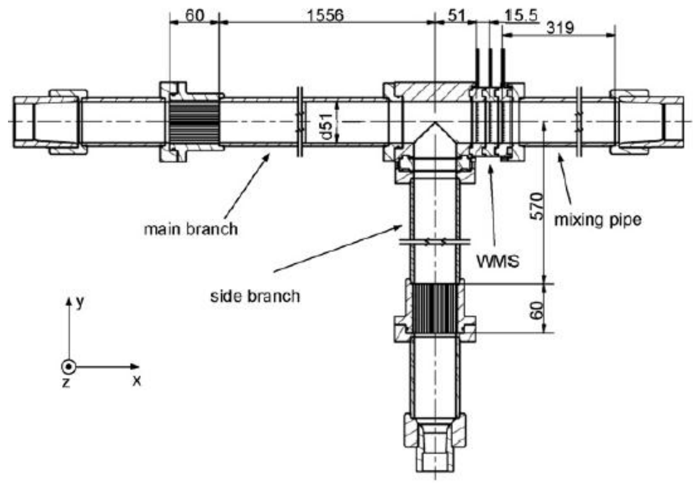


(a) Geometry of T-junction (dimensions in mm)

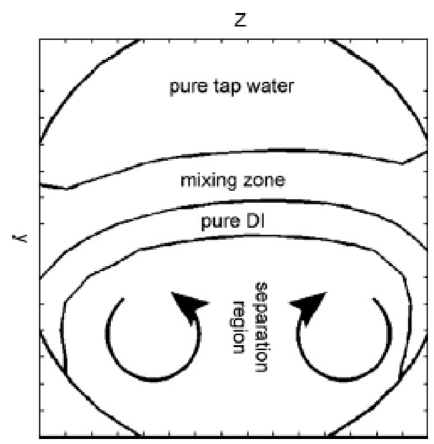


(b) Sketch of four fluid regions

Fig. 2.9: Isothermal mixing of streams in horizontal T-junction (Walker et al., 2009).

Steady state numerical simulation of the experiment was also carried out by Walker et al. (2010) using ANSYS-CFX-10 (2006). The simulation domain consisted of 600 mm long main pipe and 300 mm long side branch discharging in the middle of the main pipe. All the pipes had the same diameter of 50 mm. Three different turbulence models were applied. Two of them were using the eddy viscosity assumption – i) $\kappa$-$\varepsilon$ model ii) SST model. The second model was a blend between the $\kappa$-$\varepsilon$ and the $\kappa$-$\omega$ models. The $\kappa$-$\omega$ model was more accurate in the boundary layer (Menter, 1994). The third model was the BSL Reynolds stress model. It was observed that neither of the models was able to predict the correct mixing behaviour of water from the main and the side branches. Turbulent dispersion of scalar was generally underestimated in the numerical models. A decrease in turbulent Schmidt number showed better agreement. Comparison of velocity profiles revealed under-prediction of turbulent momentum transport. Profiles measured at downstream (x/D =6) showed almost fully established pipe flow in the experiment as compared to the prediction of code. It was observed that turbulent momentum transfer would be enhanced by artificially increasing the model coefficient $C\mu$ for the case of $\kappa$-$\varepsilon$ model. This led to a better reproduction of the velocity profiles and measured profile of the transport scalar. A modification of turbulent Schmidt number was superfluous.

Mixing behaviour of hot and cold water jets in a T-junction was experimentally and numerically investigated by Kamide et al. (2009). The T-junction had main to branch diameter ratio of 3. Detailed temperature and velocity field was measured by a movable thermocouple tree and particle image velocimetry (PIV). The PIV system consisted of a double pulse YAG laser, a CCD camera and a timing controller. The nylon powder of around 30μm in diameter was used as a tracer particle. Flow patterns observed in the tee were classified into three groups: wall jet, deflecting jet and impinging jet depending on momentum ratio between the main and branch pipes. The temperature difference was kept constant at 15°C (48°C in the main pipe and 33°C in the branch pipe). Momentum ratio was defined as ratio of the momentums of the fluid in the main pipe and the jet exiting from the branch pipe based on the inlet flow conditions. The inlet momentum of branch jet was based on cross section area of branch pipe. The momentum of main pipe flow was based on projection area ($D_m \times D_b$) of a cylinder with a diameter of $D_b$ and length $D_m$. The experimental results indicated that the flow pattern could be predicted by the momentum ratio, $M_R$ as i) Impinging jet ($M_R < 0.35$) ii) Deflecting jet ($0.35 < M_R < 1.35$) iii) Wall jet ($M_R > 1.35$). Numerical analyses were carried out using thermal-hydraulic simulation code AQUA (Maekawa, 1990). This code was based on a finite difference method and used QUICK scheme for convection terms in momentum and energy equations. Instead of time averaged turbulence models, MILES (Fureby and Grinstein, 1999; Grinstein and Fureby, 2002) approach was used in the simulation to know the frequency characteristics of temperature fluctuations. This approach employed numerical diffusion derived from high order upwind scheme, which was used as an implicit model of turbulence diffusion instead of the physical model. The Cartesian co-ordinate system was used in the analysis. Boundary conditions of temperature and velocity at the inlets in the main and branch pipes were spatially uniform and constant in time. The pipe surface was set as no-slip wall with adiabatic conditions. Simulation of turbulence was introduced in the form of turbulent flow behind obstacles. The dispersed blocks were set at $D_m$ distance from the inlet side and 3.3 $D_m$ away towards the upstream side of the T-junction. The total flow area was reduced to 65% and a good comparison of fluctuation intensity of axial velocity between analyses and experiments was observed. The calculated temperature distribution was in good agreement with that of the experiment. The temperature fluctuation intensity was well simulated in the analysis except the peak value was slightly overestimated. The calculated prominent frequency of the temperature was in good agreement with the measured data. It was shown that relatively large vortex structure like Karman vortices caused major fluctuation at the T- junction in the case of wall jet.

Mixing of cold water and hot water in a T-junction was also investigated experimentally and numerically by Naik-Nimbalkar et al. (2010). T- junction was constructed of acrylic pipes. Cold water entered through a horizontal main pipe and hot water entered through a branch pipe. Main pipe diameter was kept constant (0.05 m) and branch pipe diameters considered were 0.025 m and 0.015 m. For lower velocity ratios ($V_h/V_c$=0.5, 1.0) branch pipe of 0.025 m diameter was used. For larger velocity ratios ($V_h/V_c$=2.0, 4.0) lower size branch pipe diameter (0.015 m) was used. Velocities and temperatures at the main and branch pipes were confirmed to be at steady-state before each experiment was performed. Velocity and temperature measurements were carried out using hot-wire anemometer. A constant temperature module (CTA) was used for the measurement of local velocity in the system. Steady state 3-dimensional CFD simulations were carried out using the FLUENT software version 6.3.26 by the finite volume method and values of mean velocity, mean temperature and temperature fluctuations were predicted at x=0.5D and x=1.25D. The standard k–ε turbulence model was used. No slip and adiabatic condition was given to the wall. Boundary conditions at the inlet for this model were mass flow rate based on the experimental conditions. The outlet boundary condition was constant pressure. The variation in density of working fluid due to temperature change was considered using Boussinesq approximation. The transport equations for momentum, k and ε were discretized using second order upwind scheme. The transport equations for energy were discretized using first order upwind scheme. The pressure values at the faces were interpolated using the standard scheme and the transport equations were solved using the SIMPLE algorithm. The predicted mean velocities and temperatures were in good agreement with the measurements.

Investigations were carried out by Frank et al. (2010) for simulation of turbulent and thermal mixing in T-junction of Vattenfall test facility using URANS and scale resolving turbulence models with ANSYS CFX. The setup had 140 mm diameter ($D_2$) horizontal pipe for the cold water flow ($Q_2$) and a vertically oriented pipe of 100 mm diameter ($D_1$) for the hot water flow ($Q_1$) as shown in Fig. 2.10. The hot water pipe was attached to the upper side of the horizontal cold water pipe. The length of straight pipes upstream of the T-junction was more than 80 diameters for the cold water inlet and approximately 20 diameters for the hot water inlet. A stagnation chamber with flow improving devices (tube bundles and perforated plates) was located at the entrance to each of the inlet pipes. The temperature fluctuations were measured using thermocouples. Velocity profiles were measured with laser Doppler velocimetry (LDV) in each inlet pipe. The pipes near the T-junction was made of plexiglass tubes surrounded by rectangular boxes filled with water in order to reduce the diffraction when the laser beams pass the curved pipe walls. The experiments were carried out with a constant flow ratio $Q_2/Q_1=2$ which corresponds to almost equal velocities in the two inlet pipes. The hot and cold water temperatures were 30ºC and 15ºC respectively. Reynolds numbers in both inlet pipes were approximately $1.9\times10^5$ considering bulk velocities of about 1.53 m/s in the hot leg and 1.56 m/s in the cold leg (corresponding flow rates Q1=12 l/s and Q2=24 l/s).

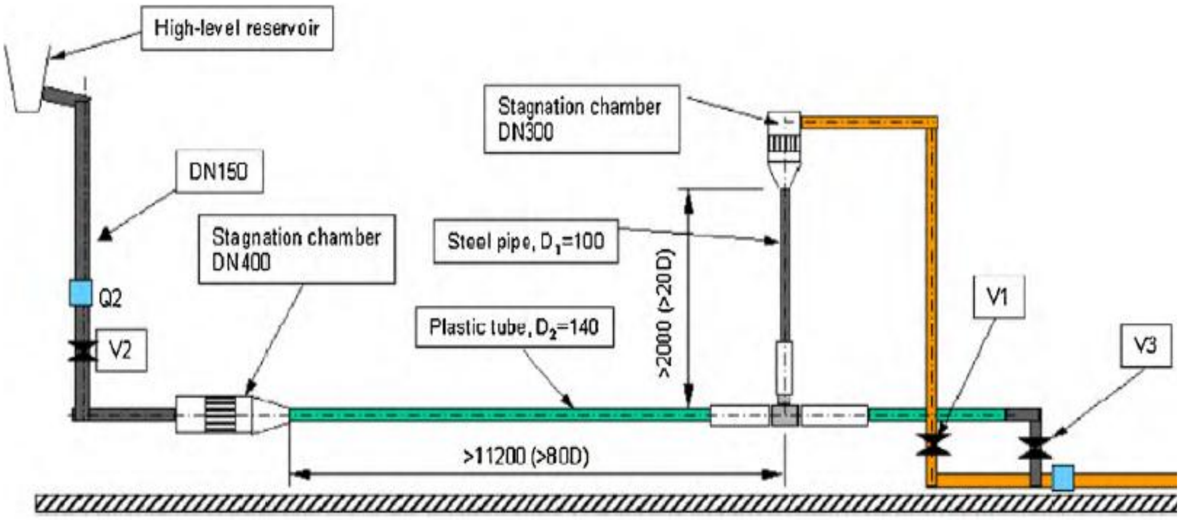


Fig. 2.10: Vattenfall T-junction test facility (Elevation view) (Frank et al., 2010)

Investigations have shown that Reynolds averaging based (U)RANS turbulence models like SST(shear stress transport) or BSL RSM (baseline Reynolds stress model) are able to satisfactorily predict the turbulent mixing of isothermal fluid in T-junctions. In case of mixing of streams of different temperatures, in some cases the high turbulent viscosity predicted by the RANS-based turbulence models in the mixing zone (due to the locally high shear rates) suppress any transient flow development and the CFD results tend to a steady-state solution. However, experimental observations show strong and high-frequency temperature transients at pipe walls downstream of the T-junction – so called thermal striping effect. Investigation of this behaviour is important because, it can lead to high-cycle thermal fatigue, crack formation and pipeline break in practical applications. Recent studies show promising results considering advanced scale resolving turbulence modelling approaches like LES (Large eddy simulation), DES (Detached eddy simulation) or SAS (scale adaptive simulation) in order to simulate the strongly transient flow and temperature fields. It was observed that SAS-SST approach was able to predict transient thermal stripping in the T-junction. The predicted velocity fluctuations and RMS values were in good agreement with experimental results.

Fluid flow simulation in a T-junction with 50 mm diameter of each branch was done by Jaroslav Stigler et. al (2012) using both numerical modeling and PIV measurement. The model of the T-junction was made from the optical glass to suit PIV measurement. The investigated area was illuminated by the Nd:YAG 532 nm green pulse laser. The test fluid (liquid water) was seeded with Rhodamine B coated 10 μm particles. Rhodamin B absorbs the laser light of 532 nm and emits the light of wave lengths close to 570 nm. Orange optical filters (for wave length 570 nm) were mounted on the lenses of cameras to reduce the glass wall reflections. The geometrical model of the T-junction was created in the pre-processor GAMBIT 2.2.30 and the analysis was done using Fluent 12.1. Number of hexahedral cells used in the simulation was 2.3 millions. The turbulence model used was κ-ε realizable with non-equilibrium wall functions. Flow ratios were varied from 0 to 1 in steps of 0.2. Numerical results were compared with the experiment and found to be in good agreement.

Numerical simulation of jet and cross flow mixing in T-junction was reported by Guobing Kang (2014). The model of Realizable k-ε turbulence model of ANSYS FLUENT was employed to calculate the flow field and the model was validated with experimental results. The working fluid was water and the velocity of jet was 0.874 m/s and velocity of cross flow was 0.277 m/s. The diameter of the jet was 10 mm and the diameter of the cross flow pipe was 60 mm. The numerical results were compared with the experimental data of Gang Pang and Hui Meng (2001) and good agreement was observed.

### 2.2.2 Turbulent mixing of hot water jet from an oblique pipe

Turbulent mixing of a hot water jet into a cold cross flow stream from an oblique pipe at an angle of 45º was experimentally investigated by Dang et al. (2008) as shown in Fig. 2.11. The experimental study was carried out to obtain local fluid temperatures and to provide qualitative understanding of the flow structure in the mixing region so that those regions could be identified where the component would be subjected to more thermal shock. The test section was 1/9 scale mock up model and it was fabricated entirely out of Plexiglass, thus allowing flow visualisation from all directions. Potassium permanganate powder was injected to dye the flow. The hot water jet temperature was 30°C more than the temperature of the main cold flow stream. Thermocouples were used to measure the fluid temperature. Velocity ratio of jet flow and uniform cross flow was varied from 0 to 40 and flow visualisation & temperature measurements were carried out.

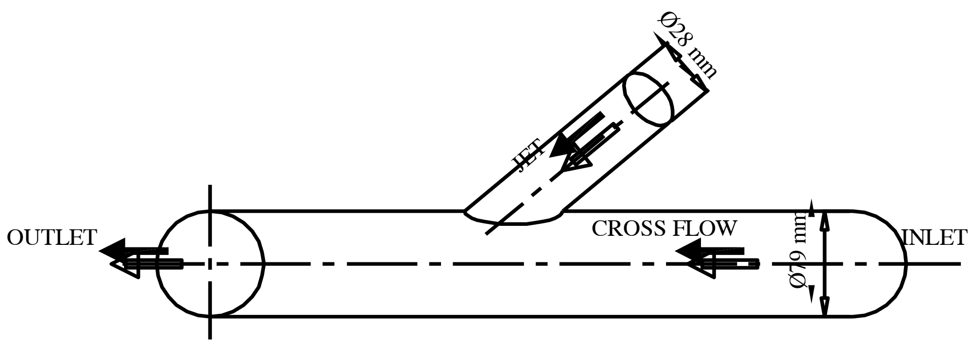


Fig. 2.11: Mixing of jets from an oblique pipe to cross flow stream (Dang et al., 2008)

The experimental study showed that the interference between jet flow and cross flow resulted in the bending of jet towards the region of downstream of jet exit and with the increasing velocity ratio the jet penetrated into the cross flow gradually and impinged on the bottom wall of the tube at extremely high velocity ratio. The fluid temperature measurement showed that mixed fluid temperature close to the wall varied significantly with the change of velocity ratio. At low velocity ratios, the temperature had a top hat profile at both jet exit plane and the region downstream of jet. This was due to the mixing flow around the jet and the wake flow behind the jet, respectively. At high velocity ratios due to the presence of jet impinging on the wall, the fluid temperatures in the region at the bottom and the side of main tube increased rapidly with increasing velocity ratio.

### 2.2.3 Turbulent mixing in cross pipe using LES

Turbulent mixing study of two water flow streams was performed using Large Eddy Simulation (LES) approach by Webb and Waanders (2006) for a pipe cross (Fig. 2.12) where inlet pipes were at right angle. Each pipe internal diameter was about 50 mm and Reynolds number was 40000 corresponding to nominal inlet mass flow rate of 1.6 kg/s. Water density and viscosity were assumed to be 998.2 kg/m$^3$ and 0.001003 Pa.s respectively. The molecular diffusivity for the tracer water mixture was 10 $^{-9}$ m$^2$/s. The turbulent Schmidt number was taken 0.7. Clean fluid entered the North inlet, while contaminated water entered the west inlet. The numerical results showed that about 91% of the contaminated water from the west inlet went out to the south outlet, while only about 9% went out to the east outlet. The experimental data of Ho et al. (2006) showed that about 87% of the contaminated water from the west inlet went out to the south outlet, while only about 13% went out to the east outlet.

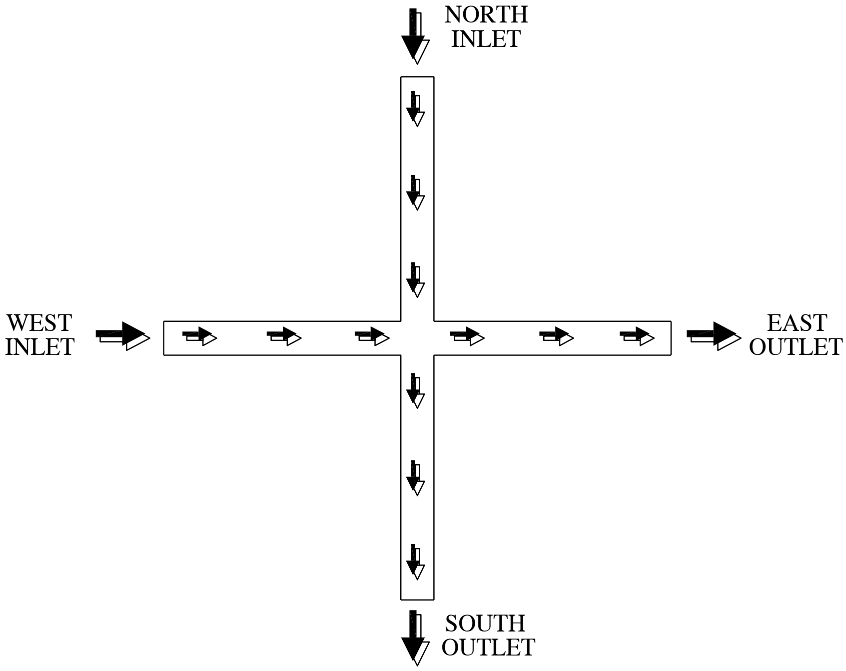


Fig. 2.12: Turbulent mixing in cross pipe junction (Webb and Waanders, 2006)

### 2.2.4 Mixing of two fluids in an X-junction

A computational fluid dynamic model was used to analyse the transport processes of a passive scalar in mixing of two fluids in an X-junction by Vicente et al. (2008) where the angles between the two inlet pipe lines were considered to be 45°, 67.5°, 90°, 112.5° and 135°. The X-junction consisted of two pipes with two inlets and two outlets as shown in Fig. 2.13. Both the pipes were used to transport clean water but a specified concentration of a passive scalar was added in one of the two inlets. Inlet-1 was supplied with a mixture of clean water and a passive scalar (dye). Inlet-2 was supplied with only clean water. Volumetric flow rate for inlet-1 was kept constant (Re=28000) and for inlet-2 it was varied to obtain flow ratio from 0.02 to 2.0.

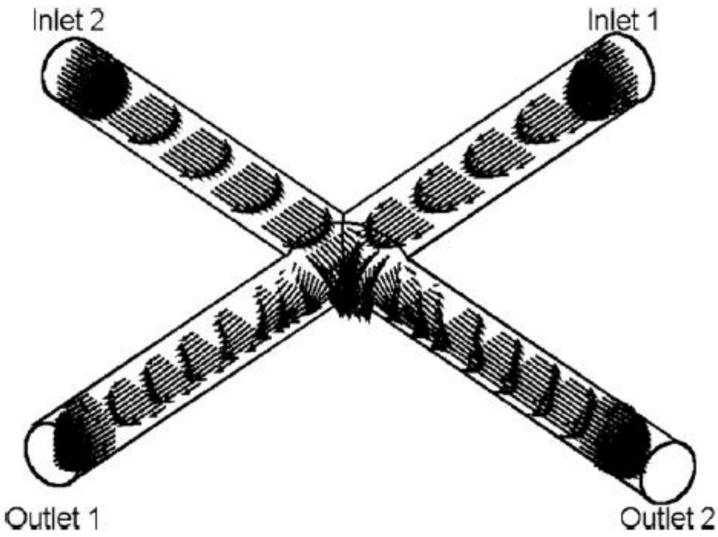


Fig. 2.13: Mixing of two fluids in an X-junction (Vicente et al., 2008)

In the numerical model, the turbulent flow was assumed to be homogeneous, incompressible and viscous with constant properties. The concentration was modelled through the conservative species equation. Laminar Schmidt number was considered to be 1.0 and the turbulent Schmidt number was considered to be 0.6 (Reynolds, 1975). The hydrodynamic equations were represented with the Reynolds averaged continuity, momentum and conservative species equations. The standard k- ε model was used to consider turbulence effects within the flow. The boundary conditions considered (i) Flow entered the pipe with a uniform longitudinal velocity (ii) Turbulent kinetic energy (k) and its dissipation rate (ε) for the inlet was specified. The hydrodynamic equations were solved using a finite volume method. ASAP method (Arbitrary Source Allocation Procedure) was used to determine the intersections of the complex geometry with the Cartesian gridlines and to calculate the free areas and volumes of the partially blocked cells. When the intersection angle between two pipes was non-orthogonal (not 90°), this method only was able to converge the results for 3-D case specifically.

Experimental validation was carried out considering two inlets at 90°. Inlet-1 was supplied with a mixture of clean water and a dye (hipochlorine) blue ink. Inlet-2 was supplied with only clean water. Volumetric flow rate for inlet-1 was kept constant (Re=28000) and for inlet-2 it was varied to obtain Re from 23000 to 50000. The concentrations were measured through a Hach spectrophotometer, which employed a colour technique in terms of platinum-cobalt units. The experimental results were compared with numerical models for both 2-D & 3-D simulations and good agreement was found.

### 2.2.5 Mixing of opposing jets

#### 2.2.5.1 Laminar mixing of opposing jets

The flow field created by two impinging liquid jets in a cylindrical chamber was investigated using particle tracing technique and laser Doppler anemometry by Wood et al. (1991). Three dimensional numerical solutions were also obtained for a range of jet Reynolds number (based on mean jet velocity and diameter) 50 – 300. It was assumed that both the jets had same fluid and equal velocity. A schematic diagram of the impingement mixer used in their study is shown in Fig. 2.14. The jet diameter (d), chamber diameter (D), chamber length (L), position of jet tube from the blocked end (H) and the jet tube length (I) considered were 2.38 mm, 25.4 mm, 159 mm, 12.7 mm and 32 mm respectively. Mineral oil ($\eta_o$ = 1.4622 at 24.6ºC) was used as representative fluid with refractive index closely matching that of acrylic ($\eta_o$ = 1.49) to reduce optical distortion. The flow structures present were observed by seeding the fluid with polystyrene spheres (average diameter 100 μm) and the model was illuminated with a sheet of light created by passing the beam from a He-Ne laser through a cylindrical glass rod. The sheet passed through the axis of the jet and was parallel to the axis of the cylindrical chamber so that the vertical plane containing the jets and the impingement point was illuminated. Radial and axial velocities were measured with laser Doppler anemometer. At Reynolds number less than

90, steady flow field was observed as shown in Fig 2.14b. At higher Reynolds number flow oscillations were observed. At jet Reynolds number less than 130, the two opposed jets impinged head on and formed a radial or “fan” jet that travelled radially relative to the jet axis outward from the impingement point. The part of the fan jet travelling towards the closed end impinged on the bottom and got divided. Similarly, the fluid leaving the impingement towards the cylindrical wall also impinged on the wall and was divided. Re-entrainment of fluid by the jets created a 3-D recirculation zone going around each jet. These zones were counter rotating ring vortices on either side of the impingement plane.

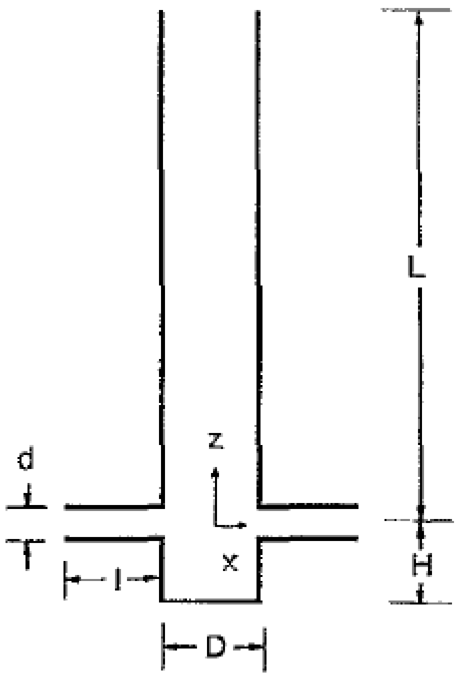


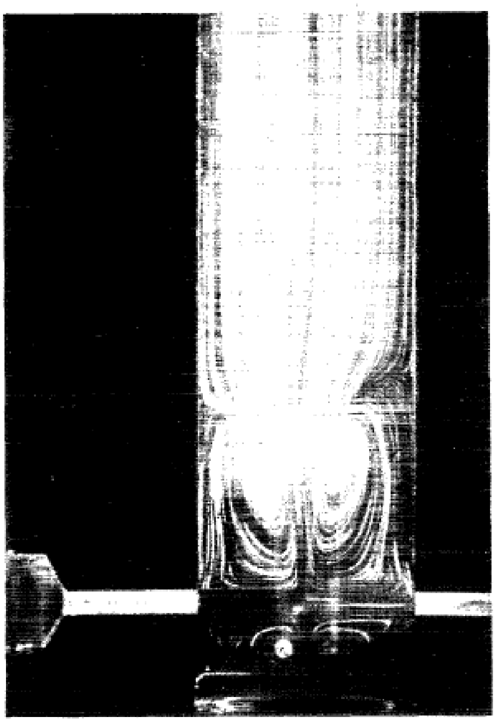

(a) Geometry of the impingement mixer (b) Flow pattern at $Re_j = 60.5$

Fig. 2.14: Geometry and Flow pattern of impingement mixer (Wood et al., 1991).

Numerical simulation of transport processes occurring in a symmetric two dimensional confined opposing jet configuration in steady laminar flow was reported by Hosseinalipour and Mujumdar (1997a). The two jets were identical with equal Reynolds number ($Re_b = Re_t$) as shown in Fig. 2.15. Effect of the jet Reynolds number on mixing and heat transfer characteristics were studied. At small Reynolds number ($Re_b$=$Re_t$=50), no recirculation zones were observed in the flow field. When Jet Reynolds number was increased, recirculation zones appeared. The separation regions along the side walls behaved as a convergent-divergent nozzle for the flow in the core region. The flow was accelerated towards the throat and decelerated further downstream. With increase in Reynolds number, the size of the separation zone increased and throat size decreased. Consequently flow in the core was accelerated further and therefore, recovery of the fluid velocity profile took place over a longer axial length.

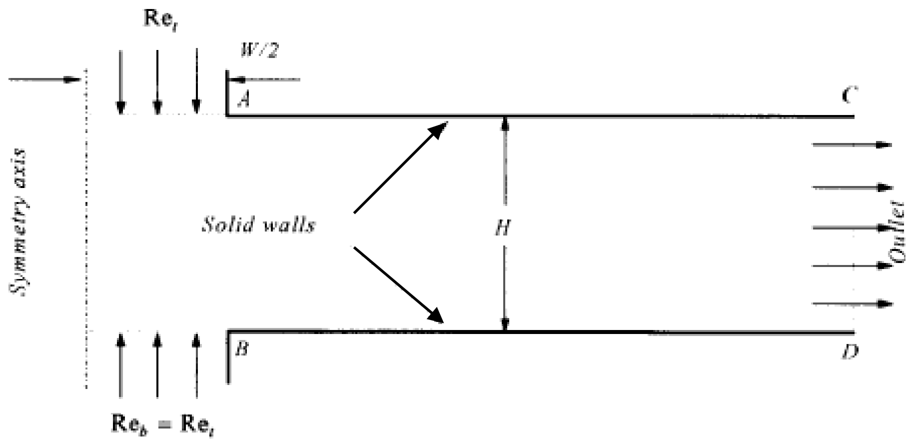


Fig. 2.15: Two dimensional confined laminar opposing equal jets (Hosseinalipour and Mujumdar, 1997a).

Numerical simulations of opposing jets considering equal jet width (W) but with different momentum were also reported by Hosseinalipour and Mujumdar (1997b). Reynolds number ($Re_t$) of the top jet was varied in the range 50 to 500 while Reynolds number of the bottom jet was maintained at 100 (i.e., momentum ratio range of 0.5 to 5). Channel height to jet width ratio (H/W) was also varied from 0.5 to 5. At H/W = 0.5, no recirculation zones were observed in the flow field over the whole range of Reynolds number ($Re_t$). For higher values of H/W, flow field had two recirculation zones and always had asymmetric pattern for all Reynolds numbers except $Re_t$ = 100. Recirculation zones were identical at $Re_t$ = 100. With increase in $Re_t$, the fluid from top jet moved further lower i.e., beyond the vertical symmetry plane before interacting with the bottom stream and then was forced towards the exit channel.

Experimental and numerical characterization of viscous flow and mixing in an impinging jet contactor was reported by Unger et al. (1998). The velocity field was predicted for low jet Reynolds number ($Re_j$ < 80) flow using three dimensional numerical simulations. The geometry of the impingement jet contactor is shown in Fig. 2.16. It was made of glass and the working fluid was glycerin for $Re_j$ < 10. The working fluid was water or glycerin-water mixtures for 10 < $Re_j$ <80. Flow structures were visulaised by injecting a pulse of different fluorescent die into one or both the streams. Velocity field in the experiment was obtained using PIV. The flow was seeded with 12 μm diameter silver coated hollow glass spheres (Potter's Industries) that have a specific gravity 1.17. A 10 mJ pulsed laser was used as illumination source. Computation was done using FLUENT.  Computational pathlines and experimental flow pattern for $Re_j$ = 10 is shown in Fig. 2.16b. At this low Reynolds number, the jets did not impinge upon each other and a distinct vertical plane of symmetry was observed. Both the jets did not reach this symmetry plane and left the device without contacting each other. At higher Reynolds number ($Re_j$ = 40), direct impingement of the two jets were observed and the formation of recirculation loops above and below the jets were found as shown in Fig. 2.16c. After impingement, each jet fanned out radially relative to the jet axis as if they were impinging on a flat plate. The portion of the jet travelling downward towards the closed end, curled back and moved towards the jet

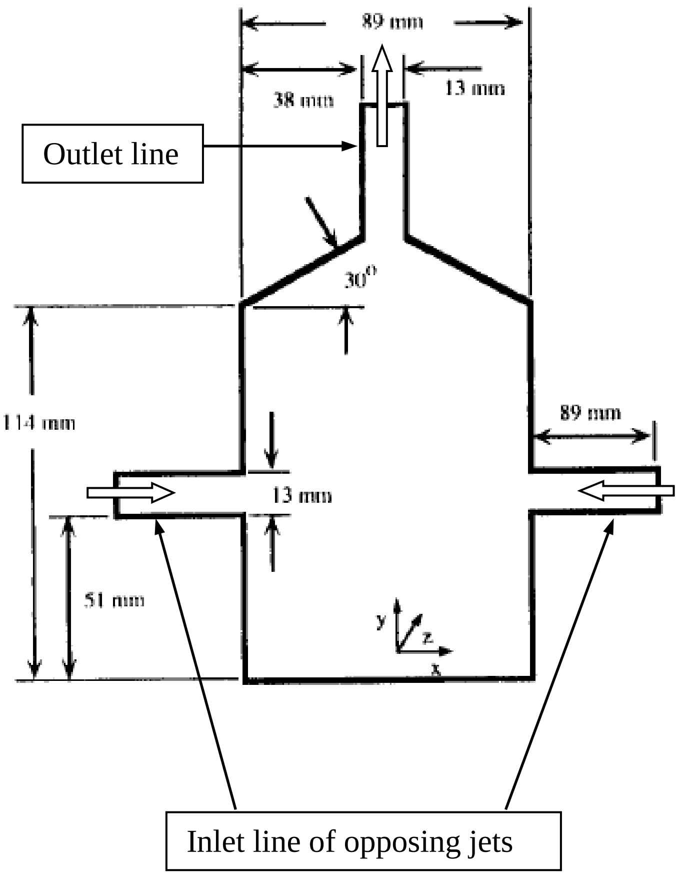


(a) Geometry of impingement jet contactor

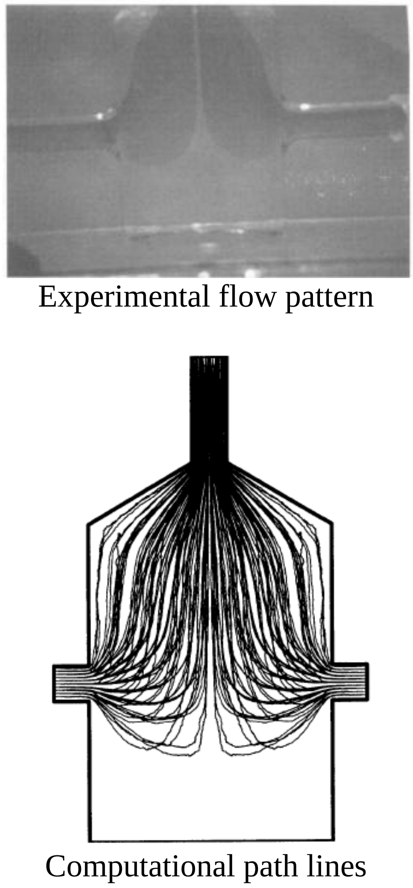


(b) Experimental and Computational results ($Re_j$=10)

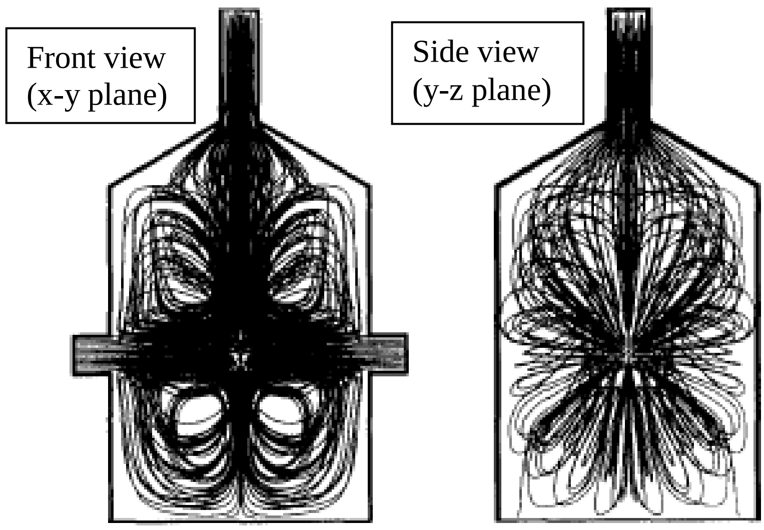


(c) Computational path lines for $Re_j$=40

Fig. 2.16: Geometry and results of impingement jet contactor (Unger et al., 1998)

inlet. Similarly, the portion of the jet travelling radially outwards impinged on the cylindrical wall and divided. This caused two U-shaped counter rotating vortices on each side of the impingement plane.

The flow field of opposed axisymmetric jets in a confined cavity was examined for instabilities due to various geometrical and fluid parameters by Johnson and Wood (2000). The impingement behaviour of the opposing jets was investigated through flow visualization and laser Doppler anemometry. Various flow regions were identified such as stable steady, regular oscillatory and irregular oscillatory. When Reynolds number (based on the nozzle diameter, fluid kinematic viscosity and velocity through the nozzle) was less than 90, a steady flow field was observed. Subsequent increase in fluid velocity caused a regular oscillating flow behaviour. This was described as a class of self-sustaining oscillations where instabilities in the jet shear layer was amplified because of pressure disturbance in the impingement region. Two acrylic models i) 20 mm square chamber ii) 25.5 mm circular chamber were used in the experiment. Nozzle diameters were 2 mm and 2.38 mm respectively. Mineral oil was used as representative fluid for flow visualisation. A fluorescent dye (Fluorol Yellow) was injected through one jet and the other jet was free from dye. Vortices aligned with the jet axis were observed in the experiment. At one instant, one jet was deflected into the head area and then deflected out, while the other jet was deflected into the head area in an almost periodic and out of phase manner.

A numerical study of flow and mixing characteristics of laminar confined impinging streams was reported by Devahastin and Mujumdar (2002). The two streams of air having equal (opposite) velocity impinged against each other and then left the system through the exit channels symmetrically on either side of the impingement region. The Reynolds numbers ($Re_j$) of inlet jets (based on inlet channel hydraulic diameter) were varied from 500 to 10000. The ratio of the height (H) of the exit channel to the width (W) of the inlet jet was varied from 1.0 to 4.0. PHOENICS Version 2.2.2 was used for solving the transient conservation equations of mass, momentum and energy. The convection terms in the momentum and energy equations were discretized using the hybrid scheme. A fully implicit scheme was used to discretize the transient terms. The discretized equations were solved using SIMPLE (Patankar, 1980) algorithm. Finally the conditions were identified, where the flow patterns shifted from laminar to transitional and then to random regimes. The velocity components were sampled at each time step at x=W/2 and y=0. It was reported that the transition Reynolds number was dependent on the geometric configuration (viz. H/W) as shown in Fig. 2.17. It was observed that at H/W =1, transition of flow from stable behaviour to oscillatory started at Reynolds number of 3500. With increase in H/W ratio transition took place at lower Reynolds number.

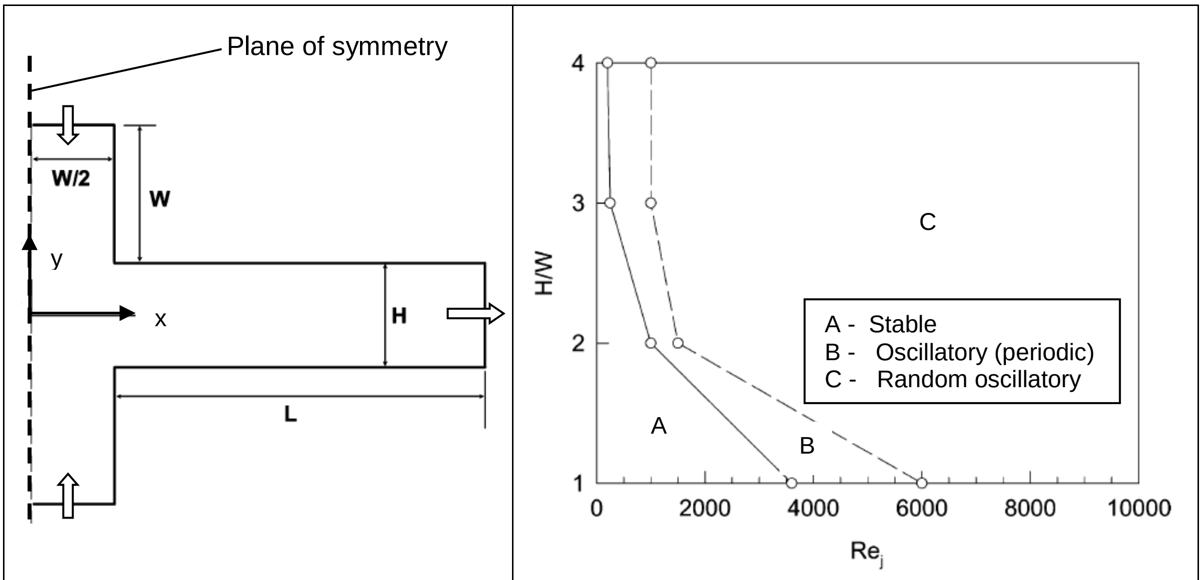


(a) Geometric flow configuration (b) Flow regime diagram

Fig. 2.17: Geometric configuration and flow regime diagram

(Devahastin and Mujumdar, 2002)

Laminar mixing of opposing jets of air was numerically studied by Wang, Devahastin and Mujumdar (2005) using CFD code FLUENT version 6.1.18 (2002). In this opposing jet system, the two opposing slot jets impinged head-on and the combined flow left symmetrically along the parallel wall channels situated on either side of the impingement zone. Due to the high ratio of slot length in the z-direction to the slot width in the y-direction, the fluid flow was treated as a two-dimensional problem. Half of the flow domain was modelled in the numerical analysis because of geometric and physical symmetry as shown in Fig. 2.18. It was assumed that the fluid was incompressible and Newtonian with constant physical properties. Temperature was used as tracer to represent species concentration. The effects of gravity and viscous dissipation were neglected.

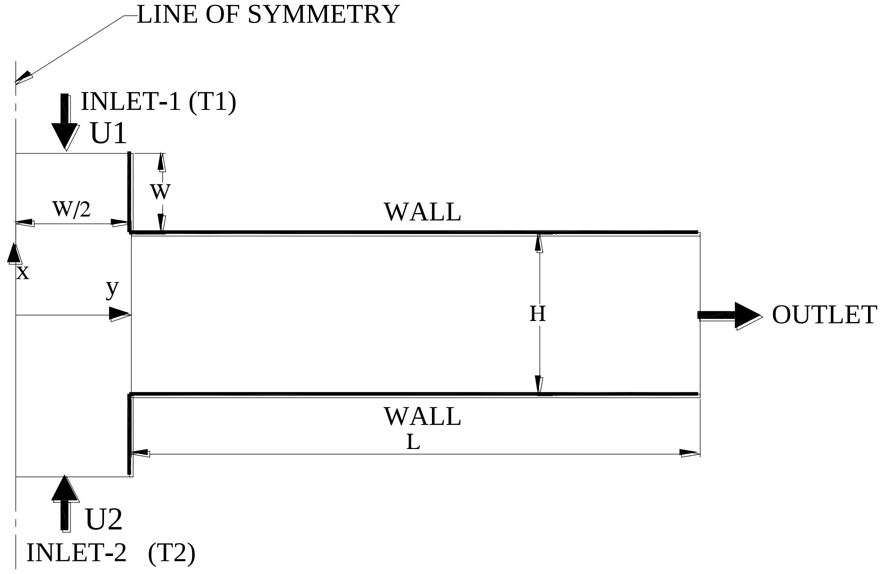


Fig. 2.18: Half domain for 2-D mixing of opposing jets (Wang et al., 2005)

The boundary conditions were as follows.

Inlet-1 : u=U1, v=0, T=T1

Inlet-2 : u=U2, v=0, T=T2

Outlet : Fully developed flow velocity specified

Walls : No slip and insulated wall

Convection terms were discretized using second order upwind scheme. Discretized equations were solved using SIMPLEC method. Convergence criteria considered was sum of normalised residuals i) for continuity < $10^{-5}$ ii) for momentum < $10^{-5}$ iii) for energy < $10^{-6}$. Analysis were reported for cold (downward) jet from top and hot (upward) jet from bottom with H/W=1 and Re=1000. Ratio of inlet mass flow rate of the hot jet flow to that of the cold jet was varied from 1 to 3. The results indicated that the impingement center came closer to the weaker top cold jet and vortex formation took place in the exit channel near the bottom just after the T junction.

Validation of the numerical model was done with the experimental data for the case of single exit with two opposing impinging streams of Roy et al. (1994). Width of inlet-1 and inlet-2 considered was H/2 and the width of the exit channel was H. Results were obtained for Re=500 with exit channel height and mean velocity as characteristic dimensions for diameter and velocity. Axial velocity profile was compared with experimental LDV (laser Doppler velocimetry) and found to be in good agreement.

#### 2.2.5.2 DNS simulation of confined jets from opposing feeder pipes

Direct Numerical Simulation (DNS) was carried out by Schwertfirm et al. (2007) for a confined impinging jet reactor with water as the working fluid at a Reynolds number of 500 and Schmidt number of 1. The basic geometry consisted of two opposing feeder pipes which opened into a main duct of square cross section at angle 90° as shown in Fig. 2.19. The main duct was closed at one side and the feeding pipes were flush with the wall. The flow entered the mixer symmetrically via feeding pipes with same Reynolds number and left the mixer at the open side of main mixing duct.

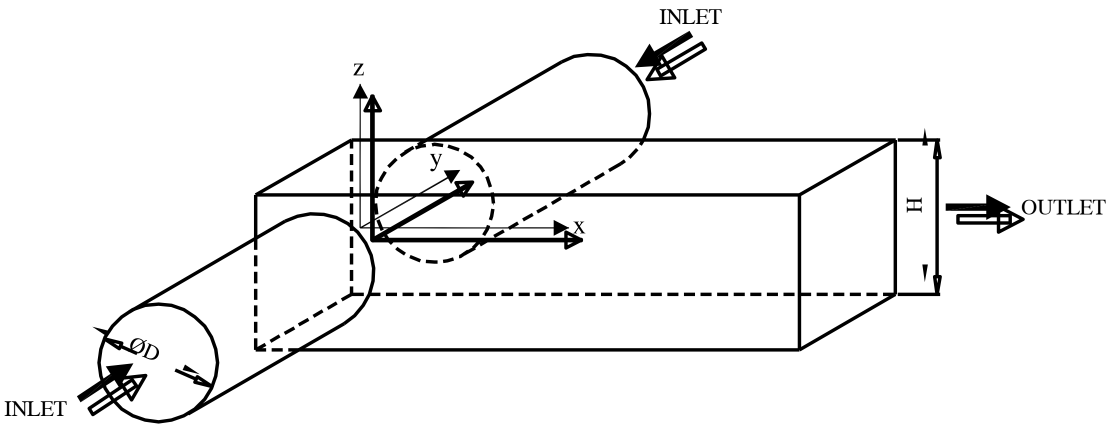


Fig. 2.19: Mixing in a confined impinging jet reactor (Schwertfirm et al., 2007)

Numerical analysis was carried out considering incompressible Navier-Stokes equations along with passive scalar transport equation using MGLET code (Manhart et al., 2001). The equations were solved using finite volume method on Cartesian system using staggered grid approach. The discretization in space and the approximation of derivatives and the interpolation was accomplished by second order central scheme. For the integration over time a third order Runge-Kutta method was used. The incompressibility constraint was satisfied by solving the Poisson equation for the pressure with incomplete lower-upper decomposition and applying correction for the velocities and the pressure. The no-slip boundary condition for the velocities and zero gradient condition for the scalar at the walls of the geometry were modeled by immersed boundary technique (Peller et al., 2006). At the outflow a zero velocity gradient and at the inflow planes of the feeding pipes laminar parabolic inflow profiles with peak inflow velocity were prescribed. The scalar was set to 1.0 and 0.0 at the inflow of the feeding pipes and zero gradient scalar condition was set at outflow. The grid was chosen to resolve the wall friction and the Kolmogorov length scale in the flow field. Results indicated that symmetry of the fluid flow was broken in the symmetry plane. Dominating flow of one inflow gave rise to the main vortex and secondary vortices in the off-set planes.

The numerical study was validated with experimental results using 2D particle image velocimetry (PIV) technique. The periphery of the PIV system contains a Nd-Yag double pulsed laser with a frequency of 10 Hz, two lenses for stretching and focusing the laser beam to a 1 mm thin sheet, a CCD camera with a Nikon AF Micro 60f/2.8D lens for recording images in a double frame mode. The evaluation system generated the final vector maps of flow field by a cross correlation technique. The maximum energy of the laser was 200 mJ and consequently one pulse with a length of 10 ns had the theoretical power of 20 MW. The camera detecting the scattered laser light under an angle of 90° used a CCD chip which included 768 × 484 pixels and the same number of storage cells. The CCD chip allowed the recording of two different images, which were exposed by two consecutive laser pulses. Ployamide seeding particles of a mean particle size of 20 μm and a density of 1020 $kg/m^3$ were used. The experimental data also showed break of the symmetry and a development of large vortex in the main mixing duct due to the passing of the jets. The direction of rotation was undetermined, but once established it was stable for the experiment.

#### 2.2.5.3 Turbulent mixing of opposing jets

Computational fluid dynamic predictions for confined two dimensional opposing turbulent jets over a range of jet Reynolds number and nozzle to nozzle separation were reported by Hosseinalipour and Mujumdar (1995).The standard k-ε model was used for turbulence modeling where the turbulent eddy viscosity $\mu_t$ was related to the turbulent kinetic energy, k and its dissipation rate, ε (where $\mu_t = \rho c_\mu k^2 / \varepsilon$ and $c_\mu$=0.09). The flow configuration simulated was as shown in Fig. 2.20. Both upper and bottom surfaces were held at constant temperature. Considering the symmetry of the configuration, the computational domain was specified by halving the domain from the middle nozzle as shown in Fig 2.20b.

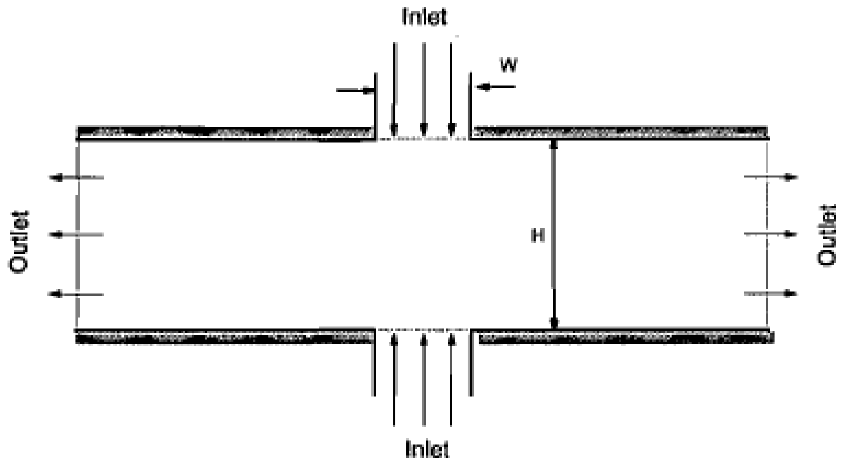


(a) Geometric flow configuration

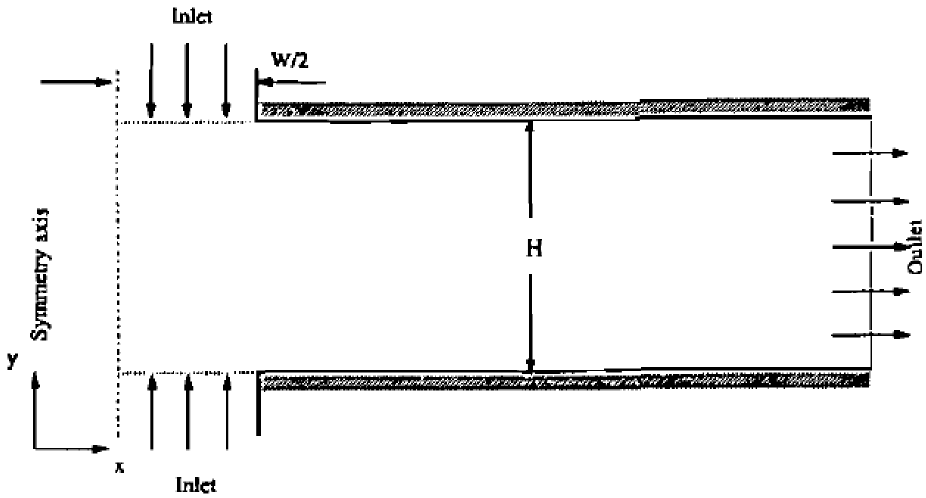


(b) Computational domain

Fig. 2.20: Geometric flow configuration and computational domain for 2-D opposing turbulent jets (Hosseinalipour and Mujumdar,1995)

At inlet turbulent velocity profile was used.

$v_x = 0$ ; $v_y = v_j$; $T = T_j = 25$ºC; $k = 0.003v_j^2$ ; $\varepsilon = c_\mu k^{3/2} / 0.03(W/2)$.

At jet centerline axis (shown as symmetry axis) symmetric boundary conditions were specified. The variable gradients ($\partial v_y/\partial y = \partial T/\partial y = \partial k/\partial y = \partial \varepsilon/\partial y = 0$) were zero and the velocity component $v_x$ was zero.

At solid wall the Dirichlet boundary condition for temperatures was used along the side walls and both top wall and bottom wall temperatures were 45ºC ($T_{tw}$ = $T_{bw}$ = 45 ºC). The law of the wall was applied at the top and bottom walls. The boundary conditions for $k$ and $\varepsilon$ were based on vanishing normal derivative of $k$ at the wall and the production rate were equal to the dissipation rate near the wall.

At outlet, fully developed boundary conditions were assumed. Thus all variable gradients ($\partial v_x/\partial y = \partial T/\partial y = \partial k/\partial y = \partial \varepsilon/\partial y = 0$) were zero except for the velocity component $v_y$ which was zero.

A control volume based finite difference method was used to discretize the governing equations by integration of the control volume. A fully staggered system was adopted for the velocity components and the scalar variables. A hybrid scheme was used to discretize the convection terms. The SIMPLEC algorithm was used for solution of the variables. The parameter ranges studied were $Re_j$ = 4000 – 40000 and H/W = 1– 4. Resulting flow fields obtained in the form of streamlines are shown in Fig. 2.21. Two recirculation zones were found along the top and bottom walls. It was observed that the effect of Reynolds number on the length of these zones was negligible.

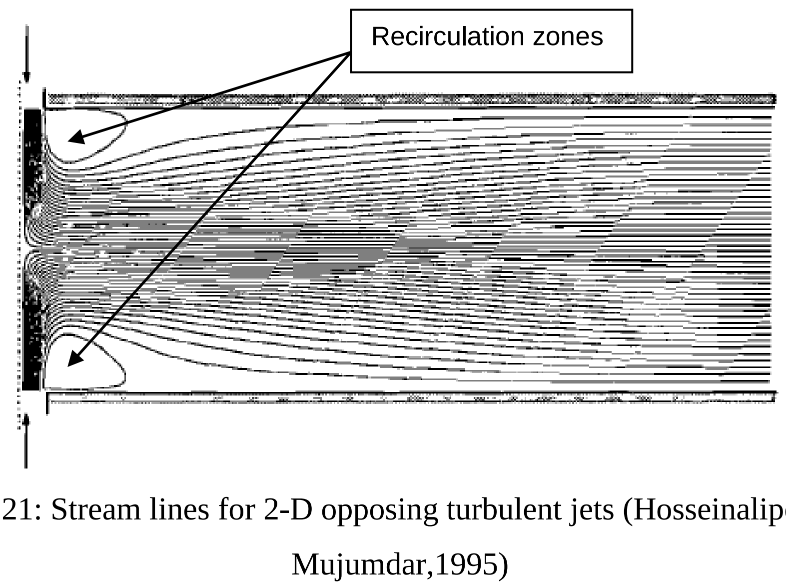


Fig. 2.21: Stream lines for 2-D opposing turbulent jets (Hosseinalipour and Mujumdar,1995)

Three-dimensional Turbulent mixing of opposing jets were numerically studied using CFD code FLUENT version 6.1.18 by Wang and Mujumdar (2005). Fluid was assumed to be incompressible and Newtonian with constant physical properties. Reynolds averaged Navier-Stokes equation and time averaged energy equation were solved. Based on Boussinesq approximation, the Reynolds stress was related to the local velocity gradients by an eddy viscosity $\mu_t$. Turbulent mass flux was related to the local concentration gradients by turbulent diffusion coefficient $D_t$. The low Reynolds number k-$\varepsilon$ turbulence model was used in this study. Species equation was also solved.

Pure water and sodium chloride solution were introduced at the nozzle inlets which were forming two opposing jets. After impingement in the mixer, the combined fluid left symmetrically via two symmetric exit channel outlets. Due to geometric and physical symmetry, only flow field within the half domain was solved numerically as shown in Fig. 2.22.

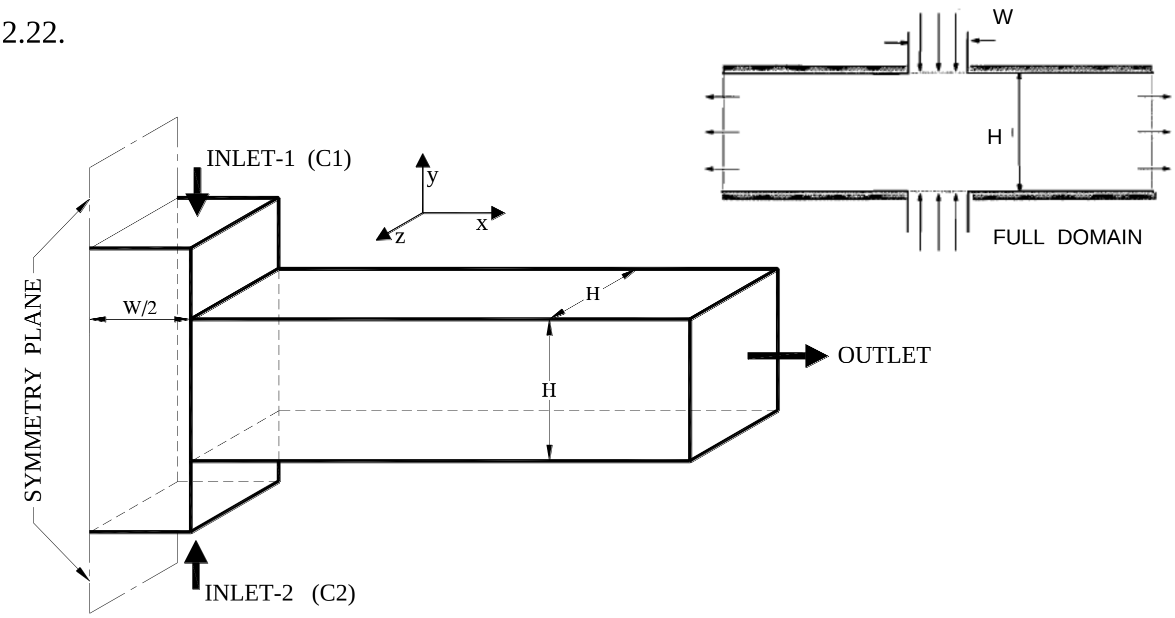


Fig. 2.22: Three dimensional mixing of opposing jets (Wang and Mujumdar, 2005)

The boundary conditions were (i) uniform velocity, species concentration, turbulent kinetic energy and its dissipation rate at the nozzle inlets (ii) symmetric boundary condition imposed along the symmetry plane (iii) fully developed flow velocity considered at the outlet plane (iv) no-slip and insulated wall boundary conditions specified in the confinement walls.

The turbulence intensity and length scale at the exit nozzle were set to be 2% and $0.07D_h$ respectively. The governing equations were discretized using second order upwind scheme. The convergence criteria were the normalized residuals of all dependent variables less than$10^{-5}$.

Results were reported for Re=30000, H/W=1 and H/W=2. Total exit mass flow rate was kept constant and the ratio of inlet mass flow rate of two jets was varied from 1.0 to 1.5. Results indicated that mixing effectiveness improved with increase in the ratio of inlet mass flow rate of two jets as compared to equal jets.

A comparison was also made with 2-D and 3-D case for H/W=1 with Re=30000. It was indicated that 2-D case predicted much faster mixing than 3-D case due to the lack of wall effect in z-direction. The opposing jets retarded slowly in 2-D case and led to stronger jet impingement which was also due to lack of corner wall effect in 2-D. Therefore, it was recommended that 3-D simulation might be necessary to understand the actual mixing effect.

#### 2.2.5.4 Mixing of multiple opposing jets

Three dimensional flow and mixing characteristics of multiple confined turbulent round opposing jets were numerically analysed by Wang and Mujumdar (2007). Air was considered as the working fluid and its temperature served as a passive tracer to characterize the mixing performance. Standard k- ε turbulence model in the CFD code FLUENT version 6.2 was selected to model the turbulent mixing. Steady, three dimensional, incompressible and turbulent flow with constant fluid properties was assumed for the governing equations of conservation of mass, momentum and energy. Numerical simulation was carried out for dual-inlet inline mixer where two opposing jets (i) a cold jet (304 K) and (ii) hot jet (315 K) were introduced from the side onto the main pipe 0.3D away from the closed end of the main pipe as shown in Fig. 2.23.

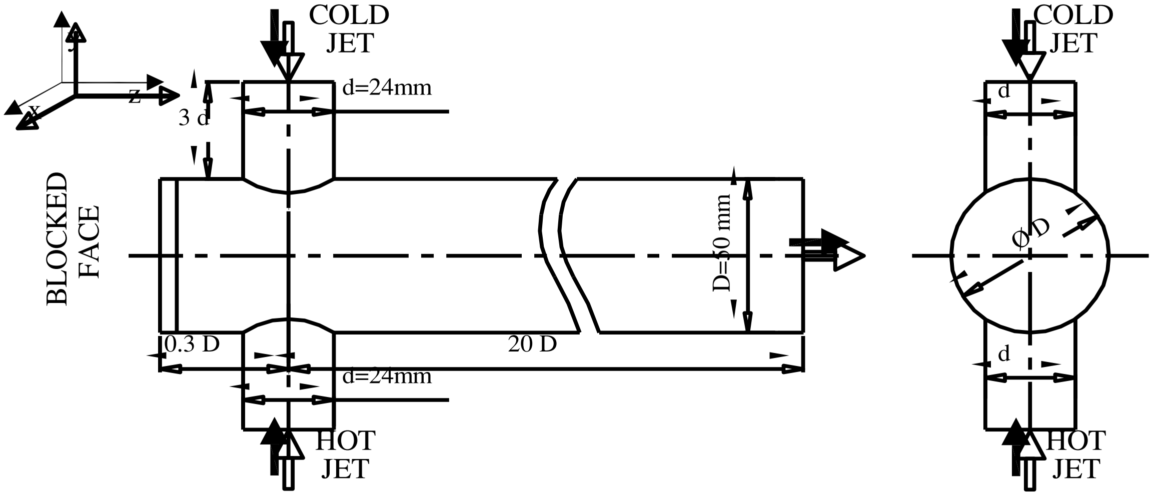


Fig. 2.23: Mixing of two opposing jets (Wang and Mujumdar, 2007)

The boundary conditions were (i) uniform velocity and temperature profiles at the inlet of the opposing jet pipes. The initial turbulence intensity of 5% was assumed and kinetic energy and its dissipation rate were specified at the inlets. (ii) Pressure was specified to be atmospheric at the outlet. (iii) No-slip and adiabatic wall boundary condition was specified on the walls of the side and main pipes. The governing equations were descretized using QUICK interpolation scheme and solved using the SIMPLE algorithm. The solution was considered converged when the normalized residual of energy equation was less than $10^{-6}$ and the normalized residuals of all other variables were less than $10^{-4}$.

To understand the effect of multiple opposing jets, two pairs of opposing jets spaced 90° apart were analysed as shown in Fig. 2.24. To remove the effect of flow residence time in the exit, the total mass flow rate was kept identical to the dual inlet inline mixer. The results indicated that mixing was better in two opposing jets case in the impingement zone and its vicinity. This was due to the vortex motion induced mixing which was created mainly by head on collision with double the velocity than that for the two pairs of opposing jets case.

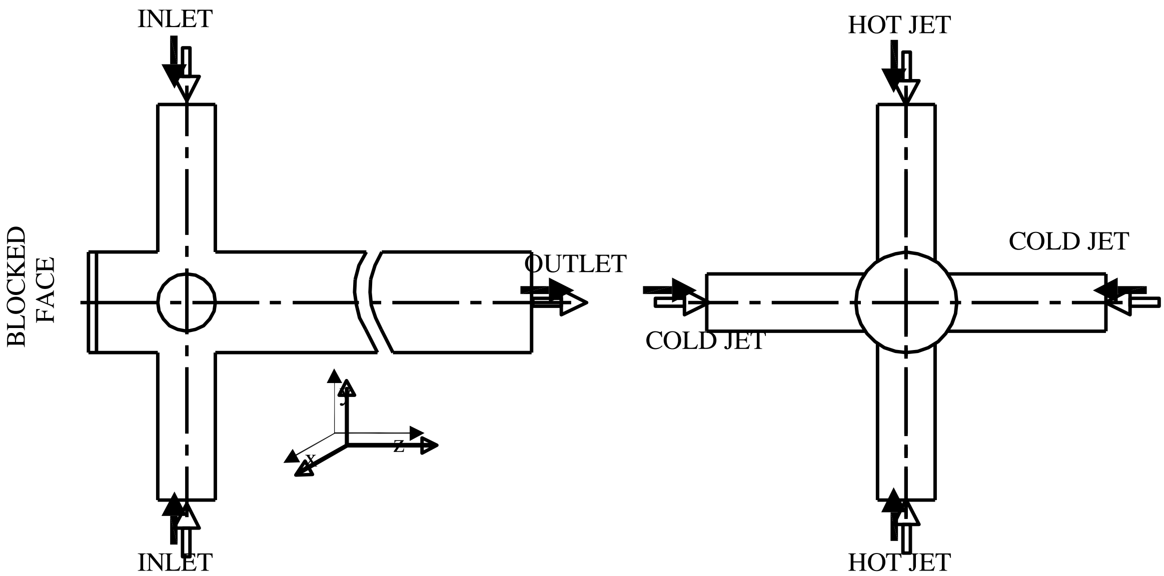


Fig. 2.24: Mixing in two pairs of opposing jets (Wang and Mujumdar, 2007)

The standard k-ε turbulence model was verified by comparing the predicted temperature profiles with published experimental results of Tang et al. (1993) in a Tee junction. The experiment considered a single right-angle stream injection into a cross flow. The fluid temperature of the main cross flow was 296 K and that of the side inlet stream was 303 K. Fully developed velocity profiles were specified at both pipe inlets corresponding to the inlet flow conditions in the experiments. The results indicated that the standard k- ε model prediction was in good agreement with the experimental results.

2.2.5.5 Stagnation point offset due to impingement of opposing jets

Dynamic behaviours in a three dimensional confined impinging jets reactor (CIJR) were experimentally studied by Li et al. (2014) using a flow visualization technique. The effects of inlet jet Reynolds number ($100 \leq Re \leq 2000$) and geometry configurations ($2 \leq D/d \leq$

12) of the CIJR on the flow regimes were investigated by particle image velocimetry. The confined opposing jets were obtained by two identical axisymmetric nozzles (diameter d) installed in a cylindrical chamber (diameter D) as shown in Fig. 2.25. The instantaneous flow patterns in the CIJR were visualized by the white smoke generated by some small fuming tablets. In the experiment air flow was supplied through inlet nozzles and the smoke was introduced to only one jet to observe the shape and location of the impingement plane more clearly. The visualization images were captured by a PIV system and a high speed camera. Various types of flow regimes captured are shown in Fig.2.25b to 2.25f. Segregated flow regime (Re <150), self-sustained radial deflective oscillation ($150 \leq Re \leq 300$), transition from radial deflective oscillation to axial oscillation ($300 \leq Re \leq 500$) and combination of vortex shedding & axial instability ($Re > 500$) were observed in the CIJR. With increase in Reynolds number, the vortex shedding regime was pronounced with increasing axisymmetric waves on the impingement plane caused by collision instability in the stagnation point. The increasing perturbation in the jets with Re and the confined boundary was the causes of the axial instability in CIJR. It was reported that at Re > 1000, it was difficult to get the impingement point located at the midpoint between the nozzles and the impingement plane moved the position near to the two nozzles which is similar to the stagnation point offset studied by Li et al. (2010). Here, stagnation point offset was defined as the distance from the stagnation point to the midpoint of the exit nozzles and was denoted as $\Delta x$ as shown in Fig. 2.26. The experiments were done at higher Reynolds number Re > 4500 using the hot-wire anemometer measurement and the smoke-wire flow visualization technique. The nozzle separation distance (L) was varied from 1 to 20 times the nozzle diameter (d). Flow velocity at exit of jet 1 ($= u_1$) was 2.36 m/s and exit velocity ratio ($a = u_2/u_1$) was 1.0 and 0.97. It was observed that at L = 4d, the stagnation plane was very unstable and it could

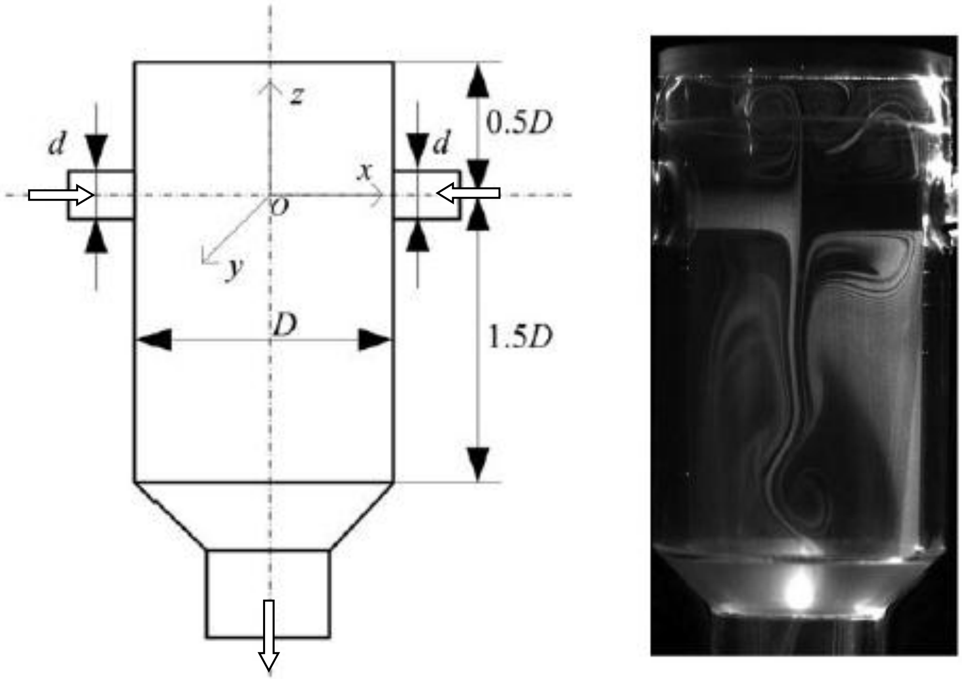


(a) Geometry of CIJR (b) Re = 100

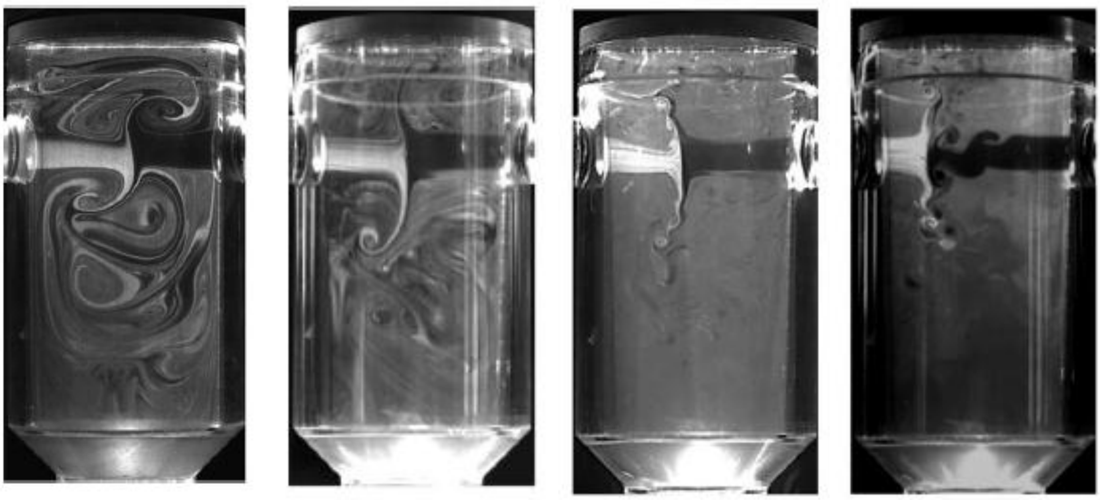

(c) Re = 150 (d) Re = 300 (e) Re = 1000 (f) Re = 2000

Fig. 2.25: Geometry of CIJR and flow patterns at various Re (Li et al., 2014)

only stay at the two semi-stable positions very close to the jet exits as shown in Fig. 2.26b and Fig. 2.26c. It was reported that jet exit conditions such as velocity profile, Reynolds number and the turbulence intensity had influence on the stagnation point. Uniform exit velocity profile and increasing turbulence intensity decreased the stagnation point offset.

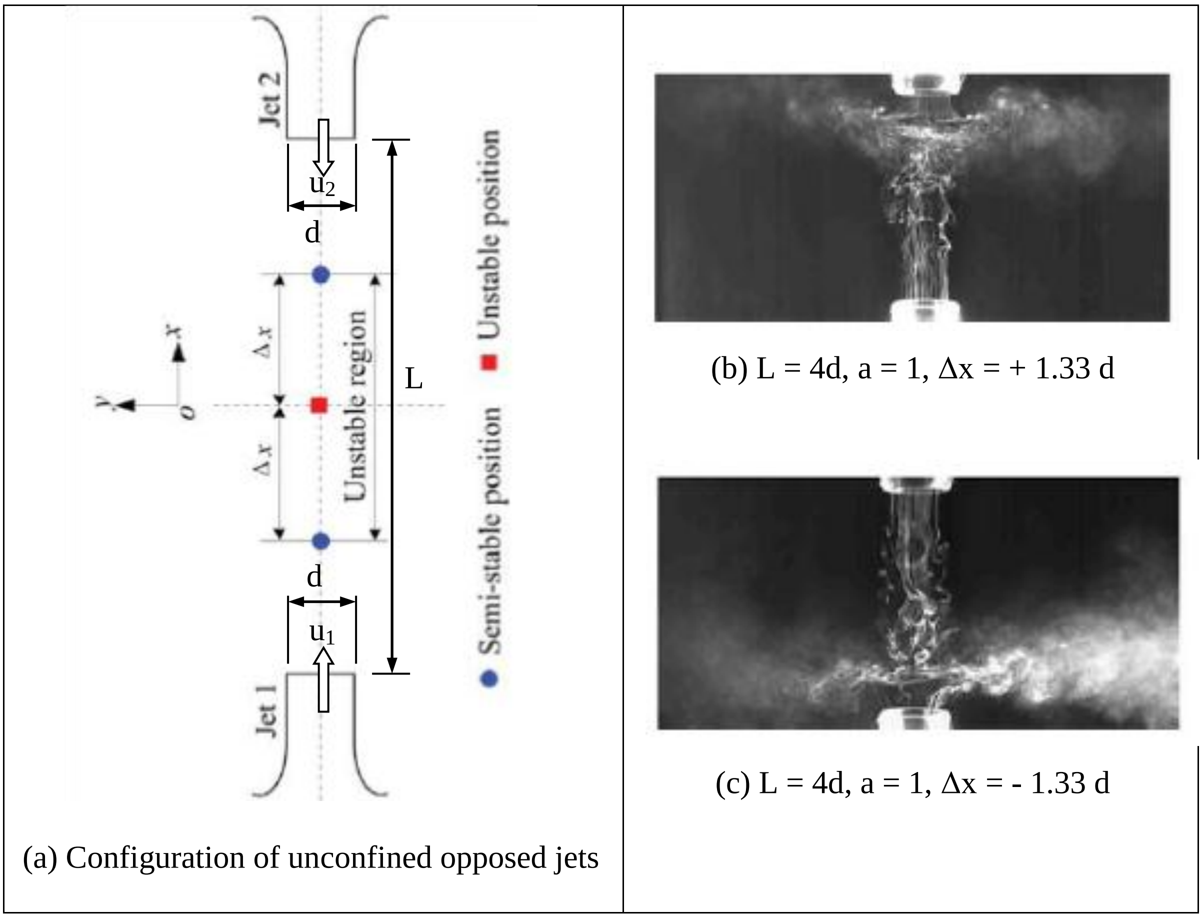


(a) Configuration of unconfined opposed jets

(b) L = 4d, a = 1, Δx = + 1.33 d

(c) L = 4d, a = 1, Δx = - 1.33 d

Fig. 2.26: Mixing of unconfined opposed jets (Li et al. 2010)

The studies carried out for mixing with two streams for various geometries is indicated in Table-2.1.

## 2.3 Closure of literature review

From the literatures it is observed that a lot of studies have been reported where experiments were carried out for mixing of opposing jets (Wood et al., 1991; Unger et al., 1998; Schwertfirm et al., 2007; Li et al., 2010; Li et al., 2014). The focus of these studies was mainly the flow field created by impinging jets. It was observed that re-entrainment of fluids by the jets created a 3-D recirculation zone where counter rotating ring vortices were found. Wood et al. (1991), observed unsteady flow oscillations at Reynolds number higher than 90 using particle tracing laser doppler anemometry. Unger et al., (1998) studied upto a Reynolds number (Re) of 40 and found counter rotating vortices using different fluorescent die to visualise flow structure and PIV for velocity field measurement. Schwertfirm et al., (2007) carried out experiments using PIV for Re=500 and found break of symmetry and development of large vortex. Li et al. (2010) carried out experiments of mixing of unconfined opposed jets at Re > 4500 using the hot-wire anemometer measurement and the smoke-wire flow visualization technique. It was observed that the stagnation plane was very unstable when the distance between the two opposite jets is four times the diameter of the jet. Li et al. (2014) did experiments for mixing of confined opposing jets in the range of Reynolds number 100 to 2000. Flow patterns were visualized by the white smoke generated by some small fuming tablets. Combination of vortex shedding and axial instability is observed at Re > 500. With the increase in Reynolds number, the vortex shedding regime was pronounced with increasing axisymmetric waves on the impingement plane caused by collision instability in the stagnation point. Form these experiments it is observed that mixing of opposing jets at higher Reynolds number (Re> 2000) has not been reported and needs to be studied for the application mixing of opposing flows inside chimney structure. It is also seen that the opposing flows reported have similar flow rates (flow ratio ≈ 1), however the interest of present study considers flow ratio from 0.0 to 0.15.

Though literatures on mixing of opposing flows at high Reynolds number are less, experiments on mixing in T- junctions at higher Reynolds number have been of interest to many researchers (Tang et al., 1993; Kok and Van der Wal, 1996; Gang Pang and Hui Meng, 2001; Hirota et al., 2005; Ogawa et al., 2005; Hosseini, Yuki and Hashizume, 2008; Kamide et al., 2009; Walker et al., 2009; Naik-Nimbalkar et al., 2010; Hirota et al. 2010;Stigler et al., 2012). These studies mainly focus on quantification of mixing between the main flow and the branch flow. Gas mixing was experimentally characterized by measuring the temperature distribution downstream of a T-junction by Tang et al. (1993) for Reynolds number of the main flow ranging from 8380 to 79000. Kok and Vander Wal (1996) carried out experiment and measure the velocity profile using laser Doppler velocimetry in a T-junction with water as fluid (Re at outlet is about 10000). Characteristics of velocity field and temperature fields due to mixing were predicted by Hirota et al. (2006) in a T-junction with rectangular cross section with main flow Re = 25000 with air as working fluid. Velocity distributions were measured using a PIV system. Temperature distributions were measured using thermocouples. The interface of two flows were found to deform quite irregularly and mushroom like discrete longitudinal eddies were observed along the interface of two flows. Influence of upstream elbow in the main pipe was studied by Ogawa et al. (2005). Temperature distribution was measured by a movable thermocouple tree and velocity field was measured by high speed PIV. The flow pattern was classified into three patterns; (i) wall jet (ii) deflecting jet and (iii) impinging jet according to momentum ratio between main flow and branch flow. Here T-junction was in horizontal plane (i.e., main pipe and branch pipe were placed in horizontally). Hosseini, Yuki and Hashizume (2008) had done similar experiments with a 90° bend upstream of the T-junction, but the T-junction was kept in vertical plane with main flow direction vertically upward and branch flow in horizontal direction. Flow patterns were visualised using PIV and temperatures were measured using thermocouples. It was reported that at high Reynolds number (33000-150000), mixing phenomenon was controlled by the mechanism of large eddy. Walker et al. (2009) carried out experiments in a horizontal T-junction geometry considering isothermal mixing of two fluid streams. Instead of temperature as transport scalar, the concentration of dissolved salts was measured using conductivity sensors to predict the mixing behaviour in Reynolds number range 8770 to 43860 based on outlet flow velocity. Velocity ratio between branch flow and main flow was varied from 0.40 to 1.67. Kamide et al. (2009) also did experiments of mixing of hot and cold water in a T-junction at higher Reynolds number (327000 – 435000) and visualised the flow patterns using PIV. Naik-Nimbalkar et al. (2010) carried out velocity and temperature measurements using hot-wire anemometer. A constant temperature module was used for the measurement of local velocity in the system. Hirota et al. (2010) did experiments in a T-junction with rectangular cross section with main flow Re of 15000 and water as working fluid. They visualised the velocity field using PIV and measured the temperature field with thermocouples. Jaroslav Stigler et. al (2012) did experiments in a T-juction where flow ratios were varied from 0 to 1 in steps of 0.2 with water as working fluid and velocity field was measured using PIV.

Studies were also reported to numerically simulate turbulent mixing behaviour of opposing flows as well as mixing in T-junctions. Majority of the simulations were based on RANS modelling. In Reynolds-averaged Navier-Stokes (RANS) modelling, attention was focused on the mean flow and the effects of turbulence on the mean flow properties. Nevertheless, the effect of turbulence on the mean flow properties was considered. Extra terms (like Reynolds stresses) appeared in the time averaged flow equations due to the interactions between various turbulent fluctuations. These extra terms were modelled with classical turbulence models: among the best known ones were k-ε model and the Reynolds stress model. The computing resources required for reasonably accurate flow computations were modest in RANS modelling. Tang et al. (1993), Kok and Van der Wal (1996), used standard k-ε model to predict the turbulent mixing for T-junction with air as main working fluid for Re upto 80000 and compared their results with experiments. Naik-Nimbalkar et al. (2010), Walker et al. (2010) studied mixing of water in T-junction for similar range of Reynolds number using same turbulence model and compared experimental data. Hosseinalipour and Mujumadar (1995), Wang and Mujumdar (2007) simulated numerically mixing of opposing jets for steam and air respectively using standard k-ε model for Re=40000 and 35000 respectively. Vicente et al. (2008) used this model for mixing in X-junction with water as working fluid upto Re=50000 and compared with experimental results.

Wang and Mujumdar (2005) numerically simulated mixing of opposing jets of water (Re=24000-36000) using low Reynolds number k- ε model in order to capture the heat/mass transfer rates for wall-bounded flows specifically at lower range of Re. Stiger et al. (2012) and Guobing Kang (2014) used k-ε realizable model for mixing of water in T-junction at Reynolds number of 200000. The realizable model more accurately predicted the spreading rate of both planar and round jets. It provided superior performance for flows involving rotation, boundary layers under strong adverse pressure gradients, separation and recirculation.

Frank et al. (2010) used steady-state RANS simulation with the shear stress transport (SST) turbulence model for turbulent isothermal mixing of water in T junction. The SST model applied the k–ω based model in proximity of the wall and the k–ε model in the bulk of the flow, while a blending function ensured a smooth transition between the two models. Automatic wall functions were used where a maximum y+ = 4.5 on the finest mesh assured that the boundary layer can be fairly well resolved on the fine mesh. Since the flow in the T-junction was highly anisotropic where both flow streams mixed, further studies were carried out by applying the k–ω based baseline Reynolds stress model (BSL RSM).

Webb and Wanders (2006) studied turbulent mixing of two water flow streams using Large Eddy Simulation (LES) approach for a pipe cross where inlet pipes were at right angle. Large eddy simulation (LES) was an intermediate form of turbulence calculations which tracked the behaviour of the large eddies. The method involved space filtering of the unsteady Navier-Stokes equations prior to the computations, which passed the large eddies and rejected the smaller eddies. However, the effects of the smallest unresolved eddies were included on the resolved flow (mean flow plus large eddies) by means of a sub-grid scale model. In LES, unsteady flow equations were solved, so the demands on computing resources in terms of storage and volume of calculations were large. The study of Webb and Wanders considered water as working fluid with Re 40000.

Schwertfirm et al. (2007) modelled mixing of opposing water jets by Direct numerical simulations (DNS) where the mean flow and all turbulent velocity fluctuations were solved. The unsteady Navier-Stokes equations were solved on spatial grids that were sufficiently fine that they could resolve the Kolmogorov length scales at which energy dissipation took place and also with time steps sufficiently small to resolve the period of the fastest fluctuations. These calculations were highly costly in terms of computing resources, so the method was not used for industrial flow computations. The numerical simulation of Schwertfirm et al. (2007) considered Re= 500. Since mixing opposing flows caused highly turbulent flow field even at low Re> 150, DNS was applied for the problem.

The literature mentioned above mainly focused to establish the effectiveness of mixing of the two streams. It was also observed that studies were reported up to Reynolds number of $4.35\times10^5$ for the case where cross flow takes place in a T-junction. The maximum Reynolds number for the cases with mixing of opposing flows was found to be about

40000. The flow behavior observed for opposing flows were found to be highly turbulent even with Reynolds number more than 150. Hence the dynamic behavior of mixing of opposing flows inside the chimney where maximum Reynolds number can be as high as $3\times10^6$ needs to be studied. Geometry of the chimney with variation in angle between the central axis of the chimney and side outlet arm is also not studied and reported. Moreover, the boundary conditions for both the fluid streams were known as inlet boundary conditions for the cases mentioned in the literature. In the mixing studies inside the chimney structure, boundary condition of the top inlet of the chimney is unknown. The bypass flow which is sent into the water pool is expected to be drawn inside the chimney from the top inlet and the velocity distribution at the inlet depends on the behavior of water flowing within the pool. Hence, a large domain of pool water in which the chimney is immersed also needs to be simulated. Moreover, in typical reactors, Reynolds number is one order higher (about $3\times10^6$) for which the mixing study is required to be done. The geometry considered in this work with various nozzle inclinations needs to be understood. Hence the focus of the study here is to investigate the mixing behavior of the upward and downward flows inside the prototype chimney structure for various bypass flow ratios, inclination angles and chimney heights. Numerical solutions and experimental validation on scaled down models of chimney structure are done to study the effects of all these parameters so as to establish the mixing behaviour for the prototype chimney.

Table-2.1: Summary of literature

| Reference (year) | Geometrical configuration in mixing study | Fluid flowing during mixing | Pipe diameter / cross section (velocity): Main / Cross flow | Pipe diameter / cross section (velocity): Branch /Jet | Study approach: Numerical simulation | Study approach: Experiment | Reynolds number of inlet streams | Turbulence model in CFD |
|---|---|---|---|---|---|---|---|---|
| Wood et al. (1991) | Opposing jets | Mineral oil | 0.0254 m | 0.00238 m | - | Particle tracing, laser Doppler anemometry | 50 – 300 / 50 – 300 | - |
| Chen et al. (1991) | T-junction | Air-Methane | 0.0635 m | 0.0127 m | Mathematical modelling | - | 100000 (main) | - |
| Tang et al. (1993) | T-junction | Air | 0.0381 m (3.52 – 29.5 m/s) | 0.0095 m (2 – 20.62 m/s) | FLUENT | Temperature measurement using thermocouples | 8380 – 79000 / 1200 – 12200 | standard k- ε |
| Fric and Roshko (1994) | Cross flow | Air | 0.5 m× 0.5 m (1.5 – 4.5 m/s) | 0.038 m (3 – 45 m/s) | - | Smoke-wire flow visualisation | 3800 – 11400/ 7600 – 114000 | - |
| Hosseinalipour and Mujumadar (1995) | Opposing jets | Steam | | | CVFDM | - | 4000 - 40000 | standard k- ε |
| Kok and Van der Wal (1996) | T-junction | Air-Nitrogen / Water | 0.100 m | 0.010 m 0.026 m | FLOW3D | Laser Doppler velocimetry and Oxygen analyzer | 10000 (outlet) | standard k- ε |
| Hosseinalipour and Mujumdar (1997) | Opposing jets | | | | CVFDM | - | 100 / 50 – 500 | - |
| Unger et al. (1998) | Opposing jets | Glycerin /water | 0.013 m | 0.013 m | FLUENT | PIV | < 80 | - |

| | | | | | | | | |
|---|---|---|---|---|---|---|---|---|
| Smith and Mungal (1998) | Cross flow | Air | 0.54 m× 0.54 m ( 5 m/s ) | 0.010 m | - | Planar laser induced fluorescence using acetone as tracer | 8400 – 41500 (jet) | - |
| Johnson and Wood (2000) | Opposing jets | Mineral oil | 0.020 m × 0.020 m / 0.0255 m | 0.002 m | - | Dye and laser Doppler anemometry | <150 | - |
| Gang Pang, Hui Meng (2001) | T-junction | Water | 0.0762 | 0.0127 | - | PIV and PLIF | 20850 /10630 20850 / 17500 | - |
| Devahastin and Mujumdar (2002) | Opposing jets | Air | | | PHOENICS Version 2.2.2 | - | 500 – 10000 / 500 - 10000 | - |
| Wang, Devahastin and Mujumdar (2005) | Opposing jets | Air | | | FLUENT version 6.1.18. | - | < 1000 | - |
| Wang and Mujumdar (2005) | Opposing jets | Water | 0.010 m | 0.010 m | FLUENT Version 6.1.18 | -- | 30000 / 30000 34000 / 26000 36000 / 24000 | Low Re k-ε |
| Hirota et al. (2006) | T-junction | Air | 0.060 m × 0.120 m | 0.030 m × 0.120 m | - | PIV and temperature measurement using thermocouples | 25000 (main) | - |
| Ogawa et al. (2005) | T-junction | Water | 0.150 m (1.46 m/s 0.46 m/s 0.23 m/s) | 0.050 m (1 m/s) | - | PIV and temperature measurement using thermocouples | | - |
| Webb and Waanders (2006) | Cross pipe | Water | 0.050 m | 0.050 m | FLUENT Version 6.2 | -- | 40000 / 40000 | LES |

| | | | | | | | | |
|---|---|---|---|---|---|---|---|---|
| El-Morshdy (2007) | Reactor chimney | Water | 0.438 m × 0.489 m | 0.438 m × 0.489 m | FDM | -- | | - |
| Wang and Mujumdar (2007) | Opposing jets | Air | 0.050 m | 0.024 m | FLUENT Version 6.2 | - | 35000 / 35000 | standard k- ε |
| Schwertfirm et al. (2007) | Opposing jets | Water | 0.080 m × 0.080 m | 0.040 m | MGLET | PIV | 500 | DNS |
| Vicente et al. (2008) | X-junction | Water | 0.019 m | 0.019 m | PHOENICS | Hipochlorine Blue ink DYE | 28000 / 23000 28000 / 50000 | standard k- ε |
| Dang et al. (2008) | Oblique pipe | Water | 0.079 m | 0.018 m | - | Potassium permanganate powder | | - |
| Hosseini, Yuki and Hashizume (2008) | T-junction | Water | 0.108 m | 0.021 m | - | PIV | 33000 / 15000 150000 / 5000 | - |
| Kamide et al. (2009) | T-junction | Water | 0.150 m | 0.050 m | AQUA (FDM) | PIV | 327000 / 75000 435000 / 50000 | MILES approach |
| Walker et al. (2009) | T-junction | Water | 0.051 m | 0.051 m | - | Electrical conductivity measurement | | - |
| Li et al. (2010) | Opposing jets | Air | 0.030 m to 0.360 m | 0.030 m | - | Hot-wire anemometer and the smoke-wire visualization | > 4500 | - |
| Naik-Nimbalkar et al. (2010) | T-junction | Water | 0.050 m | 0.025 m | FLUENT version 6.3.26 | Hot-wire anemometer | 80000 / 20000 | standard k- ε |
| Walker et al. (2010) | T-junction | Water | 0.050 m | 0.050 m | ANSYS CFX-10 | - | | standard k- ε, SST |
| Frank et al. (2010) | T-junction | | 0.140 m | 0.100 m | ANSYS CFX | - | 190000 / 190000 | SST, RSM, SAS-SST |

| | | | | | | | | |
|---|---|---|---|---|---|---|---|---|
| Hirota et al. (2010) | T-junction | Air | 0.060 m × 0.120 m | 0.030 m × 0.120 m | - | PIV and Temperature using Thermocouple | 15000 (main) | - |
| Stigler et al. (2012) | T-junction | Water | 0.050 m | 0.050 m | FLUENT | PIV | ~200000/~200000 | realizable κ-ε |
| Li et al. (2014) | Opposing jets | Air | 0.050 m | 0.004 m to 0.025 m | - | PIV | 100 – 2000 | - |
| Guobing Kang (2014) | T-junction | Water | 0.060 (0.247 m/s) | 0.010 (0.847 m/s) | FLUENT | - | | realizable κ-ε |

Note : FDM - Finite Difference Method
LES – Large Eddy Simulation
DNS – Direct Numerical Simulation
PIV – Particle Image Velocimetry
MILES – Monotonically Integrated LES
CVFDM – Control Volume based Finite Difference Method
SST – Shear Stress Transport
SAS – Scale Adaptive Simulation
RSM – Reynolds Stress Model

## 2.4 Scope of present work

The behaviour of turbulent mixing inside the chimney being complex in nature, CFD codes are used to realistically simulate the turbulent mixing. This includes the methodology of numerical simulation to understand the effect of variation of downward flow through the chimney, nozzle inclination, chimney height etc. on the stagnation height. Since the turbulent mixing takes place in reactors at high Reynolds number (order of $10^6$) and no specific numerical and experimental results are available in literature, methodology for numerical simulation and benchmarking of the numerical solution through experimental validation needs to be done. Scaling philosophy is adopted for arriving at various non-dimensional numbers from the basic conservation equations of mass, momentum and energy for the mixing phenomenon. The experiments are designed to cover a range of non-dimensional numbers so that its effect on the mixing can be observed.

Experimental validation of the computer simulation is presented using test models designed using appropriate scaling laws relevant for the mixing phenomena governed by both the inertia as well as the buoyancy forces depending on the process conditions. Temperature distribution within the chimney is measured and compared with the predicted results. Velocity distribution is also measured and compared with the computational results after non-dimensionalisation of the results.

Experimental investigations are done using Particle Image Velocimetry (PIV) technique for acquiring the velocity field in a smaller set up to cover a range Reynolds number upto 40000 for comparison with numerical results. Due to limitation of space and facility, temperature difference between the opposing flows is not simulated and the core flow in the experiment is limited upto 1 kg/s in this setup.

In another larger setup, the core flow is simulated upto 25 kg/s corresponding to a Reynolds number of $4.5\times10^5$. In this set up provision is made to carry out the experiments with temperature differential between the two opposing flows as expected in any pool type research reactors. Measured temperature variation along the centre of the chimney is used for quantitative comparison with simulation results.

The primary aim of this computational and experimental validation study is to understand the flow physics of turbulent mixing in the chimney configuration which has not been previously reported in literature. The following objectives are defined to achieve this goal.

i) To perform the numerical analysis of turbulent mixing for the chimney geometry

ii) To evaluate the effect of bypass flow ratio, outlet nozzle angle and chimney height on turbulent mixing characteristics of the flow field

iii) To study the asymmetric features in the velocity field due to eddies and vortices created within the chimney

iv) To study the effect of turbulence modelling on mixing characteristics

v) To study the effect of buoyancy on mixing characteristics

vi) To observe the flow patterns through visualistaion studies

vii) To validate the numerical analysis by comparing the simulation results with the experimental data

viii) The results of prototype and both the test models are compared to establish the scaling philosophy adopted for the study and to develop a generalized correlation of the mixing behaviour.

ix) Finally to predict the limiting bypass flow which would completely prevent the core activity from reaching the exit of chimney.

# Chapter 3

# Numerical Simulation of Prototype Chimney

## 3.1 Introduction

Numerical simulations are performed to study the turbulent mixing behavior of two opposing flows inside prototype chimney structure of High Flux Research Reactor. The chimney design facilitates drawing pool water in the downward direction and thereby suppresses the upward flow of radioactive water jet, so that radiation field at the reactor pool top is limited. Analyses were carried out considering the flow rate required for cooling the reactor core during normal reactor operation. Since the height and nozzle inclination of the chimney structure should be optimised, various heights of the chimney as well nozzle inclination are considered in the analyses which are discussed in the subsequent sections. Flow ratio between the downward bypass flow and the upward core flow are also varied in these simulations to establish the bypass flow requirement. The pool water temperature is 40 ºC. The effects of flow ratio, chimney height on the velocity and temperature distribution inside three-dimensional chimney structure are evaluated using PHOENICS. The effect of temperature difference between the opposing flows on the velocity distribution is also analysed.

## 3.2 Flow mixing inside prototype chimney geometry

A simplified schematic of flow mixing behaviour inside prototype chimney geometry (with 45° angle of inclination) is shown in Fig. 3.1. The core outlet hot radioactive water at 49°C ($T_{in}$) flows upward through chimney bottom inlet (I). The inlet cross section is a square geometry with side (D) of 450 mm. The upward flow velocity is $U_{in}$ which corresponds to a mass flow rate of $W_{in}$ (750 kg/s). Core bypass flow ($W_b$) is sent to the pool to compensate for the flow entering through the chimney top inlet (II) in the downward direction. Core bypass flow depends on the bypass flow ratio (R) considered for the mixing study. The temperature of the core bypass flow is 40ºC ($T_p$) which is the same as the core inlet temperature. Both upward flow (from the bottom) and downward flow (from the top) mix together just before the side nozzles of the chimney. The mixed flow is sucked out of the chimney with the help of pumps through outlet lines (IIIa, IIIb) of the two loops of the primary coolant system. Each side outlet line is of rectangular cross section of dimension 450 mm x 225 mm. The total core bypass flow ($W_b$) is distributed through two inlet lines (IVa, IVb) into the pool. These two inlet lines are of circular cross section with internal diameter of 225 mm. The equivalent amount of flow, which is equal to the total flow through these two lines, enters through the top of the chimney as shown in Fig. 3.1.

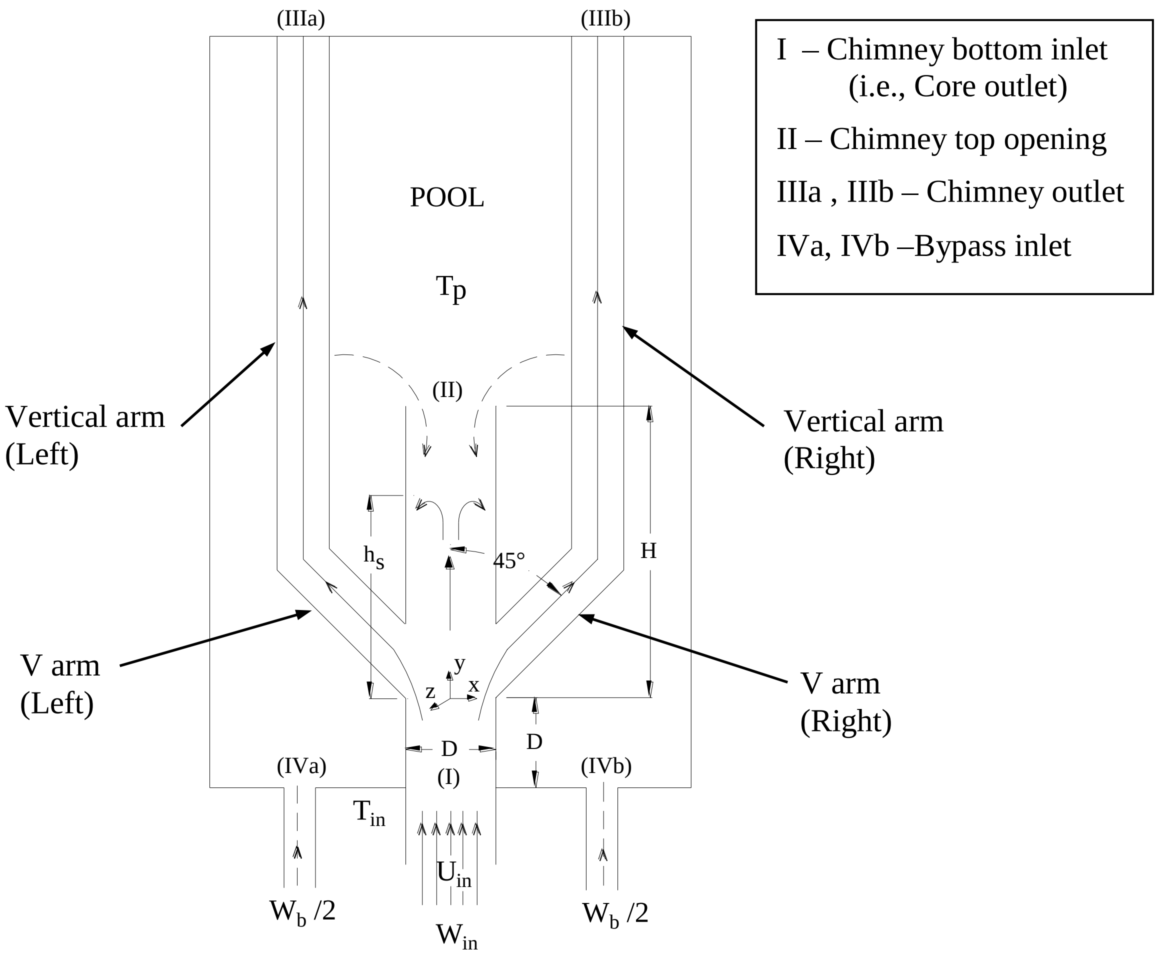


Fig. 3.1: Schematic diagram of flow mixing inside the chimney structure

This downward flow from chimney top will suppress the upward flow within the chimney. However, because of the momentum of the inlet flow, the upward flow prevails up to a certain maximum height. This is called the stagnation height ($h_S$). It is defined as the distance from the bottom (i.e., y = 0) of the chimney to the location, where the upward velocity becomes zero.

Computational fluid dynamics software PHOENICS (Ledwig, 2004) is used for the simulation of this mixing phenomenon. The code PHOENICS is acronym for Parabolic Hyperbolic Or Elliptic Numerical Integration Code Series. It is a general-purpose software package which predicts quantitatively how fluids (air, water, steam, oil, blood, etc.) flow in and around engines, process equipment, buildings, human beings, lakes, river and oceans, etc. It has modular design, including a central solver, a pre-processor (mesh generator), a post-processor (graphical display of results) and modules to link in. Three dimensional continuity, momentum and energy conservation equations in Cartesian co-ordinates are solved in this computer code. The solution domain is subdivided into a number of control volumes, each associated with a grid point, where the scalar variables such as pressure, temperature, concentration etc. are stored. The control volumes for the velocity are staggered in relation to the control volumes for the scalar variables. The governing equations used in the code are as follows.

Mass continuity:

$$\frac{\partial \rho}{\partial t} + \frac{\partial}{\partial x_j}\left(\rho u_j\right) = 0 \tag{3.1}$$

Momentum transfer:

$$\frac{\partial(\rho u_i)}{\partial t} + \frac{\partial}{\partial x_j}(\rho u_i u_j) = B_i - \frac{\partial p}{\partial x_i} + \frac{\partial}{\partial x_j}\sigma_{ij} \tag{3.2}$$

Energy transfer:

$$\frac{\partial(\rho H)}{\partial t} + \frac{\partial}{\partial x_j}(\rho u_j H) - \frac{\partial}{\partial x_j}\left(\lambda \frac{\partial T}{\partial x_j}\right) = \frac{\partial p}{\partial t} \tag{3.3}$$

Here, σ is the viscous stress tensor and $B_i$ is a body force. For a Newtonian fluid, the stress tensor is linearly related to the rate of strain tensor according to:

$$\sigma_{ij} = \mu D_{ij} + \left(\varsigma - \tfrac{2}{3}\mu\right)\frac{\partial u_k}{\partial x_k}\delta_{ij} \tag{3.4}$$

$$D_{ij} = \tfrac{1}{2}\left(\frac{\partial u_i}{\partial x_j} + \frac{\partial u_j}{\partial x_i}\right) \tag{3.5}$$

where $\mu$ and $\varsigma$ are the shear and bulk viscosity coefficients. $H$ is the total enthalpy, given by:

$$H = h + \tfrac{1}{2}\mathbf{u}\cdot\mathbf{u} \tag{3.6}$$

The equations refer to laminar flow situations only. Turbulent flows are characterised by rapid fluctuations and some form of turbulence model needs to be employed. The most popular model for industrial applications based on the Reynolds-Averaged Navier-Stokes (RANS) approach is the k-ε model.

The turbulence flow equations start with a decomposition of all instantaneous flow quantities into their mean and fluctuating parts as shown in Eqn. 3.7 and averaging the basic conservation equations:

$$u_i = \bar{u}_i + u_i' \qquad H = \bar{H} + H' \qquad p = \bar{p} + p' \tag{3.7}$$

This process results in a set of equations similar to those for laminar flow. However, the non-linear terms in these equations give rise to products of fluctuating quantities, the most important of which are the Reynolds stress $-\overline{\rho u_i' u_j'}$ and Reynolds flux $-\overline{\rho u_i' H'}$. These quantities cannot formally be expressed in terms of the mean quantities, and require modelling assumptions. Analogous to the reasoning for Newtonian fluids in laminar flow, the most popular assumption is to express the Reynolds stress tensor as a linear function of the rate of deformation tensor (expressed in terms of mean velocities):

$$-\overline{\rho u_i' u_j'} = -\tfrac{2}{3}\rho k - \tfrac{2}{3}\mu_t\frac{\partial \bar{u}_k}{\partial x_k} + \mu_t\left(\frac{\partial \bar{u}_i}{\partial x_j} + \frac{\partial \bar{u}_j}{\partial x_i}\right) \tag{3.8}$$

Here, $k = \frac{1}{2}\overline{u'_k u'_k}$ is the mean turbulent kinetic energy and $\mu_t$ the turbulent (or eddy) viscosity.

Likewise, the Reynolds flux is assumed to be linearly related to the mean total enthalpy gradient as follows:

$$-\overline{\rho u'_i H'} = \Gamma_t \frac{\partial \overline{H}}{\partial x_i} \tag{3.9}$$

Here, $\Gamma_t$ is the turbulent heat diffusivity and it is usually related to the turbulent eddy viscosity according to the following relation.

$$\Gamma_t = \mu_t / \sigma_t \tag{3.10}$$

where $\sigma_t$ is the turbulent Prandtl number which needs to be supplied empirically.

The equations governing turbulent flows used in PHOENICS are as follows:

Mass conservation:

$$\frac{\partial \rho}{\partial t} + \frac{\partial}{\partial x_j}\left(\rho \overline{u}_j\right) = 0 \tag{3.11}$$

Momentum conservation:

$$\frac{\partial(\rho \overline{u}_i)}{\partial t} + \frac{\partial}{\partial x_j}(\rho \overline{u}_i \overline{u}_j) = \overline{B}_i - \frac{\partial \overline{P}}{\partial x_i} + \frac{\partial}{\partial x_j}\left((\mu + \mu_t)\frac{\partial \overline{u}_i}{\partial x_j}\right) \tag{3.12}$$

Energy conservation:

$$\frac{\partial(\rho \overline{H})}{\partial t} + \frac{\partial}{\partial x_j}(\rho \overline{u}_j \overline{H}) - \frac{\partial}{\partial x_j}\left(\left[\frac{\lambda}{c_p} + \frac{\mu_t}{\sigma_t}\right]\frac{\partial \overline{H}}{\partial x_j}\right) = \frac{\partial \overline{p}}{\partial t} \tag{3.13}$$

Where, $$\overline{P} = \overline{p} + \tfrac{2}{3}\rho k - \left(\varsigma - \tfrac{2}{3}\left[\mu + \mu_t\right]\right)\frac{\partial u_k}{\partial x_k} \tag{3.14}$$

These equations are combined with the transport equations for $k$ and $\varepsilon$ to form a closed set.

The CFD simulation of turbulent mixing inside the chimney structure is carried out using standard k-ε turbulence model proposed by Launder and Spalding (1974) for high Reynolds number. In this turbulence model, the following equations of k and ε are used.

$$\frac{\partial \rho k}{\partial t} + \frac{\partial}{\partial x_i}\left(\rho U_i k - \left\{\frac{\rho \nu_t}{\sigma_k}\right\}\frac{\partial k}{\partial x_i}\right) = \rho(\mathrm{P}_k + G_b - \varepsilon) \qquad (3.15)$$

$$\frac{\partial \rho \varepsilon}{\partial t} + \frac{\partial}{\partial x_i}\left(\rho U_i \varepsilon - \left\{\frac{\rho \nu_t}{\sigma_\varepsilon}\right\}\frac{\partial \varepsilon}{\partial x_i}\right) = \rho\frac{\varepsilon}{k}(C_{1\varepsilon}\mathrm{P}_k + C_3 G_b - C_{2\varepsilon}\varepsilon) \qquad (3.16)$$

$$\upsilon_t = C_\mu \frac{k^2}{\varepsilon} \qquad (3.17)$$

Where, $P_k$ is the volumetric production rate of k by shear forces. $G_b$ is the volumetric production rate of k by gravitational forces interacting with density gradients. The constants used in the simulation are $C_\mu$=0.09, $C_{1\varepsilon}$=1.44, $C_{2\varepsilon}$=1.92, $C_3$=1.0, $\sigma_k$=1.0, $\sigma_\varepsilon$=1.3. The terms $P_k$ and $G_b$ are calculated from the following equations.

$$\mathrm{P}_k = \nu_t\left(\frac{\partial U_i}{\partial x_j} + \frac{\partial U_j}{\partial x_i}\right)\frac{\partial U_i}{\partial x_j} \qquad (3.18)$$

$$G_b = \nu_t \beta g_i \frac{\partial T}{\partial x_i}\mathrm{Pr}_t(T) \qquad (3.19)$$

Where $g_i$ is the gravitational vector and $Pr_t(T)$ is the turbulent Prandtl number.

**Wall function**

The wall-function approach bridges the near-wall layer by employing empirical formulae to provide near-wall boundary conditions for the mean-flow and turbulence-transport equations. The following equilibrium log-law wall function is used in the simulation.

$$\frac{U_i}{U_\tau} = \frac{1}{\kappa}\ln\left(Ey^+\right) \qquad (3.20)$$

Where, $\kappa$ is Von Karman's constant and E is an integration constant that depends on the roughness of the wall. The values of $\kappa$ and E considered here are 0.41 and 8.6 respectively. The other variables of the logarithmic law of the wall are defined as follows.

Resultant friction velocity, $$U_\tau = \sqrt{\frac{\tau_w}{\rho}} \tag{3.21}$$

Dimensionless wall distance, $$y^+ = \frac{U_\tau y}{\nu_l} \tag{3.22}$$

### 3.3 Validation for applicability of PHOENICS

In order to ascertain the applicability of CFD code PHOENICS for turbulent mixing inside chimney structure, verification studies are presented with available numerical and experimental results. Since the mixing of upward flowing hot fluid and downward flowing cold fluid inside the chimney has similarity with respect to the impingement of opposing jets in a mixer, numerical results of Wang et al. (2005) have been taken for verification. The three-dimensional numerical simulation of in-line static opposing jet mixer was reported by Wang et al., where pure water and sodium chloride solution were introduced at the nozzle inlets. After impingement in the mixer, the combined fluid left symmetrically via two symmetric exit channel outlets. Due to geometric and physical symmetry, only flow field within the half domain was solved numerically as shown in Fig. 3.2. The boundary conditions were (i) uniform velocity, species concentration, turbulent kinetic energy and its dissipation rate at the nozzle inlets (ii) symmetric boundary condition imposed along the symmetry plane (iii) constant pressure at the outlet plane (iv) no slip wall boundary conditions specified in the confinement walls.

For comparison purposes, three dimensional CFD simulation is carried out considering Re=30000 (based on the flow velocity and the hydraulic diameter of the outlet square cross section) and H/W=1 using PHOENICS code. The ratio (M) of inlet mass flow rates of two jets considered in the simulation is 1.0. Concentration (C1) at inlet-1 is assumed to be 0.0 and that of inlet-2 is 0.05.

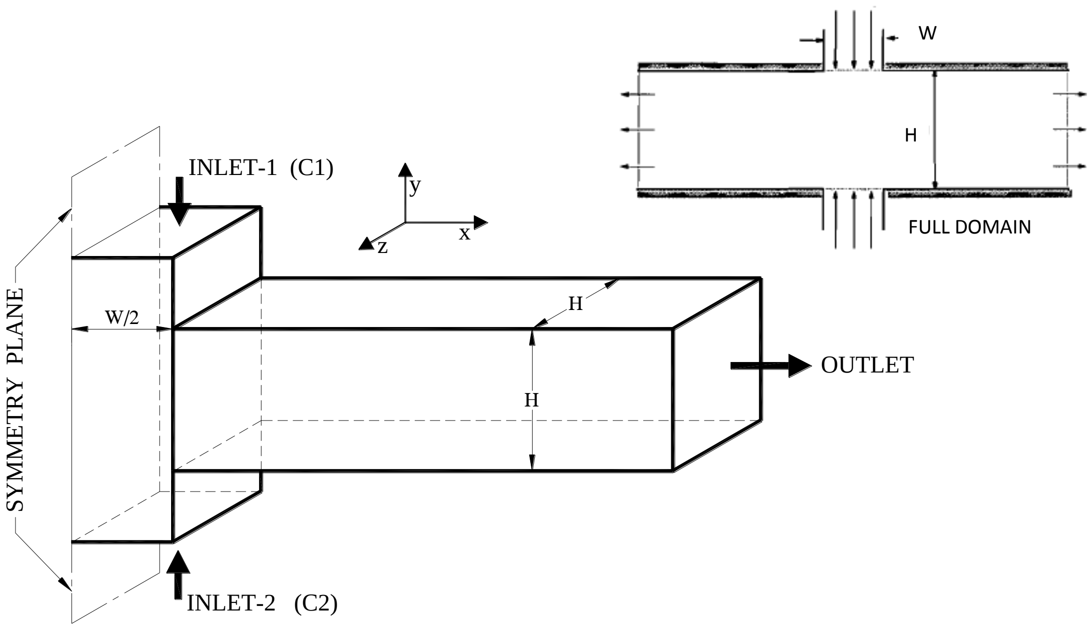


Fig. 3.2: Half domain model for 3-D mixing of opposing jets

The Lam-Bremhorst variant of low Reynolds number k-ε turbulence model is used in this study. This low-Reynolds-number turbulence model differs from the standard high-Reynolds-number model in that the empirical coefficients $C_\mu$, $C_{1\varepsilon}$ and $C_{2\varepsilon}$ are multiplied respectively by the following damping functions:

$$f_\mu = \{1 - \exp(-0.0165\,\mathrm{Re}_{yn})\}^2 \left(1 + \frac{20.5}{\mathrm{Re}_{yt}}\right) \tag{3.23}$$

$$f_1 = 1.0 + \left(\frac{0.05}{f_\mu}\right)^3 \tag{3.24}$$

$$f_2 = 1.0 - \exp\left(-\mathrm{Re}_{yt}^2\right) \tag{3.25}$$

where, $\mathrm{Re}_{yn} = \dfrac{k^{0.5} y_n}{\nu_l}$ (3.26) $\mathrm{Re}_{yt} = \dfrac{k^2}{\varepsilon \nu_l}$ (3.27)

Here, $y_n$ is the distance to the nearest wall. $\mathrm{Re}_{yt}$ the functions $f_\mu$, $f_1$ and $f_2$ multiplying the three constants tend to unity. Standard wall functions have not been used and the following boundary conditions are applied at the wall.

$$k = 0 \qquad (3.28) \qquad\qquad \frac{\partial \varepsilon}{\partial y} = 0 \qquad (3.29)$$

The nodalisation scheme used for the simulation is shown in Fig. 3.3. Overall domain size considered is 1500 mm × 30 mm × 10 mm in x, y and z directions respectively. Boundary conditions are marked in the Fig. 3.3a showing the computational domain. Simulations are done considering grids (190×60×40 ≈ 4,56,000 nodes and 250×80×55 ≈ 11,00,000 nodes) in x, y and z directions respectively and variation in results are found to be insignificant. The maximum ratio of distance between neighbouring cells is kept to 1.6. The wall y+ values obtained for these mesh are ≈1-2.

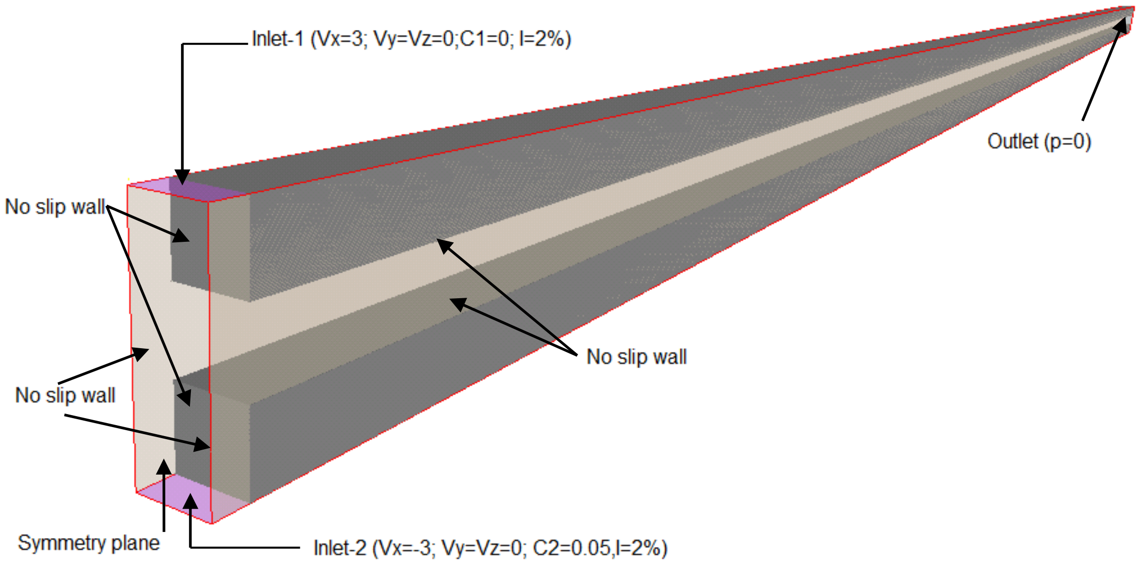


(a) Computational domain and boundary conditions

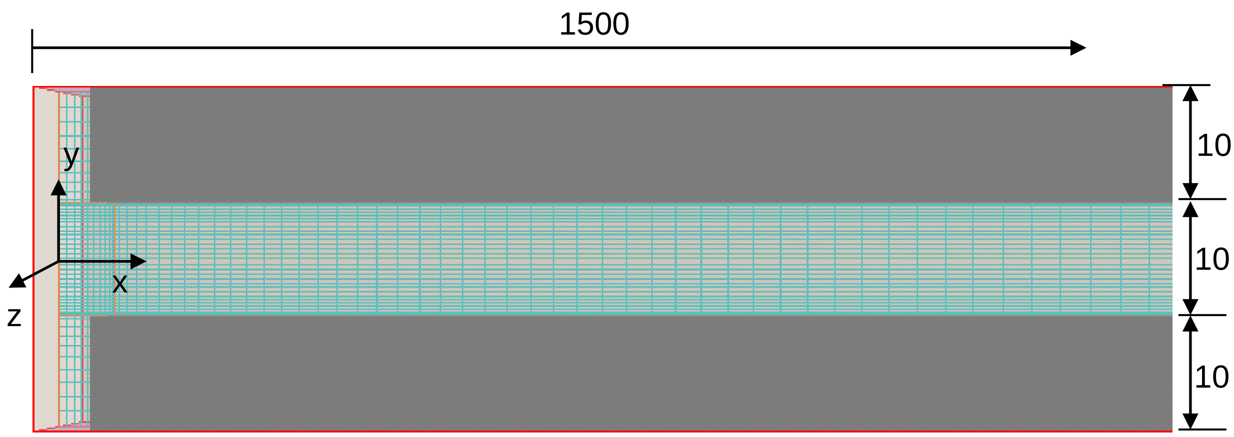


(b) Meshing of domain

Fig. 3.3: Nodalisation scheme (dimensions in mm)

The velocity distribution results obtained using PHOENICS code at central x-y plane (i.e. z=0) are shown in Fig. 3.4a. The velocity distribution reported by Wang et al. (2005) is shown in Fig. 3.4b for comparison and is found to be similar with the results obtained from PHOENICS.

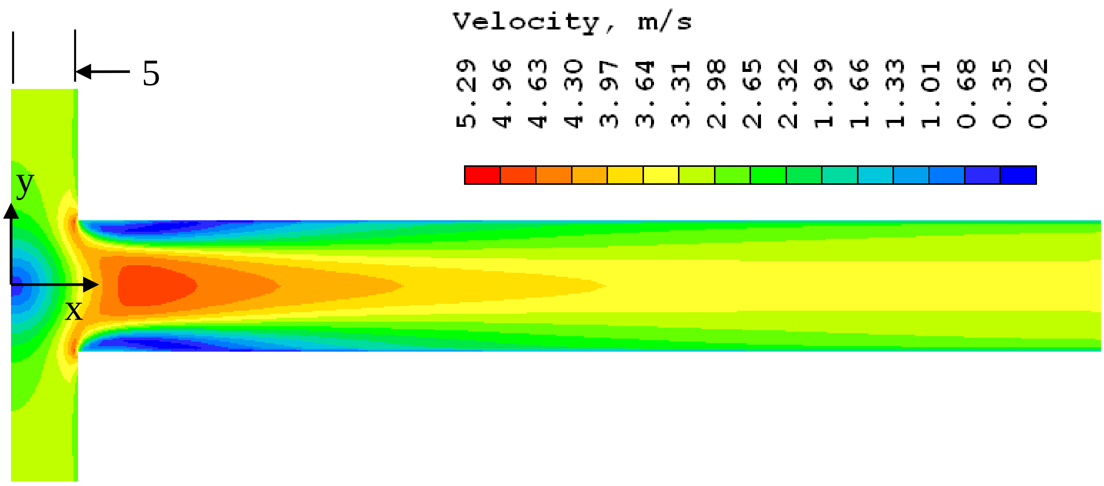


(a) Velocity distribution (PHOENICS)

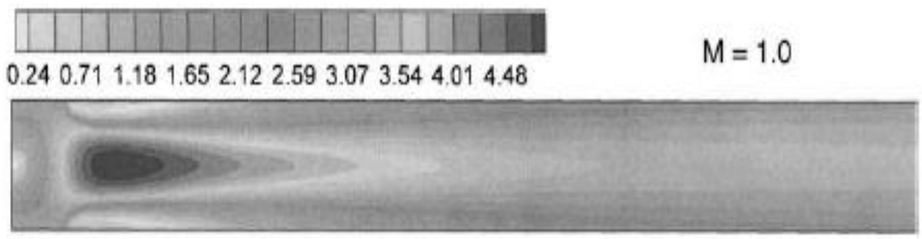


(b) Velocity distribution (Wang et al., 2005)

Fig. 3.4: Comparison of velocity distribution

The concentration distribution is also evaluated and finally, mixing index (MI) as defined by Wang et al. (2005) is predicted using the following relations.

$$MI(\%) = \frac{S_c}{C_b} \times 100 \tag{3.1}$$

$$S_c = \sqrt{\left[\sum_{i=1}^{n} (C_i - C_b)^2\right] / (n-1)} \tag{3.2}$$

$$C_b = \frac{\int C v_x dA}{\int v_x dA} \tag{3.3}$$

Here $v_x$ is the fluid flow velocity in the x direction. Sc is the standard deviation of species concentration at any cross section in the exit channel and $C_b$ is the bulk concentration of species at the corresponding cross section. $C_i$ is the concentration of $i^{th}$ node of the total "n" nodes of the cross section. The mixing index variation along the channel length (x-direction) is compared with the results reported by Wang et al., as shown in Fig. 3.5. The results show good agreement between the results reported and results obtained by PHOENICS code.

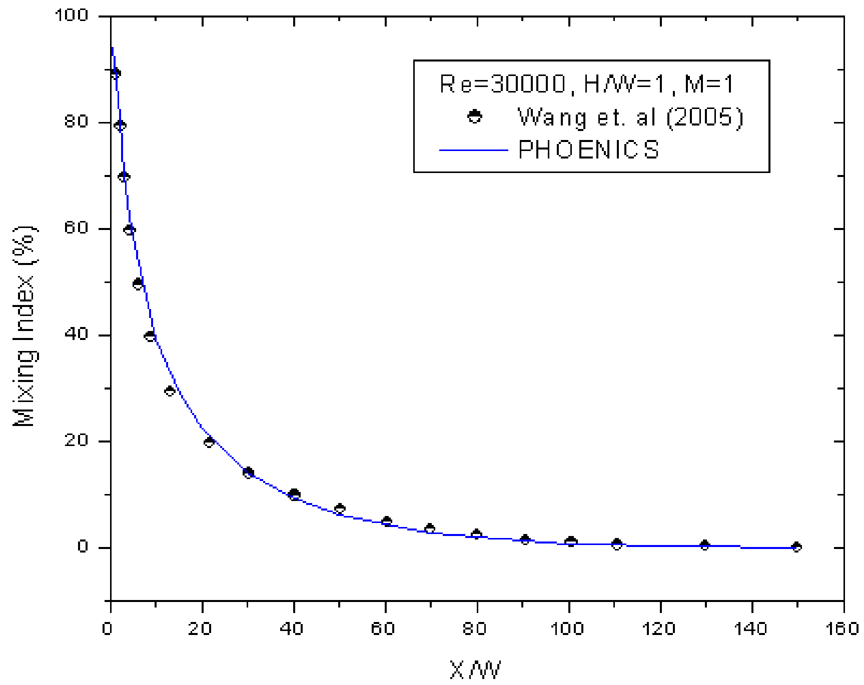


Fig. 3.5: Comparison of concentration distribution

Another verification study is also carried out by comparing the experimental data (with similar Reynolds number range based on pipe diameter) of Naik-Nimbalkar et al. (2010) to establish the suitability of PHEONICS code for predicting the mixing phenomena in a T-junction using standard k–ε turbulence model. The experiment of Naik-Nimbalkar et al. involved mixing of cold water and hot water in a T-junction test section (Fig. 3.6a). The numerical simulation is carried out for the conditions shown in Table-3.1.

Table-3.1: Experimental conditions for simulation (Naik-Nimbalkar et al., 2010)

| Parameters | Diameter (m) | Velocity (m/s) | Temperature(ºC) | Reynolds number |
|---|---|---|---|---|
| Main pipe | 0.05 | $V_c = 1.0$ | $T_c = 30$ | $Re_c \sim 8 \times 10^4$ |
| Branch pipe | 0.025 | $V_h = 0.5$ | $T_h = 45$ | $Re_h \sim 2 \times 10^4$ |

Here Reynolds number of the cold fluid ($Re_c$) is based on the average fluid velocity ($V_c$) of cold water at the inlet of main pipe considering main pipe diameter as the characteristic dimension. Similarly Reynolds number of the hot fluid ($Re_h$) is based on hot water velocity ($V_h$) in the branch pipe and its diameter as the characteristic dimension.

T- junction was constructed of acrylic pipes. Cold water entered from horizontal main pipe and hot water entered from the branch pipe. Velocities and temperatures at the main and branch pipes were confirmed to be at steady-state before each experiment was performed. Velocity and temperature measurements were carried out at two locations (1- at 0.5D downstream and 2- at 1.25D downstream from X=0) using hot-wire anemometer. A constant temperature module (CTA) was used for the measurement of local velocity in the system.

In the PHOENICS simulation, computational model used is shown in Fig. 3.6b. The overall dimension is 800 mm × 200 mm × 50 mm in x, y and z direction respectively. No slip and adiabatic boundary conditions are used for the wall. Inlet boundary condition is considered with uniform velocity. The outlet boundary condition is specified as constant pressure. The variation in density of working fluid due to temperature change was considered using Boussinesq approximation. The standard k–ε turbulence model is used.

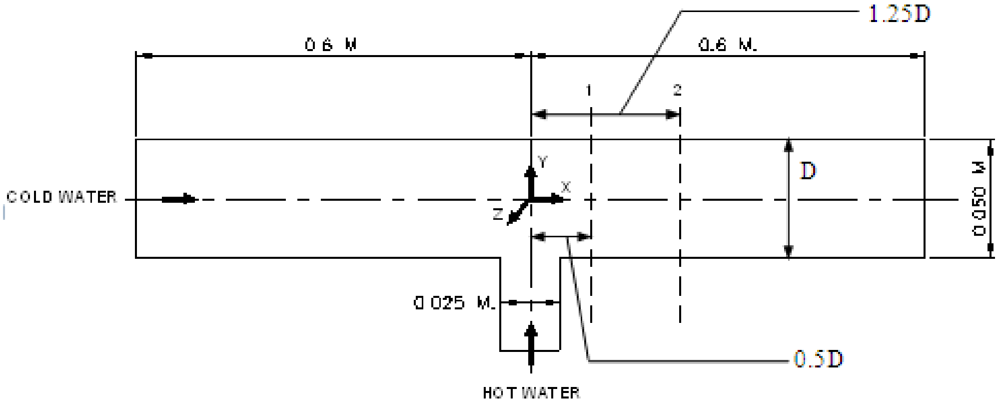


(a) Experiment (Naik-Nimbalkar et al., 2010)

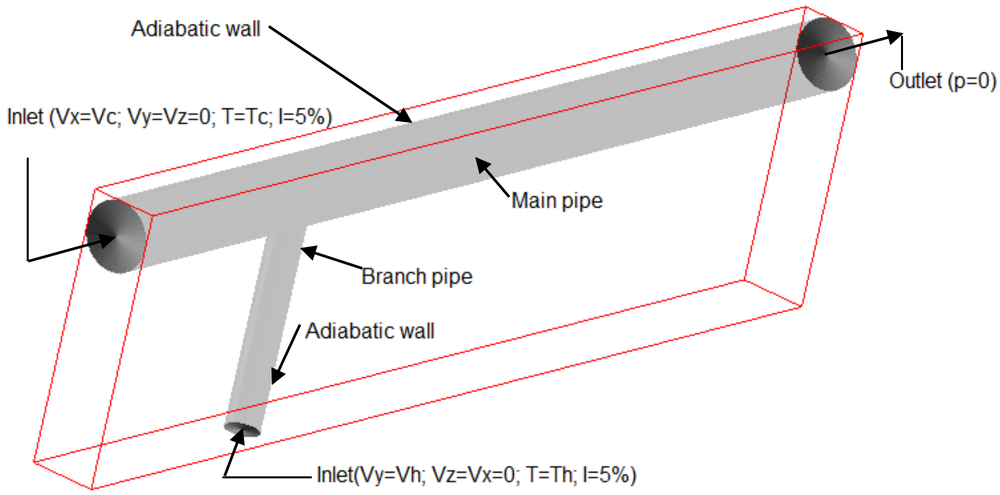


(b) Computational domain (PHOENICS)

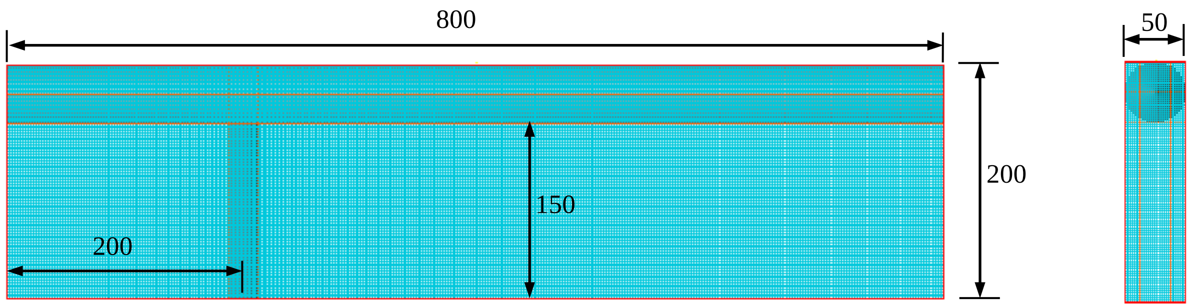


(c) Nodalisation (PHOENICS)

Fig. 3.6: T-junction test section for cross flow experiment (Naik-Nimbalkar et al., 2010)

Wall functions have been used while modelling turbulence. The nodalisation scheme consists of 285×95×27 grids (≈ 7,31,000 nodes) as shown in Fig. 3.6c. Grid sensitivity is checked considering 375×125×36 grids (≈ 16,87,500 nodes) and no significant variation in results is found. The maximum ratio of distance between neighbouring cells is 1.1. The wall y+ values obtained for the mesh are ≈35. Comparison of the simulation results using PHOENICS and the experimental data is presented in Fig. 3.7a to 3.7d.

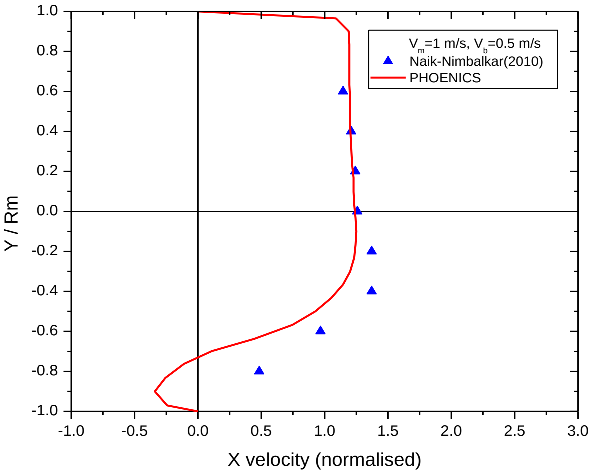


(a) Normalised X-velocity at 0.5D

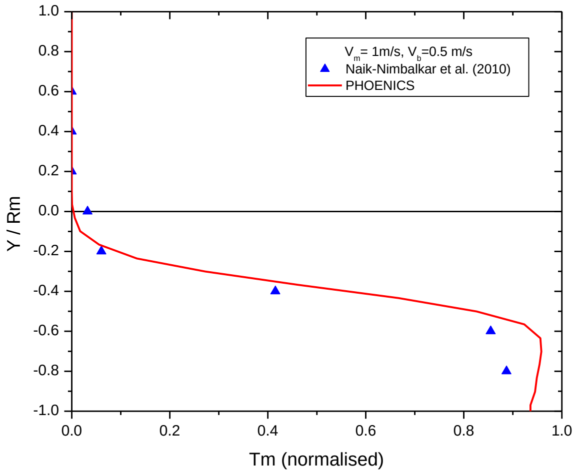


(b) Normalised temperature at 0.5D

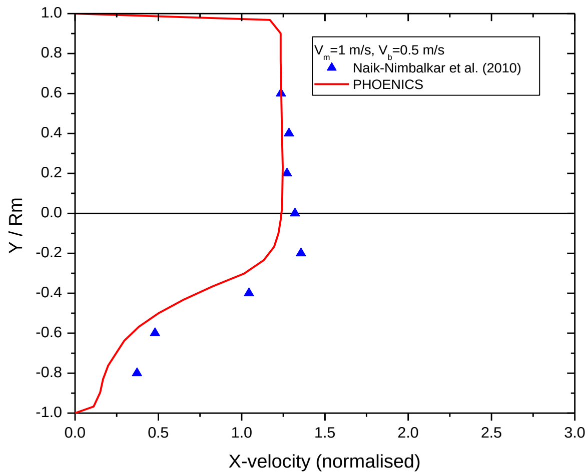


(c) Normalised X-velocity at 1.25D

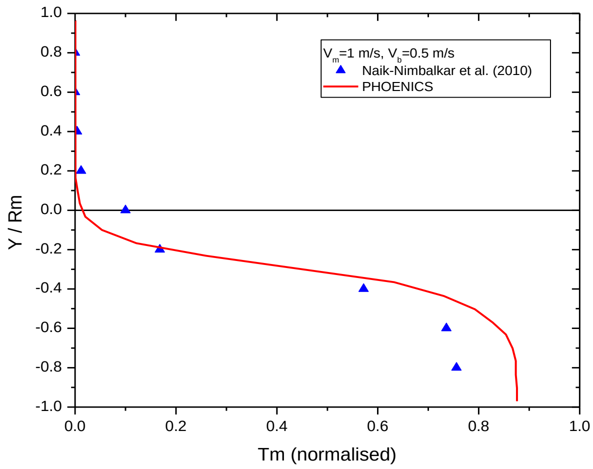


(d) Normalised temperature at 1.25 D

Fig. 3.7: Comparison of normalised velocity and temperature distribution between experiment data and numerical results

In these plots distance Y from the axis of the main pipe is normalized with the radius ($R_m$) of main pipe. X-velocity is normalized with respect to the fluid velocity ($V_c$) at the inlet of the main pipe. The mean temperature of coolant is normalized using the following relation as defined by Naik-Nimbalkar et al. (2010), where $T_h$ is hot water temperature and $T_c$ is the cold water temperature.

$$\text{Normalised temperature } T_m = \frac{T - T_c}{T_h - T_c} \qquad (3.4)$$

The normalized X-velocity variation across Y-direction in the central plane is compared at 0.5D downstream in Fig. 3.7a. The results for normalized X-velocity variation at 1.25 D downstream are shown in Fig. 3.7c. Similarly normalized temperature variation across Y-direction in the central plane is compared at 0.5D downstream in Fig. 3.7b and at 1.25D downstream in Fig. 3.7d. It is observed that the velocity as well as temperature distribution predicted by numerical simulation are in good agreement with the experiment.

### 3.4 Numerical Simulation for 45º Prototype Chimney

In the numerical analysis using PHOENICS, the fluid (water) is assumed to be incompressible and Newtonian with constant fluid properties. The buoyancy force is accounted by using Boussinesq model. This model assumes that the density is constant in all terms except the buoyancy force term. Since the governing equations are non-linear and coupled, SIMPLE algorithm (Patankar, 1980) is used. Numerical solution of the mean flow and temperature field is obtained by solving the continuity equation, Reynolds Averaged Navier-Stokes (RANS) equation and time averaged energy equation. The Boussinesq approximation provides the closure for the set of RANS equations, which is commonly known as eddy-viscosity concept. It assumes that the turbulent shear stresses (Reynolds stresses) are proportional to the mean velocity gradient in analogy to viscous stresses in laminar flow. At high Reynolds number, the standard k-ε model (Harlo and Nakyama, 1968) has been successfully applied for three-dimensional wall boundary layers (Rastogi and Rodi, 1978), confined flows (Sharma, 1974) and jets (McGuirk and Rodi, 1979). Accordingly, the CFD simulation of turbulent mixing inside the chimney structure is carried out using standard k-ε turbulence model proposed by Launder and Spalding (1974) for high Reynolds number.

### 3.4.1 Nodalisation and boundary conditions

The computational model of the system prepared in PHOENICS code is shown in Fig. 3.8.

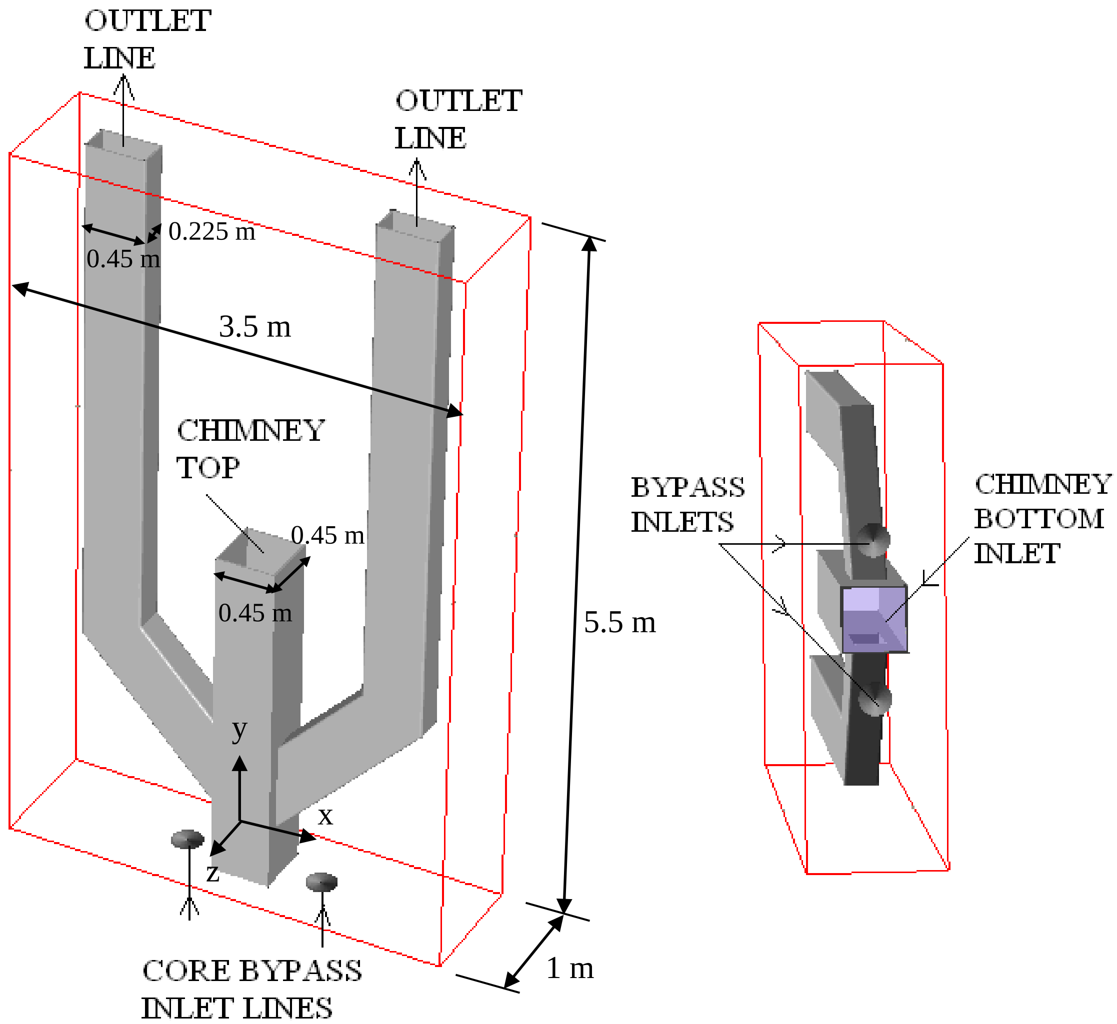


(a) Front view of chimney (b) View from bottom side of chimney

Fig. 3.8: Isometric view of computational model

The model includes the reactor pool along with the chimney structure. The computational domain considered for the simulation is 3.5 m × 5.5 m × 1 m in x, y and z directions respectively. The chimney geometry simulated is similar in dimensions as that of the full scale size. The chimney is immersed 11 m deep in water inside the reactor pool having 5 m diameter. Considering the large dimension of the water pool and limitation of the number of grids which can be simulated in the CFD code, the model dimensions of water pool is restricted to the dimensions mentioned above. Since the extent of chimney is more in x-direction (2.7 m) than z direction (0.45 m), the computational domain is chosen accordingly. The extent of y dimension of the pool domain is taken as the height of the chimney.

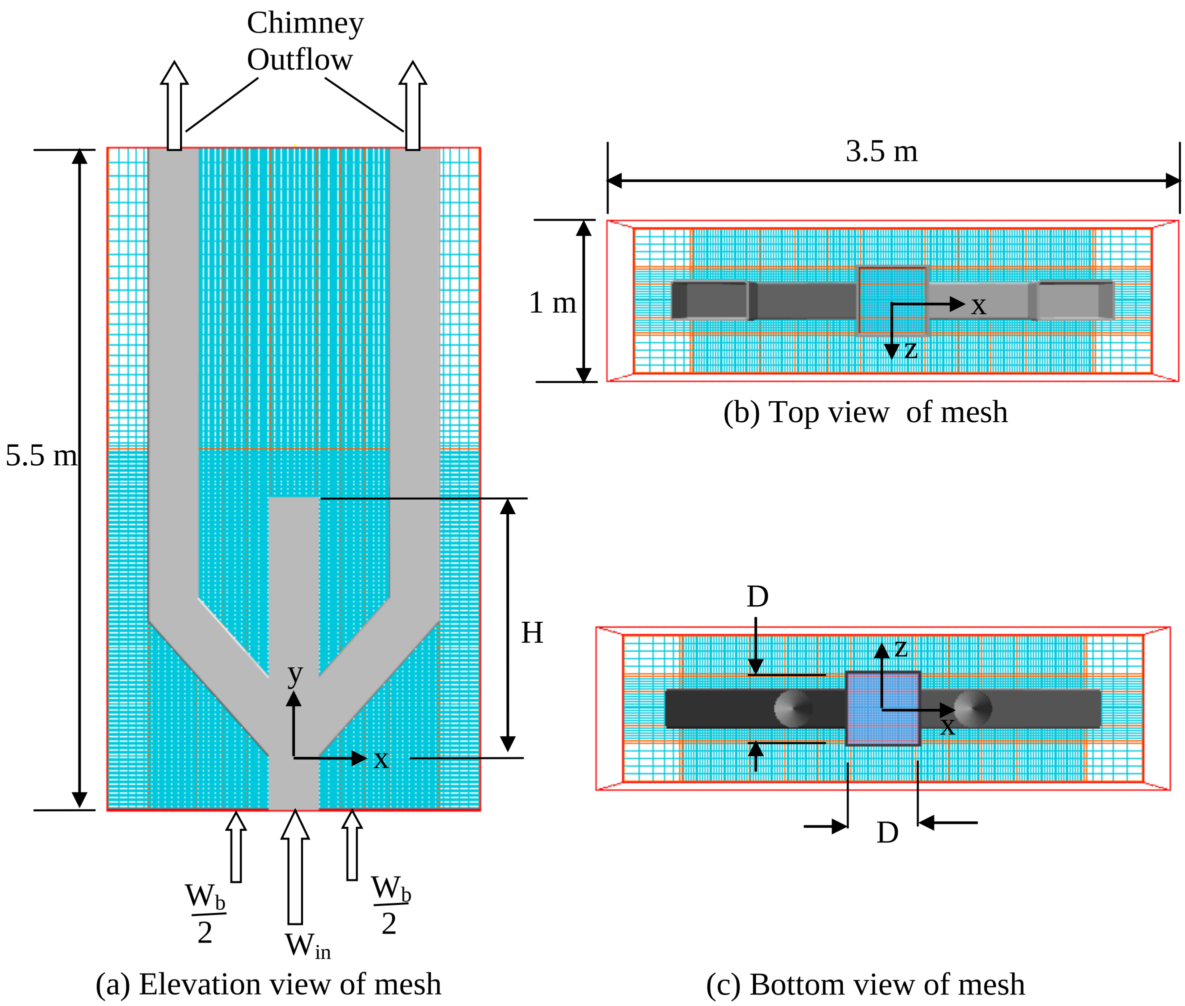


Fig. 3.9: Mesh prepared in PHOENICS

Chimney bottom square inlet through which upward flow takes place is shown in Fig. 3.8b. The two bypass inlets of circular cross section through which water is sent to the pool are also shown in the figure. The chimney top square opening through which downward flow enters the chimney from the pool is shown in Fig. 3.8a. Two rectangular outlet lines through which the mixed flow of hot and cold fluid moves out of the system are also shown. Free surface at the interface between the pool water and air at the top is not modeled considering larger pool water depth (about 8 m) above the chimney top end, which is in communication with the pool water.

The material properties are assumed to be constant. A uniform velocity profile has been set at the inlet. As a boundary condition, the values of turbulent kinetic energy (k) and turbulent energy dissipation rate (ε) are prescribed at the inlet in terms of the turbulence intensity which is considered to be 5% for all the cases. Considering chimney surface walls, no slip boundary condition is imposed on the surfaces. For the pool water domain boundary, zero gradient boundary condition is applied. Inlet flow rate ($W_{in}$) through the bottom of the chimney is 750 kg/s (with Reynolds number of $3\times10^6$ based on hydraulic diameter of square chimney). Bypass flow rate ($W_b$) into the pool through the two bottom nozzles are specified based on the bypass flow ratio considered for the simulation cases. Bypass flow ratio (R) is defined as the ratio between the bypass flow ($W_b$) and core flow ($W_{in}$). Outlet boundary condition with fixed pressure is specified for the outlet nozzles on x-z plane (at y=5.5 m).

The mesh is nonuniform as shown in Figures 3.9a to 3.9c. More number of cells is kept in the chimney region where the gradients of velocity and temperature are larger than those in the top and side regions of the pool domain. In all the computations, k-ε model has been used with wall functions. The mesh is so chosen that the wall function is applied to a point whose $y^+$ value is in the range $30<y^+<100$ (Rodi,W., 1993). Grid sensitivity studies are made considering 8,40,000 meshes (155 × 155 × 35) and 18,90,000 meshes (205 × 205 × 45). The grid sensitivity was tested by comparing the velocity distribution at the central x-y plane and y-z plane near the chimney top entry elevation (at y=2m). No significant variations in the results are found between these two cases.

### 3.4.2 Results and Discussion

The simulations are carried out for various bypass flow ratios (R = 0.0, 0.05, 0.1 and 0.15).

#### 3.4.2.1 Effect of bypass flow ratio on velocity distribution

In this section effect of bypass flow ratio on the flow pattern and the stagnation height is discussed considering constant chimney height (H/D = 5), where H and D are the height and side of the square chimney as shown in Fig. 3.9.

i) Bypass flow ratio, R = 0.0

Velocity distribution for R = 0.0 (i.e., without bypass flow) is shown in Fig. 3.10. The velocity contour plot of x-y plane at z = 0 in Fig. 3.10a shows how the upward flow gets diverted into two side outlet nozzles. The velocity pattern in the junction of four paths clearly shows that the velocity decreases with increase in chimney height. The flow pattern of upward jet is observed in y-z plane at x=0 as shown in Fig. 3.10a. At the tip of the upward jet, upward velocity is zero and beyond this height, downward velocity is observed. This is due to the suction effect in the junction of four paths, downward velocity in the central region of the chimney takes place.

The velocity vector plots in the x-y plane (at z = 0) and y-z plane (at x = 0) in the region from y/D = 0 to 4 are shown in Fig. 3.10b. The upward flow jet along with two vortices is clearly observed here. Due to the vortex formation, downward flow is observed in the peripheral region of the central square section of the chimney.

The velocity distribution for the vertical arms of the chimney in the x-y plane (at z = 0 from y/D = 6 to 11) is shown in Fig. 3.10c. It is observed that for each vertical arm, the flow impinges towards the outer wall of the chimney. Velocities towards the inner wall are comparatively less. This is due to change in direction of flow from V arm section to vertical arm with same cross section. From the location of turning point (i.e., junction between the V arm and the vertical arm), the velocity gradually becomes uniform between the outer and inner walls of the vertical arms. It is observed that even at the top most outlet cross section

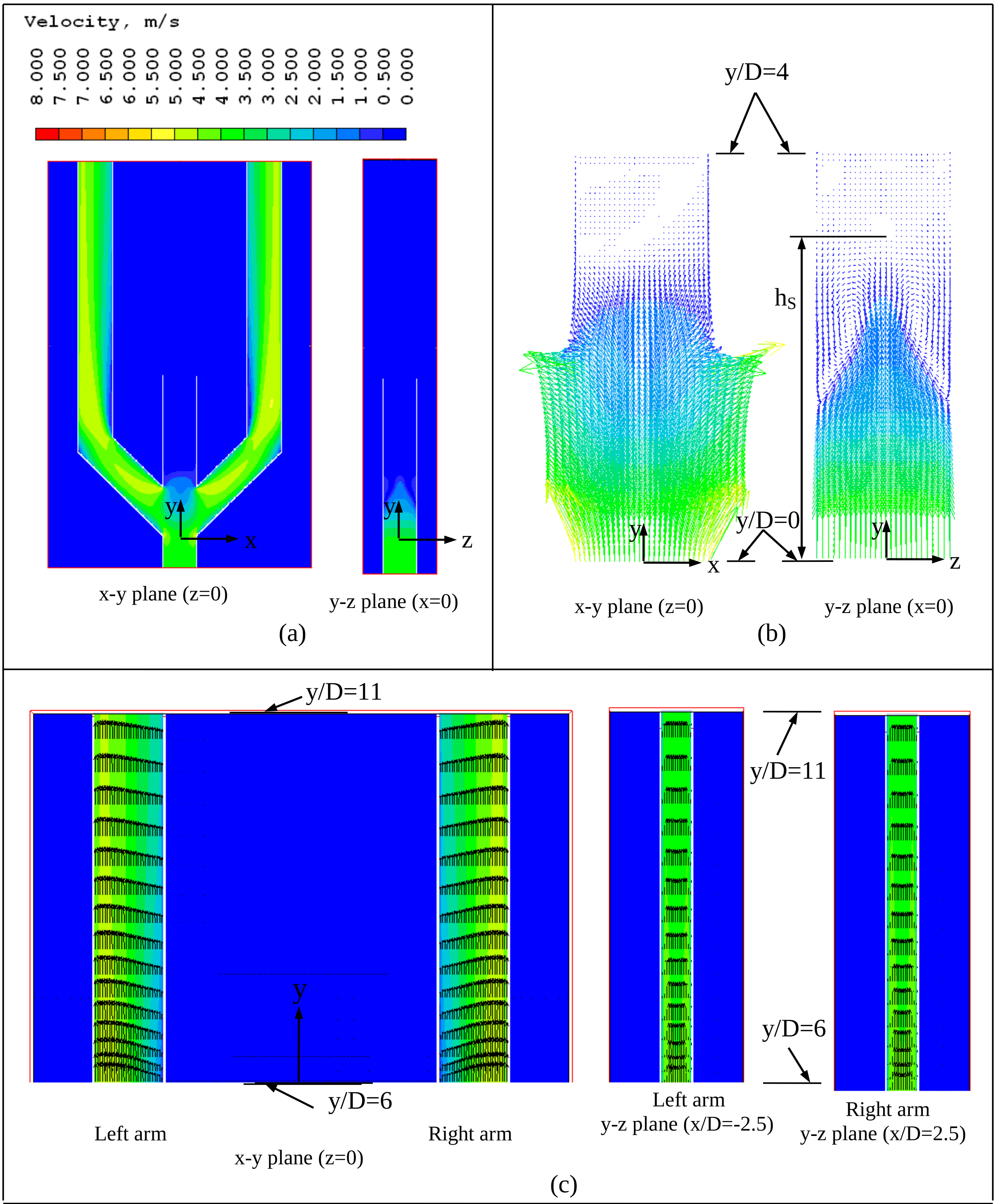


Fig. 3.10: Velocity distribution with R = 0.0 (H/D = 5)

(a) Contour plot (b) Vector plot (c) Velocity distribution in vertical arms

plane, the maximum velocity is observed away from the centerline towards the outer vertical wall. The velocity distribution in the y-z plane of left arm (at x/D = - 2.5) and right vertical arm (at x/D = 2.5) is shown in Fig. 3.10c. It is observed that the magnitude of velocity gradually decreases with increase in height because of flow redistribution towards the inner wall from outer wall as explained in Fig. 3.10c.

The contour plots of upward velocity ($v_y$) at 1.5D, 2D and 4D are shown in Fig. 3.11a, 3.11b and 3.11c. At y = 1.5D, in the central location of chimney upward flow velocity is more than 1.5 m/s. In the peripheral region velocity is downward in this section. The eye of the two vortices explained earlier which moves downward at the periphery is clearly seen at y = 2D. It is observed that the velocity in the central region is in the upward direction even beyond y = 2D. At y = 4D, the velocity in the central region is in the downward direction and in the peripheral region upward velocity is observed.

Since, no bypass flow (i.e. $W_b$) is provided into the pool, to maintain the overall flow balance of the central part of the chimney, upward flow is observed at the peripheral region. This is clearly observed from the upward velocity contour plot (Fig. 3.11d) in the x-z plane of the chimney region at y = 5D. Upward velocity variation in the central plane (z = 0) from x = - 0.225 to + 0.225 m at y = 5D is also shown in Fig. 3.11e indicating downward flow taking place in the central region and upward flow at the peripheral region. Similar velocity variation at x = 0 from z = = - 0.225 to + 0.225 m is also shown in Fig. 3.11f. This indicates that radioactive water from the core reaches the pool water through the top opening of the chimney, which is not acceptable.

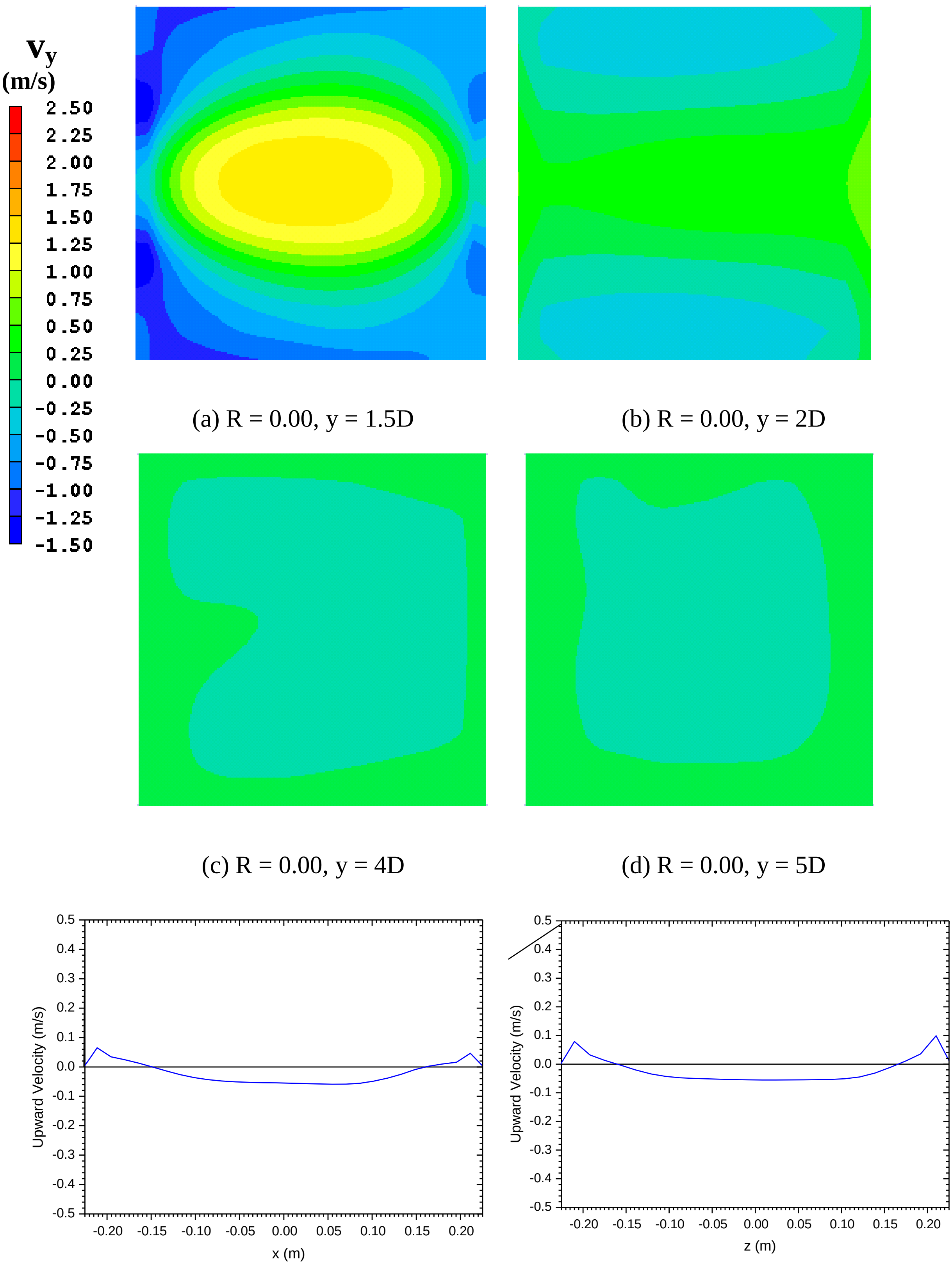


(a) R = 0.00, y = 1.5D

(b) R = 0.00, y = 2D

(c) R = 0.00, y = 4D

(d) R = 0.00, y = 5D

(e) $v_y$ at y = 5D and z = 0.0

(f) $v_y$ at y = 5D and x = 0.0

Fig. 3.11: Upward velocity ($v_y$) plots in x-z plane at y = 1.5D, 2D, 4D, 5D (R = 0.00)

ii) Bypass flow ratio, R = 0.05

Velocity contour and vector plots for R = 0.05 are shown in Figures 3.12a and 3.12b respectively. The x-y contour plot of Fig. 3.12a shows similar behavior except that chimney central square section sees downward flow velocity of about 0.2 m/s. The velocity pattern in the junction of four paths shows that the velocity decreases faster than that observed in Fig. 3.10a. The momentum of upward flow being more than that of the downward flow, the upward jet extends more into the weaker jet. The stagnation height is found here less than that of R = 0.0, because no net downward momentum is present in the earlier case. The velocity vector plot of Fig. 3.12b from y/D = 0 to 4 shows that downward flow is present in the central square section of the chimney. The stagnation height shown in Fig. 3.12b is found to be less than that observed in Fig. 3.10b. The vortices are also observed in Fig. 3.12b but of smaller size than in Fig. 3.10b.

The velocity distribution of the vertical arms of the chimney in x-y plane and y-z plane is shown in Fig. 3.12c. Here also the similar nature of velocity pattern is observed as explained for the R = 0.0 case except that the magnitude of velocity is more by 5% due to additional flow (bypass = 5%) provided.

The upward velocity contour plots in the x-z plane at y = 1.5D, 2D, 3D and 5D are shown in Fig. 3.13. In comparison to Fig. 3.11a, the region where velocity is in the upward direction is found to be smaller in Fig. 3.13a due to increase in bypass flow. The downward flow region in the periphery is found to be more in Fig. 3.13a. The two vortices with central upward velocity and peripheral downward velocity is observed in Fig. 3.13b. Flow is found to be completely downward at y=3D and beyond. In Fig. 3.13d, upward velocity contour plot clearly shows that the no upward flow taking place through the top opening of the chimney (at y=5D). Upward velocity variation along x-axis and z-axis in the central plane of the chimney at y = 5D are also shown in Fig. 3.13e and 3.13f. Here the downward velocity is clearly observed in Fig. 3.11e and 3.11f, which is different from the case explained for no

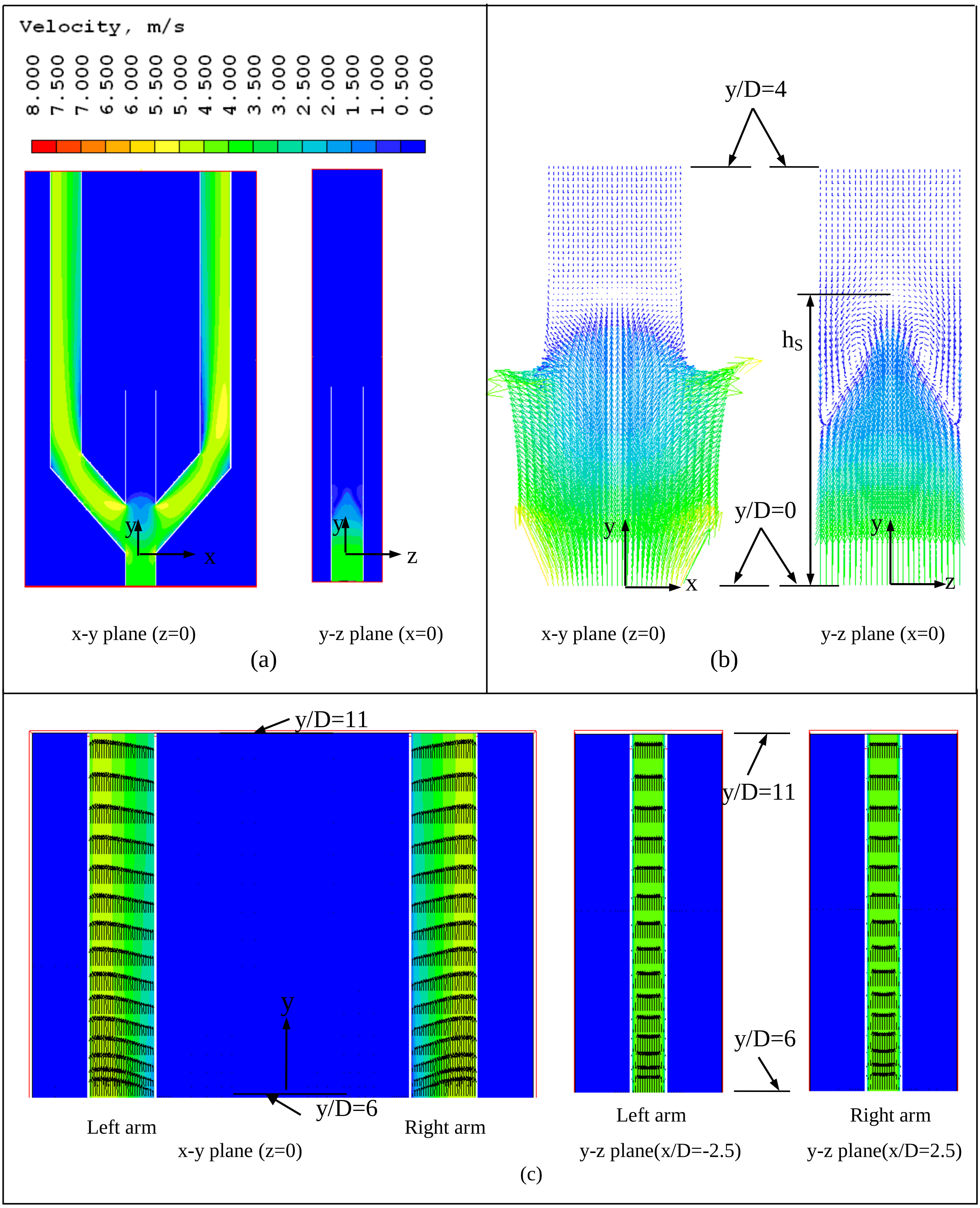


Fig. 3.12: Velocity distribution with R = 0.05 (H/D = 5)

(a) Contour plot (b) Vector plot (c) Velocity distribution in vertical arms

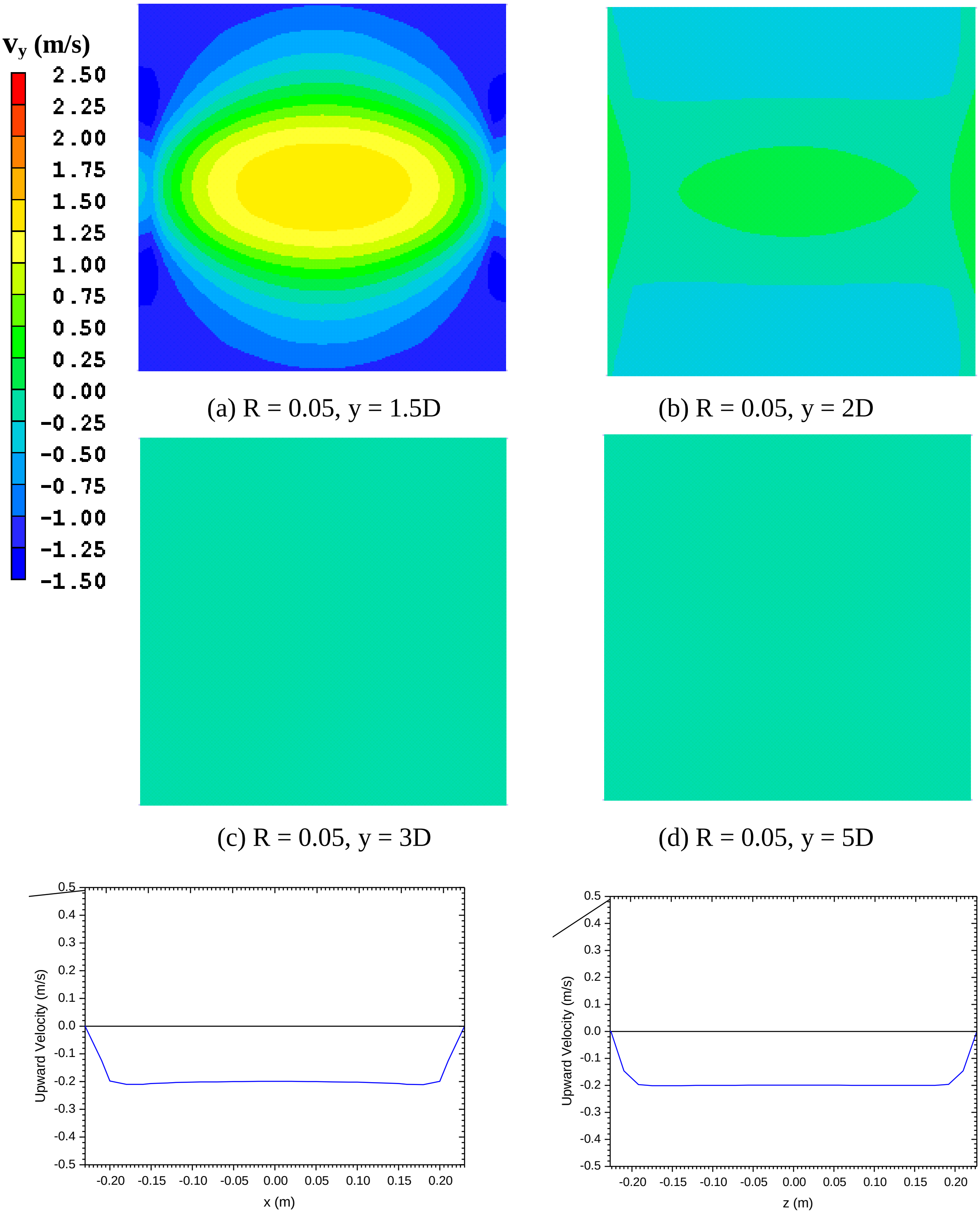


(a) R = 0.05, y = 1.5D

(b) R = 0.05, y = 2D

(c) R = 0.05, y = 3D

(d) R = 0.05, y = 5D

(e) $v_y$ at y = 5D and z = 0.0

(f) $v_y$ at y = 5D and x = 0.0

Fig. 3.13: Upward velocity ($V_y$) plots in x-z plane at y = 1.5D, 2D, 3D, 5D (R = 0.05)

bypass flow case. It is clear from these plots that no radioactive water reaches the pool top when bypass flow is 5%.

iii) Bypass flow ratio, R = 0.15

Velocity distribution for R = 0.15 is shown in Fig. 3.14. The velocity through two bypass flow lines are clearly observed from the bottom of the pool in the velocity contour plot shown in Fig. 3.14a. This flow enters through the top opening of the chimney. The downward velocity through the square section is about 0.6 m/s. Due to this higher velocity, stagnation height has further reduced and area of recirculation region is also shortened in height as seen from Fig. 3.14b. Velocity distribution of vertical arms of chimney is shown in Fig. 3.14c which indicates that developing flow continues throughout the vertical arm as observed for the earlier cases (R = 0.0, 0.05) also.

Velocity ($v_y$) contour plots at various elevations of the chimney (y = 1.5D, 1.75D, 2D and 5D) in the x-z plane is shown in Fig. 3.15. It is observed that the elliptical region where velocity is in the upward direction has further reduced in Fig. 3.15a than that observed in Fig. 3.13a due to increase in bypass flow from 5% to 15%. At y = 1.75D, the region of upward velocity has reduced to almost zero. At elevations y = 2D and beyond, complete downward velocity is observed as shown in Fig. 3.15c and Fig. 3.15d.

In order to quantify the location where central elliptical region of upward velocity becomes zero (i.e., the point of stagnation height), the upward velocity of water on the central axis of the chimney is plotted along the height of the chimney as shown in Fig. 3.16. The x- axis of the plot is the dimensionless vertical distance (y/D). The results clearly show that the centre line velocity of water decreases with increase in height. After certain height, the upward velocity crosses zero value and subsequently velocity becomes negative (i.e., downward flow exists). The location where the upward velocity becomes zero is called the stagnation point. The distance of this location of stagnation point from the origin (y = 0) is the stagnation

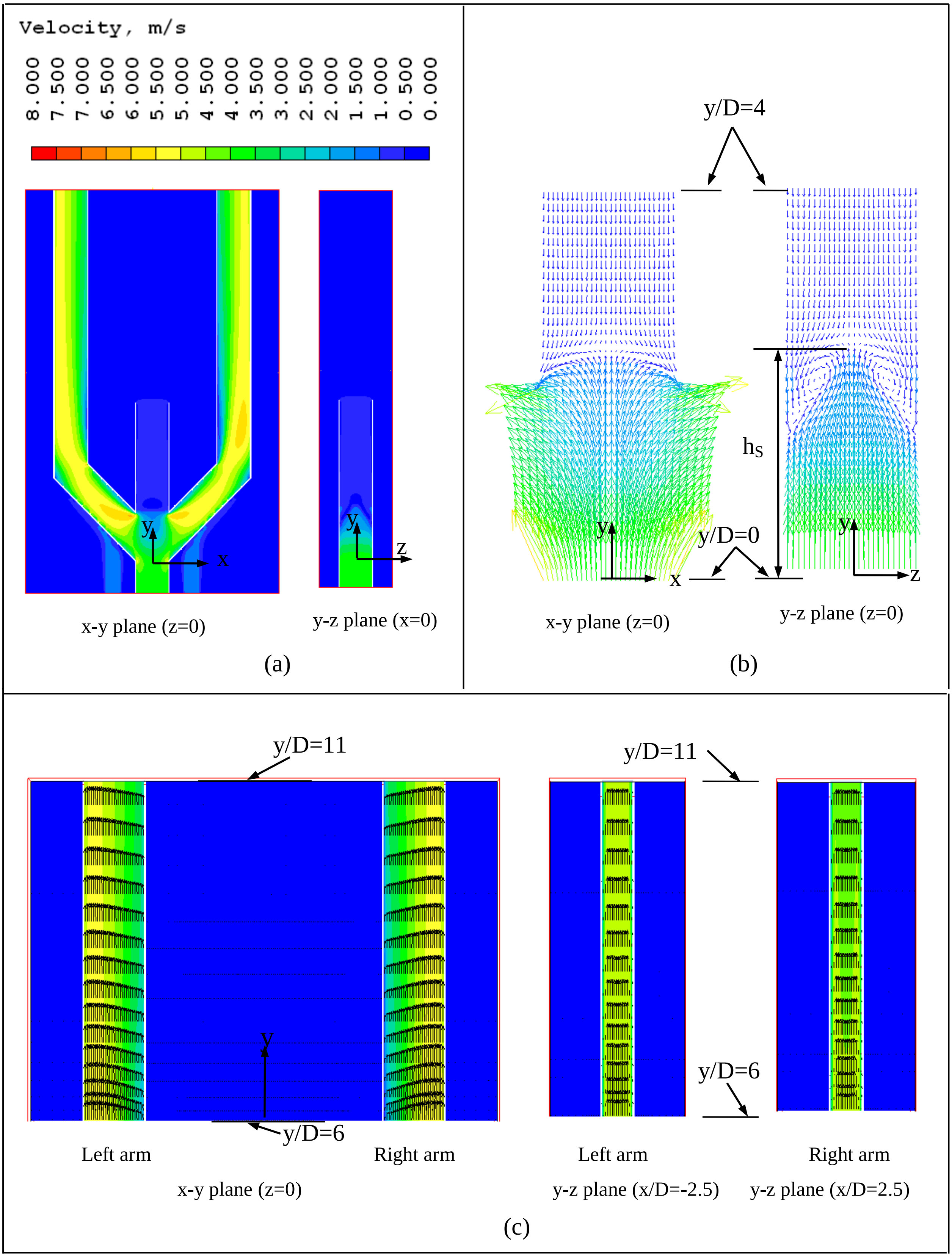


Fig. 3.14: Velocity distribution with R = 0.15 (H/D = 5)

(a) Contour plot (b) Vector plot (c) Velocity distribution in vertical arms

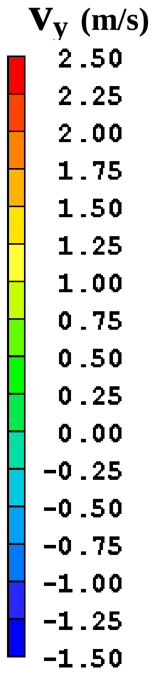


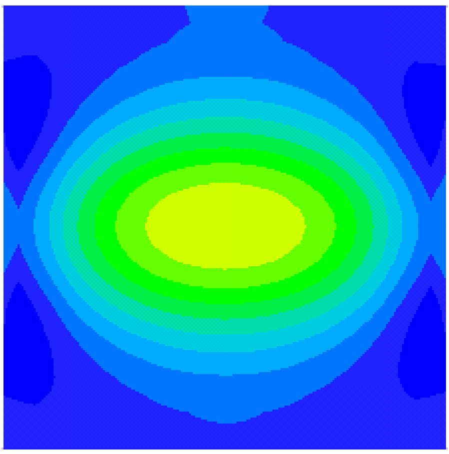

(a) R = 0.15, y = 1.5 D

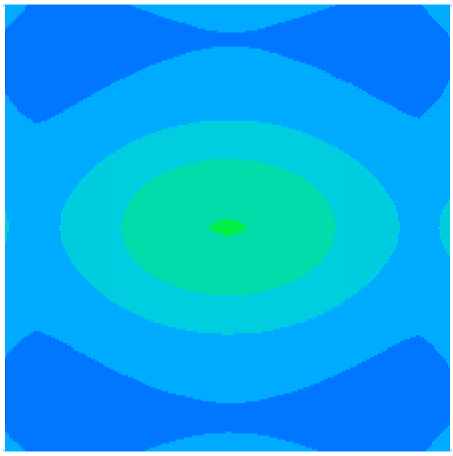

(b) R = 0.15, y = 1.75 D

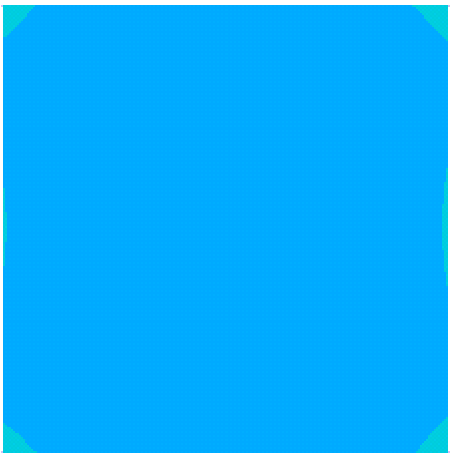

(c) R = 0.15, y = 2 D

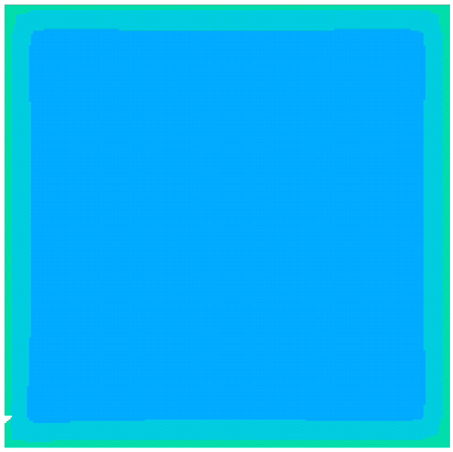

(d) R = 0.15, y = 5 D

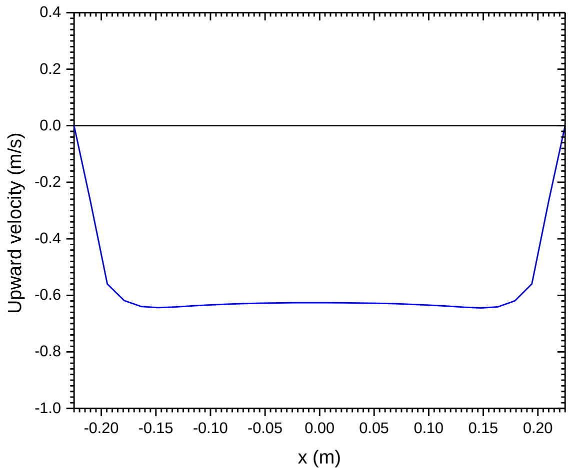


(e) $V_y$ at y = 5D and z = 0.0

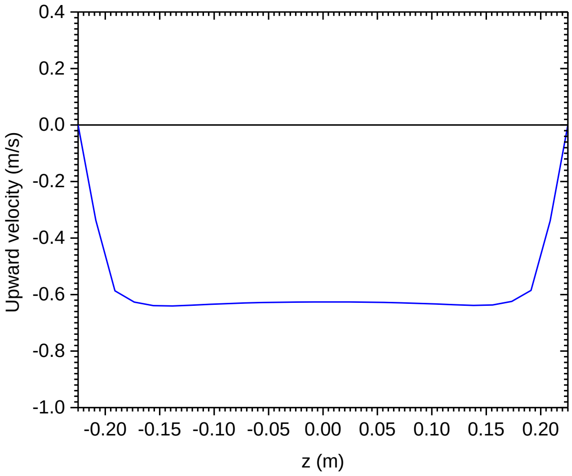


(f) $V_y$ at y = 5D and x = 0.0

Fig. 3.15: Velocity ($V_y$) contour plots in x-z plane at y = 1.5D, 1.75D, 2D, 5D (R = 0.15)

height. Directly from the Fig. 3.16, dimensionless stagnation height ($h_S/D$) can be obtained from the co-ordinates of the stagnation point. The values of dimensionless stagnation height for R = 0.0, 0.05, 0.10 and 0.15 are 2.4, 2.07, 1.89 and 1.76 respectively. From these results, it is clearly observed that with increase in bypass flow ratio the stagnation height decreases. However, the decrease of the stagnation height with increase of bypass flow ratio gradually decreases.

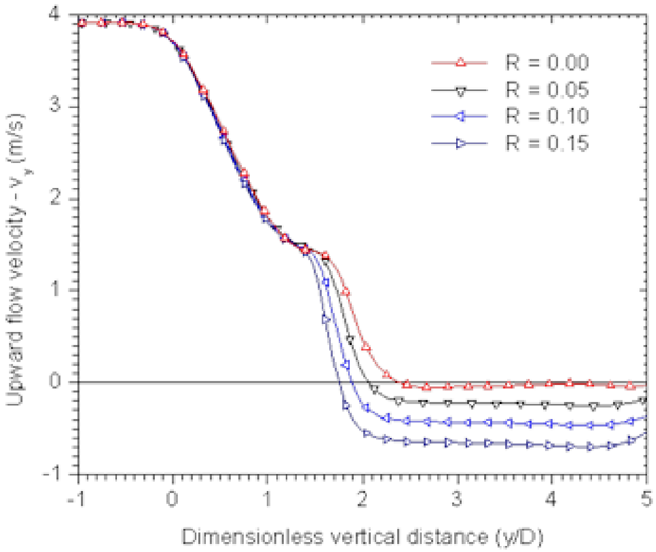


Fig. 3.16: Centre line velocity variation along the height of chimney (H/D = 5)

#### 3.4.2.2 Effect of bypass flow ratio on temperature distribution

The temperature distribution in the x-y plane (at z = 0) and y-z plane (x = 0) for bypass flow ratios (R = 0.05 and 0.15) are shown in Fig. 3.17. As described in the mixing of the two opposing streams, hot water at 49ºC enters from the bottom of the chimney. Pool water temperature is maintained at 40 ºC by providing additional flow equivalent to the downward flow entering through the top opening of the chimney from the pool. Depending on the bypass flow ratio between the downward flow and the upward flow, the mixed mean temperature of the outlet lines are shown in Fig. 3.17. As bypass flow ratio increases from 0.05 to 0.15, the outlet line temperature decreases. It is observed from Figures 3.17a and 3.17b that temperature gradient exists at the rectangular cross section of the outlet line. The temperature near to the outer wall is more than that of the inner wall. This is because of the higher flow velocities observed towards the outer wall as indicated in previous section. The hot upward flow from the bottom of the chimney takes preferential path towards the outer wall, whereas the cold downward flow follows the path adjacent to the inner wall. This affects the temperature difference across the cross section. With progression towards downstream, difference in temperature gradually decreases.

In this simulation, temperature indirectly can be considered as tracer of radioactivity and the pool temperature (at 40 ºC) is free from any radioactivity. The temperature front of pool water (i.e., 40 ºC) has reached to a certain depth from the chimney top due to the presence of upward jet of hot water from the bottom of the chimney. As seen from figures the minimum depth of pool temperature front is observed at the central line of the square chimney. With increase in bypass flow ratio, the pool temperature front depth increases.

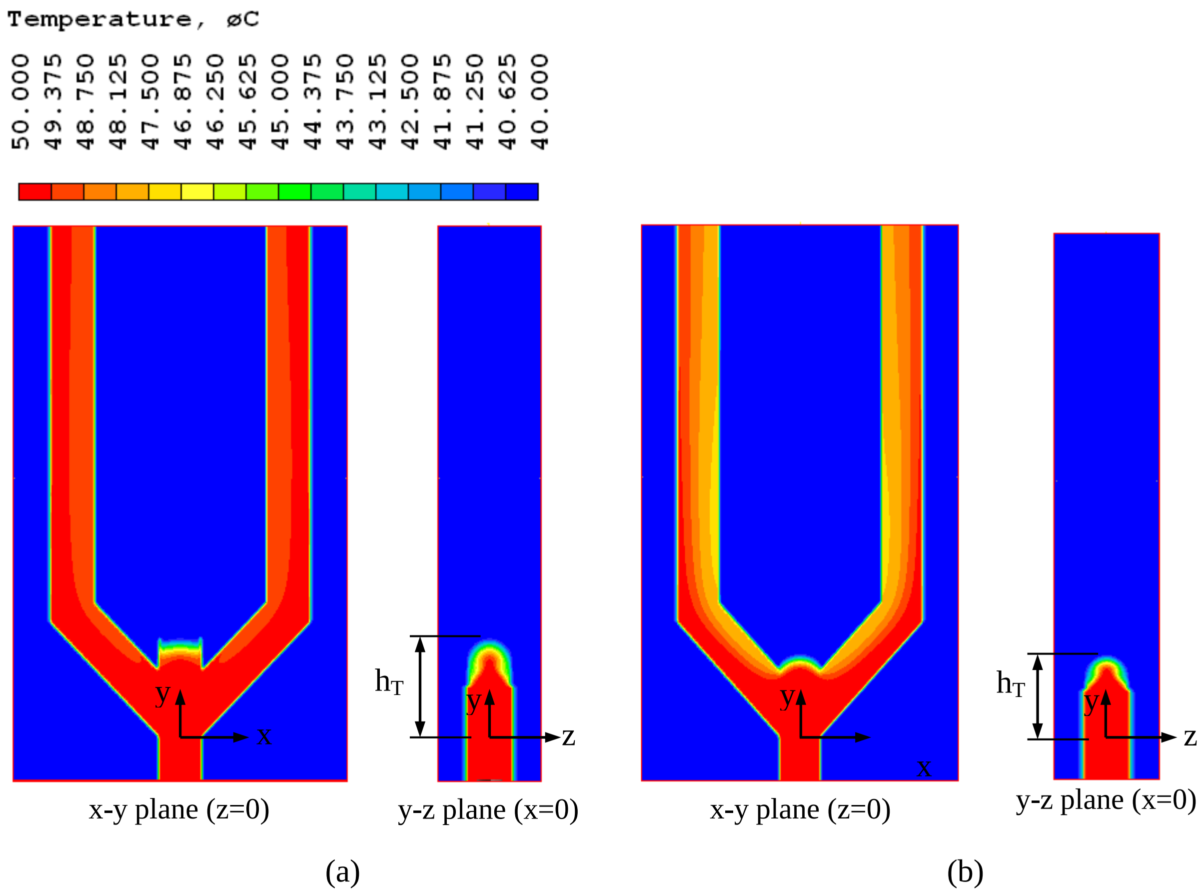


Fig. 3.17: Temperature contours (H/D = 5)

(a) R = 0.05 (b) R = 0.15

In order to quantify the depth upto which the pool temperature front can be expected, the centre line water temperature of the square chimney is plotted with respect to the height of the chimney as shown in Fig. 3.18. It is observed that with increase in bypass flow ratio (R) this depth increases and therefore pool temperature front height ($h_T$) inside the chimney with respect to its bottom (y = 0) reduces. This height is also non-dimensionalised with respect to square side (D) of the chimney. Non-dimensional pool temperature front height ($h_T/D$) for various bypass flow ratios R = 0.05, 0.10 and 0.15 are found to be 2.4, 2.19 and 2.02 respectively from Fig. 3.18. All these results are obtained considering a fixed chimney height corresponding to (H/D) of 5.

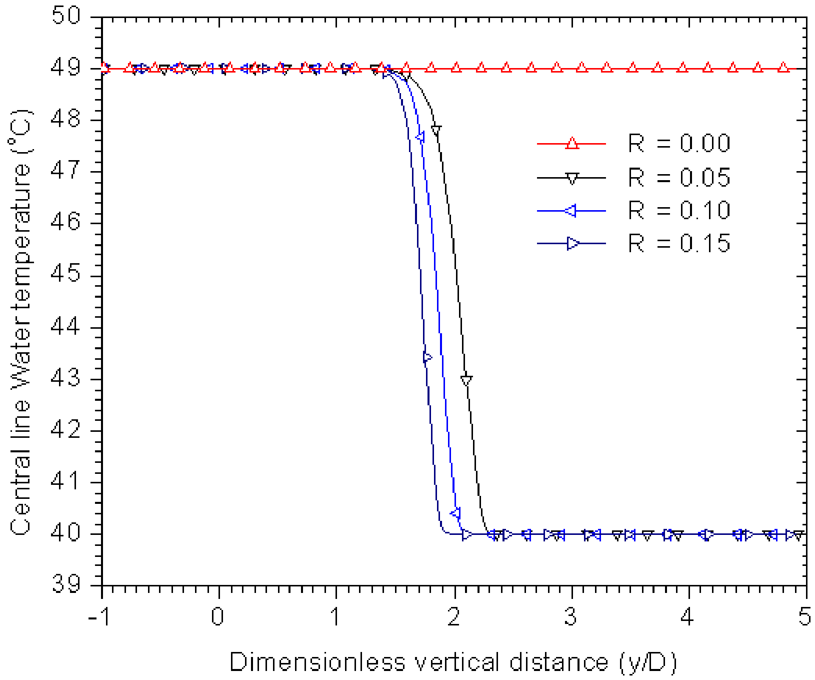


Fig. 3.18: Centre line water temperature variation along the height of chimney (H/D = 5)

### 3.4.2.3 Effect of chimney height

In order to understand the effect of chimney height (H) on the mixing behaviour of the opposing jets inside the chimney, the ratio of chimney height to diameter (H/D) is varied to 4, 5 and 6. The results for all these cases are shown in Fig. 3.19 and 3.20. The centre line velocity variation along the height is shown in Fig. 3.19. The results show that the stagnation height (where the upward velocity becomes zero) does not change significantly due to change in chimney height. However, slight variation is observed near to the top opening of the chimney. The velocity is found to be lower near the top entry of the chimney because the velocity is almost uniform there. With progression of flow downward inside the chimney, the velocity at the centre line increases due to the surrounding wall effect of the chimney. This trend of velocity variation is observed for all the three chimney heights. It is also observed that the centre line velocity distribution mainly depends on bypass flow ratio between the two opposing flows.

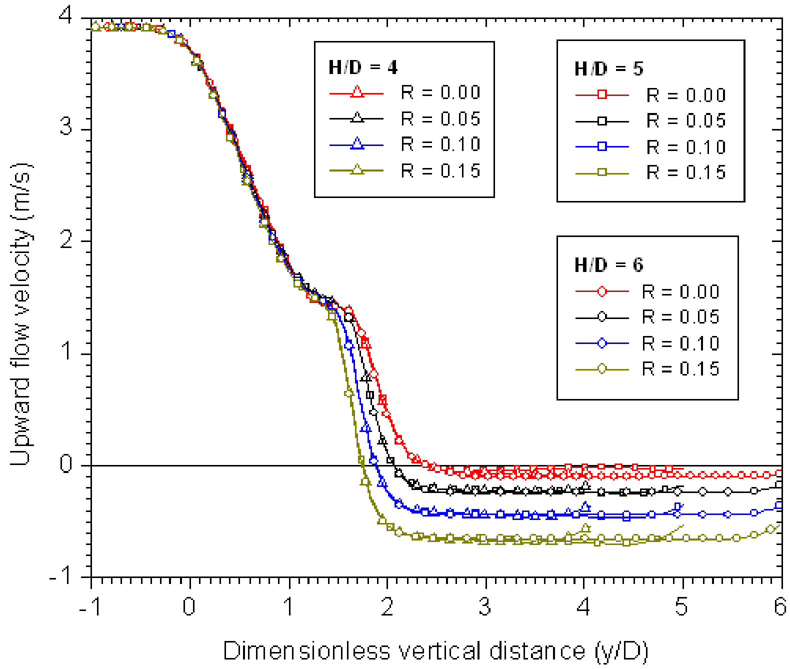


Fig. 3.19: Effect of H/D ratio on centre line velocity variation along the height

The centre line fluid temperature variation in the square chimney is shown in Fig. 3.20. It is observed that the effect of chimney height (H) on temperature profile is also found to be insignificant.

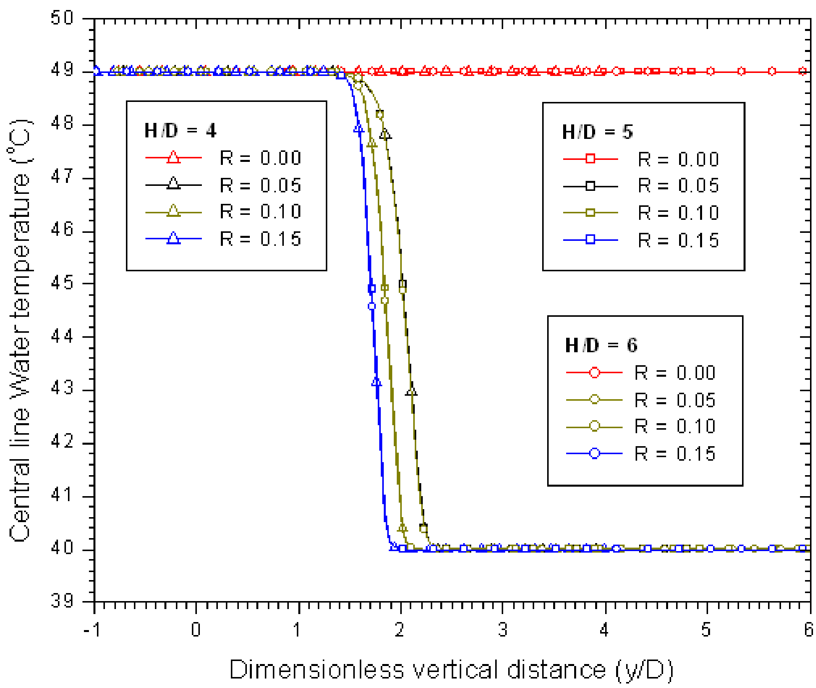


Fig. 3.20: Effect of H/D ratio on centre line water temperature variation along the height

#### 3.4.2.4 Effect of temperature difference

To estimate the effect of buoyancy on the stagnation height, additional simulations are carried out without any temperature difference between the opposing flows inside the chimney. The variation of center line upward velocity obtained for the case without any temperature differential is compared with that of the case with differential of 9 ºC between the opposing flows for various bypass flow ratios. The results are shown in Fig. 3.21 to 3.23 for H/D ratios of 5, 4 and 6 respectively. It is observed from the results that the effect of buoyancy on the velocity distribution is insignificant with respect to the fluid inertia. After non-dimensionalisation of the stagnation height and temperature front height, the results are shown in Fig. 3.24 and Fig. 3.25. It is observed that dimensionless stagnation height ($h_S/D$) is almost constant if the bypass flow ratio is (R) is maintained. Chimney height and temperature differential between the opposing flows have little influence on the dimensionless stagnation height. Similarly, dimensionless pool temperature front height ($h_T/D$) remains almost the same and does not vary significantly with the chimney height.

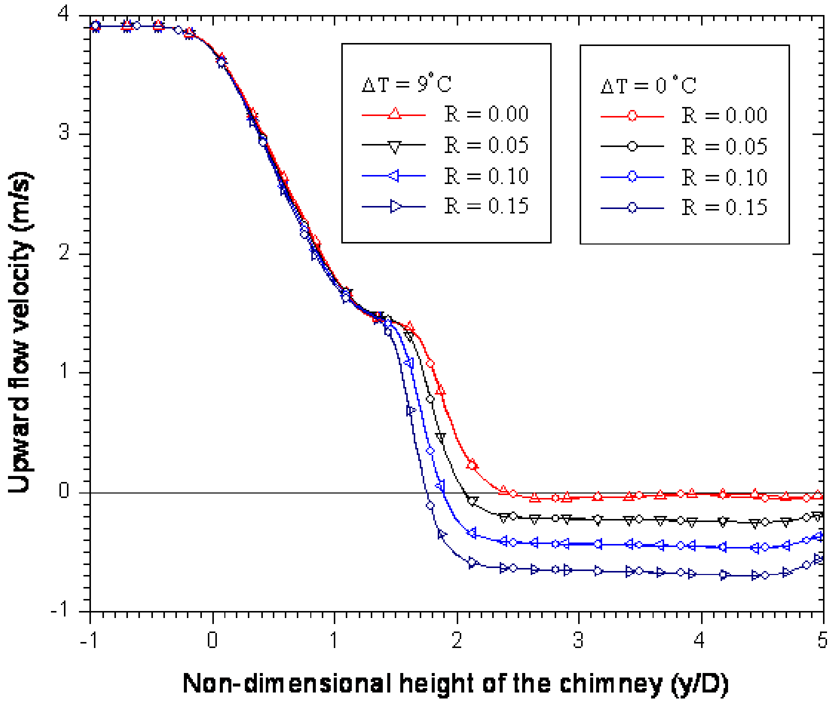


Fig. 3.21: Effect of temperature differential on centre line velocity variation (H/D = 5)

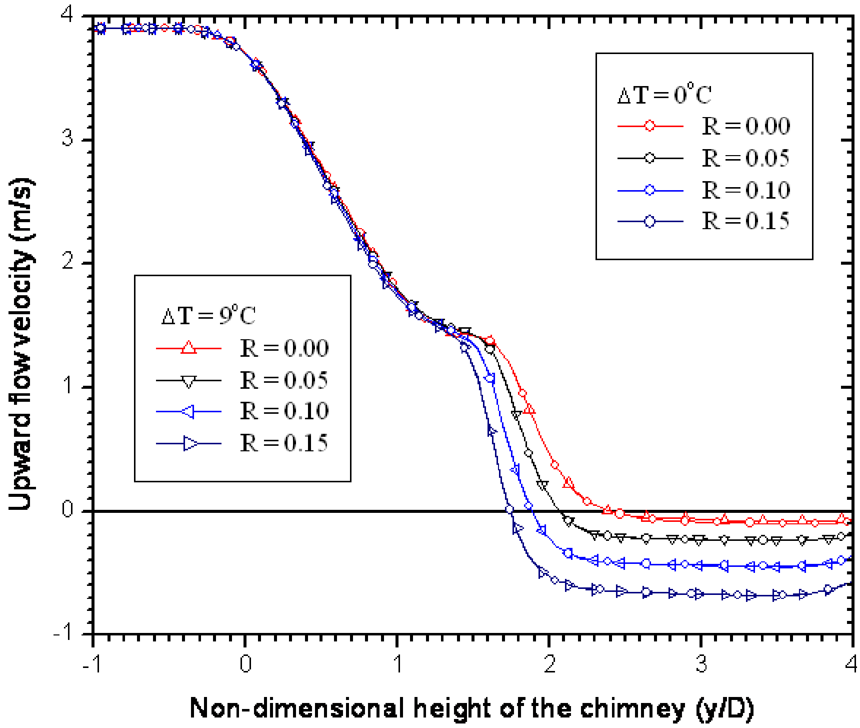


Fig. 3.22: Effect of temperature differential on centre line velocity variation (H/D = 4)

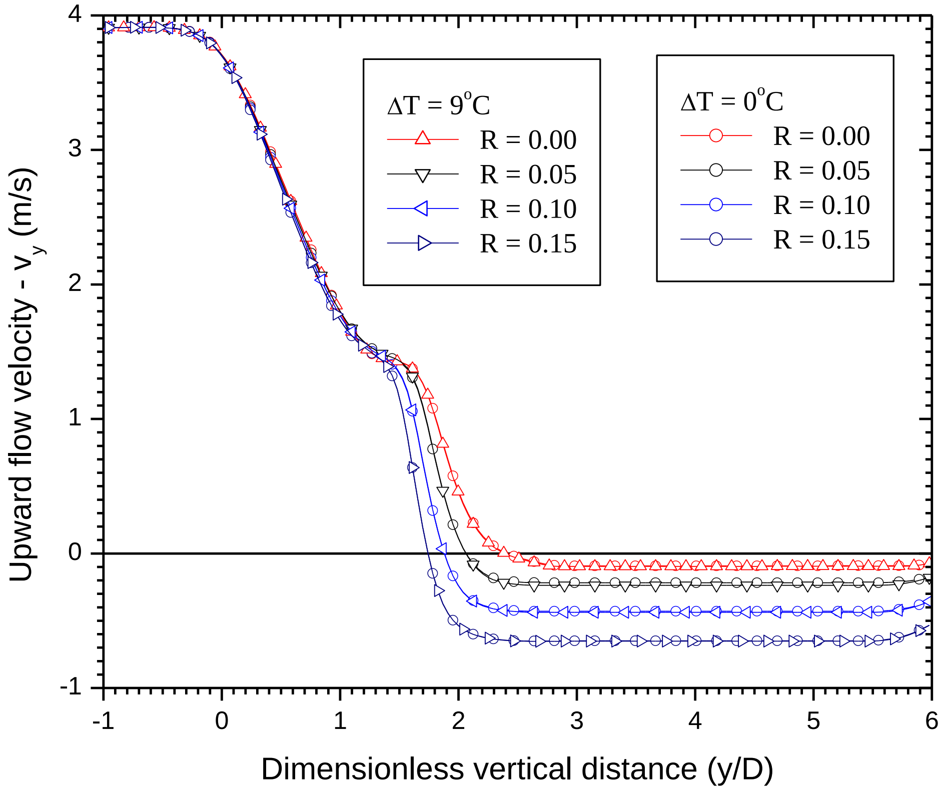


Fig. 3.23: Effect of temperature differential on centre line velocity variation (H/D = 6)

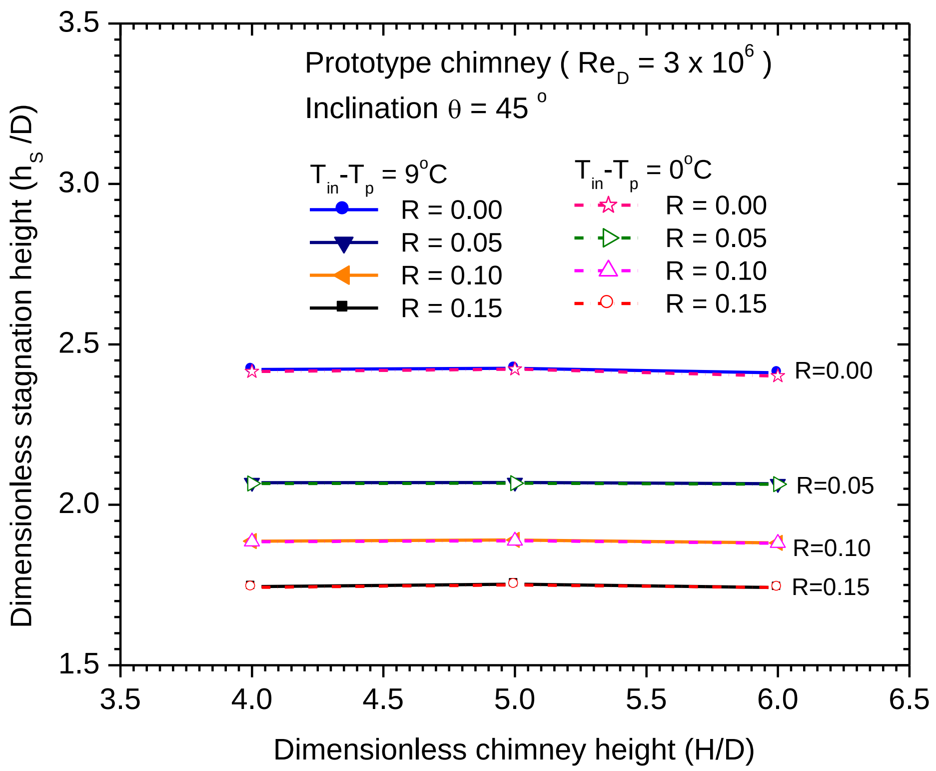


Fig. 3.24: Effect of height and temperature differential on dimensionless stagnation height

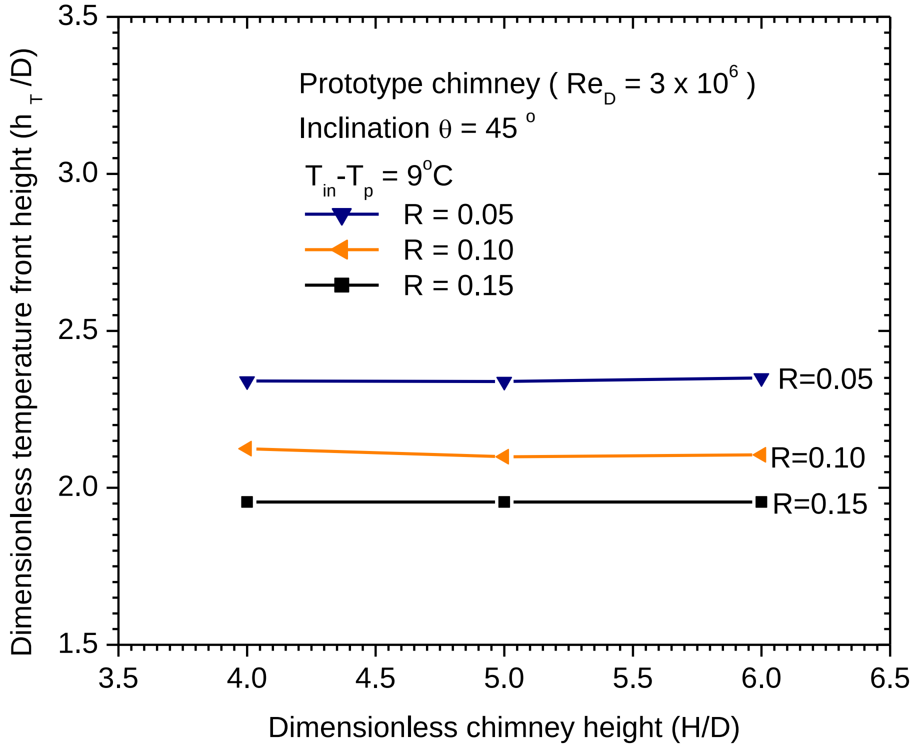


Fig. 3.25: Effect of height on dimensionless pool temperature front height

## 3.5 Effect of nozzle inclination for prototype

Numerical studies are performed to examine the effect of nozzle inclination on the turbulent mixing behaviour inside the chimney structure by reducing the angle from 45º to 35º and 25º. For each nozzle inclination, chimney height is varied to see its effect on the mixing behaviour. Chimney height to diameter ratio (H/D) considered in the simulations are 5 and 6 respectively.

### 3.5.1 Numerical discritisation

The computational domain considered for the simulation is 3.5 m × 5.5 m × 1 m. The chimney geometry simulated is similar in dimensions as that of the full scale size. Analyses are done with about 840000 grid points (155 × 155 × 35) with similar discritisation mentioned earlier (Section 3.4.1). Chimney cross section (450 mm × 450 mm) and side outlet nozzle cross section (450 mm × 225 mm) are also unchanged. Only nozzle inclination (θ) is changed. A typical model with its mesh for 35° nozzle inclination prepared in PHOENICS code is shown in Fig. 3.26.

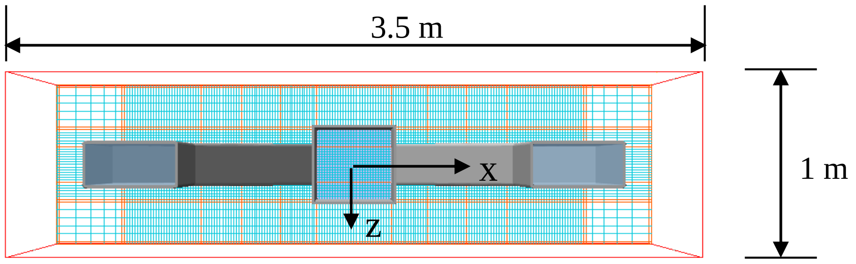

(a) Top view (Plan)

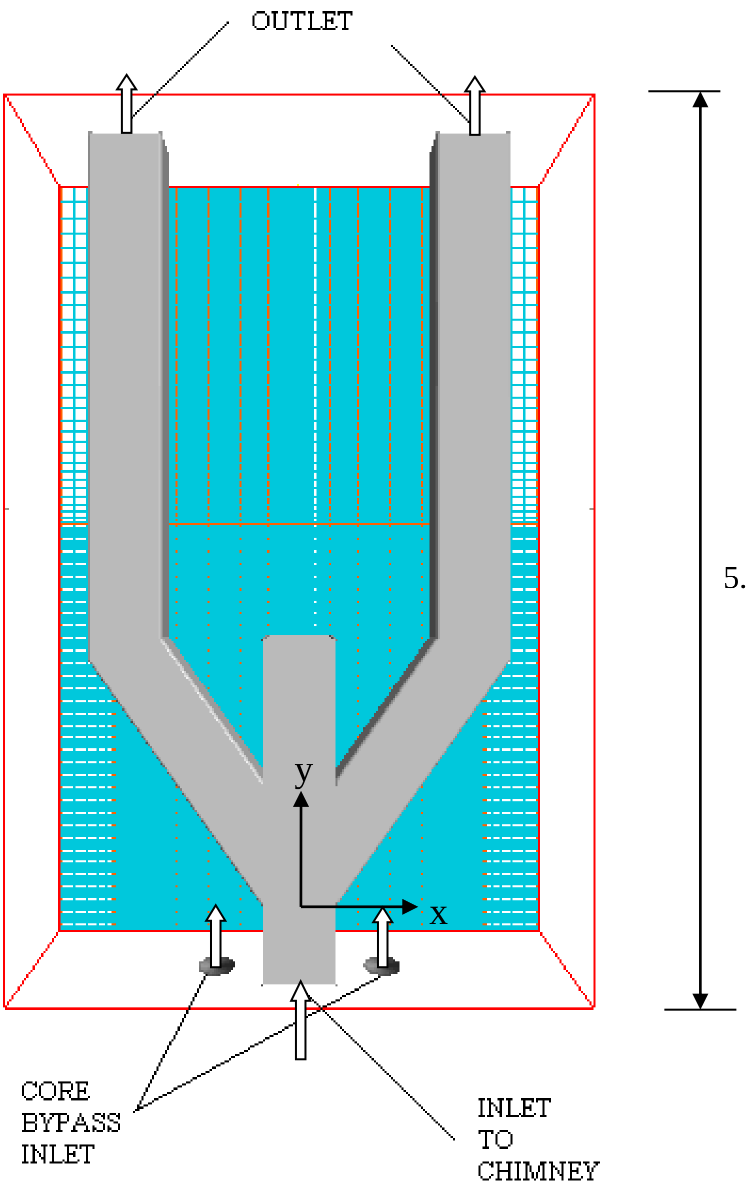

(b) Front view (Elevation)

Fig. 3.26: Computational domain and mesh (H/D=5, H= 2.25 m, θ=35°)

All the four types of chimney geometry considered in the simulations are shown in Fig. 3.27.

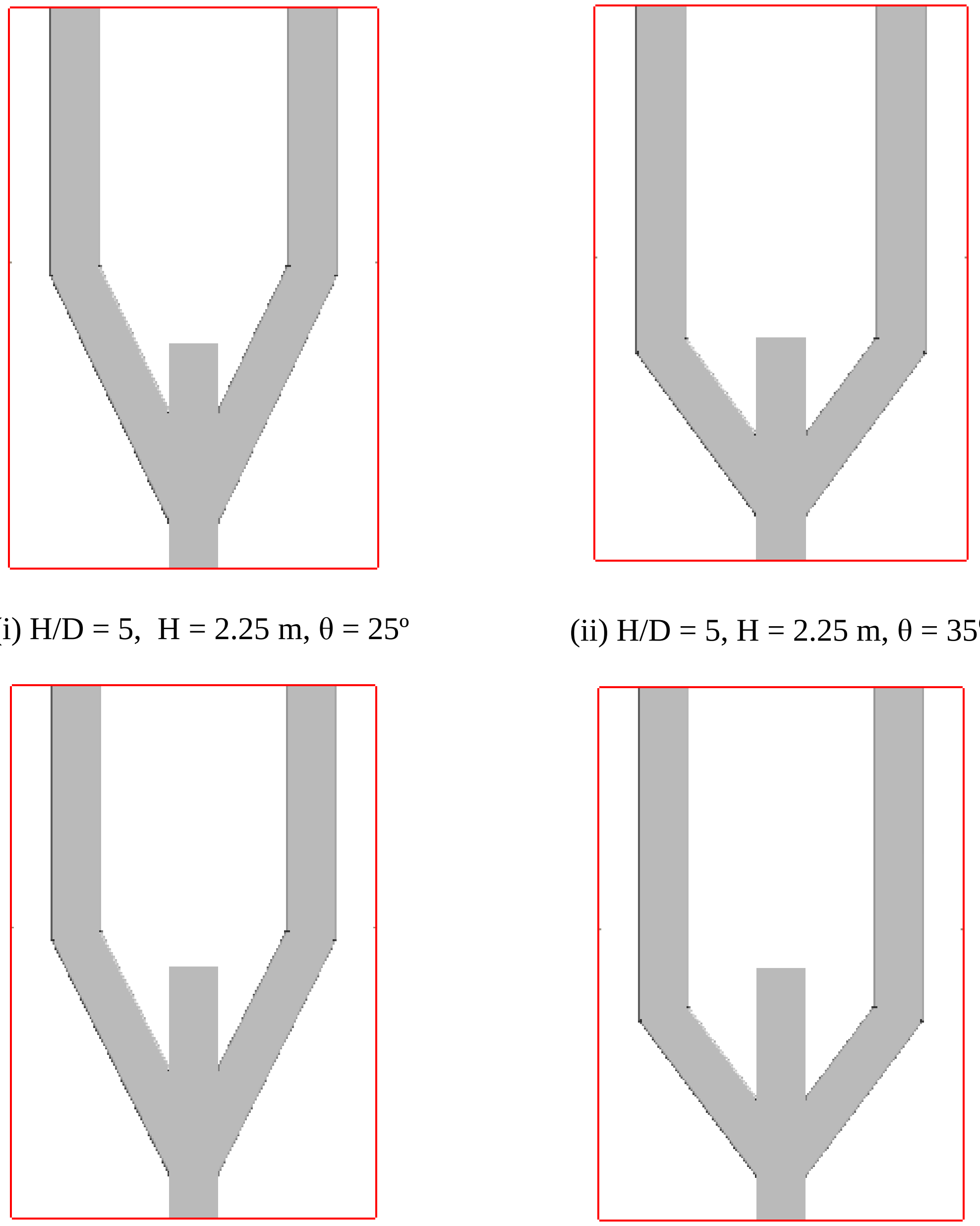

(i) H/D = 5, H = 2.25 m, θ = 25º

(ii) H/D = 5, H = 2.25 m, θ = 35º

(iii) H/D = 6, H = 2.7 m, θ = 25º

(iv) H/D = 6, H = 2.7 m, θ = 35º

Fig. 3.27: Geometry of chimney structures with various height and nozzle inclination considered for simulation

The fluid properties are assumed to be constant. A uniform velocity profile has been set at the inlet. As a boundary condition, the inlet values of turbulent kinetic energy (k) and turbulence energy dissipation rate (ε) are prescribed in terms of the turbulence intensity which is considered to be 5% for all the cases.

Considering chimney surface walls, no slip boundary condition is imposed on the surfaces. For the pool water domain boundary, zero gradient boundary condition is applied. Inlet flow through the bottom of the chimney and bypass flow into the pool through the two bottom nozzles are specified based on the flow considered for the simulation cases.

### 3.5.2 Results and discussion

The turbulent mixing behaviour for the chimney with different heights of 2.25 m and 2.7 m is found to be similar in nature. The results for chimney height of 2.25 m have been discussed in detail here. Velocity distribution for 25º and 35º nozzle inclination has been shown in Fig. 3.28 and Fig. 3.29 respectively. In both these cases core bypass flow is considered to be 0%. The velocity contour plots in the x-y plane (Fig. 3.28 and Fig. 3.29) show that the upward flow is observed during diversion of flow through two side nozzles due to the inertia of the upward flow. It is also observed that upward jet has reached higher height for 25º inclination case than that for the case of 35º inclination. This height (where the upward velocity becomes zero) is defined as stagnation height ($h_S$). This location is clearly observed in the vector plot of velocity in the y-z plane (Fig. 3.30b and Fig. 3.31b). In these figures, vortices are also observed by the two sides of the central upward water jet. These vector plots are shown for the entire chimney height (H) starting from the side outlet nozzle opening edge (y=0 m) to the top opening edge (y=2.25 m) of the central chimney.

The vector plots in the x-y plane (Fig. 3.30a and Fig. 3.31a) show that core outlet water reaches the pool top through the outer periphery of the central chimney to compensate for the flow sucked in from the pool through the top opening in the central region. Therefore to restrict the core flow reaching the pool top, it is essential to provide core bypass flow.

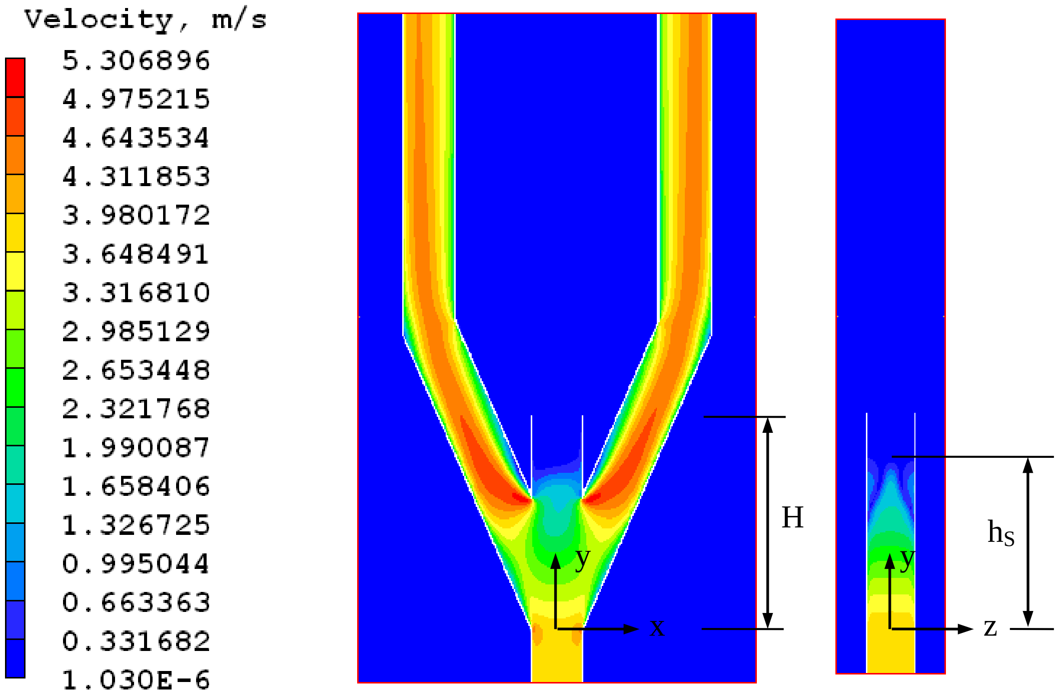


(a) x-y plane (z=0) (b) y-z plane (x=0)

Fig. 3.28: Velocity distribution with 25° nozzle inclination for height 2.25 m (R =0.0)

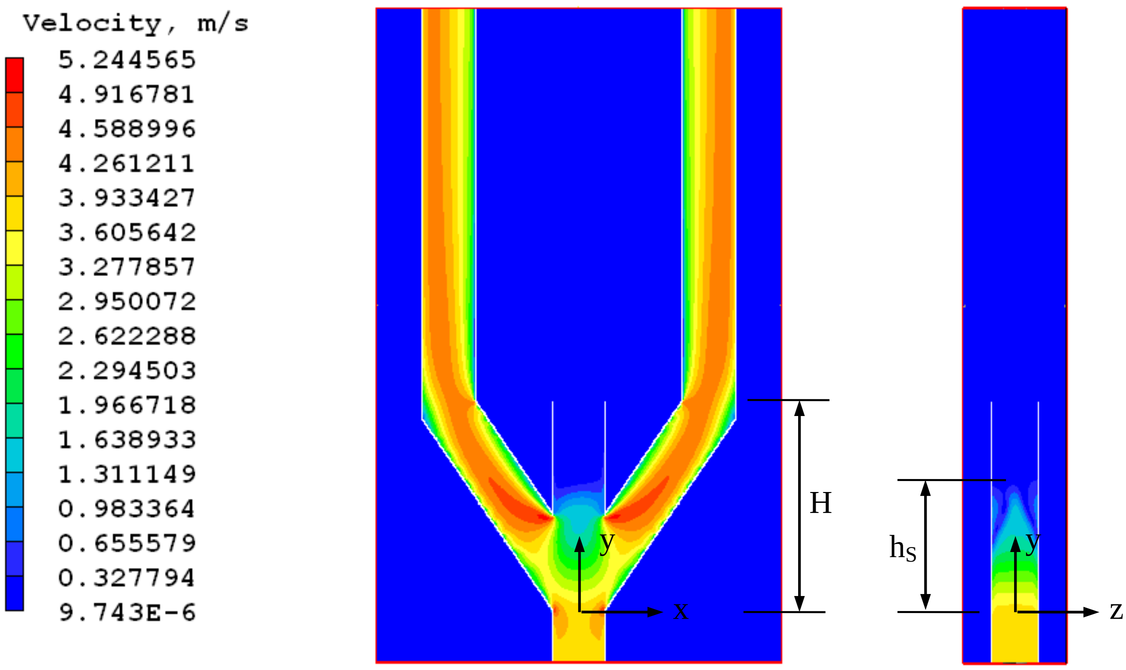


(a) x-y plane (z=0) (b) y-z plane (x=0)

Fig. 3.29: Velocity distribution with 35° nozzle inclination for height 2.25 m (R =0.0)

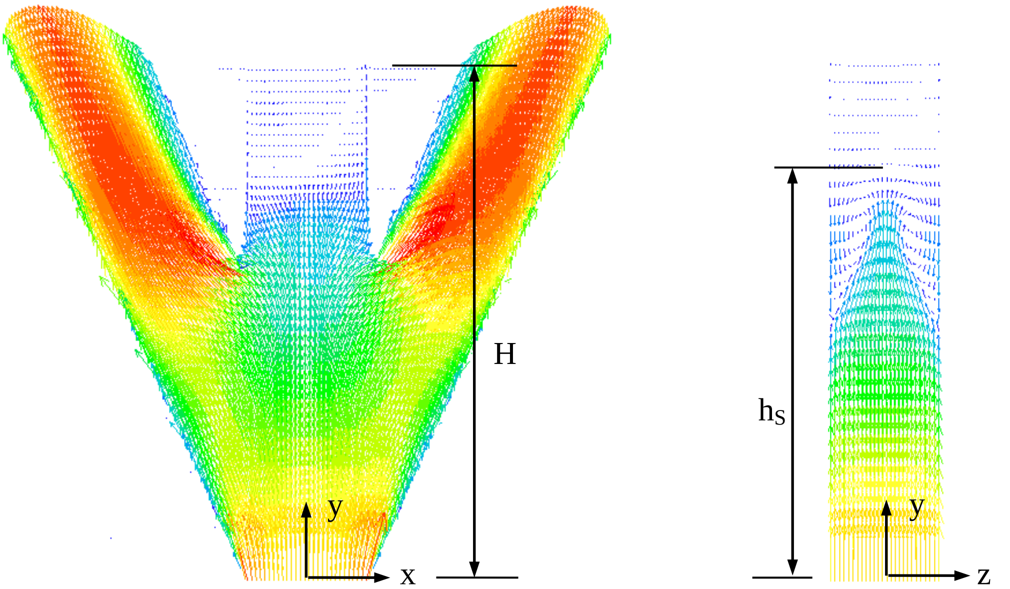


(a) x-y plane (z=0) (b) y-z plane (x=0)

Fig. 3.30: Velocity vector plot between y=0.0 m to 2.25 m with 25° nozzle inclination for height 2.25 m (R=0.0)

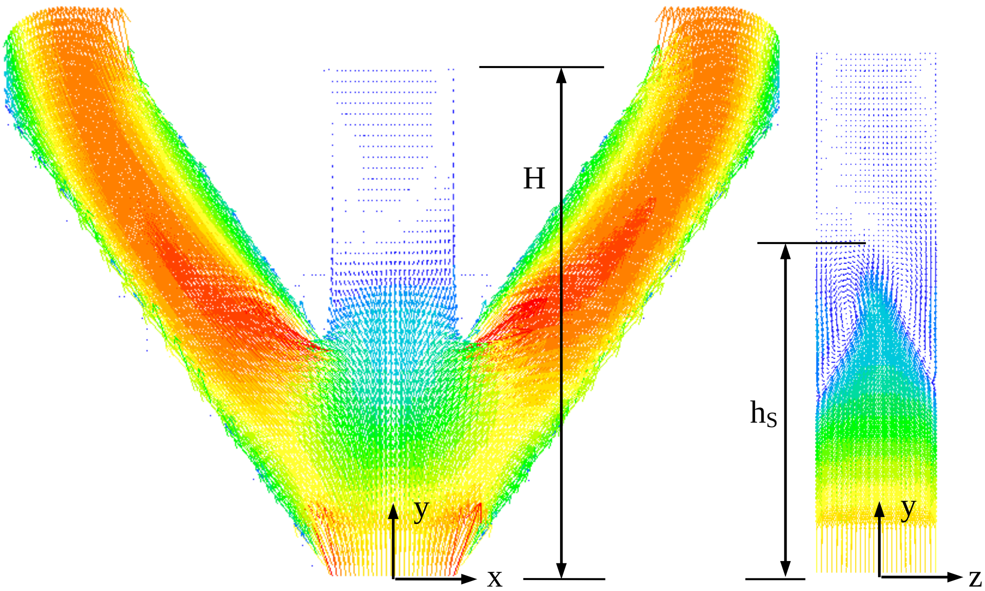


(a) x-y plane (z=0) (b) y-z plane (x=0)

Fig. 3.31: Velocity vector plot between y=0.0 m to 2.25 m with 35° nozzle inclination for height 2.25 m (R=0.0)

The results with 15% bypass flow cases for 25° and 35° nozzle inclinations are shown in Fig. 3.32 to Fig. 3.35. The velocity distribution plots in x-y and y-z planes (Fig. 3.32 and Fig. 3.33) show clearly the stagnation point at the central axis of the chimney. This is the location where changeover of velocity direction from upward to downward takes place while moving in the positive y-direction. In the x-y plane, the velocity distribution of the core bypass flow mixing in the pool water (through two bypass nozzles) is also observed. The entrainment of adjacent water is clearly seen in velocity vector plots of x-y plane (Fig. 3.34a and Fig. 3.35a).

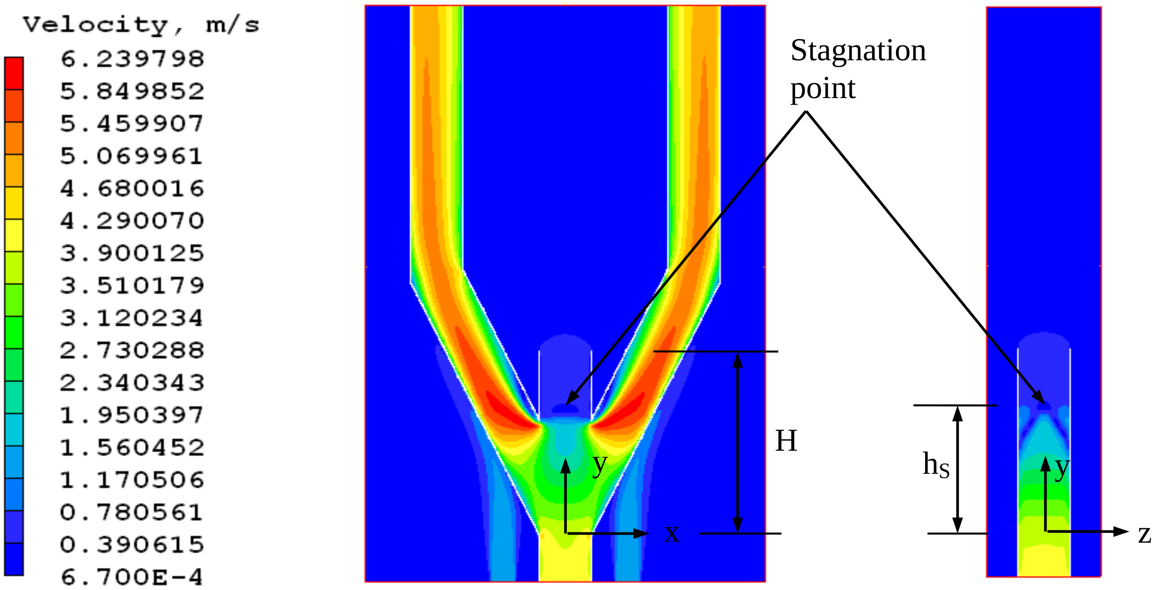


(a) x-y plane (z=0) (b) y-z plane (x=0)

Fig. 3.32: Velocity distribution with 25° nozzle inclination for height 2.25 m (R=0.15)

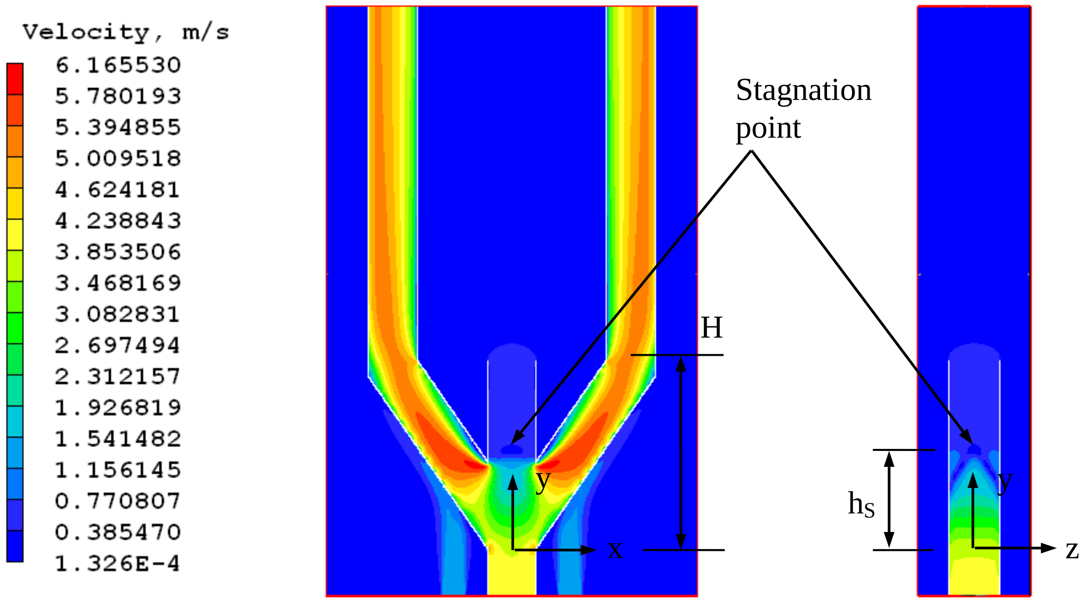


(a) x-y plane (z=0) (b) y-z plane (x=0)

Fig. 3.33: Velocity distribution with 35° nozzle inclination for height 2.25 m (R=0.15)

The velocity vector plots (Figures 3.34b and 3.35b) show that the extent of upward jet reaching towards the chimney top opening has reduced with respect to the case with 0% core bypass flow. Here also two recirculation zones are observed on the two sides of the central jet. Because of provision of core bypass flow only downward flow takes place now through the top opening of the chimney. The stagnation height is found to be 1.208 m and 0.921 m for 25° and 35° nozzle inclination angles respectively.

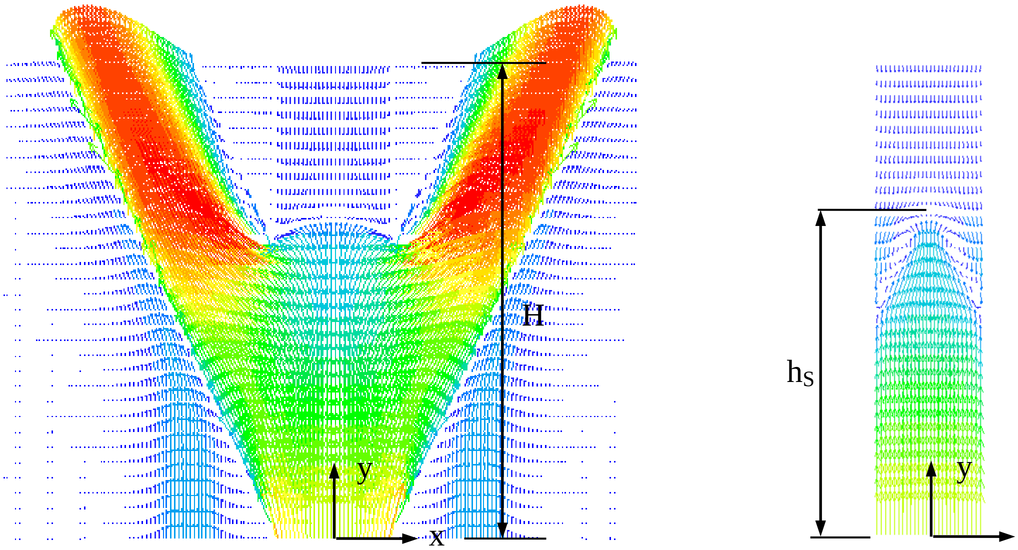


(a) x-y plane (z=0) (b) y-z plane (x=0)

Fig. 3.34: Velocity vector plot between y=0.0 to 2.25 m with 25° nozzle (H=2.25 m, R=0.15)

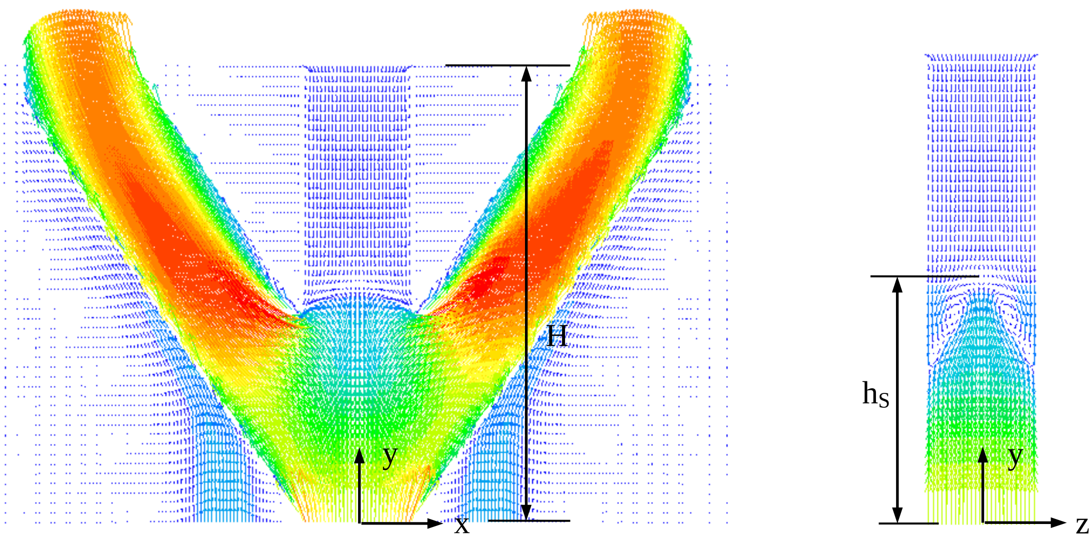


(a) x-y plane (z=0) (b) y-z plane (x=0)

Fig. 3.35: Velocity vector plot between y=0.0 to 2.25 m with 35° nozzle (H=2.25 m, R=0.15)

The variation of stagnation height ($h_S$) due to change in nozzle inclination ($\theta$) considering height (H) of 2.25 m is shown in Fig. 3.36. It is observed that stagnation height decreases by increasing the nozzle inclination. However, the extent of decrease in stagnation height (for similar increase in angle) decreases with increase in angle. It is also observed that stagnation height decreases with increasing bypass flow ratio (R) for any chimney angle.

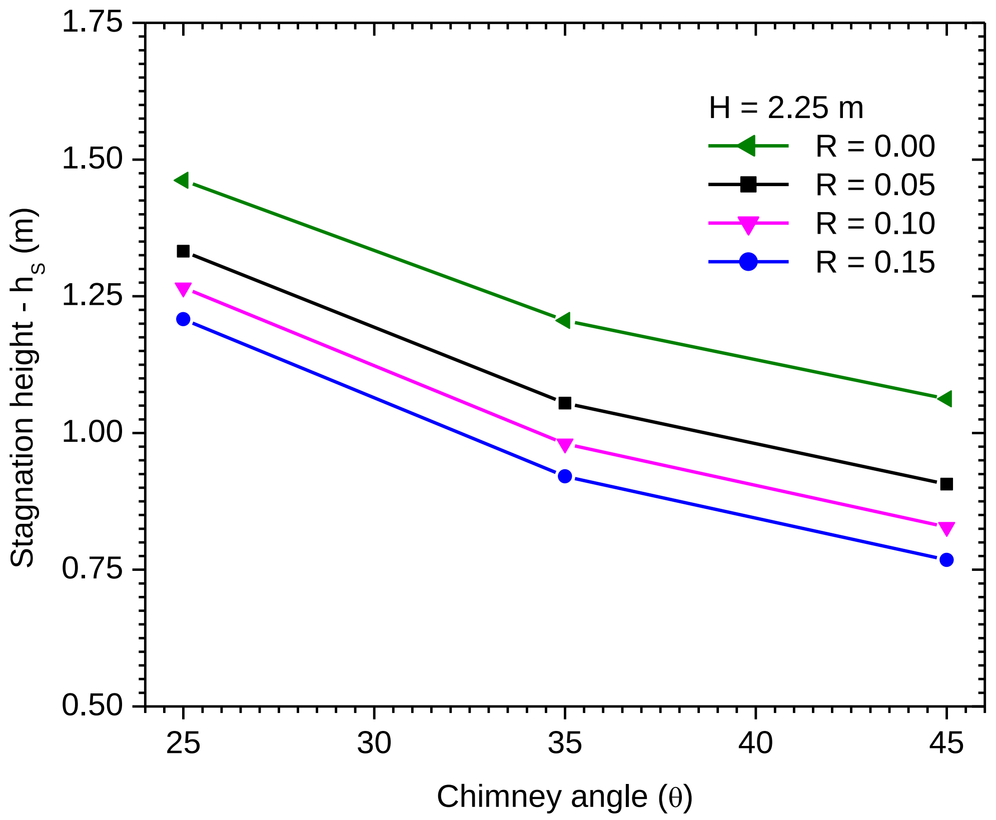


Fig. 3.36: Variation of stagnation height with nozzle inclination (H= 2.25 m)

For chimney height of 2.7 m, the variation of stagnation height due to change in chimney angle is shown in Fig. 3.37. Similar trend of results as mentioned above for 2.25 m chimney height is observed.

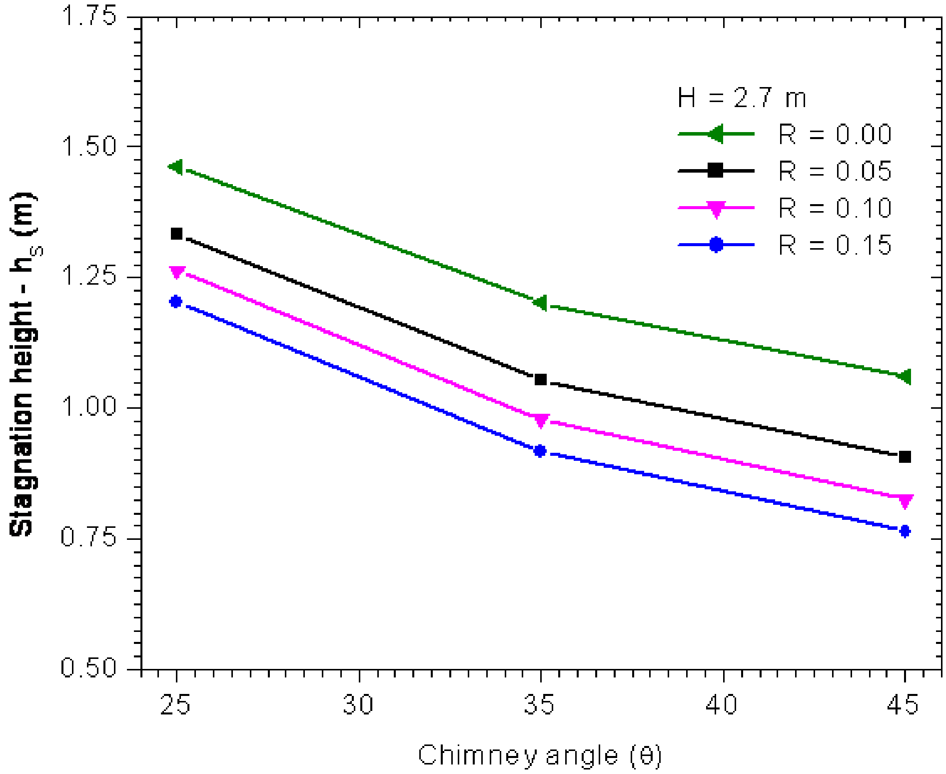


Fig. 3.37: Variation of stagnation height with nozzle inclination (H=2.7 m)

Temperature distribution of the core outlet water and the pool water due to mixing inside the chimney is predicted. It is observed that pool water temperature stabilises at 49°C (i.e., core outlet temperature) if no core bypass flow is sent into the pool. Pool water temperature stabilises at the core outlet temperature because hot water from the core outlet reaches the chimney top opening through the peripheral region as described earlier. When bypass flow is provided, pool water is sucked inside the chimney. However, due to upward flowing hot fluid from the bottom of the chimney, pool water front (40°C) reaches only upto a certain depth with respect to the top of the chimney. The results of temperature contours in x-y and y-z planes are shown in Fig. 3.38 and Fig. 3.39 for 25° and 35° inclination respectively when core bypass flow is 5%. The results with 15% core bypass flow for 25° and 35° nozzle inclinations are shown in Fig. 3.40 and Fig. 3.41 respectively.

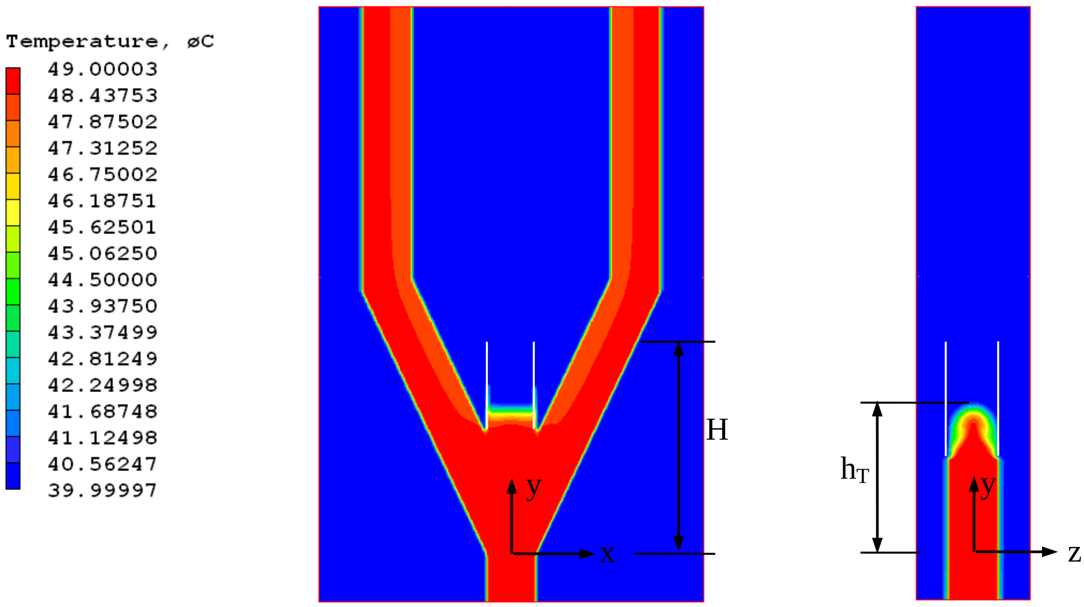


(a) x-y plane (z=0) (b) y-z plane (x=0)

Fig. 3.38: Temperature contour plot with 25° nozzle inclination (H= 2.25 m, R=0.05)

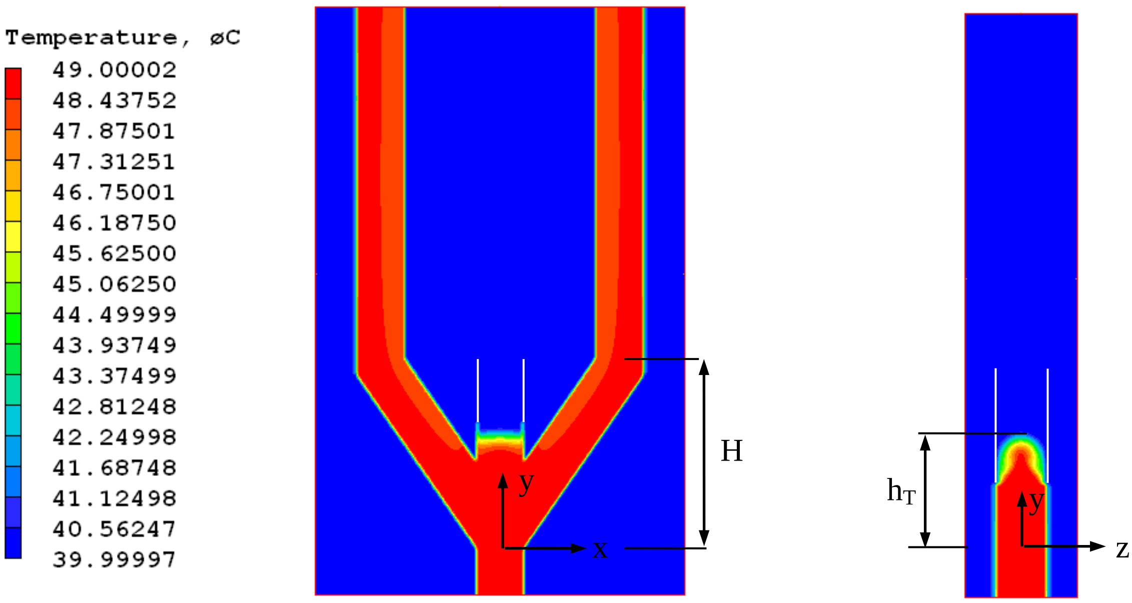


(a) x-y plane (z=0) (b) y-z plane (x=0)

Fig. 3.39: Temperature contour plot with 35° nozzle inclination (H=2.25 m, R=0.05)

Here the pool water temperature is thought to be a tracer of the non-radioactive water. This signifies that radioactivity will spread throughout the pool in case no bypass flow is provided into the pool (as explained earlier that pool water temperature stabilises to core outlet temperature).

When bypass flow is provided, this pool water temperature front reaches inside the chimney. The non-radioactive region boundary of the chimney is defined by pool temperature front. Pool temperature front height is defined as the distance from the chimney reference (zero height) to that location where centre line temperature is equal to pool water temperature (40°C). It is observed from Fig. 3.38 and Fig. 3.39 that for a chimney height of 2.25 m, the pool temperature front height ($h_T$) is 1.441 m and 1.163 m for 25° and 35° nozzle inclinations respectively for 5% core bypass flow. When bypass flow is increased to 15%, the pool temperature front height ($h_T$) further decreases to 1.293 m and 1.007 m (Fig. 3.40 and 3.41).

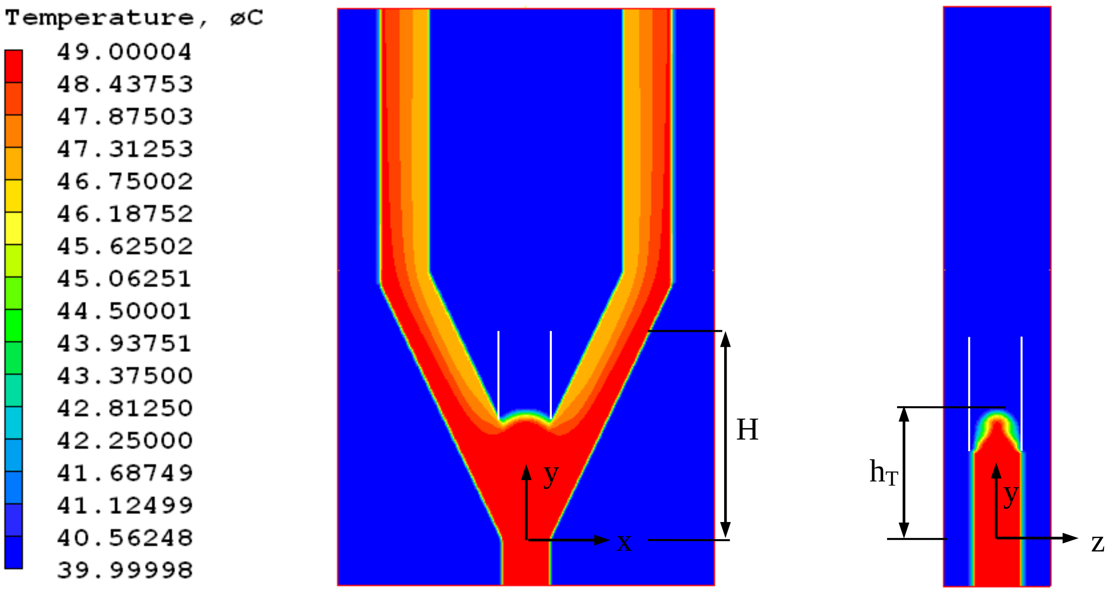


(a) x-y plane (z=0) (b) y-z plane (x=0)

Fig. 3.40: Temperature contour plot with 25° nozzle inclination (H= 2.25 m, R=0.15)

Variation of pool temperature front height ($h_T$) with nozzle inclination ($\theta$) is shown in Fig. 3.42 and Fig. 3.43 for chimney height of 2.25 m and 2.7 m respectively. It is observed from the results that pool temperature front height decreases with increase in nozzle inclination. As core bypass flow increases from 5% to 15%, pool temperature front height also decreases. Comparing figures 3.42 and 3.43, it is observed that the pool temperature front height does not change significantly with increase in chimney height.

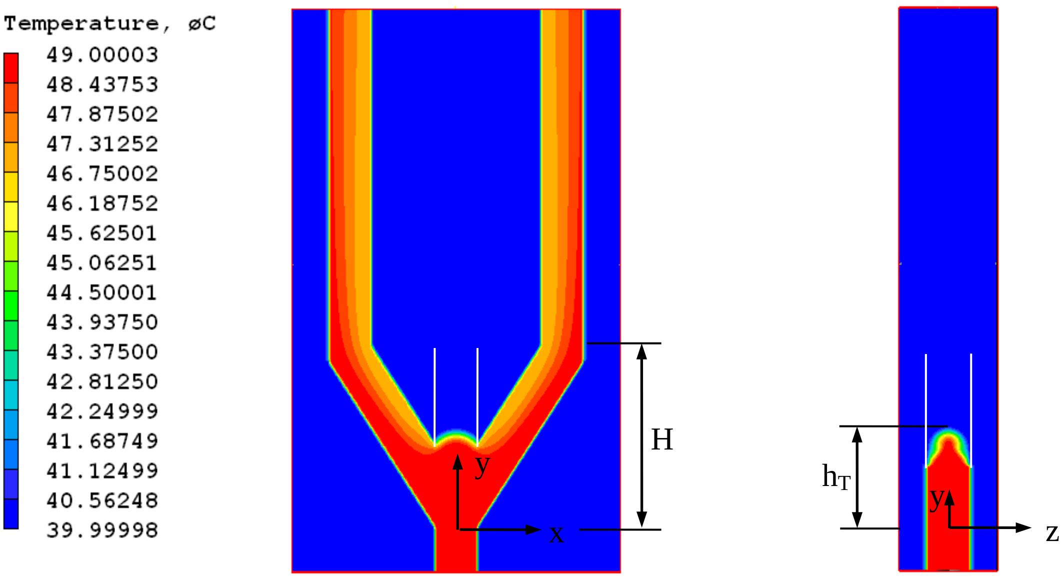


(a) x-y plane (z=0) (b) y-z plane (x=0)

Fig. 3.41: Temperature contour plot with 35° nozzle inclination (H= 2.25 m, R=0.15)

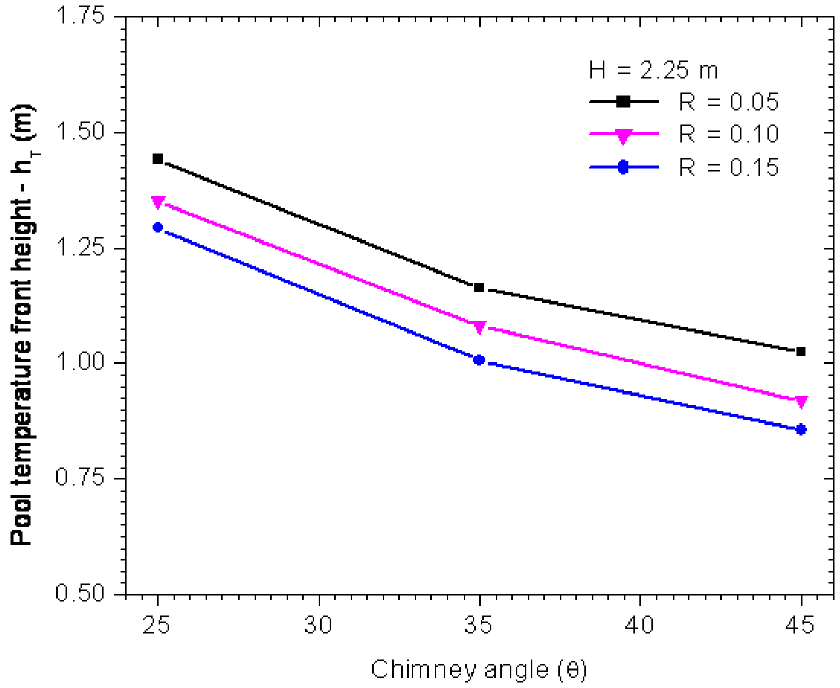


Fig. 3.42: Variation of pool temperature front height with nozzle inclination (H=2.25 m)

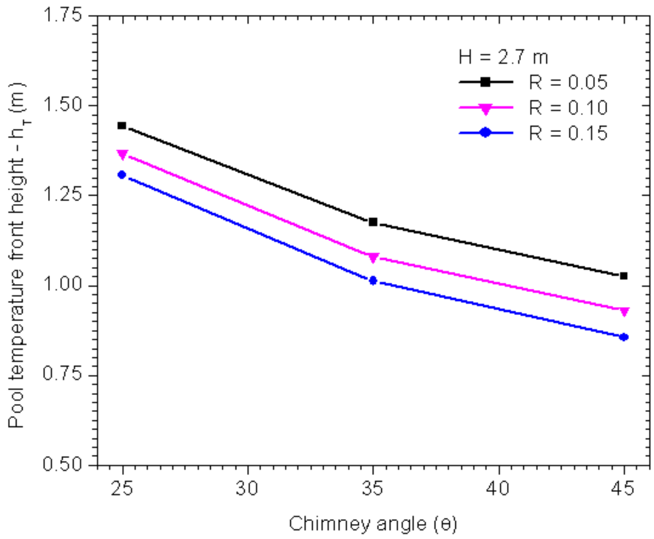


Fig. 3.43: Variation of pool temperature front height with nozzle inclination (H=2.7 m)

To understand the effect of buoyancy force due to temperature difference of core outlet water and pool water on the stagnation height, computations are done considering both the temperatures as equal. Variation of stagnation height with bypass flow ratio for 25°, 35° and 45° nozzle inclinations with chimney height of 2.25 m is shown in Fig. 3.44 in dimensionless from and compared with the results with unequal temperature of core outlet water and pool water. The results are shown in Table -3.2.

Table-3.2: Variation of $h_S/D$ with inclination and bypass flow ratio for H/D=5

| **H/D=5** | **θ =25°** | | **θ=35°** | | **θ =45°** | |
|---|---|---|---|---|---|---|
| **R** | *ΔT=0°C* | *ΔT=9°C* | *ΔT=0°C* | *ΔT=9°C* | *ΔT=0°C* | *ΔT=9°C* |
| **0.00** | 3.33137 | 3.33815 | 2.73943 | 2.74336 | 2.41493 | 2.42178 |
| **0.05** | 3.03319 | 3.04155 | 2.40573 | 2.40672 | 2.06646 | 2.06895 |
| **0.10** | 2.88313 | 2.88422 | 2.23292 | 2.23504 | 1.88514 | 1.88661 |
| **0.15** | 2.74801 | 2.74869 | 2.09438 | 2.09701 | 1.74253 | 1.74486 |

It is observed that dimensionless stagnation height is not affected significantly due to difference between the core outlet temperature and the pool water temperature. It is also observed that stagnation height decreases with increase in bypass flow ratio.

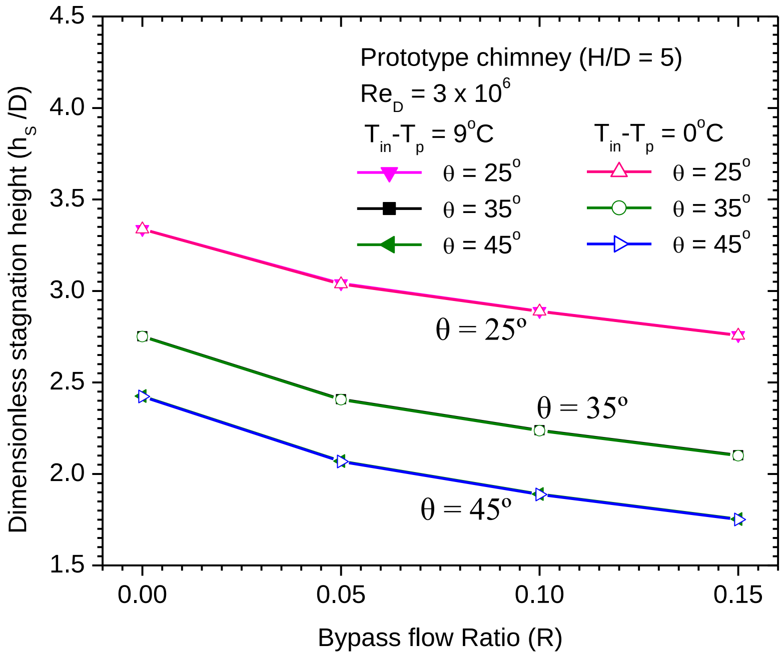


Fig. 3.44: Variation of dimensionless stagnation height (H/D= 5)

Similar trend of results is observed for chimney height of 2.7 m (i.e. H/D=6) as shown in Fig. 3.45. The effect of temperature difference on stagnation height ($h_S$) is found to be negligible because the inertia force due to higher velocity is dominant than the buoyancy force (due to lower temperature difference) for the present study. The results are shown in Table-3.3.

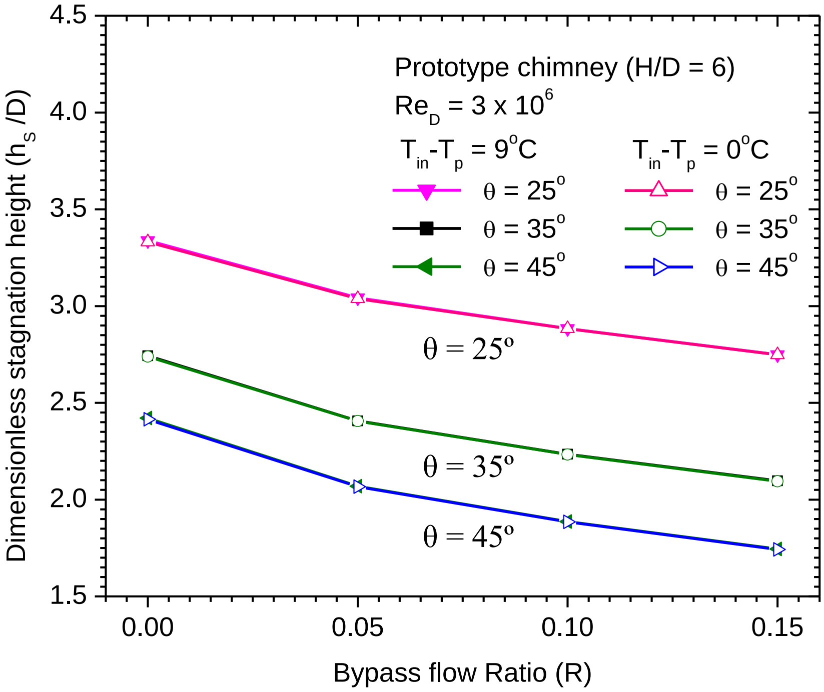


Fig. 3.45: Variation of dimensionless stagnation height (H/D= 6)

Table-3.3: Variation of $h_S/D$ with inclination and bypass flow ratio for H/D=6

| **H/D=6** | **θ =25°** | | **θ=35°** | | **θ =45°** | |
|---|---|---|---|---|---|---|
| **R** | *ΔT=0°C* | *ΔT=9°C* | *ΔT=0°C* | *ΔT=9°C* | *ΔT=0°C* | *ΔT=9°C* |
| **0.00** | 3.33669 | 3.33838 | 2.75082 | 2.75265 | 2.42292 | 2.42564 |
| **0.05** | 3.03724 | 3.04276 | 2.40614 | 2.40799 | 2.06731 | 2.06973 |
| **0.10** | 2.88822 | 2.88982 | 2.23655 | 2.23888 | 1.88744 | 1.89023 |
| **0.15** | 2.75598 | 2.75788 | 2.09956 | 2.10212 | 1.75039 | 1.75279 |

Variation of dimensionless pool temperature front height ($h_T/D$) for three different angles as well as for two different chimney heights is shown in Fig. 3.46 It is observed that major variation of pool temperature front height depends on the chimney angle. For 45° angle, the dimensionless pool temperature front height has the minimum value and it increases with decrease in angle. With increase in bypass flow ratio (R), the dimensionless pool temperature front height decreases. The height of the chimney does not have significant effect on pool temperature front height.

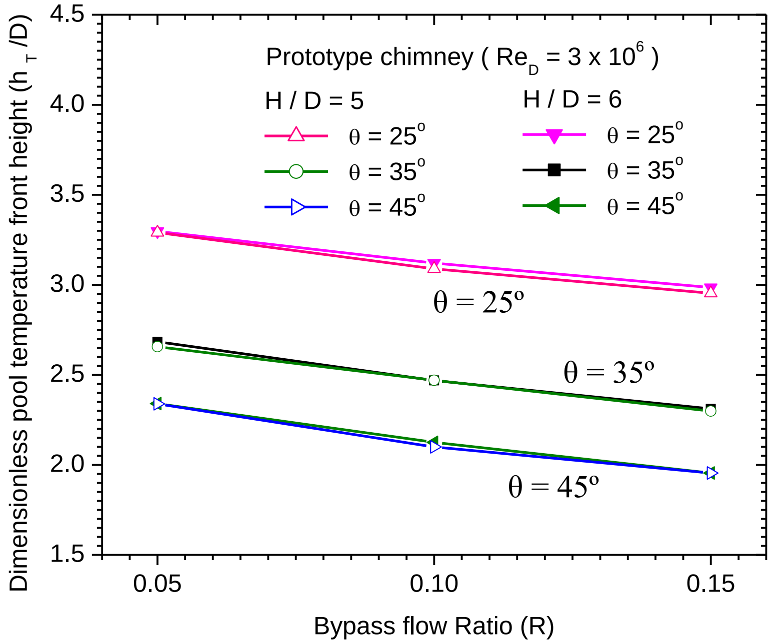


Fig. 3.46: Variation of dimensionless pool temperature front height (H/D=5, H/D=6)

### 3.6 Closure

The turbulent mixing studies of upward hot fluid and downward cold fluid inside the prototype chimney show that with increase in bypass flow ratio, stagnation height decreases. It is also found that rate of decrease in stagnation height gradually diminishes as bypass flow ratio increased from 0.0 to 0.15. Similarly pool temperature front height is also observed to decrease with increase in bypass flow ratio. Even with change in nozzle inclination (θ) of the chimney to 45º, 35º and 25º, similar behaviour of decrease in stagnation height as well as temperature front height with increase in bypass flow ratio take place. Considering the fact that the decrease in dimensionless stagnation height as well as dimensionless temperature front height is about 1-2% of the overall chimney height, when bypass flow ratio is increased from 0.10 to 0.15, it is proposed to provide a bypass flow ratio of 0.10 in the reactor.

From the analyses it is also observed that stagnation height and pool temperature front height are dependent on the nozzle inclination of the chimney. It is found that dimensionless stagnation height as well as dimensionless pool temperature front height decreases with increase in nozzle inclination. Therefore, nozzle inclination of 45º is planned to be used in the chimney design of the reactor. Though the chimney inclination has significant effect on the flow behaviour, the chimney height does not affect the stagnation height as well as the pool temperature front height significantly in case H/D ratio is increased from 5 to 6. Therefore, further increase in chimney height is not found to be beneficial and it is planned to consider H/D ratio equals to 6 in the reactor. Analyses without temperature difference between the core outlet water and pool water show that its effect on the stagnation height is found to be marginal. In conclusion, the bypass flow ratio is the major parameter which decides the stagnation height and pool temperature front height for a chimney with a specified nozzle inclination. Provision of downward flow is beneficial to suppress the upward jet well within the chimney region.

# Chapter 4

# Scaling Philosophy

## 4.1 Introduction

In order to simulate the thermal hydraulics of the mixing phenomena inside the reactor chimney structure, it is essential to maintain geometric and dynamic similarity between the model and the chimney structure of the reactor. Turbulent mixing behaviour of opposing flows inside this chimney depends on various parameters such as core flow, bypass flow, inclination angle and height of the chimney. Accordingly, a scaled test facility has been designed to simulate the mixing behaviour inside the chimney. A scaling philosophy is developed for the simulation of the prototypical phenomena.

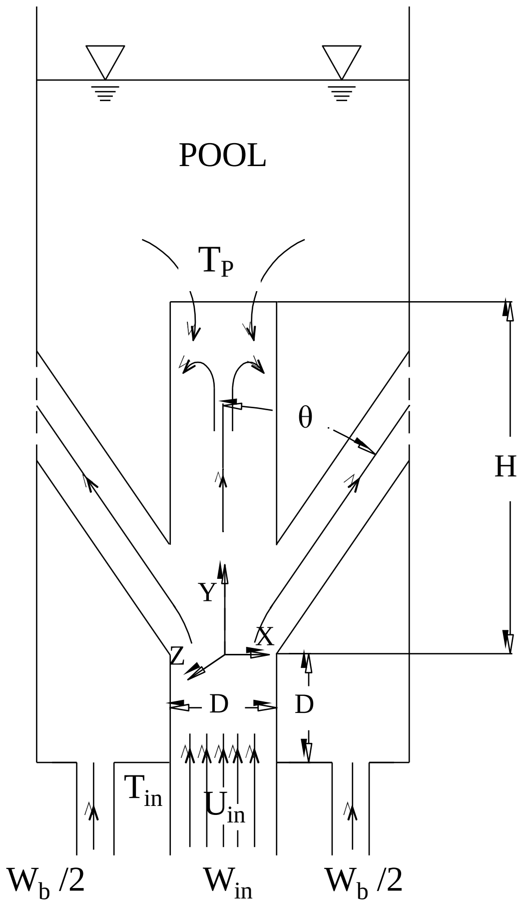


Fig. 4.1: Geometry of the chimney model

Starting with the applicable governing equations and non-dimensionalisation, a number of dimensionless parameters are obtained which are described hereunder.

## 4.2 Governing Equations

The basic conservation equations of mass, momentum and energy are used to determine the appropriate non-dimensional parameters relevant for thermal mixing of two fluid streams.

### 4.2.1 Assumptions

Following assumptions are considered in the mixing phenomenon

- The flow is steady and incompressible.
- Inlet temperature of core flow and bypass flow is constant.
- Pool water temperature is uniform over the entire pool.
- The gravity force is considered in the (-)ve y direction as shown in Fig. 4.1.
- Pool water level is maintained constant.
- Low temperature difference between the core flow and the bypass flow which allows Boussinesq approximation for density dependence on temperature.

**Continuity Equation**

$$\frac{\partial v_x}{\partial x}+\frac{\partial v_y}{\partial y}+\frac{\partial v_z}{\partial z}=0 \qquad \text{.....(4.1)}$$

**Momentum Equations**

a) *x*-momentum equation:

$$v_x\frac{\partial v_x}{\partial x}+v_y\frac{\partial v_x}{\partial y}+v_z\frac{\partial v_x}{\partial z}=-\frac{1}{\rho}\frac{\partial p}{\partial x}+\frac{\mu}{\rho}\left[\frac{\partial^2 v_x}{\partial x^2}+\frac{\partial^2 v_x}{\partial y^2}+\frac{\partial^2 v_x}{\partial z^2}\right] \qquad \text{....(4.2)}$$

b) *y*-momentum equation:

$$v_x\frac{\partial v_y}{\partial x}+v_y\frac{\partial v_y}{\partial y}+v_z\frac{\partial v_y}{\partial z}=-\frac{1}{\rho}\frac{\partial p}{\partial y}+g_y+\frac{\mu}{\rho}\left[\frac{\partial^2 v_y}{\partial x^2}+\frac{\partial^2 v_y}{\partial y^2}+\frac{\partial^2 v_y}{\partial z^2}\right] \qquad \text{...(4.3)}$$

b) $z$-momentum equation:

$$v_x \frac{\partial v_z}{\partial x} + v_y \frac{\partial v_z}{\partial y} + v_z \frac{\partial v_z}{\partial z} = -\frac{1}{\rho}\frac{\partial p}{\partial z} + \frac{\mu}{\rho}\left[\frac{\partial^2 v_z}{\partial x^2} + \frac{\partial^2 v_z}{\partial y^2} + \frac{\partial^2 v_z}{\partial z^2}\right] \qquad ....(4.4)$$

As gravity force is considered to be acting in the (-) ve $y$-direction, pressure gradient in the pool can be expressed in terms of the following relations.

$$g_y = -g \qquad .....(4.5)$$

$$\frac{\partial p}{\partial y} = -\rho_p g \qquad .....(4.6)$$

Where, $\rho_p$ is the density at pool water temperature $T_p$.

Therefore,

$$-\frac{\partial p}{\partial y} + \rho g_y = \rho_p g - \rho g = \rho g\left(\frac{\rho_p}{\rho} - 1\right) \qquad ......(4.7)$$

Using Boussinesq approximation for low temperature difference

$$\rho = \rho_p \left[1 - \beta\left(T - T_p\right)\right] \qquad .....(4.8)$$

$$\frac{\rho_p}{\rho} = \left[1 - \beta\left(T - T_p\right)\right]^{-1} = 1 + \beta(T - T_p) \qquad ....(4.9)$$

Using Eq. (9), $y$-momentum equation takes the following form:

$$v_x \frac{\partial v_y}{\partial x} + v_y \frac{\partial v_y}{\partial y} + v_z \frac{\partial v_y}{\partial z} = g\beta(T - T_p) + \frac{\mu}{\rho}\left[\frac{\partial^2 v_y}{\partial x^2} + \frac{\partial^2 v_y}{\partial y^2} + \frac{\partial^2 v_y}{\partial z^2}\right] \qquad ...(4.10)$$

**Energy Equation**

$$v_x \frac{\partial T}{\partial x} + v_y \frac{\partial T}{\partial y} + v_z \frac{\partial T}{\partial z} = \alpha\left[\frac{\partial^2 T}{\partial x^2} + \frac{\partial^2 T}{\partial y^2} + \frac{\partial^2 T}{\partial z^2}\right] \qquad ...(4.11)$$

### 4.2.2 Non-Dimensionalisation

The above governing equations are non-dimensionalised with the following substitutions.

$$X = \frac{x}{D}; \qquad Y = \frac{y}{D}; \qquad Z = \frac{z}{D} \qquad ...(4.12)$$

$$V_X = \frac{v_x}{U_{in}}; \quad V_Y = \frac{v_y}{U_{in}}; \quad V_Z = \frac{v_z}{U_{in}} \quad \text{where } U_{in} = \frac{W_{in}}{\rho D^2} \qquad ...(4.13)$$

$$P = \frac{p}{\rho U_{in}^2} \qquad ....(4.14) \qquad\qquad T^* = \frac{T - T_p}{T_{in} - T_p} \qquad ...(4.15)$$

Where side (*D)* of the chimney is the characteristic length, $U_{in}$ is the reference inlet velocity based on the upward core flow through the bottom inlet of chimney as shown in equation 4.13. Core outlet temperature is basically the inlet temperature ($T_{in}$) of water at the bottom of the chimney. Pool water temperature ($T_p$) is the reference temperature.

**Non-dimensional form of equations**

**Continuity Equation**

$$\frac{\partial V_X}{\partial X} + \frac{\partial V_Y}{\partial Y} + \frac{\partial V_Z}{\partial Z} = 0 \qquad ...(4.16)$$

**Momentum Equations**

a) *x*-momentum equation:

$$V_X \frac{\partial V_X}{\partial X} + V_Y \frac{\partial V_X}{\partial Y} + V_Z \frac{\partial V_X}{\partial Z} = -\frac{\partial P}{\partial X} + \frac{1}{\mathrm{Re}_D}\left[\frac{\partial^2 V_X}{\partial X^2} + \frac{\partial^2 V_X}{\partial Y^2} + \frac{\partial^2 V_X}{\partial Z^2}\right] \qquad ....(4.17)$$

b) *y*-momentum equation:

$$V_X \frac{\partial V_Y}{\partial X} + V_Y \frac{\partial V_Y}{\partial Y} + V_Z \frac{\partial V_Y}{\partial Z} = \frac{g\beta(T_{in} - T_p)H}{U_{in}^{\ 2}}\left(\frac{D}{H}\right)T^* + \frac{1}{\mathrm{Re}_D}\left[\frac{\partial^2 V_Z}{\partial X^2} + \frac{\partial^2 V_Z}{\partial Y^2} + \frac{\partial^2 V_Z}{\partial Z^2}\right] \qquad .(4.18)$$

c) *z*-momentum equation:

$$V_X \frac{\partial V_Z}{\partial X} + V_Y \frac{\partial V_Z}{\partial Y} + V_Z \frac{\partial V_Z}{\partial Z} = -\frac{\partial P}{\partial Z} + \frac{1}{\mathrm{Re}_D}\left[\frac{\partial^2 V_Z}{\partial X^2} + \frac{\partial^2 V_Z}{\partial Y^2} + \frac{\partial^2 V_Z}{\partial Z^2}\right] \qquad ...(4.19)$$

**Energy Equation**

$$V_X \frac{\partial T^*}{\partial X} + V_Y \frac{\partial T^*}{\partial Y} + V_Z \frac{\partial T^*}{\partial Z} = \frac{1}{\mathrm{Re}_D .\mathrm{Pr}}\left[\frac{\partial^2 T^*}{\partial X^2} + \frac{\partial^2 T^*}{\partial Y^2} + \frac{\partial^2 T^*}{\partial Z^2}\right] \qquad \ldots .(4.20)$$

From the dimensionless equations 4.16 to 4.20, it is clear that for similarity between a model and a prototype, all dimensionless ratios shall be kept same. Various non-dimensional parameters are defined as follows.

1) Reynolds number, $\mathrm{Re}_D = \frac{\rho U_{in} D}{\mu}$ …..(4.21)

2) Richardson number, $Ri = \frac{g\beta(T_{in} - T_p)H}{U_{in}^2}$ ......(4.22)

3) Height to side ratio, $H^* = \frac{H}{D}$ ......(4.23)

4) Prandtl number, $\mathrm{Pr} = \frac{c_p \mu}{k}$ ......(4.24)

5) Peclet number, $Pe = \mathrm{Re}_D .\mathrm{Pr}$ ......(4.25)

The Reynolds numbers ($\mathrm{Re}_D$) in the above equations show the significance of the inertia force to viscous force. Richardson number (Ri) shows the importance of natural convection relative to the forced convection. This number can also be expressed by using a combination of Grashof number and Reynolds number in the following way.

$$Ri = \frac{g\beta(T_{in} - T_p)H}{U_{in}^2} = \frac{g\beta(T_{in} - T_p)H^3}{\nu^2}.\frac{\nu^2}{U_{in}^2 D^2}.\frac{D^2}{H^2} = \frac{Gr}{\mathrm{Re}_D{}^2}.\frac{1}{H^{*2}} \qquad …..(4.26)$$

$$Gr = \frac{g\beta(T_{in} - T_p)H^3}{\nu^2} \qquad …..(4.27)$$

where, H is the characteristic height of Grashof number (Gr). Height to side ratio (H*) is defined as the ratio of chimney height to the side of square inlet cross section.

Prandtl number (Pr) signifies the ratio of momentum diffusivity and thermal diffusivity.

Peclet number (Pe) is the ratio of the thermal energy convected to the fluid to the thermal energy conducted within the fluid.

In addition to the non-dimensionalisation of the above governing equations, boundary conditions are also non-dimensionalised. There are three inflow boundary conditions (i) Core flow ($W_{in}$) at the bottom entry of the chimney (ii) Bypass flow ($W_b/2$) into pool from left representing bypass flow for loop1 and (iii) Bypass flow ($W_b/2$) into pool from right representing bypass flow for loop2. The total bypass flow rate ($W_b$) can be non-dimensionalised with respect to the reference core flow rate ($W_{in}$) as shown below.

$W_b = \left(\frac{W_b}{W_{in}}\right)\{W_{in}\} = (R).\{W_{in}\}$ Where, R is a dimensionless parameter and is termed as bypass flow ratio. Bypass flow ratio (R) is the ratio between the core bypass flow rate and core flow rate and it is defined as given below.

6) Bypass flow ratio, $R = \frac{W_b}{W_{in}}$ .....(4.28)

This dimensionless ratio R also can be written as follows.

$$R = \frac{W_b}{W_{in}} = \left(\frac{W_b}{\rho D^2}\right) \Big/ \left(\frac{W_{in}}{\rho D^2}\right) = \frac{U_b}{U_{in}} = \left(\frac{\rho U_b D}{\mu}\right) \Big/ \left(\frac{\rho U_{in} D}{\mu}\right) = \frac{\mathrm{Re}_b}{\mathrm{Re}_D}$$

Therefore, bypass flow ratio has another significance that it also represents the ratio of average velocity between the downward bypass flow and upward core flow inside the chimney. Here average velocity of the bypass flow for the chimney square cross section is defined as follows.

$$U_b = \frac{W_b}{\rho D^2} \qquad .....(4.29)$$

The bypass flow ratio also represents the ratio of Reynolds number of bypass flow rate through the chimney and that of the core flow rate. Here bypass flow Reynolds number is defined as,

7) Bypass flow Reynolds number, $\mathrm{Re}_b = \dfrac{\rho U_b D}{\mu}$ .....(4.30)

The other boundary conditions are outflow boundary, no slip boundary at wall and symmetry boundary condition at the pool free surface. There are two outflow boundary conditions where pressure is zero (i) at left arm chimney outlet representing flow sent to loop1 and (ii) at right arm chimney outlet representing flow sent to loop2.

Therefore, for exact similarity between the model and the prototype, values of all these above non-dimensional parameters need to be preserved. However, it is not possible to completely simulate all these non-dimensional numbers simultaneously due to various limitations. Therefore, an attempt is made to simulate as close to prototype as practically as possible.

General scaling laws for modelling nuclear reactor systems have been described by Nahavandi et al. (1979). Most of the test facilities are based on the power-to-volume scaling philosophy to predict the system behaviour. The major requirements of this scaling method are proposed by Zuber (1980) and Karwat (1985). One of the basic requirements of this scaling methodology is preservation of the geodetic elevation to be the same as that in the prototype. As a result of this, the test facility normally has flow cross-section area scaled by the volume scaling ratio.

However, the mixing phenomena studied here consider a geometrically similar model considering the chimney as a component and elevation is not conserved. However the temperature differential between the hot and cold fluid stream is preserved by maintaining the inlet temperature boundary conditions of the fluid streams. A geometrically similar model scaled down by a factor of 2:9 is considered based on the availability and ease of measurements in the experimental facility. Table-4.1 gives the details of the prototype and the scaled model.

### 4.3 Similitude Criteria

In order to simulate the thermal hydraulics of the mixing phenomena inside the reactor chimney structure, it is essential to maintain geometric and dynamic similarity between the model and the prototype chimney structure. A geometrically similar model with all the geometric dimensions (height, diameter, inclination between central chimney & outlet nozzle etc.) scaled down by a factor 2:9 was selected for the model studies. The hydraulics of the reactor chimney structure is predominantly characterized by the inertial and viscous forces and therefore it is necessary to maintain the Reynolds number ($Re_D$) of the prototype in the model. For simulation of thermal effects, it is also necessary to take into account the buoyancy effects induced by the difference in the density between the hot and cold fluids. In this case the Richardson number (Ri) needs to be maintained.

Table-4.1: Details of prototype and scaled down model

| Parameter | Prototype | 2/9$^{th}$ scaled model | $\frac{Prototype}{Model}$ ratio |
|---|---|---|---|
| Fluid | Light water | Light water | 1 |
| Chimney side (D) | 450 mm | 100 mm | 4.5 |
| Chimney height (H) | 2700 mm | 600 mm | 4.5 |
| Pool diameter | 5000 mm | 1100 mm | 4.54 |
| Pool height | 11000 mm | 2400 mm | 4.58 |
| Outlet nozzle area (Slit height x width) | 225 mm × 450 mm | 50 mm × 100 mm | 4.5 × 4.5 |
| Inclination angle between the upward flow direction | 45° | 45° | 1 |

| | | | |
|---|---|---|---|
| and outlet nozzle flow direction (θ) | | | |
| Fluid volume (pool+system) | 210 + 140=350 $m^3$ | 2.3 +.3 = 2.6 $m^3$ | 135 |
| Fluid temperature<br>Chimney top entry ($T_p$)<br>Chimney bottom entry ($T_{in}$) | <br>40°C<br>49°C | <br>40°C<br>49°C | <br>1<br>1 |
| Core flow | 45000 lpm | 1500 lpm | 30 |
| Core flow velocity | 3.7 m/s | 2.5 m/s | 1.48 |

Detailed description of the experimental facility for the model study is given in Chapter 6. The maximum flow of about 1500 lpm is sent upward through the chimney due to limitation of the experimental facility. Water at 40°C and 49 °C is used to simulate cold and hot fluids. A preheater of 60 kW capacity is provided to create the differential between the cold and hot fluids. An air cooled chiller unit of 22 TR is provided in the secondary system which transfers heat from the process system ultimately to the atmosphere using a plate heat exchanger of 100 kW rating. Provision is made to vary the flow of the process water and the chilled water through the plate heat exchanger so that experiments can be done at various bypass flow ratios. Chimney size is so chosen that flow visualisation inside the chimney can be effectively made. Provision for dye injection as well as temperature measurement inside the chimney is made. The geometrical size of the pool is so chosen that the stabilised temperature of the pool is achieved within reasonable period. The target time is to complete an experiment in a shift i.e., within 5-6 hours. The system is made ready by filling water to the desired level (2400 mm) of the pool before staring up the heater. About 3 hours is required to stabilise the temperature of the system to the set point by continuous supply of heater power and transferring equivalent heat to chilled water system. The experiment is continued for about an hour. Subsequently system is cooled down by switching off the heater and continuing chilled water supply through the heat exchanger for some time till temperature comes near to normal ambient condition.

### 4.3.1 Simulation of Reynolds number ($Re_D$):

Reynolds number needs to be preserved for the prototype and the model. The following Table-4.2 is prepared keeping the same Reynolds number for the model as that of the prototype. Flow requirement in the model is calculated as shown in the Table.

Table-4.2: Reynolds number simulation

| Parameters | Bypass flow Ratio(R) | Reference velocity (m/s) | **Reynolds Number of prototype and the model** | Model: Model velocity (m/s) | Model: Flow (lpm) | Reynolds number $\frac{Prototype}{Model}$ ratio |
|---|---|---|---|---|---|---|
| Core flow (upward) | - | 3.7 | **$Re_D$=3.0x10$^6$** | 16.65 | 10000 | 1 |
| Bypass flow (downward) | i) 0.0 | 0.0 | **$Re_b$=0.0** | 0.0 | 0 | 1 |
| | ii) 0.05 | 0.185 | **$Re_b$=1.5x10$^5$** | 0.8325 | 500 | 1 |
| | iii) 0.10 | 0.370 | **$Re_b$=3.0x10$^5$** | 1.6650 | 1000 | 1 |
| | iv) 0.15 | 0.555 | **$Re_b$=4.5x10$^5$** | 2.4975 | 1500 | 1 |

It is observed that the maximum total system flow of about 11500 lpm is required in the model so as to maintain the same Reynolds numbers ($Re_D$ and $Re_b$) as in the prototype. This requires a core outlet flow of 10000 lpm with a velocity of 16.65 m/s in the model. Depending on the bypass flow ratio (0.0 to 0.15) the requirement of bypass flow in the model varies from 0 to 1500 lpm. The bypass velocity varies from 0 to 2.5 m/s. Corresponding Reynolds numbers are also shown in the above Table-4.2. Depending on the core bypass flow, total system flow requirement in the model varies from 10000 lpm to 11500 lpm.

In order to maintain same core outlet / chimney bottom entry temperature (49°C) and chimney top entry temperature (40°C) in the model as in the prototype, the chimney nozzle outlet temperature is calculated for various core bypass flow as shown in the Table-4.3. In case of 10000 lpm core flow in the model (for simulating same Reynolds numbers) and keeping the nozzle outlet temperature same as in the prototype, the heater power requirements for various bypass flow ratios are calculated as shown in the Table. For minimum core bypass flow ratio (0.05) heater power required is about 299 kW. Maximum heat supply requirement is 818 kW for bypass flow ratio of 0.15.

Table-4.3: Heater power requirement for Reynolds number simulation

| | | Prototype | | Model | | $Re_D$ of |
|---|---|---|---|---|---|---|
| Sr. No. | Bypass flow ratio (R) | Core bypass flow (lpm) | Chimney nozzle outlet temperature (°C) | Core bypass flow (lpm) | Heater power (kW) | Prototype and model |
| 1. | 0.05 | 2250 | 48.6 | 500 | 299 | $3.0 \times 10^6$ |
| 2. | 0.10 | 4500 | 48.2 | 1000 | 570 | $3.0 \times 10^6$ |
| 3. | 0.15 | 6750 | 47.8 | 1500 | 818 | $3.0 \times 10^6$ |

Therefore, it is found that keeping same Reynolds number requires very high flow rate for the system and the resulting velocities in the chimney sections are also high. Since the chimney is made of acrylic, it is practically not achievable to attain such high velocities. Moreover, power supply requirement is also quite large. Therefore it is difficult to preserve the Reynolds number in the model as that of the prototype. Maximum upward flow is limited to 1500 lpm and maximum heater power is limited to 60 kW.

### 4.3.2 Simulation of Richardson number (Ri):

Richardson number for the prototype and the model should be same in order to understand relative importance of buoyancy force to that of the inertia force. It is considered essential that the temperature difference of the model is kept the same as in the prototype. The absolute values of the temperatures at the core outlet ($T_{in}$) and the pool ($T_p$) are also maintained the same in the model as in the prototype. Considering the chimney height (H) as the characteristic length, Grashof number (Gr) for the prototype is calculated as given below.

$$Gr\Big|_{prototype} = \frac{g\beta(T_{in}-T_p)H^3}{\nu^2} = \frac{9.81\times 4.3\times 10^{-4}\times(49-40)\times 2.7^3}{\left[5.54\times 10^{-7}\right]^2} = 2.44\times 10^{12}$$

$$Gr\Big|_{model} = \frac{g\beta(T_{in}-T_p)H^3}{\nu^2} = \frac{9.81\times 4.3\times 10^{-4}\times(49-40)\times 0.6^3}{\left[5.54\times 10^{-7}\right]^2} = 2.67\times 10^{10}$$

Richardson number (Ri) for upward flow is calculated for the prototype using the following.

$$Ri = \frac{Gr}{\mathrm{Re}_D{}^2\, H*^2} = \frac{2.44\times 10^{12}}{\left(3\times 10^6\right)^2\times 6^2} = 0.0075$$

All these above calculations are based on the chimney height of 2700 mm for the prototype and 600 mm for the model. The required Reynolds number and corresponding flow for the model to preserve the Richardson number of the prototype are shown in Table-4.4.

Table-4.4: Richardson number simulation with height H=2.7 m (model height=0.6 m)

| | | Prototype Gr = 2.44 x$10^{12}$ | | **Richardson number (Ri) of prototype and model** | Model Gr =2.67 x $10^{10}$ | | | Ratio of Ri for Prototype / model |
|---|---|---|---|---|---|---|---|---|
| Parameters | Bypass flow ratio (R) | Reference velocity (m/s) | Reynolds number | | Reynolds number | Model velocity (m/s) | Flow (lpm) | |
| Core flow (upward) | - | 3.7 | $Re_D$=3.0x$10^6$ | **0.0075** | $Re_D$=3.14x$10^5$ | 1.74 | 1048 | 1 |
| Bypass flow (downward) | i) 0.0 | 0.0 | $Re_b$=0.0 | **0.0075** | $Re_b$=0.0 | 0.0 | 0 | 1 |
| | ii) 0.05 | 0.185 | $Re_b$=1.5x$10^5$ | **0.0075** | $Re_b$=1.57x$10^4$ | 0.087 | 52.4 | 1 |
| | iii) 0.10 | 0.370 | $Re_b$=3.0x$10^5$ | **0.0075** | $Re_b$=3.14x$10^4$ | 0.174 | 104.8 | 1 |
| | iv) 0.15 | 0.555 | $Re_b$=4.5x$10^5$ | **0.0075** | $Re_b$=4.71x$10^4$ | 0.262 | 157.2 | 1 |

It is observed from the table that total system flow of about 1150 lpm is required in the model so as to maintain the same Richardson number as in the prototype when the bypass flow ratio is 0.10. This requires a core flow of 1048 lpm with a velocity of about 1.74 m/s in the model.

Core bypass flow entering from the chimney top is about 105 lpm with a velocity of about 0.174 m/s. It is observed that the total system flow required for the model varies from 1048 lpm to 1205 lpm depending on the bypass flow ratios from 0.0 to 0.15.

To maintain same core outlet temperature and chimney top entry temperature as that of the prototype, 1048 lpm upward flow is required to be sent through chimney and heater capacity required is about 60 kW in the model for the case with bypass flow ratio of 0.10. The heater power requirement varies from 31 kW to 86 kW depending on the bypass flow ratio (R) considered from 0.05 to 0.15 as shown in Table-4.5. Since the maximum upward flow available in the system is 1500 lpm and heater capacity is 60 kW, therefore, the Richardson number can be simulated in the experiment upto bypass flow ratio of 0.10.

Table-4.5: Heater power requirement for Richardson number simulation

| | | Prototype | | Model | | Richardson number of prototype and model |
|---|---|---|---|---|---|---|
| Sr. No. | Bypass flow ratio (R) | Core bypass flow (lpm) | Chimney nozzle outlet temp (°C) | Core bypass flow (lpm) | Heater power (kW) | |
| 1. | 0.05 | 2250 | 48.6 | 52.4 | 31 | 0.0075 |
| 2. | 0.10 | 4500 | 48.2 | 104.8 | 60 | 0.0075 |
| 3. | 0.15 | 6750 | 47.8 | 157.2 | 86 | 0.0075 |

### 4.3.3 Simulation of Prandtl number (Pr)

Prandtl number for the prototype and the model has been preserved by keeping the same fluid (water) as in the prototype and the similar fluid temperature. The pool water temperature is kept at 40 °C and the chimney inlet water temperature is kept at 49°C. Because of mixing with cold water of the pool, the water temperature at chimney nozzle outlet reduces, which is increased by using a heater to maintain the chimney inlet water temperature. To maintain the pool water temperature, a part of the flow is sent through a heat exchanger to send water at 40°C into the pool. Prandtl number for the prototype and model is kept similar (about 3.9).

### 4.3.4 Simulation of Peclet number (Pe)

Peclet number is the product of Reynolds number and Prandtl number. As discussed in section 4.3.3, Pr is preserved by keeping same working fluid and same temperature of the fluid as that of the prototype. However, Peclet number cannot be preserved due to difficulty in achieving Reynolds number similar to that of the prototype as discussed in section 4.3.1.

## 4.4 Closure

Since it is not feasible to exactly simulate the model with all the dimensionless parameters simultaneously as in the prototype, a test matrix is prepared by varying the flow rate of the model to study the effect of various dimensionless numbers. Corresponding heater power requirement is also indicated in Table-4.6 and Table-4.7 for cases with bypass flow ratio of 0.0, 0.05, 0.10 and 0.15 with chimney height of 2700 mm (H/D = 6) and 2250 mm (H/D = 5) respectively. The ratio of flow rates, heater power requirements, chimney heights, temperature difference between the opposing flows and dimensionless numbers ($Re_D$, Ri, Pe, etc.) between the prototype and the model are also shown in the Table. It is clearly observed that when Reynolds number ($Re_D$) and Peclet number (Pe) are conserved in the model (considering 10000 lpm flow through the model in the upward direction), Richardson number cannot be conserved. Similarly, when Richardson number (Ri) is conserved for the prototype and the model (with 1048 lpm flow through the model in the upward direction), Reynolds numbers are not conserved. Therefore, in the subsequent chapters numerical analyses and experiments are carried out for the scaled down models to establish the scaling philosophy and to validate the CFD code for predicting the behavior of turbulent mixing inside the chimney structure.

Table-4.6: Test Matrix - Comparison of prototype and model parameters (H/D = 6)

| | | Chimney height - 2700 mm | | | | Model chimney height - 600 mm | | | | | Ratio between prototype and model | | | | | | |
|---|---|---|---|---|---|---|---|---|---|---|---|---|---|---|---|---|---|
| Bypass flow ratio | Prototype / Model | Core flow rate (lpm) | $Re_D$ | Bypass rate (lpm) | Heater power (kW) | Mix temp (ºC) | Gr | Ri | Pe | | Flow rate | $Re_D$ | Heater power | Chimney height | delta T | Ri | Pe |
| | *Prototype* | *45000* | *3.0E+06* | *0* | *0* | *49.0* | *2.44E+12* | *0.0075* | *1.18E+07* | | - | - | - | - | - | - | - |
| | | 10000 | 3.0E+06 | 0 | 0 | 49.0 | 2.67E+10 | 0.0001 | 1.18E+07 | | 4.50 | 1.00 | - | 4.5 | 1 | 91.125 | 1.000 |
| | | 1500 | 4.5E+05 | 0 | 0 | 49.0 | 2.67E+10 | 0.0037 | 1.77E+06 | | 30.00 | 6.67 | - | 4.5 | 1 | 2.050 | 6.667 |
| R=0.00 | Model | 1048 | 3.1E+05 | 0 | 0 | 49.0 | 2.67E+10 | 0.0075 | 1.24E+06 | | 42.96 | 9.55 | - | 4.5 | 1 | 1.000 | 9.547 |
| | | 1000 | 3.0E+05 | 0 | 0 | 49.0 | 2.67E+10 | 0.0083 | 1.18E+06 | | 45.00 | 10.00 | - | 4.5 | 1 | 0.911 | 10.000 |
| | | 500 | 1.5E+05 | 0 | 0 | 49.0 | 2.67E+10 | 0.0330 | 5.90E+05 | | 90.00 | 20.00 | - | 4.5 | 1 | 0.003 | 20.000 |
| | *Prototype* | *45000* | *3.0E+06* | *2250* | *1344* | *48.6* | *2.44E+12* | *0.0075* | *1.18E+07* | | - | | - | - | - | - | - |
| | | 10000 | 3.0E+06 | 500 | 299 | 48.6 | 2.67E+10 | 0.0001 | 1.18E+07 | | 4.50 | 1.00 | 4.50 | 4.5 | 1 | 91.125 | 1.000 |
| | | 1500 | 4.5E+05 | 75 | 45 | 48.6 | 2.67E+10 | 0.0037 | 1.77E+06 | | 30.00 | 6.67 | 30.00 | 4.5 | 1 | 2.050 | 6.667 |
| R=0.05 | Model | 1048 | 3.1E+05 | 52 | 31 | 48.6 | 2.67E+10 | 0.0075 | 1.24E+06 | | 42.96 | 9.55 | 42.96 | 4.5 | 1 | 1.000 | 9.547 |
| | | 1000 | 3.0E+05 | 50 | 30 | 48.6 | 2.67E+10 | 0.0083 | 1.18E+06 | | 45.00 | 10.00 | 45.00 | 4.5 | 1 | 0.911 | 10.000 |
| | | 500 | 1.5E+05 | 25 | 15 | 48.6 | 2.67E+10 | 0.0330 | 5.90E+05 | | 90.00 | 20.00 | 90.00 | 4.5 | 1 | 0.003 | 20.000 |
| | *Prototype* | *45000* | *3.0E+06* | *4500* | *2566* | *48.2* | *2.44E+12* | *0.0075* | *1.18E+07* | | - | - | - | - | - | - | - |
| | | 10000 | 3.0E+06 | 1000 | 570 | 48.2 | 2.67E+10 | 0.0001 | 1.18E+07 | | 4.50 | 1.00 | 4.50 | 4.5 | 1 | 91.125 | 1.000 |
| | | 1500 | 4.5E+05 | 150 | 86 | 48.2 | 2.67E+10 | 0.0037 | 1.77E+06 | | 30.00 | 6.67 | 30.00 | 4.5 | 1 | 2.050 | 6.667 |
| R=0.10 | Model | 1048 | 3.1E+05 | 105 | 60 | 48.2 | 2.67E+10 | 0.0075 | 1.24E+06 | | 42.96 | 9.55 | 42.96 | 4.5 | 1 | 1.000 | 9.547 |
| | | 1000 | 3.0E+05 | 100 | 57 | 48.2 | 2.67E+10 | 0.0083 | 1.18E+06 | | 45.00 | 10.00 | 45.00 | 4.5 | 1 | 0.911 | 10.000 |
| | | 500 | 1.5E+05 | 50 | 29 | 48.2 | 2.67E+10 | 0.0330 | 5.90E+05 | | 90.00 | 20.00 | 90.00 | 4.5 | 1 | 0.003 | 20.000 |
| | *Prototype* | *45000* | *3.0E+06* | *6750* | *3682* | *47.8* | *2.44E+12* | *0.0075* | *1.18E+07* | | - | | - | - | - | - | - |
| | | 10000 | 3.0E+06 | 1500 | 818 | 47.8 | 2.67E+10 | 0.0001 | 1.18E+07 | | 4.50 | 1.00 | 4.50 | 4.5 | 1 | 91.125 | 1.000 |
| | | 1500 | 4.5E+05 | 225 | 123 | 47.8 | 2.67E+10 | 0.0037 | 1.77E+06 | | 30.00 | 6.67 | 30.00 | 4.5 | 1 | 2.050 | 6.667 |
| R=0.15 | Model | 1048 | 3.1E+05 | 157 | 86 | 47.8 | 2.67E+10 | 0.0075 | 1.24E+06 | | 42.96 | 9.55 | 42.96 | 4.5 | 1 | 1.000 | 9.547 |
| | | 1000 | 3.0E+05 | 150 | 82 | 47.8 | 2.67E+10 | 0.0083 | 1.18E+06 | | 45.00 | 10.00 | 45.00 | 4.5 | 1 | 0.911 | 10.000 |
| | | 500 | 1.5E+05 | 75 | 41 | 47.8 | 2.67E+10 | 0.0330 | 5.90E+05 | | 90.00 | 20.00 | 90.00 | 4.5 | 1 | 0.003 | 20.000 |

Table-4.7: Test Matrix - Comparison of prototype and model parameters (H/D = 5)

| | | Chimney height - 2250 mm | | | | Model chimney height – 500 mm | | | | | Ratio between prototype and model | | | | | | |
|---|---|---|---|---|---|---|---|---|---|---|---|---|---|---|---|---|---|
| Bypass flow ratio | Prototype / Model | Core flow rate (lpm) | $Re_D$ | Bypass rate (lpm) | Heater power (kW) | Mix temp (ºC) | Gr | Ri | Pe | | Flow rate | $Re_D$ | Heater power | Chimney height | delta T | Ri | Pe |
| - | Prototype | 45000 | 3.0E+06 | 0 | 0 | 49.0 | 1.41E+12 | 0.0063 | 1.18E+07 | | - | - | - | - | - | - | - |
| | | 10000 | 3.0E+06 | 0 | 0 | 49.0 | 1.55E+10 | 0.0001 | 1.18E+07 | | 4.50 | 1.00 | - | 4.5 | 1 | 91.125 | 1.000 |
| | | 1500 | 4.5E+05 | 0 | 0 | 49.0 | 1.55E+10 | 0.0031 | 1.77E+06 | | 30.00 | 6.67 | - | 4.5 | 1 | 2.050 | 6.667 |
| R=0.00 | Model | 1048 | 3.1E+05 | 0 | 0 | 49.0 | 1.55E+10 | 0.0063 | 1.24E+06 | | 42.96 | 9.55 | - | 4.5 | 1 | 1.000 | 9.547 |
| | | 1000 | 3.0E+05 | 0 | 0 | 49.0 | 1.55E+10 | 0.0069 | 1.18E+06 | | 45.00 | 10.00 | - | 4.5 | 1 | 0.911 | 10.000 |
| | | 500 | 1.5E+05 | 0 | 0 | 49.0 | 1.55E+10 | 0.0275 | 5.90E+05 | | 90.00 | 20.00 | - | 4.5 | 1 | 0.003 | 20.000 |
| - | Prototype | 45000 | 3.0E+06 | 2250 | 1344 | 48.6 | 1.41E+12 | 0.0063 | 1.18E+07 | | - | | - | - | - | - | - |
| | | 10000 | 3.0E+06 | 500 | 299 | 48.6 | 1.55E+10 | 0.0001 | 1.18E+07 | | 4.50 | 1.00 | 4.50 | 4.5 | 1 | 91.125 | 1.000 |
| | | 1500 | 4.5E+05 | 75 | 45 | 48.6 | 1.55E+10 | 0.0031 | 1.77E+06 | | 30.00 | 6.67 | 30.00 | 4.5 | 1 | 2.050 | 6.667 |
| R=0.05 | Model | 1048 | 3.1E+05 | 52 | 31 | 48.6 | 1.55E+10 | 0.0063 | 1.24E+06 | | 42.96 | 9.55 | 42.96 | 4.5 | 1 | 1.000 | 9.547 |
| | | 1000 | 3.0E+05 | 50 | 30 | 48.6 | 1.55E+10 | 0.0069 | 1.18E+06 | | 45.00 | 10.00 | 45.00 | 4.5 | 1 | 0.911 | 10.000 |
| | | 500 | 1.5E+05 | 25 | 15 | 48.6 | 1.55E+10 | 0.0275 | 5.90E+05 | | 90.00 | 20.00 | 90.00 | 4.5 | 1 | 0.003 | 20.000 |
| - | Prototype | 45000 | 3.0E+06 | 4500 | 2566 | 48.2 | 1.41E+12 | 0.0063 | 1.18E+07 | | - | - | - | - | - | - | - |
| | | 10000 | 3.0E+06 | 1000 | 570 | 48.2 | 1.55E+10 | 0.0001 | 1.18E+07 | | 4.50 | 1.00 | 4.50 | 4.5 | 1 | 91.125 | 1.000 |
| | | 1500 | 4.5E+05 | 150 | 86 | 48.2 | 1.55E+10 | 0.0031 | 1.77E+06 | | 30.00 | 6.67 | 30.00 | 4.5 | 1 | 2.050 | 6.667 |
| R=0.10 | Model | 1048 | 3.1E+05 | 105 | 60 | 48.2 | 1.55E+10 | 0.0063 | 1.24E+06 | | 42.96 | 9.55 | 42.96 | 4.5 | 1 | 1.000 | 9.547 |
| | | 1000 | 3.0E+05 | 100 | 57 | 48.2 | 1.55E+10 | 0.0069 | 1.18E+06 | | 45.00 | 10.00 | 45.00 | 4.5 | 1 | 0.911 | 10.000 |
| | | 500 | 1.5E+05 | 50 | 29 | 48.2 | 1.55E+10 | 0.0275 | 5.90E+05 | | 90.00 | 20.00 | 90.00 | 4.5 | 1 | 0.003 | 20.000 |
| - | Prototype | 45000 | 3.0E+06 | 6750 | 3682 | 47.8 | 1.41E+12 | 0.0063 | 1.18E+07 | | - | | - | - | - | - | - |
| | | 10000 | 3.0E+06 | 1500 | 818 | 47.8 | 1.55E+10 | 0.0001 | 1.18E+07 | | 4.50 | 1.00 | 4.50 | 4.5 | 1 | 91.125 | 1.000 |
| | | 1500 | 4.5E+05 | 225 | 123 | 47.8 | 1.55E+10 | 0.0031 | 1.77E+06 | | 30.00 | 6.67 | 30.00 | 4.5 | 1 | 2.050 | 6.667 |
| R=0.15 | Model | 1048 | 3.1E+05 | 157 | 86 | 47.8 | 1.55E+10 | 0.0063 | 1.24E+06 | | 42.96 | 9.55 | 42.96 | 4.5 | 1 | 1.000 | 9.547 |
| | | 1000 | 3.0E+05 | 150 | 82 | 47.8 | 1.55E+10 | 0.0069 | 1.18E+06 | | 45.00 | 10.00 | 45.00 | 4.5 | 1 | 0.911 | 10.000 |
| | | 500 | 1.5E+05 | 75 | 41 | 47.8 | 1.55E+10 | 0.0275 | 5.90E+05 | | 90.00 | 20.00 | 90.00 | 4.5 | 1 | 0.003 | 20.000 |

# Chapter 5

# Testing of Scaling Philosophy

## 5.1 Introduction

Testing of scaling philosophy is examined by carrying out simulations on the chimney models and comparing the results with that of the prototype. Numerical simulations are performed for the chimney model with 45º nozzle inclination considering a mass flow rate of 8.33 kg/s for the upward flowing hot water from the core, which corresponds to Reynolds number of $1.5 \times 10^5$. Ratios of the downward flow and the upward flow i.e., the bypass flow ratios considered in the simulations are 0.0, 0.05, 0.10 and 0.15. The effects of the bypass flow ratio and the chimney height on the velocity and temperature distribution inside three-dimensional chimney structure are evaluated. Analyses are also done by increasing the flow rate through the core (i.e., upward flow) to cover a range of Reynolds number ($1.5 \times 10^5 \leq Re_D \leq 4.5 \times 10^5$) to understand the effect of Reynolds number on mixing of hot and cold opposing flows inside the chimney. Subsequently nozzle inclinations are also varied to 35º and 25º to predict its effect on mixing behaviour. Finally non-dimensionalisation of the results is done to compare the numerical results obtained for the prototype mentioned in chapter 3.

## 5.2 Hydrodynamic Model

The geometrical model considered for computation has the same dimensions of the chimney model to be used for the experiments. However, free surface modeling at the interface between pool water and air at the top is not modelled considering larger pool water depth above the chimney top. Figure 5.1 depicts the computational domain (750 mm × 1000 mm × 250 mm) in x, y and z directions respectively used for the model simulated.

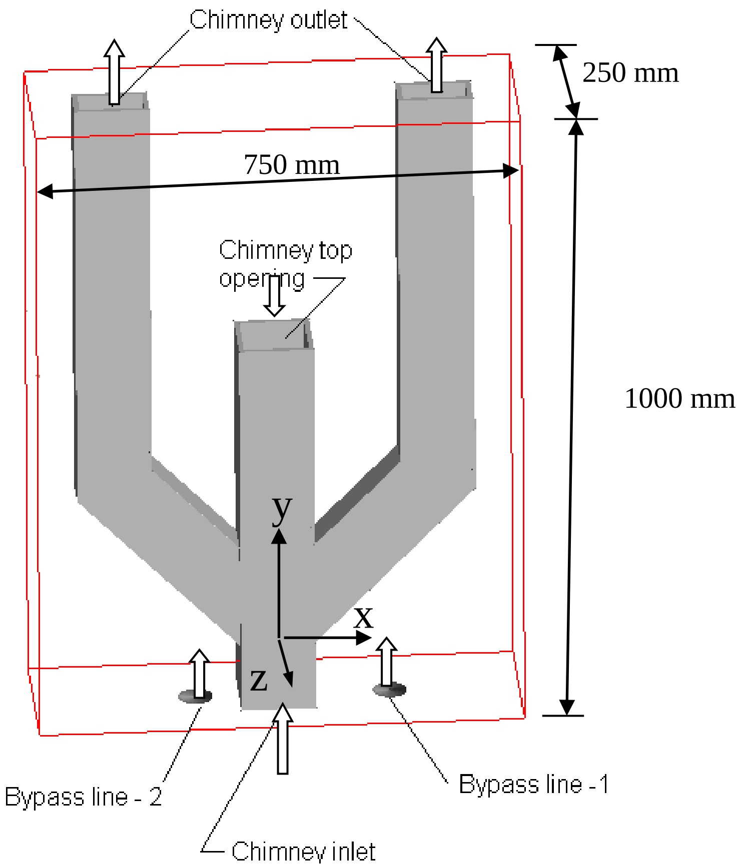


Fig. 5.1: Computational model

To simulate turbulent flow, various models are developed to determine the eddy viscosity of which the standard k-ε model has been widely used due to its robustness, economy and reasonable accuracy for various industrial flow problems. The standard k-ε model was proposed by Harlow and Nakayama (1968). The standard high Reynolds number form of k-ε model presented by Launder and Spalding (1974) is used in the simulation. Equilibrium log-law wall function is used in the simulation. The eddy viscosity ($\nu_t$) is computed as a function of k and ε as given in section 3.2 of earlier chapter. Constants in the standard k-ε model used in the simulation are shown in Table-5.1.

Table-5.1: Values of constants for turbulence model

| Constants | $c_\mu$ | $c_{1\varepsilon}$ | $c_{2\varepsilon}$ | $\sigma_k$ | $\sigma_\varepsilon$ |
|---|---|---|---|---|---|
| Values | 0.09 | 1.44 | 1.92 | 1.0 | 1.3 |

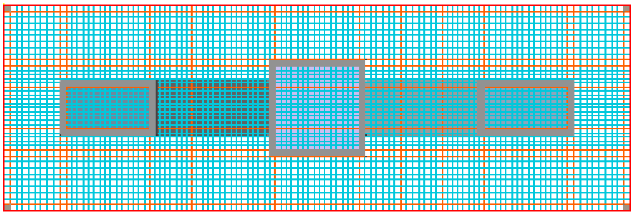

(a) Top view (x-z plane)

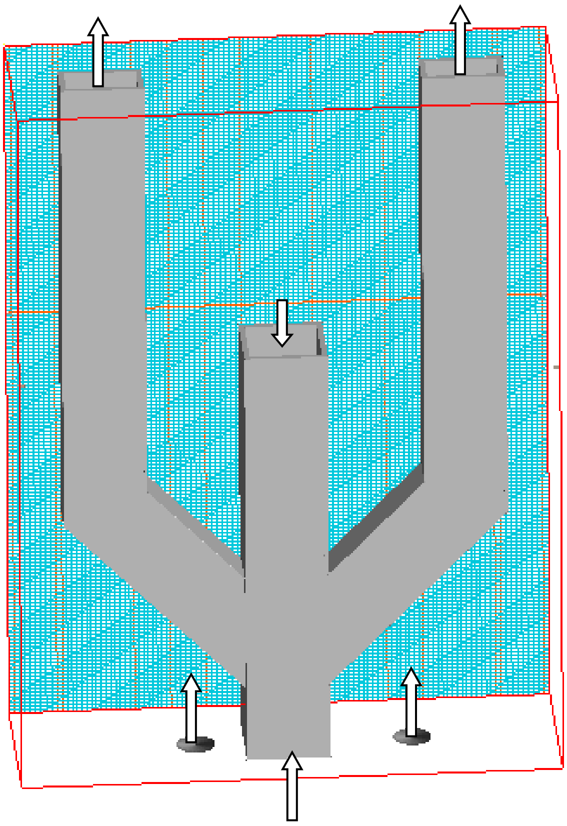

(b) Isometric view (mesh in x-y plane)

Fig. 5.2: Mesh for computation

## 5.3 Boundary Conditions

At the inlet, the flow rate of the fluid is specified considering uniform velocity profile and the direction of flow velocity is defined normal to the boundary. The values of the turbulent kinetic energy ($k$) and turbulence dissipation rate ($\varepsilon$) are prescribed at the inlet. The $k$ value is represented in terms of the turbulence intensity which typically falls in the range of 1% to 5%. In the simulation, the turbulence intensity is assumed to be 5%. The turbulence dissipation rate ($\varepsilon$) depends on turbulent kinetic energy ($k$) and mixing length ($l_m$) as shown in the following equation. Mixing length is assumed to be 10% of the characteristic inlet dimension (i.e., hydraulic radius for the inlet pipe) for all these simulations.

$$\varepsilon = 0.1643 \frac{k^{3/2}}{l_m} \qquad \text{..... (5.1)}$$

At the outlet, constant pressure boundary condition is applied. At each wall, no-slip boundary condition is imposed. Temperature at inlet of the core flow is specified to be 49°C. For core bypass flows at the inlet of two nozzles, temperature is specified to be 40°C.

Simulations are carried out considering mesh size of 110 × 200 × 40. Figure 5.2 shows the mesh in the x-z and x-y plane used for the entire domain. Simulations are carried out using two different mesh sizes - (110 × 200 × 40) and (142 × 260 × 50). No significant differences are observed.

## 5.4 Results and Discussion

The flow and temperature distribution for the case with core flow of 8.33 kg/s (~500 lpm) are described in detail in the following subsections. Basic objectives of these simulations are to find out the stagnation height and pool temperature front height, which are explained for this case. Subsequently, core flow of 16.66 kg/s (~1000 lpm) and 25 kg/s (~1500 lpm) are analysed to see the effect of core flow on velocity and temperature distribution. The chimney height (H) is also varied from 0.6 m to 0.5 m to see its effect. Finally non-dimensionalisation of the results is done to compare the results.

### Core flow – 8.33 kg/s

Upward flow ($W_{in}$) through the chimney bottom inlet is 8.33 kg/s. The temperature at the inlet ($T_{in}$) is 49°C. The bypass flow ratio (R) is varied to 0, 0.05, 0.10 and 0.15 respectively to estimate the effect of core bypass flow on the mixing characteristics inside the chimney.

The inlet temperature of bypass flow ($W_b$) is 40°C, i.e., same as the pool temperature ($T_p$). Chimney height (H) is 0.6 m.

**Velocity distribution:** The velocity field inside the chimney with no core bypass (i.e., R = 0) is shown in Fig. 5.3. Velocity distribution in the x-y plane (at z = 0) and y-z plane (at x = 0) respectively are shown in Fig. 5.3a and 5.3b. Through central square chimney, the upward velocity is observed up to a certain height in Fig. 5.3a. The water jet with two vortices is observed in Fig. 5.3b.

To clearly observe the flow distribution inside square chimney, velocity vector plots in x-y plane and y-z plane for the central chimney region are shown in Fig. 5.3c and Fig. 5.3d respectively. The results are shown from y = 0.16 m to the chimney top (i.e., y = 0.6 m). In the lower most region of Fig. 5.3c, the velocity vectors show upward flow direction along with tendency towards two side outlet openings. Above this region asymmetrical circulation with lower velocity is observed. Figure 5.3d shows how the upward jet takes a turn from both sides to move downward. It is also observed that downward flow through the top opening of the chimney takes place in the central region. Since there is no net flow provided to the top opening of the chimney, upward flow takes place through the peripheral region in order to maintain the flow balance. This upward flow through the top opening of the chimney is not acceptable because it will cause radioactive water to reach from the core outlet to the pool. Therefore, bypass flow ratio is increased to 0.05, 0.10 and 0.15 to observe their effects in keeping the radioactive water well within the chimney region.

The velocity distribution in x-y plane and y-z plane for R=0.05 are shown in Fig. 5.4a and Fig. 5.4b respectively. Velocity vector plots are shown in Fig. 5.4c and Fig. 5.4d. Because of additional bypass flow through the chimney top opening in the downward direction, velocity in the side outlet nozzles increases as shown in Fig. 5.4a. In Fig. 5.4b, the upward jet and vortex formed are observed. The stagnation height is found to be less than that observed for the case with R =0.0. Length of the two vortices is also observed to be less. This is clearly visible in the velocity vector plot of y-z plane shown in Fig. 5.4d. Comparing

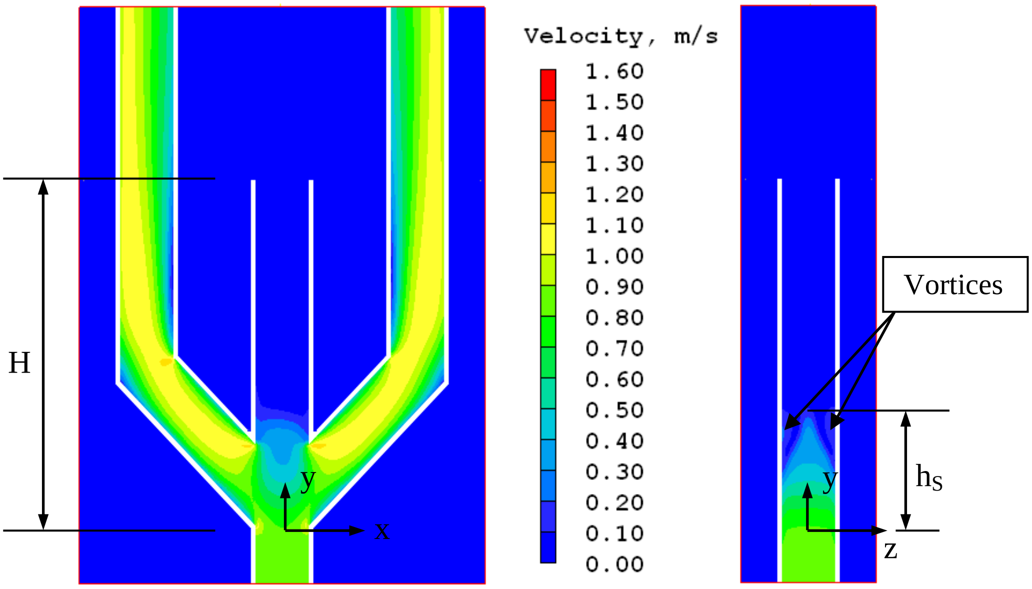


(a) x-y plane (z=0) (b) y-z plane (x=0)

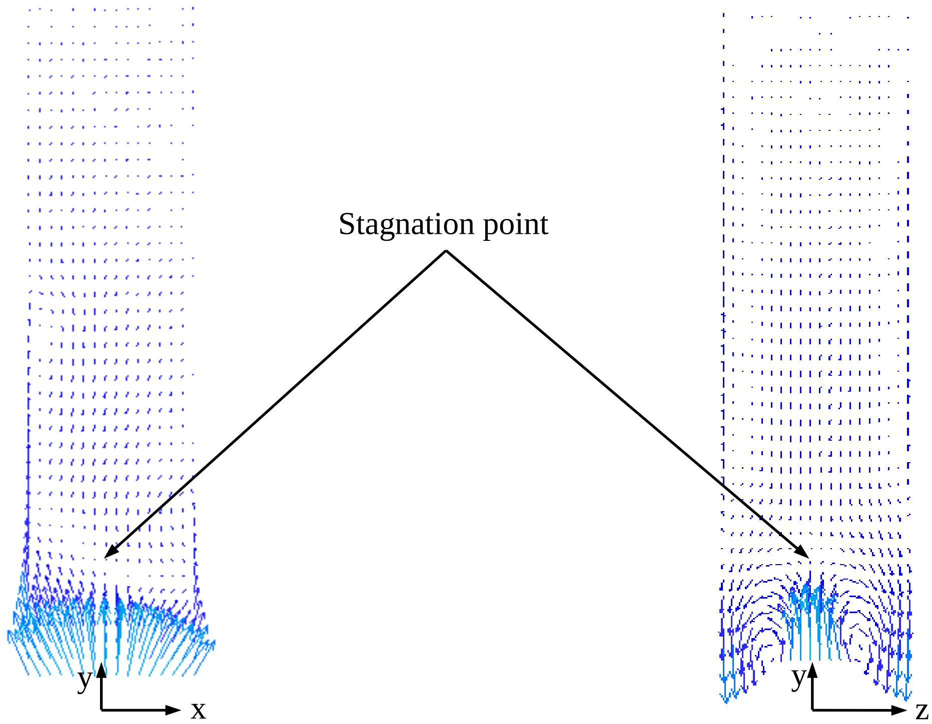


(c) x-y plane (z=0) (d) y-z plane (x=0)

Fig. 5.3: Velocity distribution (R = 0.0)

Fig. 5.3d and Fig. 5.4d, it is observed that the extent of the upward velocity region is also reduced. The downward flow velocity at the top of the chimney throughout the whole square cross section is observed in Fig. 5.4c and Fig. 5.4d. Therefore, in this case no radioactive water is able to reach the pool top. Now, the extent of suppression of upward jet due to increase in flow ratio is further analysed by varying R to 0.10 and 0.15.

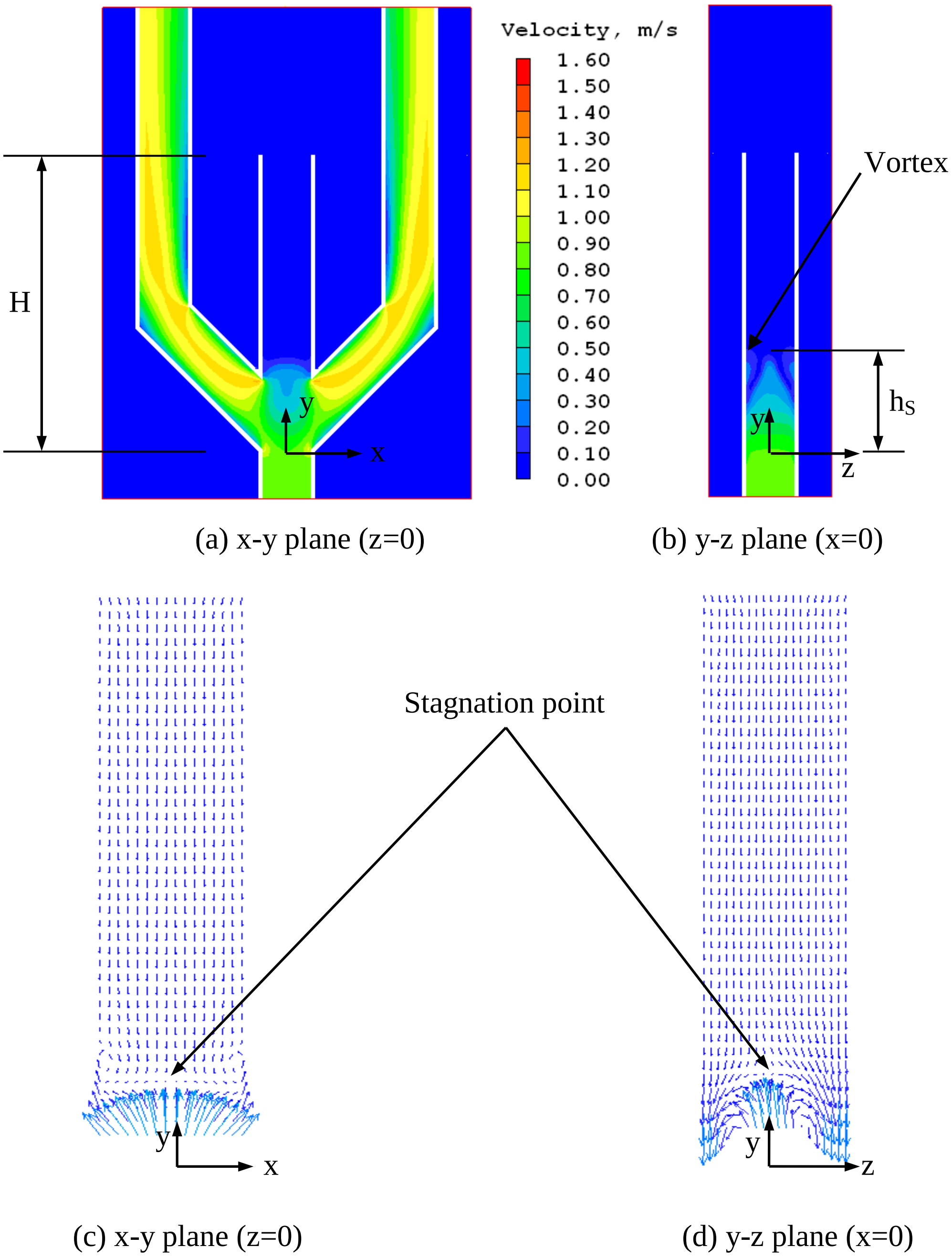


Fig. 5.4: Velocity distribution (R = 0.05)

The results for bypass flow ratio 0.10 and 0.15 are shown in Fig. 5.5 and Fig. 5.6 respectively. The increase in downward flow is clearly visible in the velocity contour plots of x-y plane which show the increase in velocity and their distribution near the bottom region of the pool of Fig 5.5a and Fig. 5.6a. This additional bypass flow when sucked in through the top of the chimney suppresses the upward velocity as observed in figures 5.5c, 5.5d, 5.6c and 5.6d.

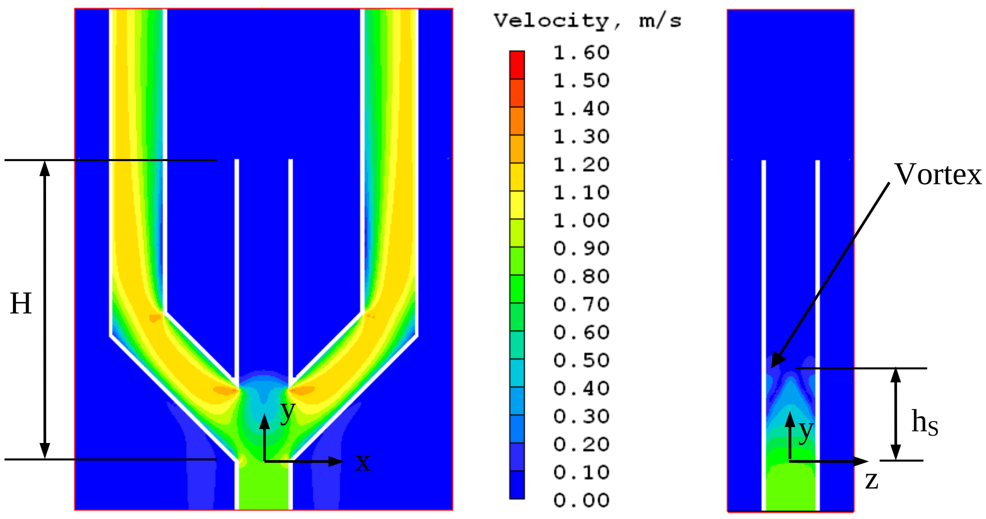


(a) x-y plane (z=0) (b) y-z plane (x=0)

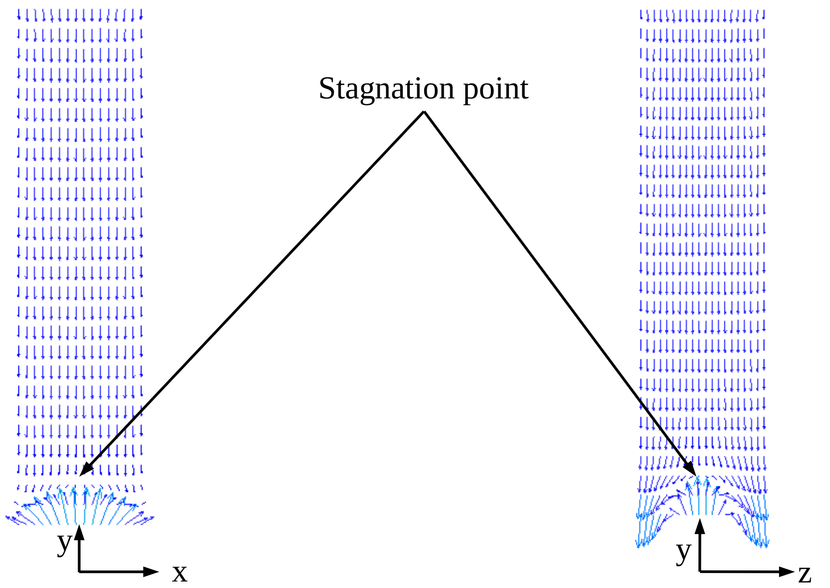


(c) x-y plane (z=0) (d) y-z plane (x=0)

Fig. 5.5: Velocity distribution (R = 0.10)

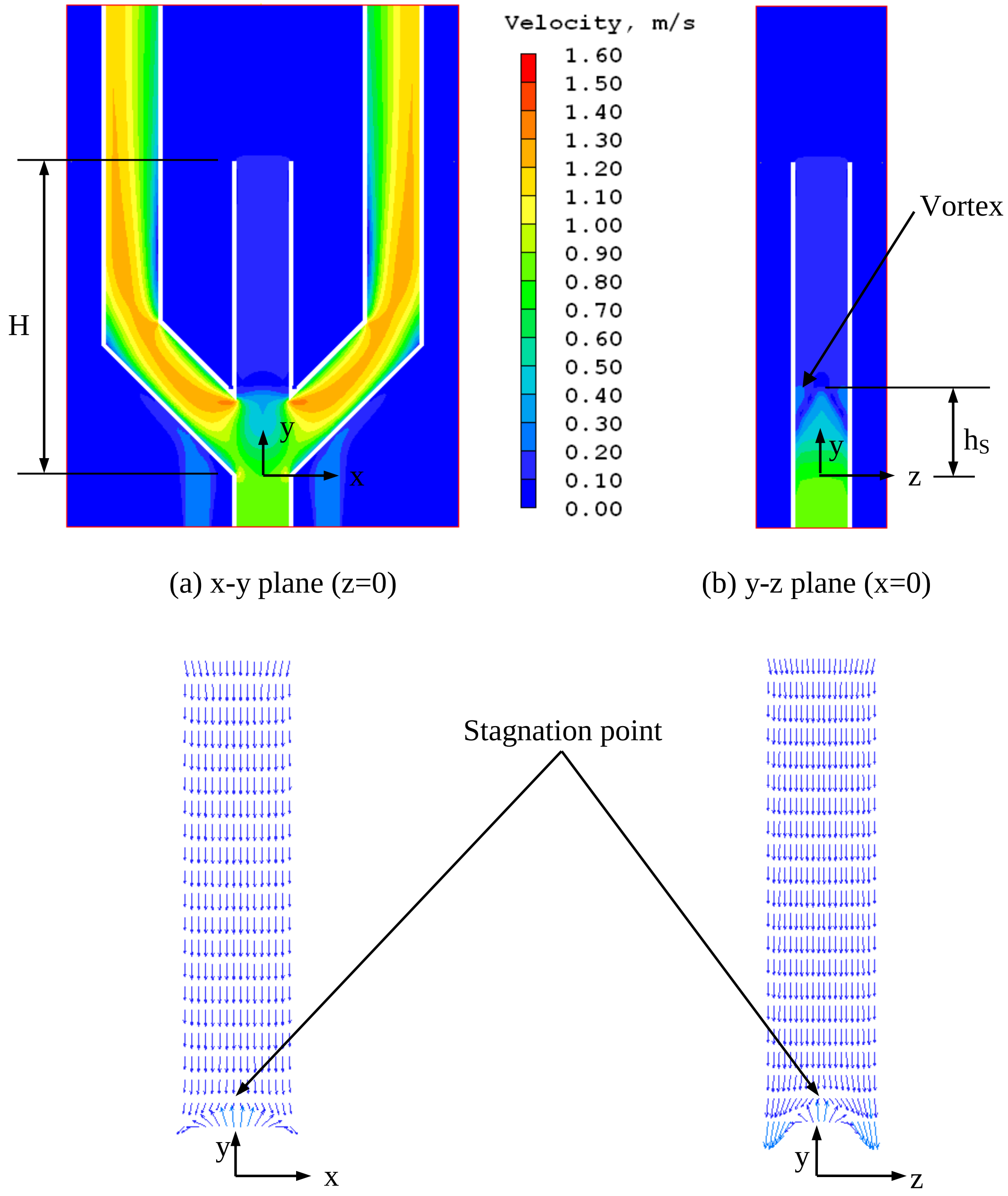


(a) x-y plane (z=0) (b) y-z plane (x=0)

(c) x-y plane (z=0) (d) y-z plane (x=0)

Fig. 5.6: Velocity distribution (R = 0.15)

It is observed from the magnitude of the velocity vector plots of Fig. 5.3 to Fig. 5.6 that the upward jet velocity is reduced as the downward velocity through the top chimney is increased. This is because of the higher downward momentum of larger bypass flow, the core outlet flow gets diverted towards the side outlet nozzles more effectively and thereby reduces the upward jet velocity. This in turn causes the stagnation height to reduce. In order to quantify the stagnation height, the centre line velocity of the chimney is plotted against the vertical axis (y) of the chimney.

The variation of upward flow velocity (i.e., y-component of the water velocity) at the centre line of square cross section of the chimney along the vertical axis of the chimney is shown in Fig. 5.7 (for bypass flow ratios of 0.0, 0.05, 0.10 and 0.15). The upward flow velocity at the bottom inlet of the chimney (at y = -0.1 m) is about 0.83 m/s. At y =0.0 m, the chimney side outlet nozzle opening starts. With further increase in y, flow moves towards side outlet nozzles and upward velocity decreases. Up to y = 0.105 m, the velocity variation is the same for all the bypass cases. At higher value of y, the velocity variation depends on the core bypass flow.

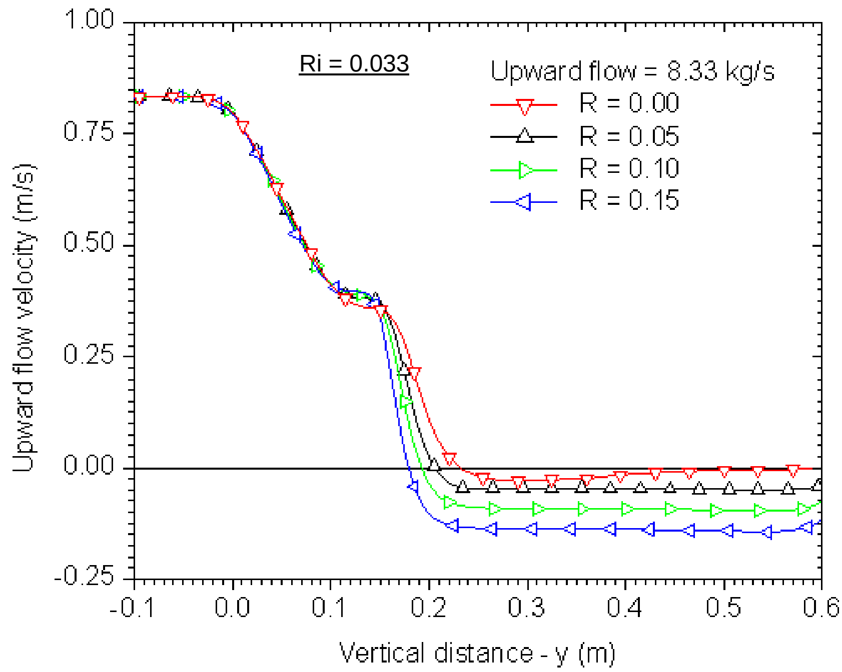


Fig. 5.7: Centre line velocity distribution along y-direction

It is observed from Fig. 5.7 that velocity decreases and reaches zero. Beyond this point, velocity becomes negative, i.e., downward velocity is observed. The value of y where upward velocity ($v_y$) is zero is defined as the stagnation height. The stagnation height ($h_S$) is 0.238 m when R is 0.0. The stagnation height decreases to 0.179 m when R is increased to

0.15. It is observed from the figure that stagnation height decreases with increase in core bypass flow.

**Temperature Distribution:** When bypass flow ratio R is 0.0, the hot water at 49°C from core outlet moves upward through the peripheral region as explained in previous subsection and it is observed that the pool temperature stabilises at 49°C. This indirectly indicates that pool water will attain the radioactivity level of core outlet water if it is assumed that temperature is acting as an indirect way of radiotracer. The temperature contour plots for R = 0.05, 0.10 and 0.15 are shown in Fig. 5.8 to Fig. 5.10. It is observed that with increase in bypass flow ratio, the temperature at the vertical arm of the side outlet nozzles decreases. The temperature distribution at the outlet section is shown in Fig. 5.8a, 5.9a and 5.10a. The variation of temperature from the inner face to the outer face is more when bypass flow ratio is more. This is because more amount of cold fluid (at 40°C) entering through the chimney and it moves out of the chimney preferentially towards the inner walls of the vertical arms of the chimney. Hot water (at 49°C) moves out of the chimney towards the outer wall of the chimney.

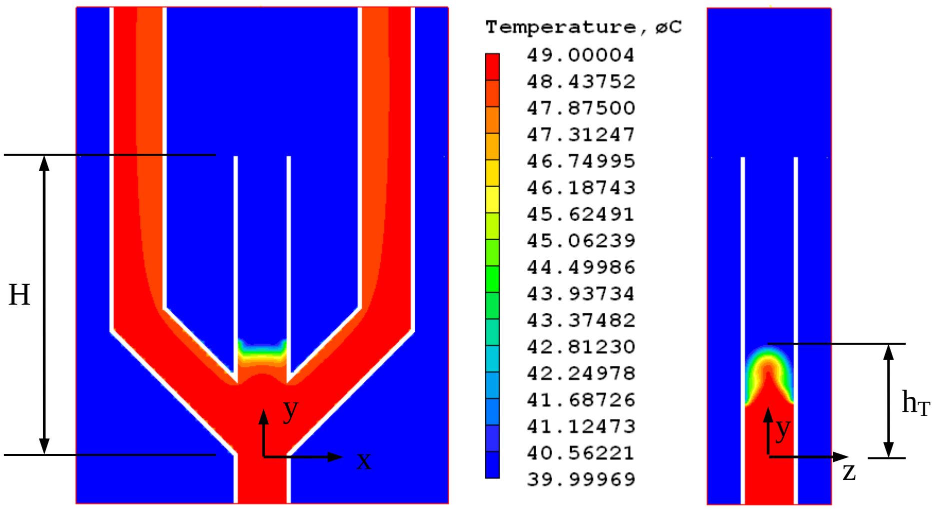


(a) x-y plane (b) y-z plane

Fig. 5.8: Temperature distribution (R = 0.05)

It is also observed that hot water penetration into the chimney becomes less with increase in core bypass flow. Due to sucking of pool water through the top of the chimney, pool water front (at 40°C) reaches inside chimney. The maximum depth upto which the temperature front of pool water will reach can be thought as the location above which hot water of core outlet does not have any effect. The value of y at this location is defined as the pool temperature front height ($h_T$). From the figures it is observed that with increase in bypass flow, the pool temperature front height decreases. To quantify these values, centre line water temperature variation is plotted along the vertical axis of the chimney.

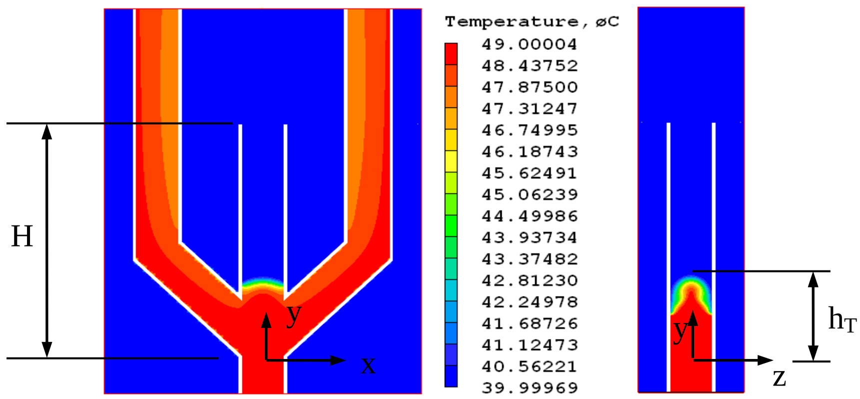


(a) x-y plane (b) y-z plane

Fig. 5.9: Temperature distribution (R = 0.10)

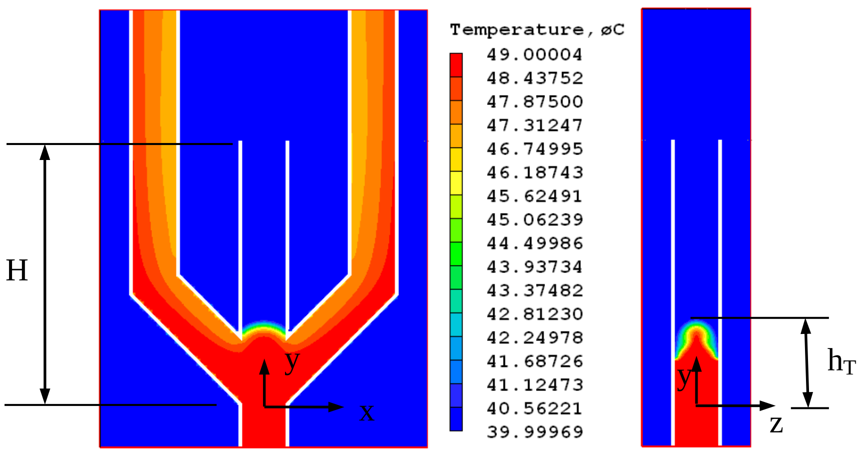


(a) x-y plane (b) y-z plane

Fig. 5.10: Temperature distribution (R = 0.15)

The water temperature variation along the central axis of the square chimney with respect to the vertical distance of chimney is shown in Fig. 5.11. At the entry of the chimney, the water temperature is 49°C. When R = 0.0, this same temperature of water is observed throughout the chimney height. For other bypass flow cases, this temperature is observed up to y = 0.115 m. At higher y values, the temperature depends on the core bypass flow. When bypass flow ratio is more, the temperature drops at a faster rate. With bypass flow ratio R = 0.05, temperature front height is 0.226 m. With increase in flow ratio 0.15, the temperature front height reduces to 0.194 m.

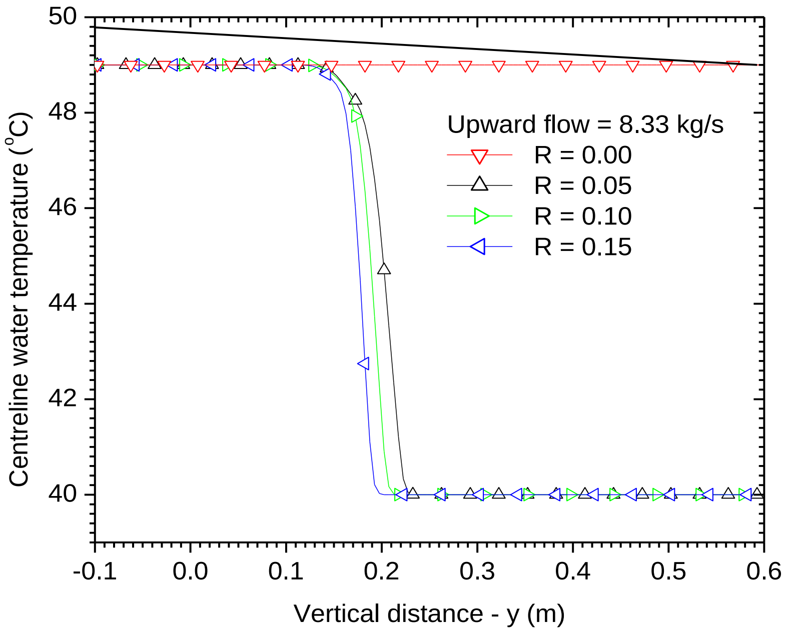


Fig. 5.11: Centre line temperature distribution along y-direction

### 5.4.1 Effect of Core Flow on velocity distribution

To understand the effect of core flow variation on velocity distribution inside the chimney, core flow is increased to 16.67 and 25 kg/s. The Reynolds numbers corresponding to these core flows are $3.0 \times 10^5$ and $4.5 \times 10^5$ respectively. Figure 5.12 shows the velocity variation with the vertical chimney height for core flow of 16.67 kg/s. At the bottom of the chimney flow velocity is about 1.67 m/s, which gradually decreases with chimney height. For bypass flow ratio zero, the velocity becomes zero at y = 0.236 m and for R = 0.15, it occurs at y = 0.176 m.

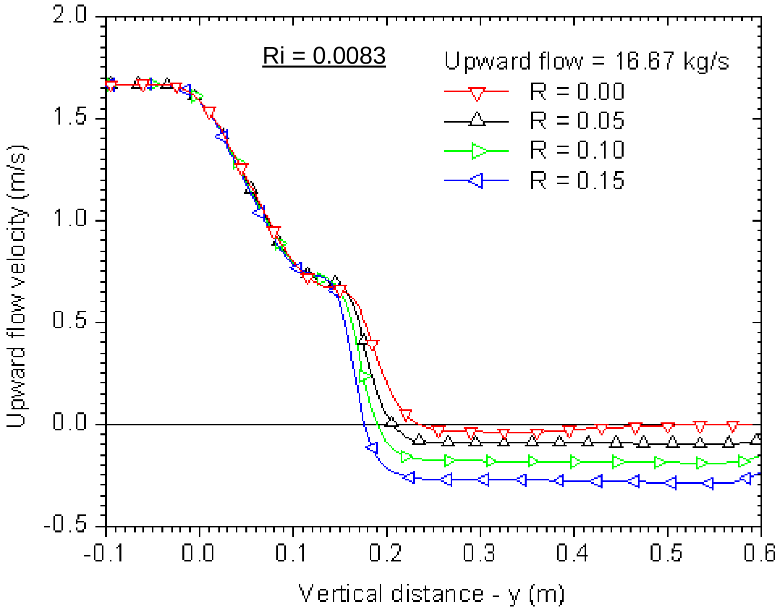


Fig. 5.12: Centre line velocity distribution along y-direction (upward flow = 16.67 kg/s)

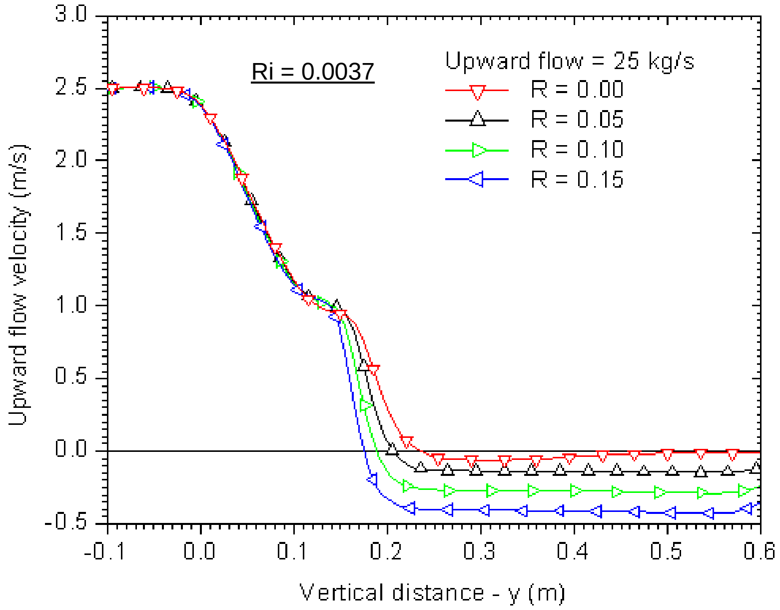


Fig. 5.13: Centre line velocity distribution along y-direction (upward flow = 25 kg/s)

The upward velocity variation along the central axis of the chimney for core flow of 25 kg/s is shown in Fig. 5.13. The inlet upward flow velocity of 2.5 m/s reduces to zero at y = 0.235 m for R = 0.0 and it occurs at y = 0.176 m for R = 0.15.

### 5.4.2 Effect of Core Flow on temperature distribution

Variations of water temperature along the central axis of the square chimney for core flow of 16.66 and 25 kg/s are shown in Fig. 5.14. It is observed that the trend of temperature variation is similar. In case bypass flow ratio (R) is 0.0, i.e., no bypass flow; entire chimney and the reactor pool water temperature stabilizes at 49°C. When core bypass flow is provided, it is observed that hot water at 49°C mixes with the cold water (at 40°C) of the pool inside the chimney. When bypass flow ratio is 0.05, pool temperature front heights are observed to be 0.230 m and 0.231 m for core flow of 16.66 and 25 kg/s respectively. With bypass flow ratio of 0.15, the pool temperature front heights reduce to 0.195 m and 0.194 m. Therefore, the pool temperature front height decreases with increase in bypass flow ratio.

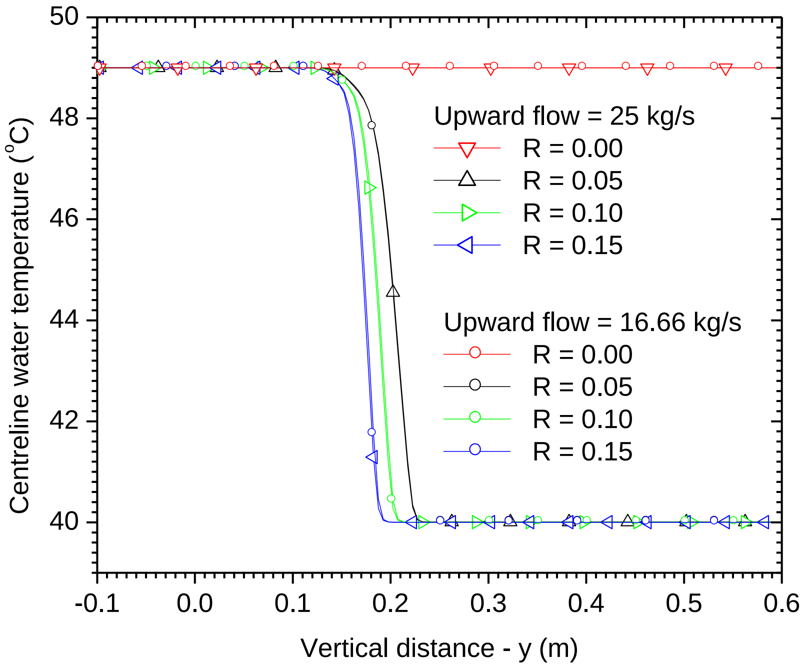


Fig. 5.14: Effect of flow on centre line temperature distribution

### 5.4.3 Non-dimensionalisation

To consolidate all the above results, the output results are represented in the dimensionless form. The velocity is non-dimensionalised with the reference inlet velocity ($U_{in}$) at the bottom inlet of the chimney. The chimney vertical distance is non-dimensionalised with respect to the side (D) of square chimney. The upward dimensionless velocity ($v_y$ / $U_{in}$) variation along the central axis of the chimney with dimensionless vertical distance (y/D) is shown in Fig. 5.15. It is clearly observed from the figure that the trends of velocity variation follow the same pattern for the Reynolds number range covered in the analysis when the bypass flow ratio R is kept the same.

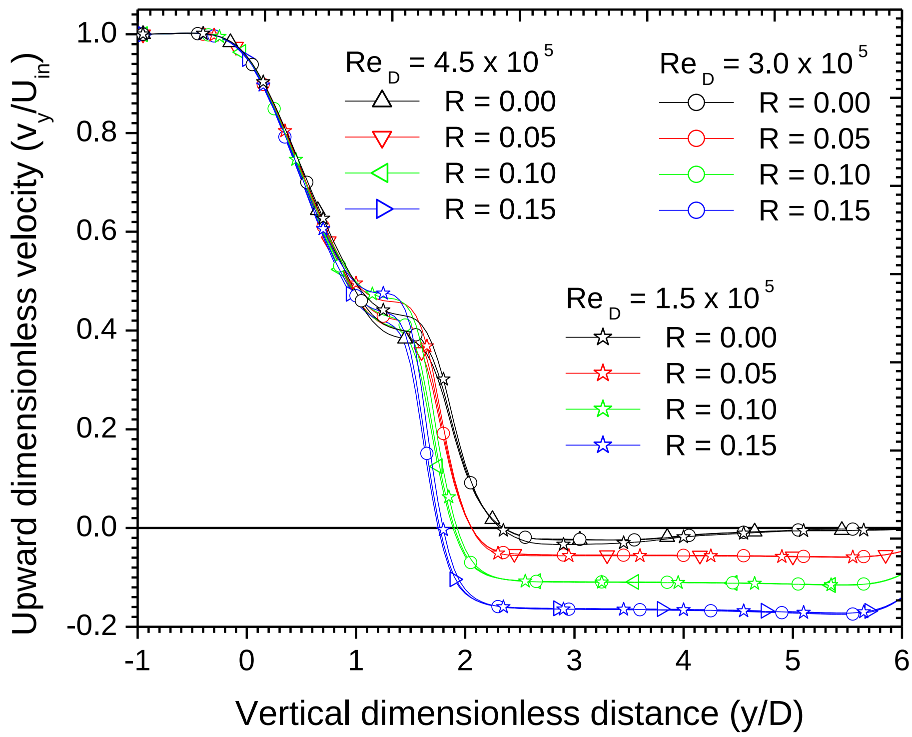


Fig. 5.15: Dimensionless centre line velocity distribution

Similarly dimensionless water temperature variation on the central axis of the chimney with respect to dimensionless vertical distance is shown in Fig. 5.16. Temperature is non-dimensionalised considering pool temperature as the reference temperature. From the results, it is observed that temperature variation follows the similar behavior, once the bypass flow ratio (R) is maintained.

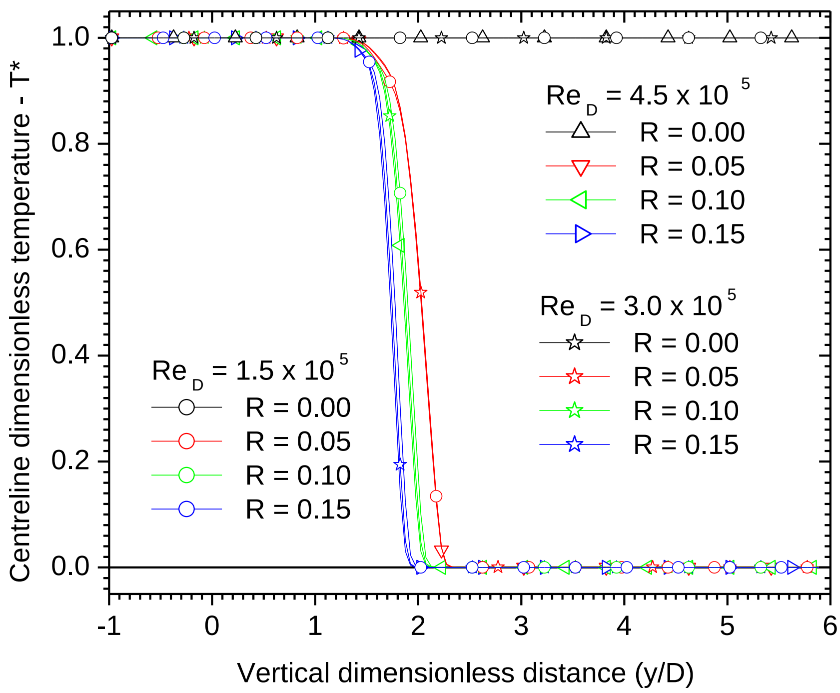


Fig. 5.16: Dimensionless centre line temperature distribution

### 5.4.4 Effect of Chimney Height

In order to understand the effect of chimney height (H) on the mixing behaviour of the opposing jets, the height (H) is reduced from 0.6 m to 0.5 m. The dimensionless results for both these cases (H/D =6 and H/D = 5) are shown in Fig. 5.17 and Fig. 5.18.

The dimensionless upward centre line velocity variation along the dimensionless distance is shown in Fig. 5.17. The results show that the stagnation height, where the upward velocity becomes zero, does not change significantly due to change in chimney height. Some variation is observed near to the top opening of the chimney. The velocity is smaller near the topmost end because the velocity is almost uniform at the entry of top chimney. With progression along the flowing length in the downward direction, the downward flow velocity at the centre line increases due to the surrounding wall effect of the chimney. This trend of velocity variation is observed for both the chimney heights. It is also observed that the centre line velocity distribution mainly depends on bypass flow ratio between two opposing flows. The centreline dimensionless temperature variation of water in the square chimney is shown in Fig. 5.18. It is observed that the effect of chimney height (H) on temperature distribution is insignificant. Therefore, it is clear from the figure that the height up to which pool temperature front can reach will not change by varying the chimney height.

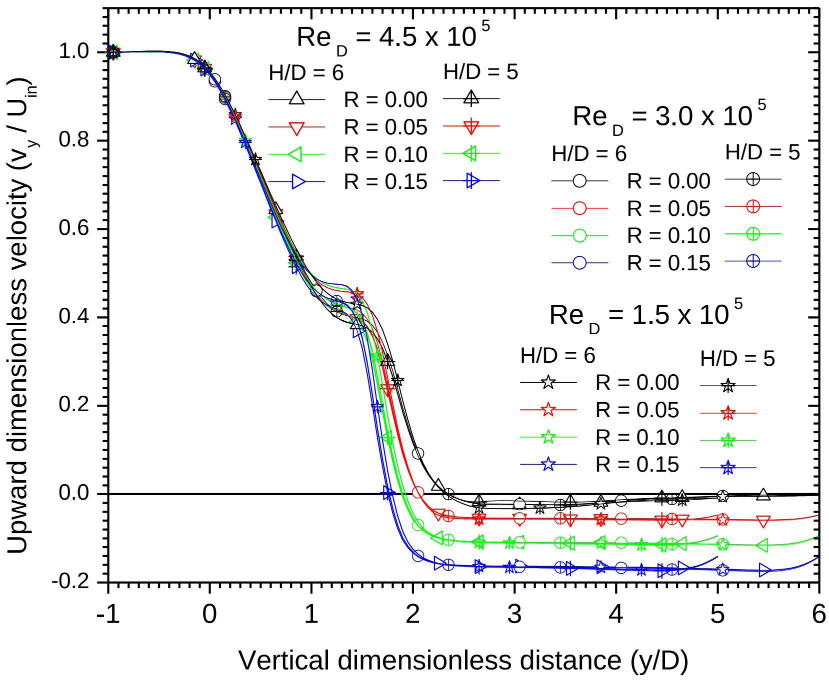


Fig. 5.17: Effect of chimney height and flow on centre line velocity distribution

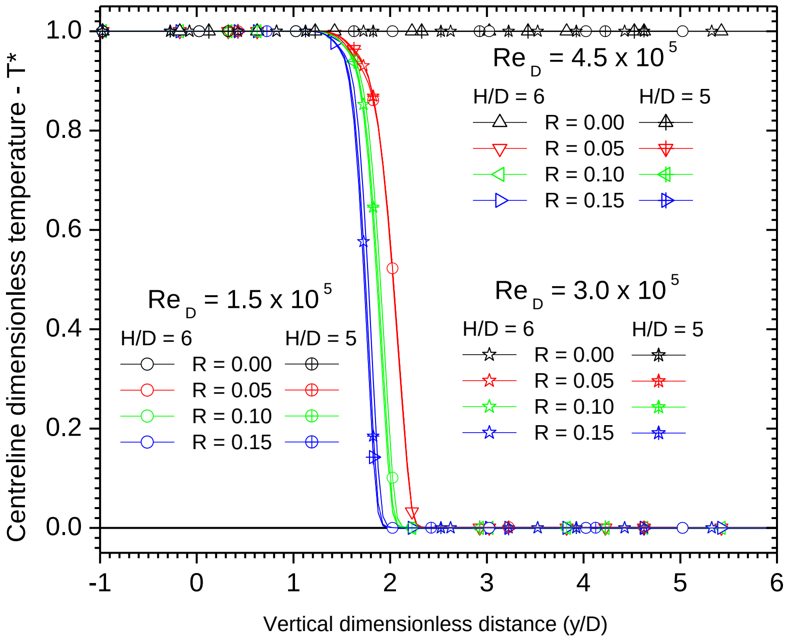


Fig. 5.18: Effect of chimney height and flow on centre line temperature distribution

### 5.4.5 Effect of nozzle inclination

Numerical simulations are carried out by changing the nozzle inclination from 45° to 35° and 25°. The modeling and results are discussed in the flowing subsections.

#### 5.4.5.1 Nozzle inclination - 35°

The chimney model with 35° inclination and height (H) of 600 mm is considered for CFD simulation. Analyses have been carried out considering core flow of 12.5, 16.67, 20.83 and 25 kg/s. The dimensionless numbers for the model for which the numerical simulations are carried out are shown in Table-5.2. Computational domain (750 mm × 1000 mm × 250 mm) in the x-z and x-y plane showing the mesh (110 × 200 × 40) for the entire domain is shown in Fig. 5.19.

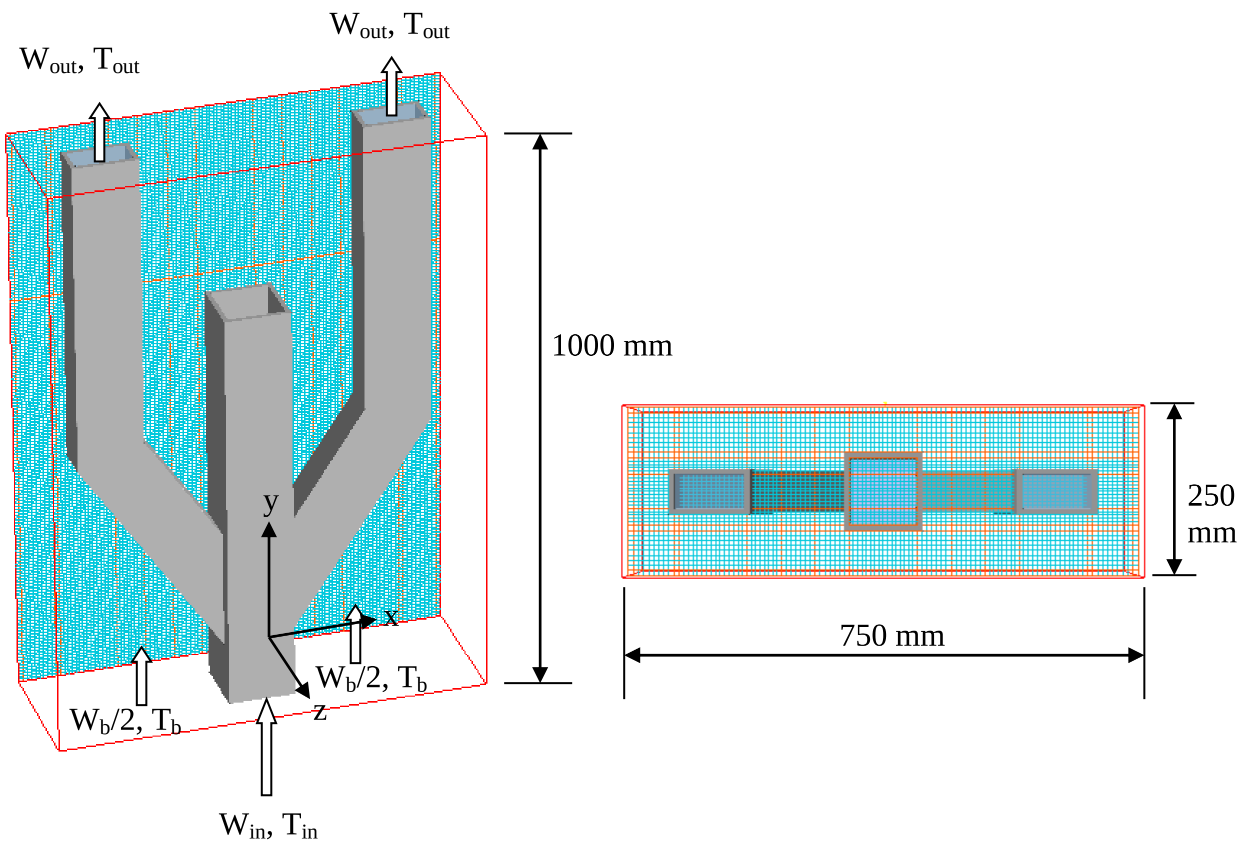


(a) Mesh in x-y plane (b) Mesh in x-y plane

Fig. 5.19: Mesh used for computation domain (θ=35°, H=0.6 m)

Table-5.2: Dimensionless numbers for chimney model with 35° nozzle inclination

| Sr. No. | $W_{in}$ (kg/s) | $U_{in}$ (m/s) | $Re_D$ | Ri | Bypass flow ratio (R) | Bypass flow entering chimney -$W_b$ (kg/s) | Downward velocity $U_b$ (m/s) |
|---|---|---|---|---|---|---|---|
| 1 | 12.5 | 1.25 | $2.25\times10^{5}$ | 0.01468 | 0.0 | 0.00 | 0.000 |
| 2 | | | | | 0.05 | 0.63 | 0.063 |
| 3 | | | | | 0.10 | 1.25 | 0.125 |
| 4 | | | | | 0.15 | 1.88 | 0.188 |
| 5 | 16.67 | 1.667 | $3.0\times10^{5}$ | 0.00826 | 0.0 | 0.00 | 0.000 |
| 6 | | | | | 0.05 | 0.83 | 0.083 |
| 7 | | | | | 0.10 | 1.67 | 0.167 |
| 8 | | | | | 0.15 | 2.50 | 0.250 |
| 9 | 20.83 | 2.083 | $3.75\times10^{5}$ | 0.00528 | 0.0 | 0.00 | 0.000 |
| 10 | | | | | 0.05 | 1.04 | 0.104 |
| 11 | | | | | 0.10 | 2.08 | 0.208 |
| 12 | | | | | 0.15 | 3.13 | 0.313 |
| 13 | 25 | 2.500 | $4.5\times10^{5}$ | 0.00367 | 0.0 | 0.00 | 0.000 |
| 14 | | | | | 0.05 | 1.25 | 0.125 |
| 15 | | | | | 0.10 | 2.50 | 0.250 |
| 16 | | | | | 0.15 | 3.75 | 0.375 |

**<u>Results and Discussion</u>**

The flow pattern and temperature distribution contours for the case with core flow of 12.5 kg/s are described in details in the following subsections. Basic objectives of these simulations are to find out the stagnation height and temperature front height for 35° inclination, which are explained for this case. Subsequently, similar procedure is adopted to find these parameters for the core flow of 16.66, 20.83 and 25 kg/s. Finally non-dimensionalisation of the results is also done for all these cases.

**Core flow – 12.5 kg/s**

Upward flow ($W_{in}$) through the chimney bottom inlet is assumed to be 12.5 kg/s. The Reynolds number corresponding to this flow is $2.25 \times 10^5$. The temperature at the inlet is 49°C. The core bypass flow is varied to 0, 0.63, 1.25 and 1.88 kg/s respectively.

<u>Velocity distribution for 0% core bypass</u>

The flow pattern inside the chimney with no core bypass (R=0.0) is shown in Fig. 5.20 and Fig. 5.21. Figures 5.20a and 5.20b show the velocity distribution in the x-y plane (at z = 0) and y-z plane (at x = 0) respectively. In this case, no flow is sent to the pool and therefore, the core flow of 12.5 kg/s is diverted into two side outlet nozzles as shown in Fig. 5.20a. The velocity vectors in the outlet nozzles show direction of velocity and its magnitude. It is observed that in the vertical arms, velocity is more towards the outer side of the arm. This is due to change in direction of flow from V arm to vertical arm.

Through central square chimney region, the upward velocity is observed to a certain height in Fig. 5.20a. The water jet with two vortices is observed in Fig. 5.20b. To clearly observe the flow pattern inside the central square chimney region, velocity vector plots in x-y plane and y-z plane are shown in Fig. 5.21a and Fig. 5.21b respectively. The results are shown upto the top (i.e., y = 0.6 m) of the chimney. In the lower most region of Fig. 5.21a, the velocity vectors show upward flow along with direction towards two side outlet openings. Above this region asymmetrical circulation with lower velocity is observed with longer length. However, Fig. 5.21b shows how the upward central jet takes turn from both sides to become downward. It is also observed in Fig. 5.21b that downward flow through the top opening of the chimney takes place in the central region. Since there is no net flow provided to the top opening of the chimney, upward flow takes place through the peripheral region in order to maintain the overall balance of flow. This upward flow tendency through the top opening of the chimney is not acceptable because it will lead to reaching of radioactive water from the core outlet to the pool. Therefore, additional bypass flow cases are analysed to observe their effect in keeping the radioactive water well within the chimney region without allowing it to go towards the pool.

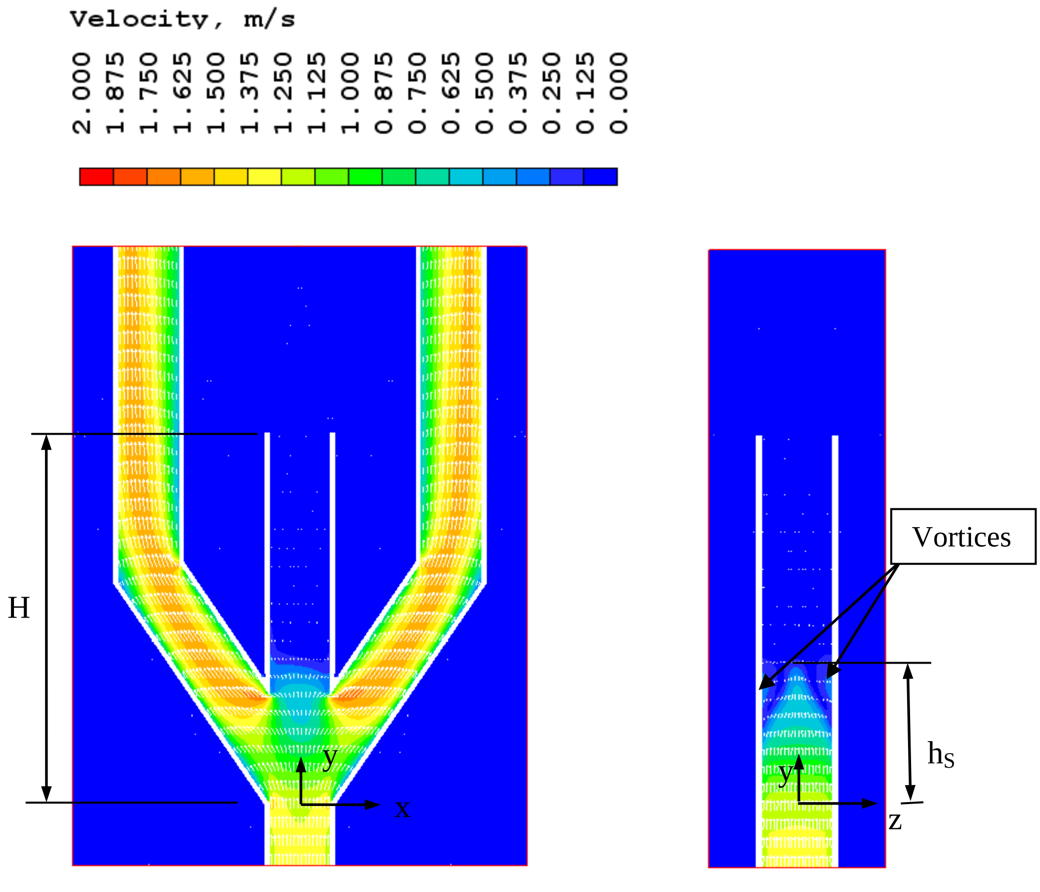


(a) x-y plane (z=0)

(b) y-z plane (x=0)

Fig. 5.20: Velocity distribution for core flow of 12.5 kg/s (R=0.0, θ=35°, H=0.6 m)

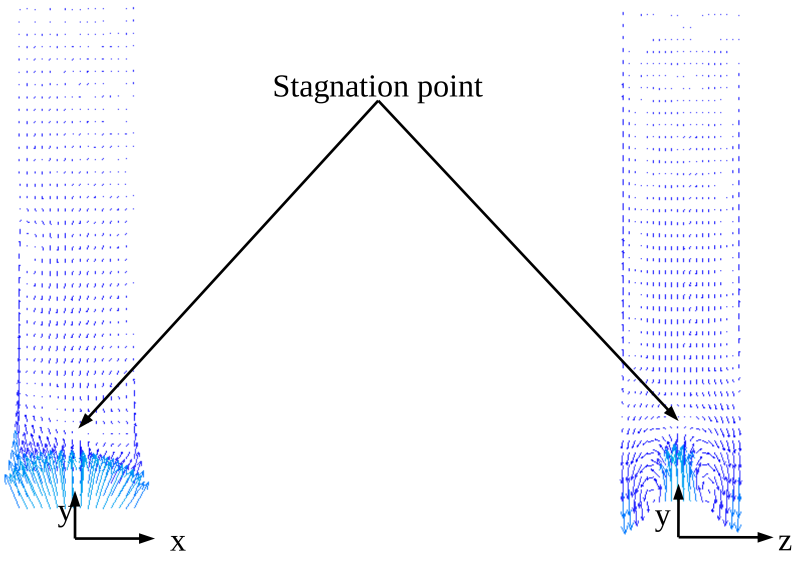


(a) x-y plane (z=0)    (b) y-z plane (x=0)

Fig. 5.21: Velocity vector in central chimney from y=0.2 to 0.6 m

($W_{in}$=12.5 kg/s, R=0.0, θ=35°)

Velocity distribution with 5% core bypass

The velocity contours in x-y plane and y-z plane for 0.63 kg/s bypass flow case (R=0.05) are shown in Fig. 5.22a and Fig. 5.22b respectively. In Fig. 5.22a, it is observed that from the bottom through two nozzles, bypass flow is sent to the tank. Because of this additional flow through the chimney top opening in the downward direction, velocity in the side outlet nozzles increases as shown in Fig. 5.22a. In this case also the flow velocities in the vertical arm are more towards the outer side than that towards the inner side. In the central square chimney region, downward flow is observed. In Fig. 5.22b, the upward velocity jet contour is observed. The stagnation height is found to be less than that observed for 0% core bypass case. Length of the two vortices is also observed to be less. This is clearly visible in the velocity vector plot of y-z plane as shown in Fig. 5.23b. When Fig. 5.21b and Fig. 5.23b are compared, the extent of the upward velocity region is also observed to be reduced. The downward flow velocity from the top of the chimney throughout the whole square cross section is observed in both Fig. 5.23a and Fig. 5.23b. Therefore, in this case no radioactive water is able to reach the pool top. Now, the extent of suppression of upward jet due to increase in core bypass flow is further analysed by varying the bypass to 10% and 15%.

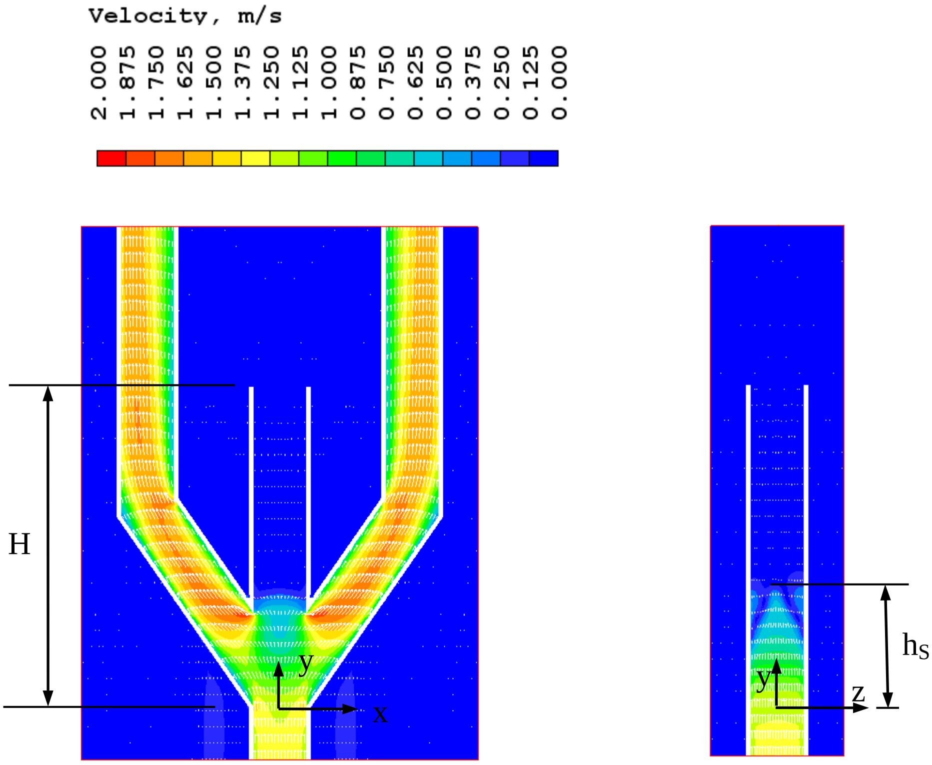


(a) x-y plane (z=0)  (b) y-z plane (x=0)

Fig. 5.22: Velocity distribution for core flow of 12.5 kg/s (R=0.05, θ=35°, H=0.6 m)

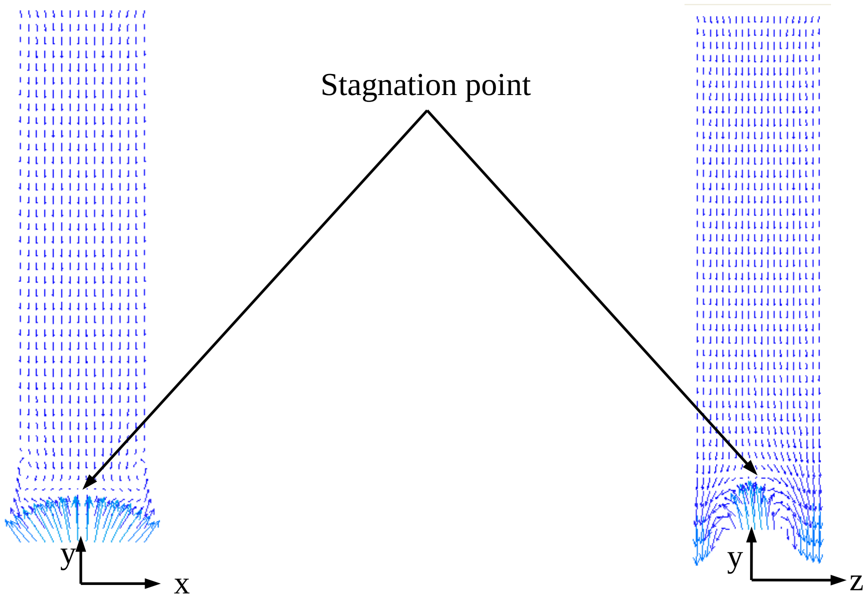


(a) x-y plane (z=0)  (b) y-z plane (x=0)

Fig. 5.23: Velocity vector in central chimney from y=0.2 to 0.6 m

($W_{in}$=12.5 kg/s, R=0.05, θ=35°)

Velocity distribution with 10%, 15% core bypass

The results for core bypass of 1.25 kg/s (i.e., 10% of core flow) and 1.88 kg/s (i.e., 15% of core flow) are shown in Fig. 5.24 to Fig. 5.27. With increase in core bypass flow, the velocity contour plots of x-y plane show increase in velocity and their distribution near the bottom region of the pool is visible in Fig. 5.24a and Fig. 5.26a. This additional bypass flow when sucked in through the top of the chimney suppresses the upward velocity as observed in Fig. 5.24b and Fig. 5.26b.

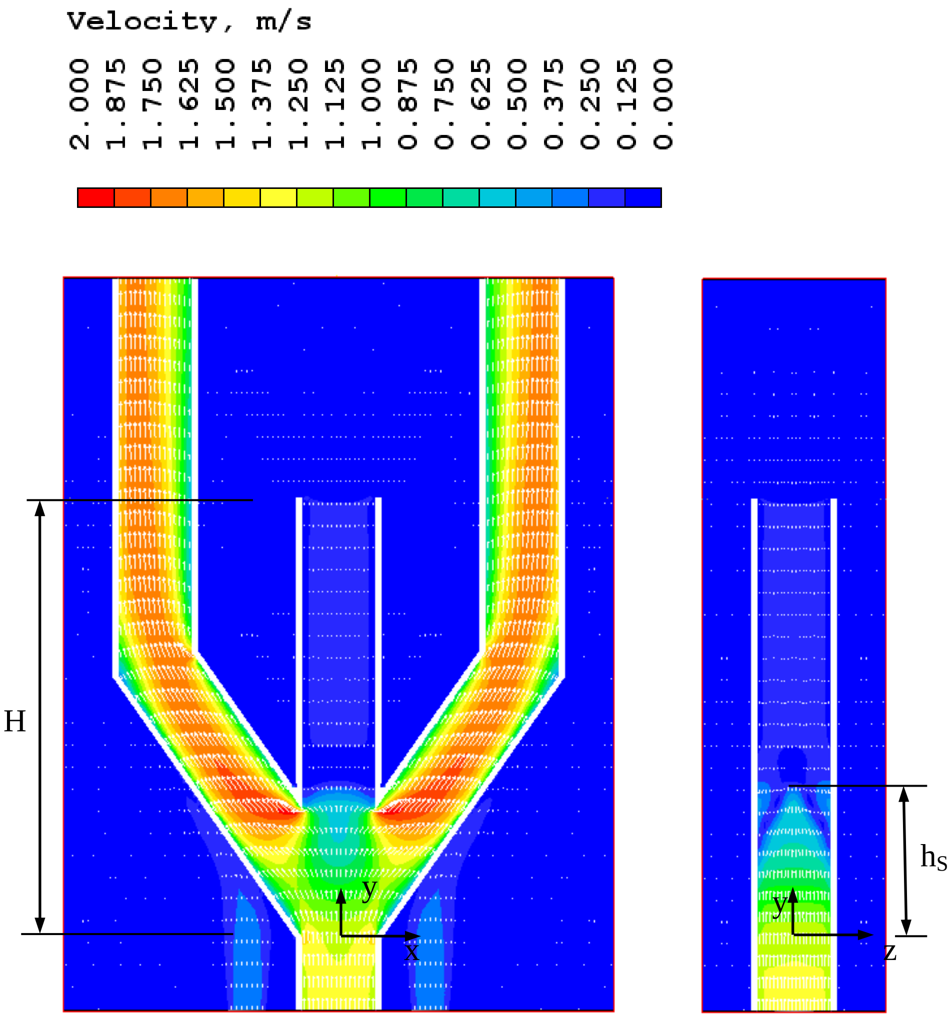


(a) x-y plane (b) y-z plane

Fig. 5.24: Velocity distribution for core flow of 12.5 kg/s (R=0.10, θ=35°, H=0.6 m)

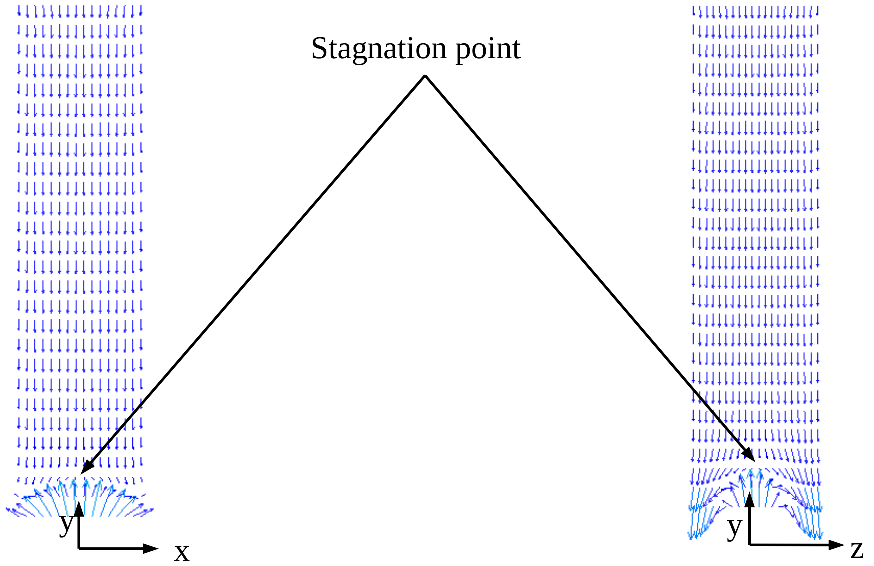


(a) x-y plane (z=0)　　(b) y-z plane (x=0)

Fig. 5.25: Velocity vector in central chimney from y=0.2 to 0.6 m

($W_{in}$=12.5 kg/s, R=0.10, θ=35°)

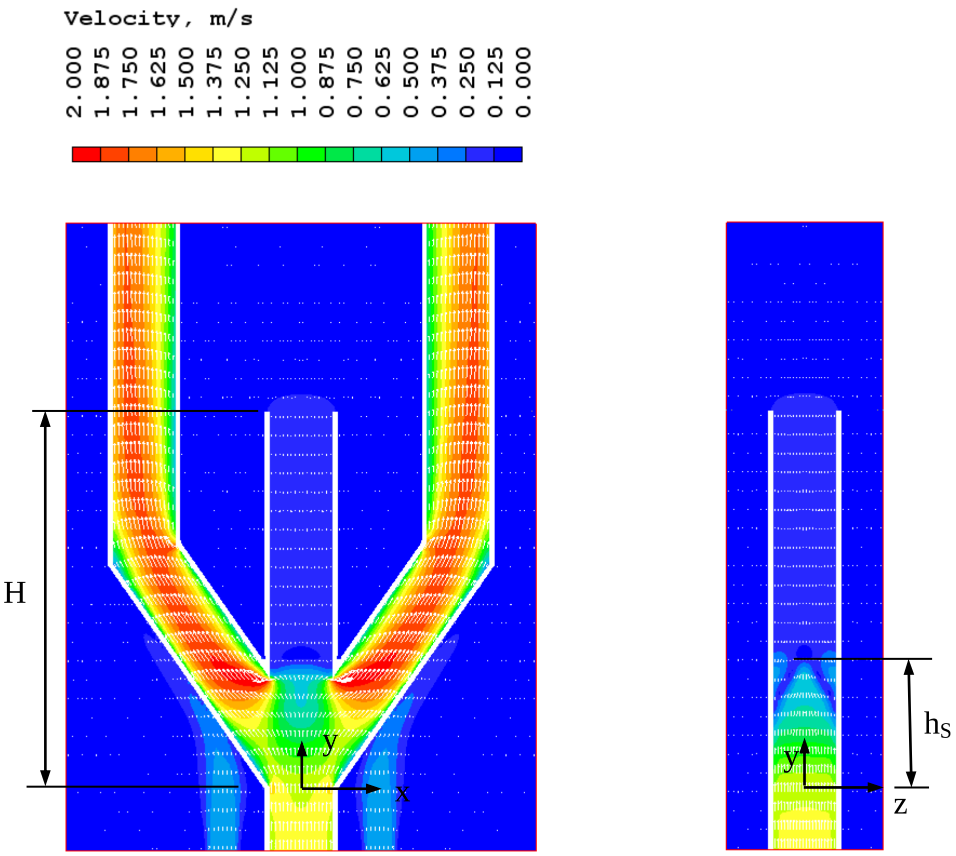


(a) x-y plane (z=0)　　(b) y-z plane (x=0)

Fig. 5.26: Velocity distribution for core flow of 12.5 kg/s (R=0.15, θ=35°, H=0.6 m)

It is observed from the magnitude of the velocity vector plots of Fig. 5.25 and Fig. 5.27 that the upward velocity at y=0.2 m is reduced as the downward velocity through the top chimney is increased. This is because of the higher downward momentum of larger bypass flow, the core outlet flow gets diverted towards the side outlet nozzles more effectively and thereby reduces the upward jet velocity. This in turn causes the stagnation height to reduce. In order to quantify the stagnation height, the centre line velocity of the chimney is plotted against the height of the chimney.

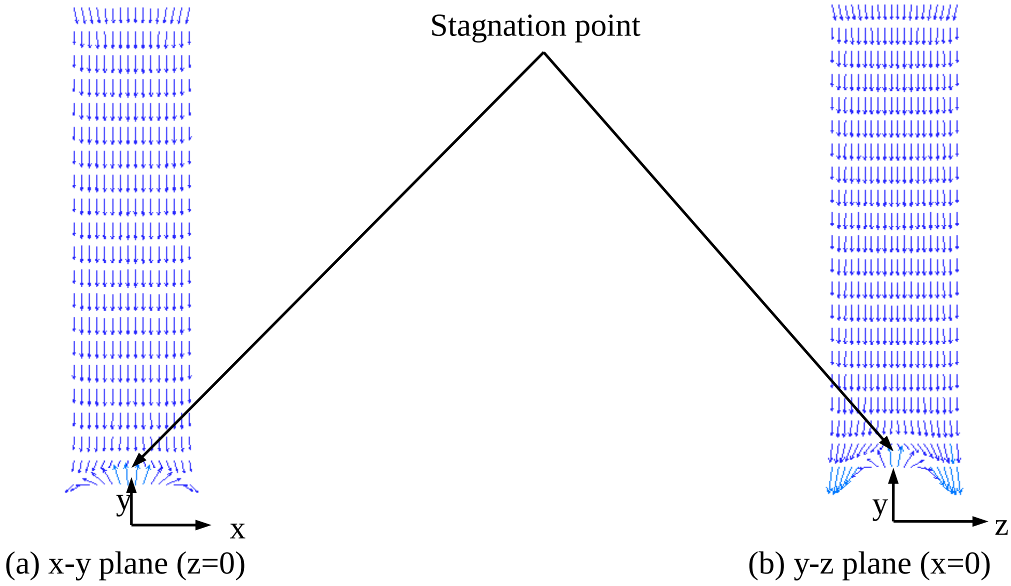


Fig. 5.27: Velocity vector in central chimney from y=0.2 to 0.6 m

($W_{in}$=12.5 kg/s, R=0.15, θ=35°)

**Centre line velocity variation along the height of chimney**

The upward velocity ($v_y$) variation along the height of the chimney is shown in Fig. 5.28 for 0%, 5%, 10% and 15% core bypass flow cases. The upward flow velocity at the bottom inlet of the chimney (at y = -0.1 m) is about 1.25 m/s.

At y =0.0 m, the side outlet nozzle opening starts. With further increase in y, flow moves towards side outlet nozzles and upward velocity decreases. Up to y = 0.13 m, the velocity variation is the same for all the bypass cases. At higher value of y, the velocity variation depends on the core bypass flow. It is observed from Fig. 5.28 that velocity decreases and reaches to zero value. Beyond this point velocity becomes negative, i.e., downward velocity is observed. The value of y where upward velocity ($v_y$) is zero is defined as the stagnation height. The stagnation height for 0% bypass flow is 0.264 m and for 15% case, it is 0.213 m. It is observed from the figure that stagnation height decreases with increase in core bypass flow.

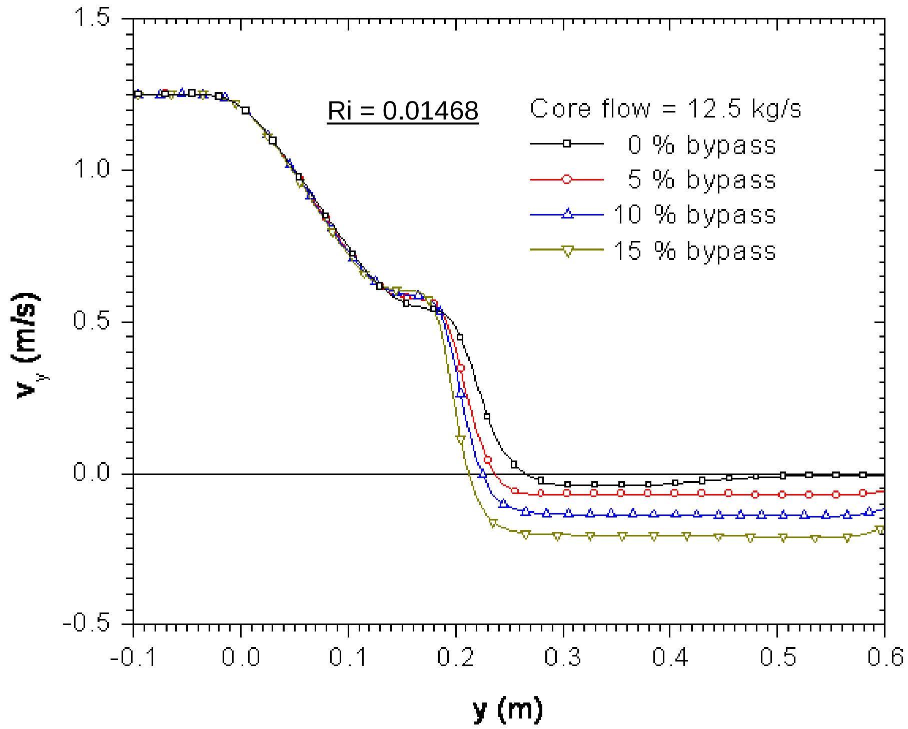


Fig. 5.28: Centre line upward velocity variation with chimney height ($Re_D = 2.25 \times 10^5$)

**Temperature Distribution**

When core bypass flow is 0%, the hot core outlet water at 49°C moves upward through the peripheral region as explained in previous subsection and it is observed that the pool temperature finally stabilises at 49°C. The temperature contour plots for 5%, 10% and 15% core bypass flow are shown in Fig. 5.29a, 5.29b and 5.29c respectively. It is observed that with increase in bypass flow, the temperature at the vertical arm of the side outlet nozzles decreases. The variation of temperature from the inner side to the outer side is more when bypass flow is more. This is because more amount of cold fluid (at 40°C) entering through the chimney moves out of the chimney preferentially towards the inner side of the chimney. Hotter water (at 49°C) moves out of the chimney preferentially towards the outer side of the chimney.

It is also observed that hot water penetration into the chimney becomes less with increase in core bypass flow. Due to sucking of pool water through the top of the chimney, pool water temperature front (at 40°C) reaches inside chimney which restricts hot core outlet temperature to propagate further in the upward direction. The pool water temperature front heights ($h_T$) have been marked for various bypass flow ratios (R) as shown in Fig. 5.29. It is observed that with increase in bypass flow ratio, the pool temperature front height decreases. To quantify these values for various cases, centre line temperature variation is plotted along the height of the chimney.

**Centre line temperature variation with chimney height**

The water temperature variation along the central axis of the square chimney with respect to the chimney height is shown in Fig. 5.30. At the entry of the bottom inlet of chimney, the water temperature is 49°C. When core bypass flow is 0%, this 49°C temperature is observed throughout the chimney height. Upto a height, y = 0.170 m, this temperature is observed for other bypass flow cases. At higher height, the temperature depends on the core bypass flow. When core bypass flow is more, the temperature drops at a faster rate. With 5% core bypass flow, temperature front height is 0.268 m. With increase in bypass flow to 15%, the temperature front height reduces to 0.237 m.

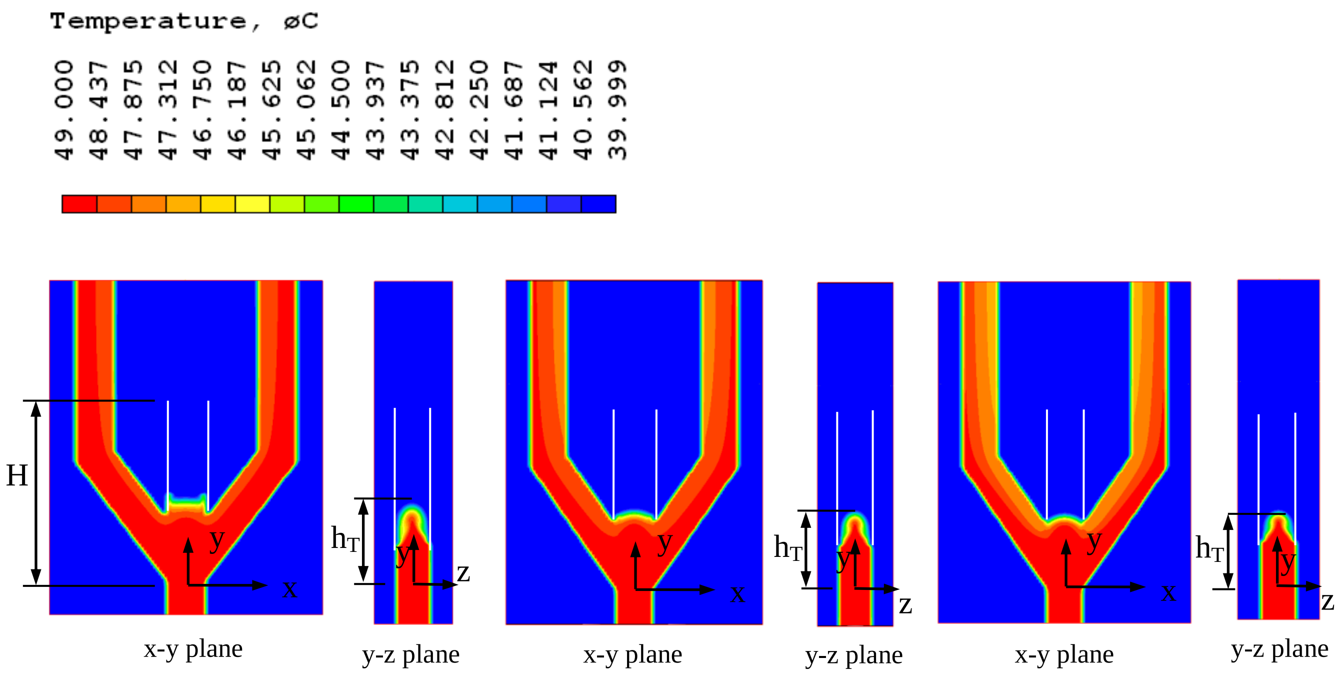


Fig. 5.29: Temperature contours - core flow 12.5 kg/s

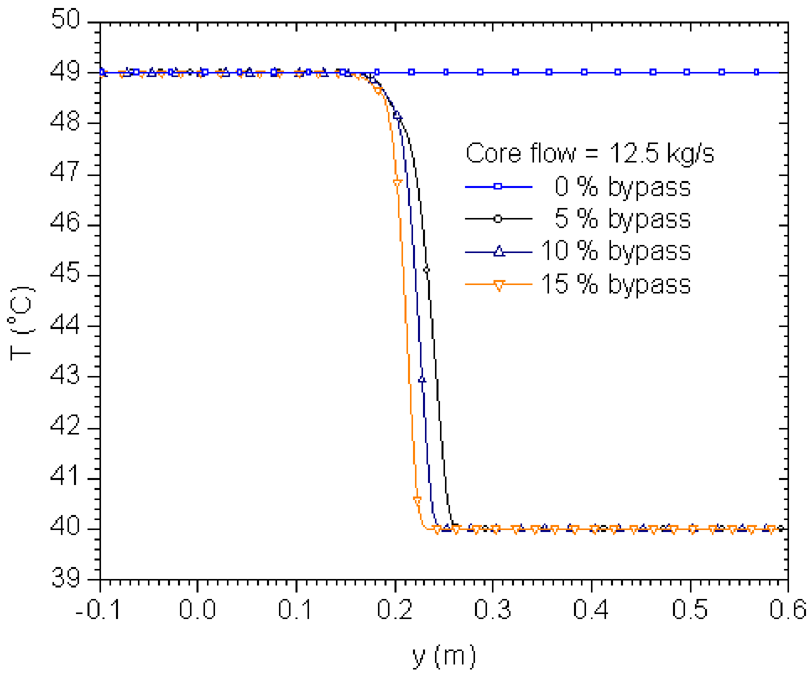


Fig. 5.30: Water centre line temperature variation with chimney height ($Re_D$= 2.25×10 $^5$)

**Effect of Core flow on Velocity distribution**

To understand the effect of core flow variation on velocity distribution inside the chimney, core flow is varied to 16.66, 20.83 and 25 kg/s. The Reynolds numbers ($Re_D$) corresponding to these core flows are $3\times10^{5}$, $3.75\times10^{5}$ and $4.5\times10^{5}$ respectively. Figure 5.31 shows the upward velocity variation along the central axis of the chimney for core flow of 16.66, 20.83 and 25 kg/s respectively. For core flow of 16.66 kg/s, flow velocity is about 1.66 m/s at the bottom of the chimney, which gradually decreases with chimney height. For 0 % bypass case, the velocity becomes zero at y = 0.266 m and for 15% bypass flow, it occurs at y = 0.212 m.

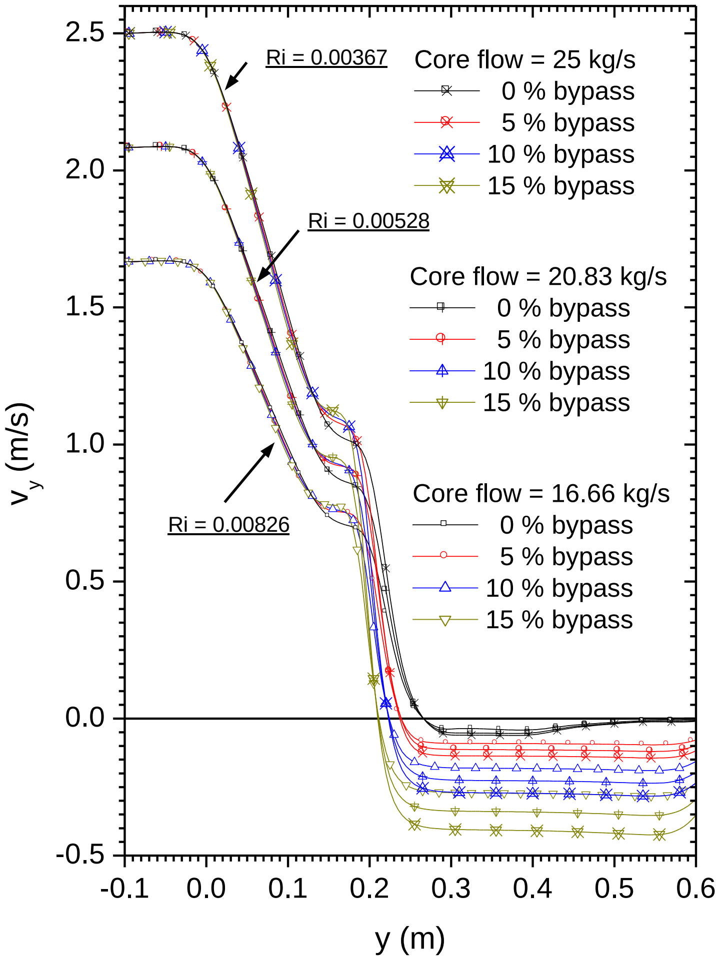


Fig. 5.31: Centre line upward velocity variation with chimney height
($Re_D = 3\times10^{5}$, $3.75\times10^{5}$, $4.5\times10^{5}$)

For core flow of 20.83 and 25 kg/s, the similar trend of velocity variation is also observed. For 20.83 kg/s core flow, the chimney flow velocity reduces from 2.08 m/s (at bottom y= -0.1 m) to zero value at y = 0.266 m for 0% bypass flow and y = 0.211 m for 15% bypass flow. For 25 kg/s core flow, the inlet velocity of 2.5 m/s reduces to zero velocity at y = 0.266 m for 0 % core bypass flow and 0.210 m for 15 % bypass flow. It is also observed that downward velocity through top of the chimney increases with the increase in inlet velocity, when similar percentage of bypass flow is considered.

**Effect of Core flow on Temperature distribution**

Temperature variation along the central axis of the chimney for core flow rates of 16.66, 20.83 and 25 kg/s is shown in Fig. 5.32. It is observed that for all these cases the trend of temperature variation is similar. Hot water at 49°C mixes with the cold water of the pool at 40°C inside the chimney in which case core bypass flow is provided. For 5% core bypass flow, temperature front height is observed to be 0.267 m, 0.268 m, 0.270 m for core flow of 16.66, 20.83 and 25 kg/s respectively. For 15% core bypass flow, the temperature front height reduces to 0.237 m, 0.237 m, 0.235 m respectively. Therefore, the pool temperature front height decreases with the increase in core bypass flow for these cases.

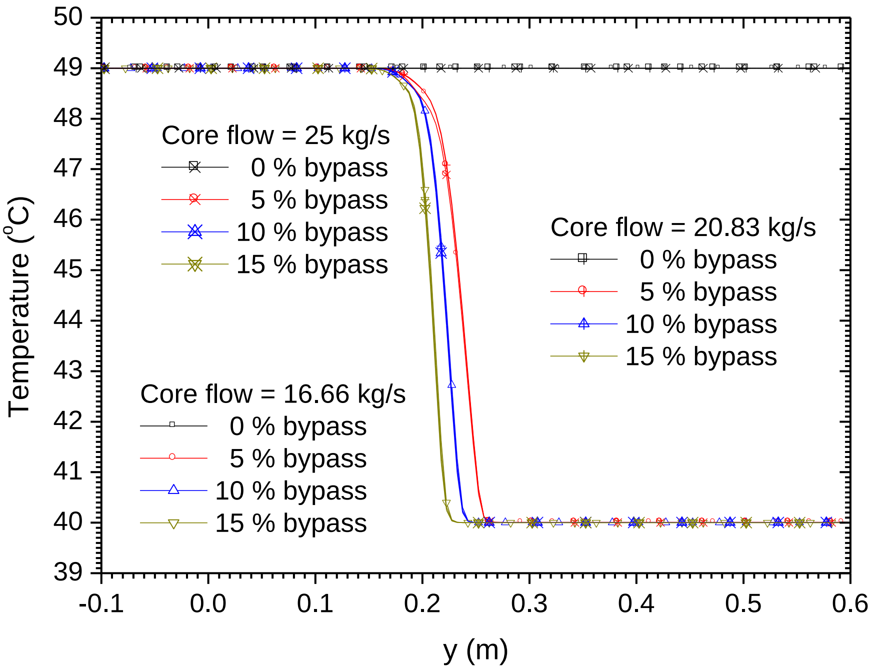


Fig. 5.32: Water centre line temperature variation with chimney height ($Re_D = 3\times10^5$, $3.75\times10^5$, $4.5\times10^5$)

**Non-dimensionalisation**

To consolidate all the above results, the output results were represented in the non-dimensional form. The dimensionless velocity variation along the central axis of the chimney with dimensionless chimney distance is shown in Fig. 5.33. It is observed from the results that for bypass flow ratio R=0.0, variation of dimensionless upward velocity with respect to dimensionless vertical distance for various Reynolds numbers2.25x$10^5$, 3x$10^5$, 3.75x$10^5$ and 4.5x$10^5$ are overlapping each other. When the bypass flow ratio is increased to R=0.05 keeping Reynolds number constant, these results are different than that observed for R=0.0. Therefore, the trend of results follow the same pattern for the Reynolds number range covered in the analysis in case the bypass flow ratio (R) is kept the same

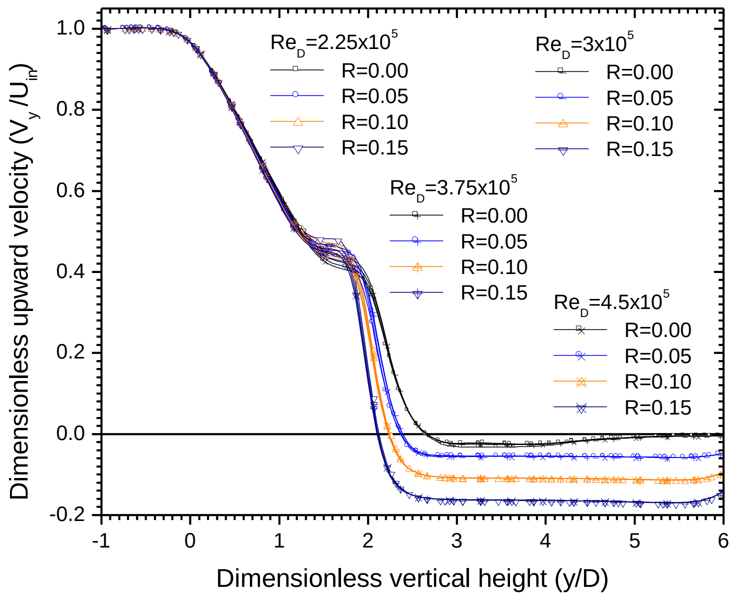


Fig. 5.33: Dimensionless velocity variation with dimensionless height (θ=35°)

Similarly dimensionless temperature variation with respect to dimensionless distance is shown in Fig. 5.34. Temperature is non-dimensionalised considering pool temperature as the reference temperature. Here also, it is observed that temperature variation follows the same behaviour once the bypass to core flow ratio (R) is maintained for the range of Reynolds number considered in these simulations.

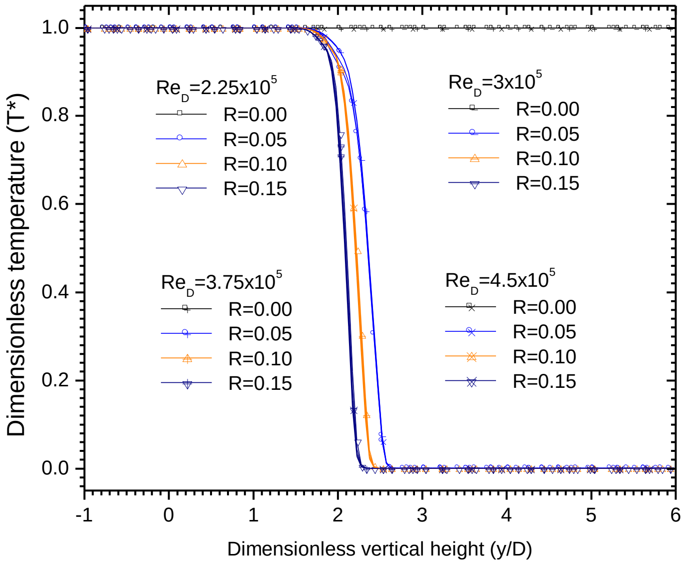


Fig. 5.34: Dimensionless temperature variation with dimensioness height (θ=35°)

### *Variation of Stagnation height with Reynolds number*

It is observed from Fig.5.33 that the dimensionless velocity variation is more dependent on the bypass flow ratio (R) and practically independent of the core flow ($W_{in}$). From Fig. 5.33, dimensionless stagnation height ($h_S$*=$h_S$ / D) is predicted by considering the value of (y/D) at which dimensionless upward velocity ($v_y/U_{in}$) equals to zero. Fig. 5.35 shows the variation of dimensionless stagnation height with the Reynolds number ($Re_D$). The results show that variation of Reynolds number has little effect on the dimensionless stagnation height. It is also observed that change in chimney height (H/D=6) to (H/D=5) as well as temperature difference ($T_{in}$-$T_p$) from 9 to 0°C do not change the dimensionless stagnation height significantly.

### **Variation of Temperature Front height with Reynolds number**

Dimensionless temperature front height is predicted from Fig. 5.34. The dimensionless height where dimensionless temperature (T*) becomes zero is taken as the dimensionless pool temperature front height ($h_T$*=$h_T$ / D). Variation of pool temperature front height with $Re_D$ is shown in Fig. 5.36. It is observed that variation of $h_T$* with Reynolds number is negligible. Also change in chimney height from (H/D=6) to (H/D=5) does not have significant effect on the dimensionless pool temperature front height.

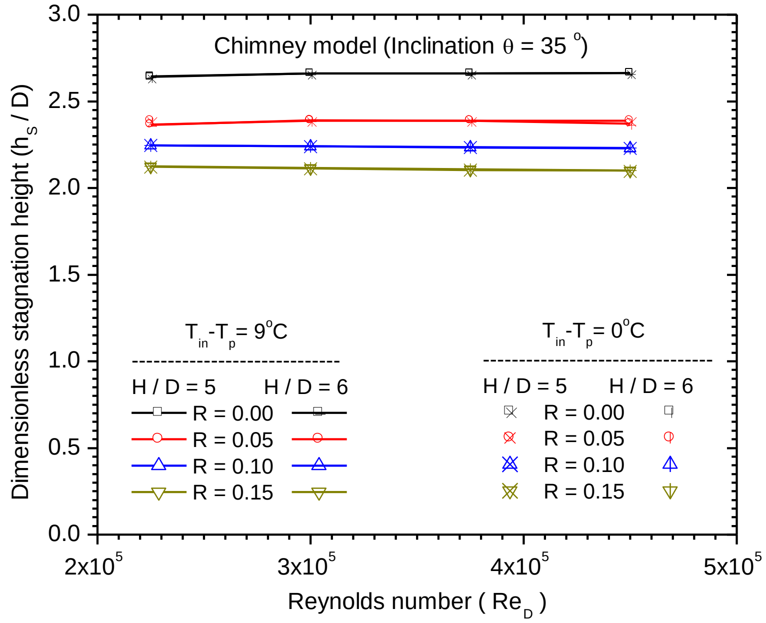


Fig. 5.35: Dimensionless stagnation height variation with $Re_D$ (θ=35°)

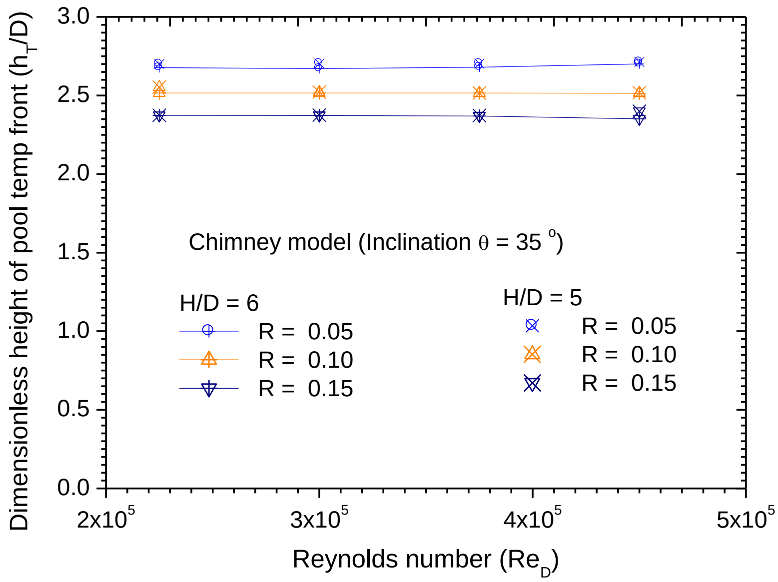


Fig. 5.36: Dimensionless pool temperature front height variation with $Re_D$ (θ=35°)

### 5.4.5.2 Nozzle inclination - 25°

Numerical study carried out for the chimney model with inclination angle 25° and height 500 mm is described in this section. The computational domain used is shown in Fig. 5.37 and the CFD simulations are carried out for the cases mentioned in Table-5.3 with core outlet temperature 49°C and bypass inlet temperature 40°C. Standard k- ε model is also used in these simulations. Calculations are done with similar grid (110 × 200 × 40) used for previous cases.

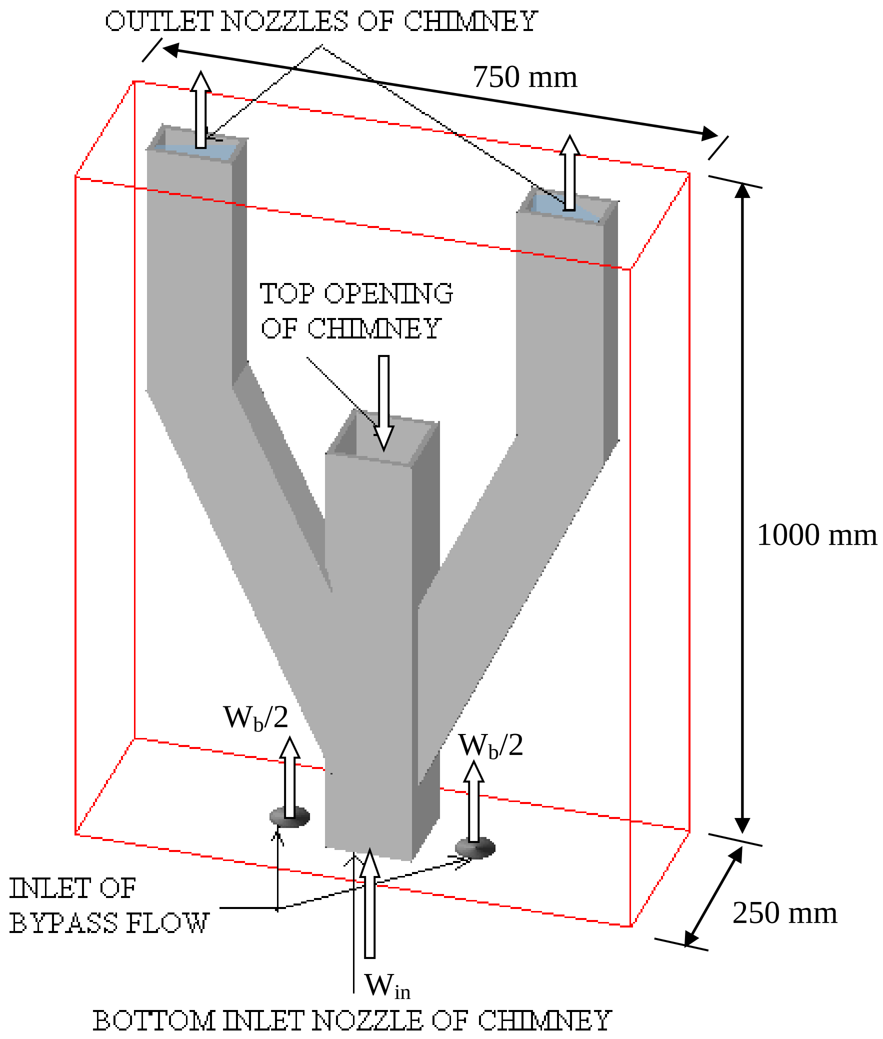


Fig. 5.37: Computational domain (H = 0.5 m, inclination θ = 25°)

Table-5.3: Dimensionless numbers for chimney model with 25° nozzle inclination

| Sr. No. | $W_{in}$ (kg/s) | $U_{in}$ (m/s) | $Re_D$ | Ri | Bypass flow ratio (R) | Bypass flow entering chimney - $W_b$ (kg/s) | Down-ward velocity $U_b$ (m/s) |
|---|---|---|---|---|---|---|---|
| 1 | 16.66 | 1.666 | $3.0\times10^{5}$ | 0.00688 $ | 0.0 | 0.00 | 0.000 |
| 2 | | | | | 0.05 | 0.83 | 0.083 |
| 3 | | | | 0.00826 # | 0.10 | 1.66 | 0.166 |
| 4 | | | | | 0.15 | 2.50 | 0.250 |
| 5 | 20.83 | 2.083 | $3.75\times10^{5}$ | 0.00440 $ | 0.0 | 0.00 | 0.000 |
| 6 | | | | | 0.05 | 1.04 | 0.104 |
| 7 | | | | 0.00528 # | 0.10 | 2.08 | 0.208 |
| 8 | | | | | 0.15 | 3.13 | 0.313 |
| 9 | 25 | 2.500 | $4.5\times10^{5}$ | 0.00306 $ | 0.0 | 0.00 | 0.000 |
| 10 | | | | | 0.05 | 1.25 | 0.125 |
| 11 | | | | 0.00367# | 0.10 | 2.50 | 0.250 |
| 12 | | | | | 0.15 | 3.75 | 0.375 |

$ H/D = 5

# H/D = 6

The results for velocity in the centerline of the chimney for all the cases mentioned above are shown in Fig. 5.38. It is observed that the upward flow velocity in the central axis of the chimney reduces from a positive value (upward flow) to zero and finally becomes negative (i.e., flow is downward) towards the upper part of the chimney. The location of zero velocity indicates the location (of stagnation height) where upward water jet motion stops. As core bypass flow increases, this location shifts away from the top end of the chimney. For core flow of 16.66 kg/s, the central upward flow velocity is found to be zero at about y =

327 mm in case of 0% core bypass flow. For 15% core bypass flow, the location is at y=275 mm. It is clear that the stagnation height decreases with increase in bypass flow.

For 20.83 kg/s core flow case, stagnation height decreases from 325 mm to 275 mm due to increase in bypass flow from 0% to 15%. For 25 kg/s core flow, stagnation height is 322 mm and 274 mm for 0% and 15% bypass flow.

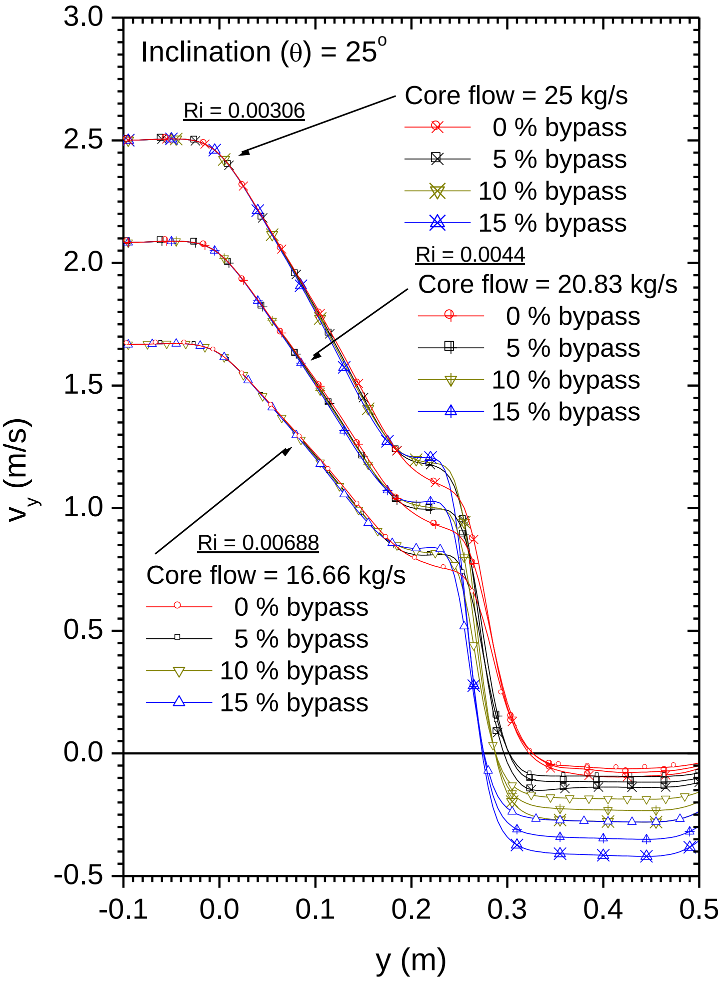


Fig. 5.38: Centre line upward velocity variation (θ=25°, $Re_D$ = 3×10 $^5$, 3.75×10 $^5$, 4.5×10 $^5$)

The temperature distribution at the central axis of the chimney is shown in Fig. 5.39. It is observed that pool water temperature stabilises at core outlet temperature (49°C) if no core bypass flow is sent into the pool. When bypass flow is provided, pool water is sucked inside the chimney. However, due to upward flowing hot fluid from the bottom of the chimney, pool water temperature front (40°C) reaches only upto a certain depth with respect to the top end of the chimney. Accordingly height of pool water temperature front varies depending on the percentage bypass flow. When core flow is 16.66 kg/s, pool temperature front height ($h_T$) is 323 mm for 5% core bypass flow. With increasing bypass flow to 15%, this pool water front height ($h_T$) reduces to 293 mm.

Similarly with core flow of 20.83 kg/s, pool water temperature front height decreases from 324 mm to 294 mm when bypass flow increased from 5% to 15%. For 25 kg/s core flow, pool water temperature front height is 325 mm and 295 mm for 5% and 15% bypass flow respectively.

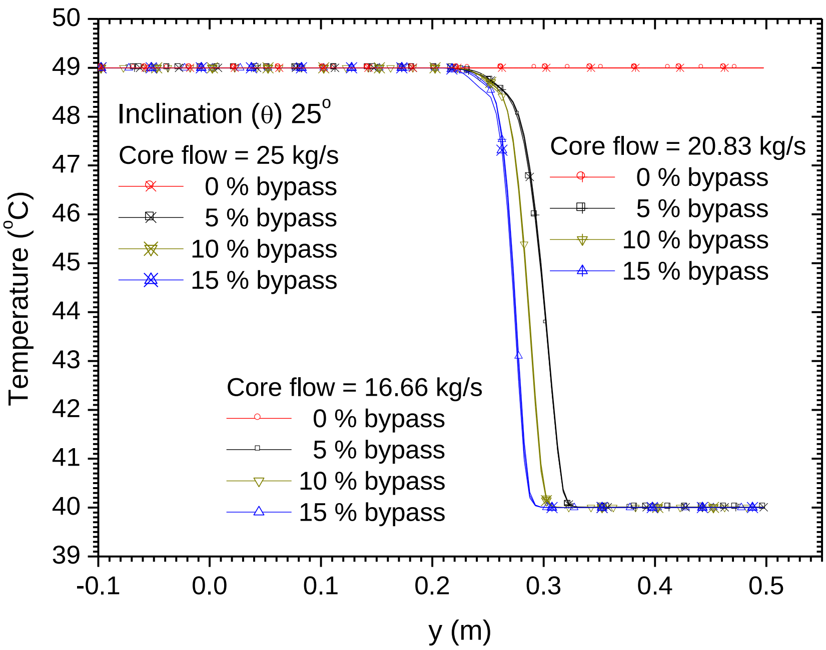


Fig. 5.39: Centre line temperature variation (θ=25°, $Re_D$ = 3×10 $^5$, 3.75×10 $^5$, 4.5×10 $^5$)

Non-dimesionalisation of the results are done to compare velocity distribution as well as temperature distribution following similar approach as described for 45° and 35° nozzle inclination cases. The dimensionless velocity distribution on central axis of the chimney with dimensionless height is shown Fig. 5.40. The dimensionless temperature distribution is shown in Fig. 5.41. It is observed from these results that the distribution is similar for all the three cases of Reynolds number - $3\times10^5$, $3.75\times10^5$ and $4.5\times10^5$ if percentage of core bypass flow is similar.

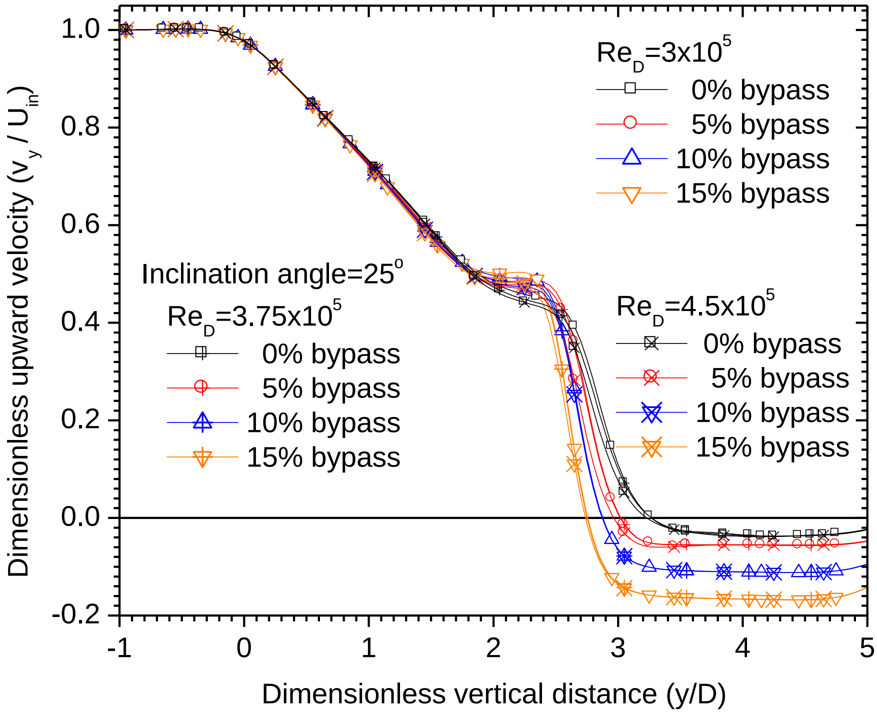


Fig. 5.40: Dimensionless velocity variation with dimensionless height (θ=25°)

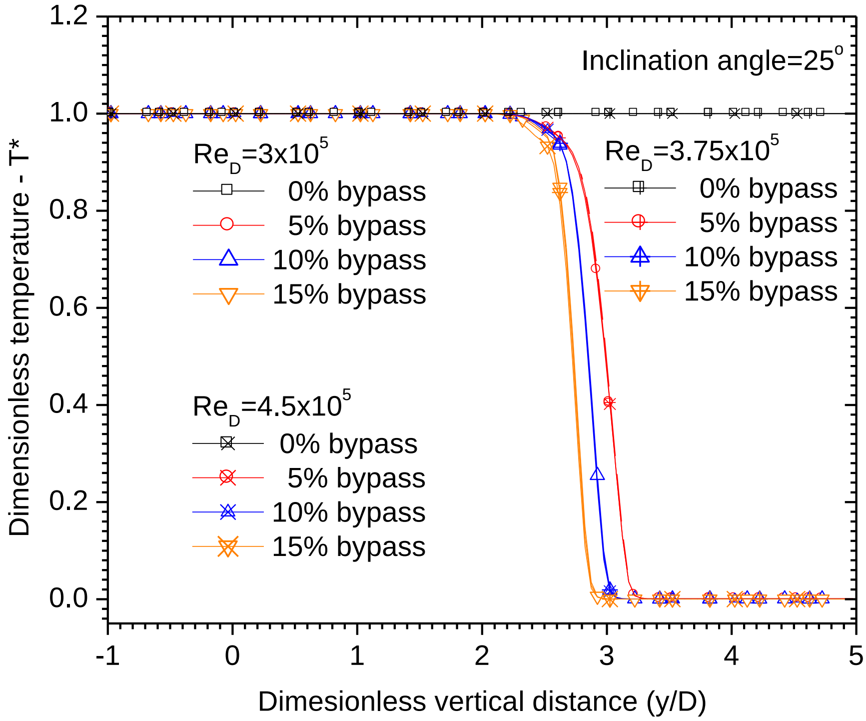


Fig. 5.41: Dimensionless temperature variation with dimensionless height (θ=25°)

Analyses are also carried out considering chimney height as 600 mm (i.e., H/D =6) with same inclination 25°. From the results obtained dimensionless stagnation height is estimated and compared with chimney having H/D = 5 as shown in Fig. 5.42. It is observed that effect on dimensionless stagnation height due to increase in chimney height is insignificant.

To estimate the effect of temperature differential, analyses are done considering zero temperature differential between core inlet and bypass temperatures. The corresponding dimensionless stagnation heights are shown in Fig. 5.42. It is observed that variation of dimensionless stagnation height is negligible due to variation in temperature differential, Reynolds number and chimney height.

Dimensionless temperature front heights of pool water for chimney heights corresponding to H/D=5 and H/D=6 are also compared and shown in Fig. 5.43. It is observed that pool temperature front height does not vary significantly due to change in height as well as Reynolds number.

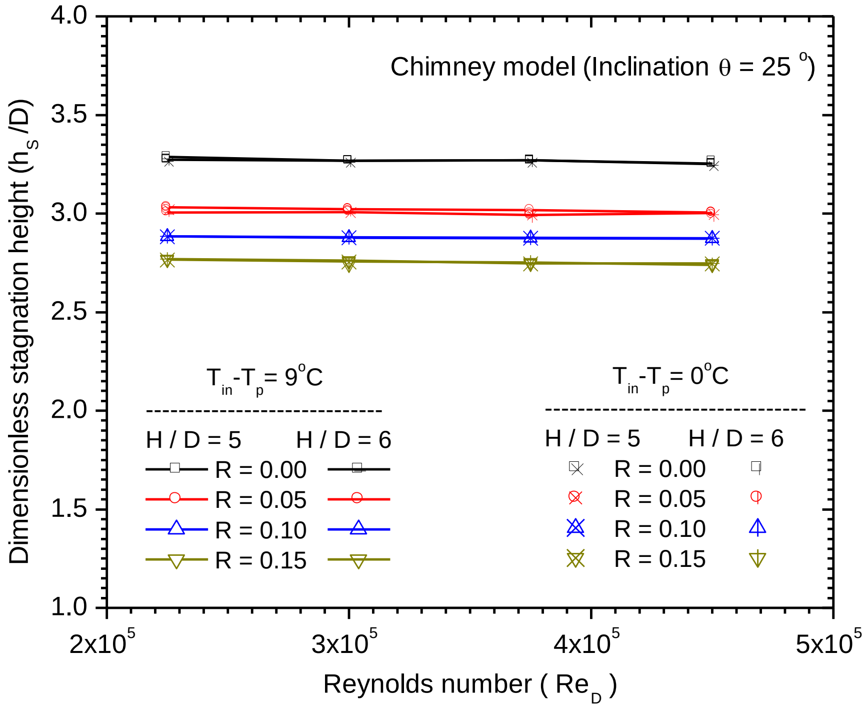


Fig. 5.42: Dimensionless stagnation height variation with Reynolds number, $Re_D$ ($\theta$=25°, H/D=5, 6 and $\Delta T$ = 9, 0ºC)

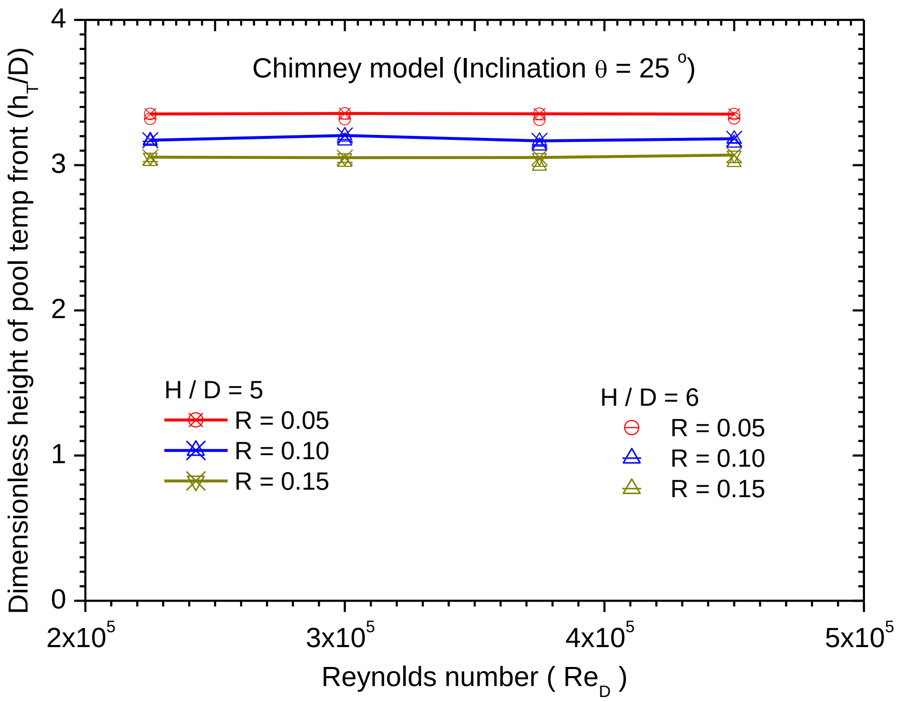


Fig. 5.43: Variation of dimensionless height of pool temperature front with ReD ($\theta$=25°, H/D = 5,6)

### 5.5 Comparison between numerical results of model and prototype

The numerical results of chimney models obtained are compared with that of the prototype as shown in Fig. 5.44 to 5.47. Variation of dimensionless centreline upward velocity ($V_y/U_{in}$) with respect to dimensionless vertical distance (y/D) is shown in Fig. 5.44 for various chimney nozzle inclinations ($\theta$=25°, 35° and 45°). Figure 5.44a shows the results for 25° nozzle inclination where variation in dimensionless upward velocity for model with Reynolds numbers ($Re_D$ = $3\times10^5$, 3.75 $\times10^5$ and $4.5\times10^5$) is compared with that for the prototype (with $Re_D$=$3\times10^6$). It is observed from the results that there exists a profile similarity between the models and the prototype. When bypass flow ratio (R) is kept same for the models and the prototype, the velocity profile matches each other. With increasing in bypass flow, stagnation point shift towards the bottom for the models as well as for the prototype. It is observed from the results that velocity profile for the prototype is slightly

(a) θ = 25º

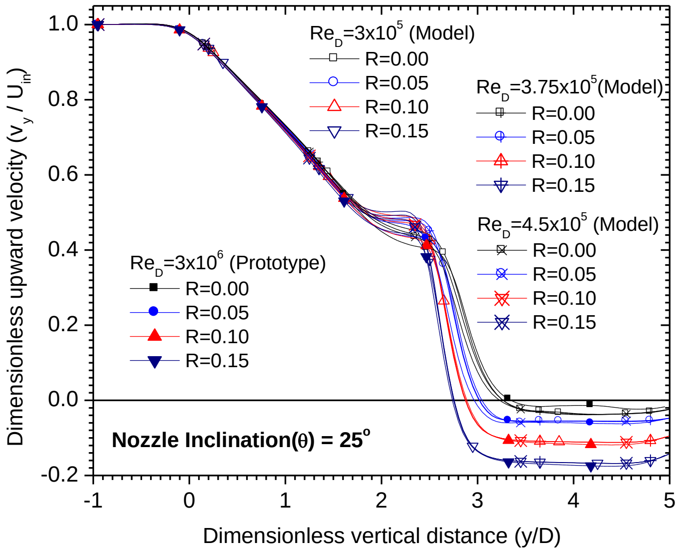


(b) θ = 35º

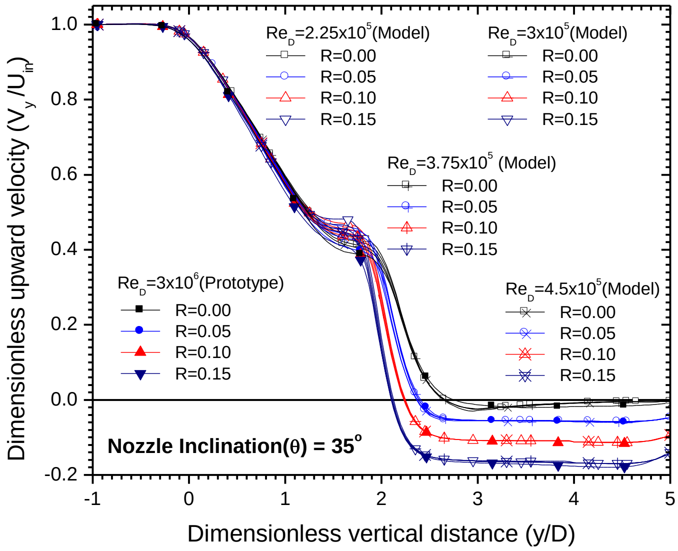


(c) θ = 45º

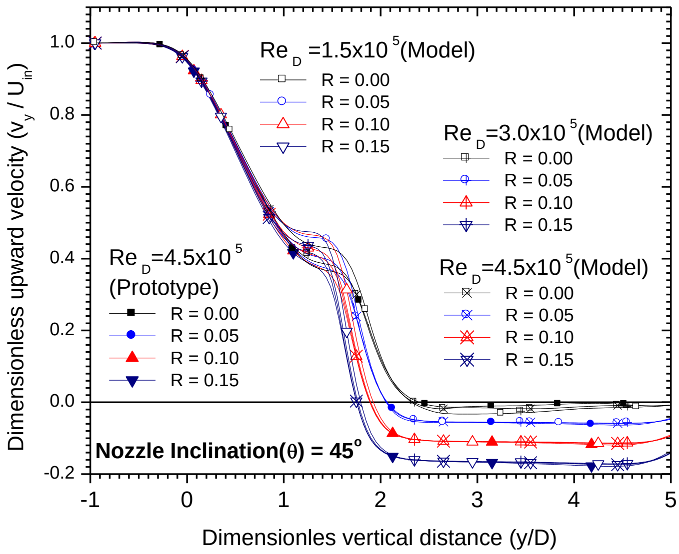


Fig.5.44: Variation of dimensionless upward velocity for model and prototype (θ =25º,35º, 45º)

different than that of the models for bypass flow ratio R=0.0. The predicted dimensionless velocity is more for the models than that for the prototype. It is due to the reason that the boundary wall in the models are very close (100 mm) which has caused lower velocity near the wall region. Hence in the central region of the channel, higher velocity is observed. In the prototype, the wall distance is about 4.5 times, hence boundary layer effect is limited to small region with respect to the full cross section of the channel. Figure 5.44b shows the velocity distribution for the cases with nozzle inclination 35º. The results of the models (with $Re_D$ $2.25\times10^5$, $3\times10^5$, $3.75\times10^5$ and $4.5\times10^5$) are compared with that of the prototype. Here also similarity of profile between the models and prototype is observed when bypass flow ratio is kept same. By increasing the inclination from 25º to 35º stagnation height has further reduced. Figure 5.44c shows the dimensionless upward velocity variation for nozzle inclination of 45º. Results of the models (with $Re_D$ $1.5\times10^5$, $3\times10^5$ and $4.5\times10^5$) and the prototype (with $Re_D$ $3\times10^6$) also show similar trends as explained above.

Dimensionless centreline temperature (T*) profiles for various nozzle inclinations (25º, 35º and 45º) of models and prototype are shown in Fig. 5.45. For nozzle inclination of 25º, the results for the models with Reynolds number of $3\times10^5$, $3.75\times10^5$ and $4.5\times10^5$ are compared with the results of the prototype ($Re_D=3\times10^6$) as shown in Fig. 5.45a. It is observed that the temperature profiles are similar for the models and the prototype in case the bypass flow ratio is same for the models and the prototype. The results show that pool temperature front height decreases with increase in bypass flow ratio for the models as well as the prototype. Figure 5.45b and 5.45c show the comparison for nozzle inclinations of 35º and 45º respectively. It is observed that increase in nozzle inclinations cause decrease in the pool temperature front height for the models as well as the models. All these results clearly show similarity in temperature profile of the prototype and the models which indicates the validity of the scaling philosophy.

(a) θ = 25º

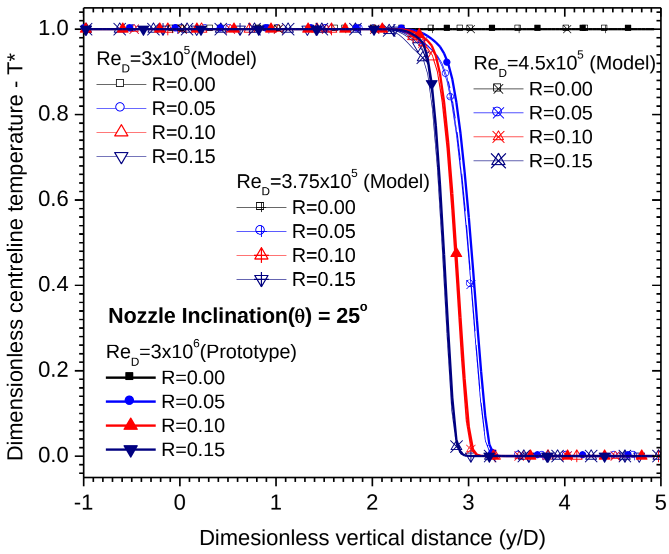


(b) θ = 35º

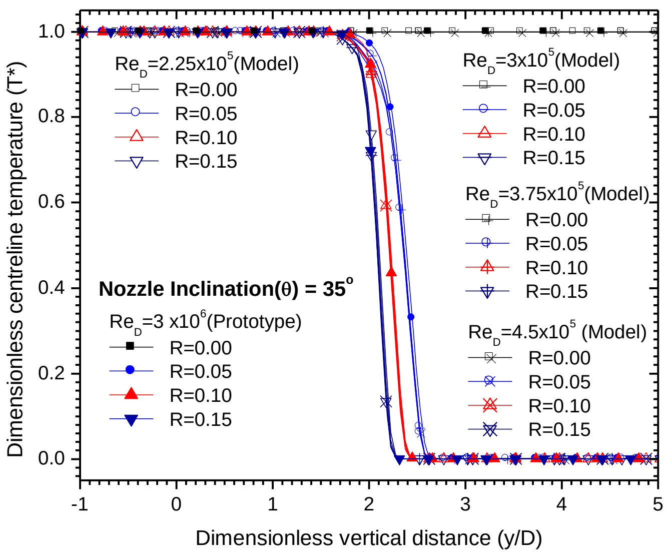


(c) θ = 45º

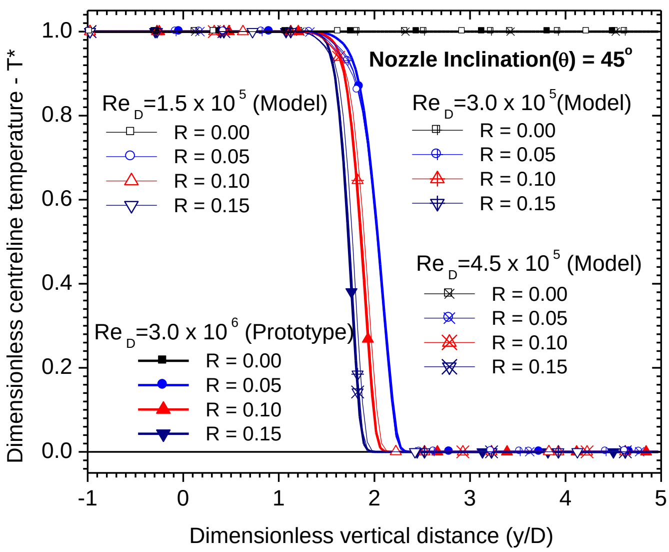


Fig.5.45: Variation of dimensionless temperature profile for model and prototype (θ =25º,35º, 45º)

Dimensionless stagnation height for various angles of chimney inclination - 25°, 35° and 45° are compared with corresponding results obtained for prototype as shown in Fig. 5.46a, b and c respectively. Chimney height to diameter ratio (H/D) considered is 5 and 6 for all these cases. It is observed that dimensionless stagnation heights are of similar value with that of the model. Increase in inclination angle from 25° to 45° has reduced the stagnation height both for the prototype and for the model. Variation in Reynolds number does not significantly affect the dimensionless stagnation height. Increase in bypass flow ratio from 0.0 to 0.15 has significantly reduced the dimensionless stagnation height for all these cases.

Dimensionless pool water temperature front heights for angles 25°, 35° and 45° are shown in Fig. 5.47a, b and c respectively. It is observed that model and prototype have shown similar trends. Increase in inclination angle from 25° to 45° has decreased the pool temperature front height. Increase in bypass flow ratio from 0.0 to 0.15 has also decreased the pool temperature front height both for the model and the prototype. Change in Reynolds number has negligible effect for all these cases. Change in chimney height (i.e., H/D ratio) also does not affect the results significantly. It is also observed from Fig. 5.46 and Fig. 5.47 that pool temperature front height is always greater than corresponding stagnation height for similar inclination angle, core flow and bypass flow ratio.

## 5.6 Closure

The computational study of turbulent mixing behaviour of two opposing flows inside the 2:9 scaled model of the square chimney of a pool type research reactor is described. Cases considering no core bypass flow show that upward flow velocity exists in the peripheral region at the chimney top opening. This is not acceptable because radioactive core outlet water will reach the pool top for these cases. The results of the simulations for 5%, 10% and

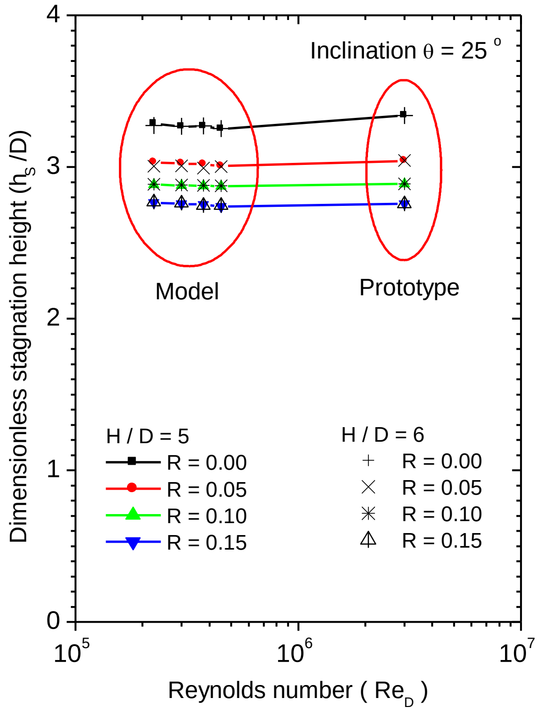


(a) θ = 25°

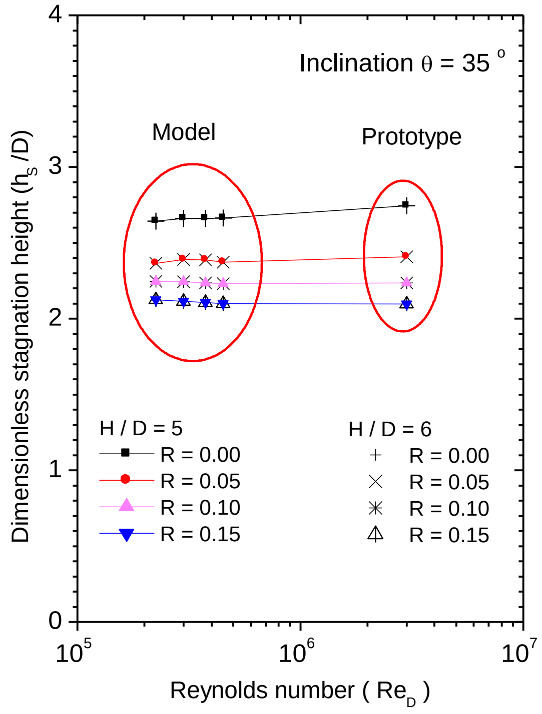


(b) θ = 35°

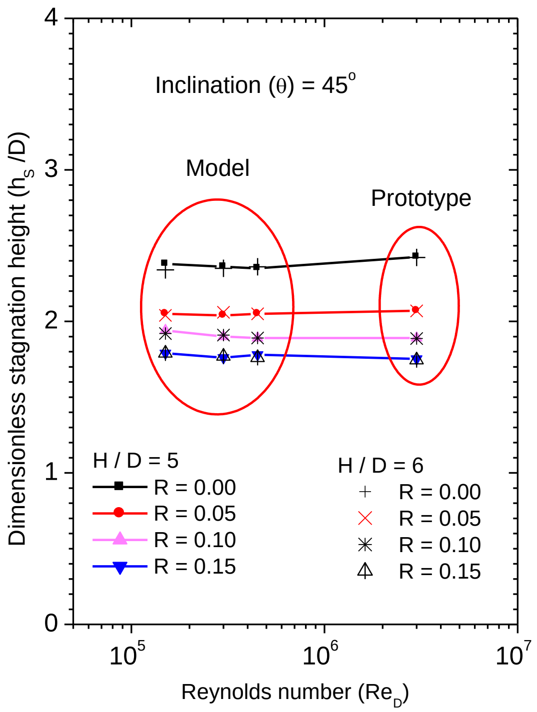


(c) θ = 45°

Fig. 5.46: Variation of dimensionless stagnation height for model and prototype (θ=25°, 35°,45°)

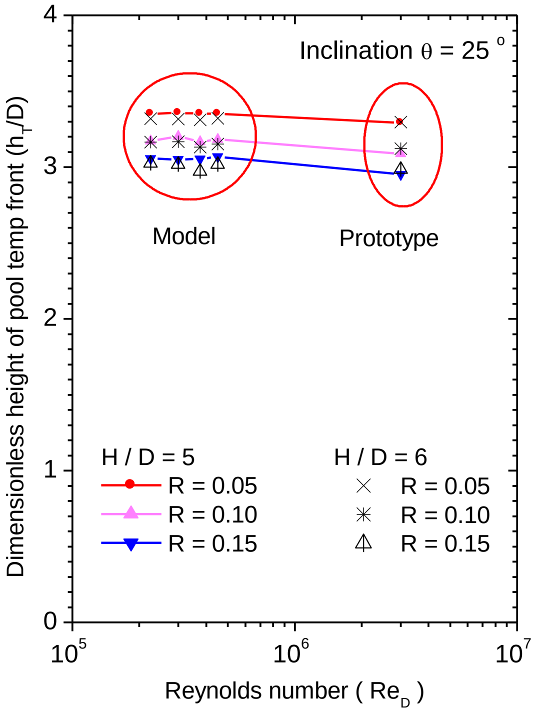


(a) $\theta = 25^o$

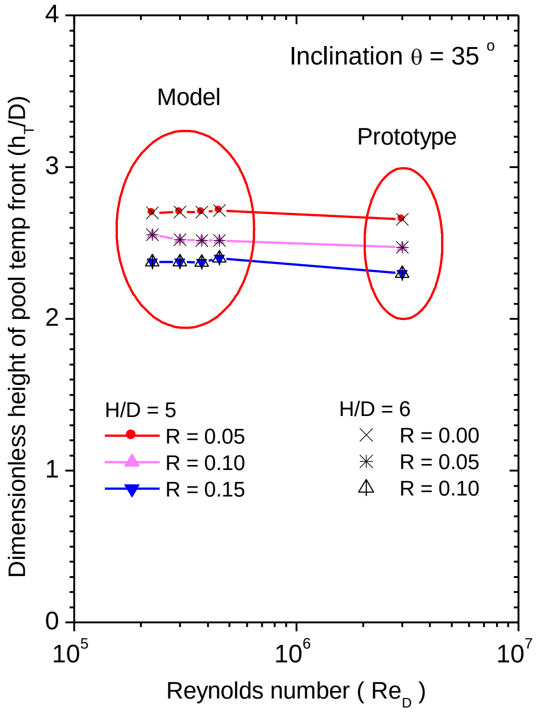


(b) $\theta = 35^o$

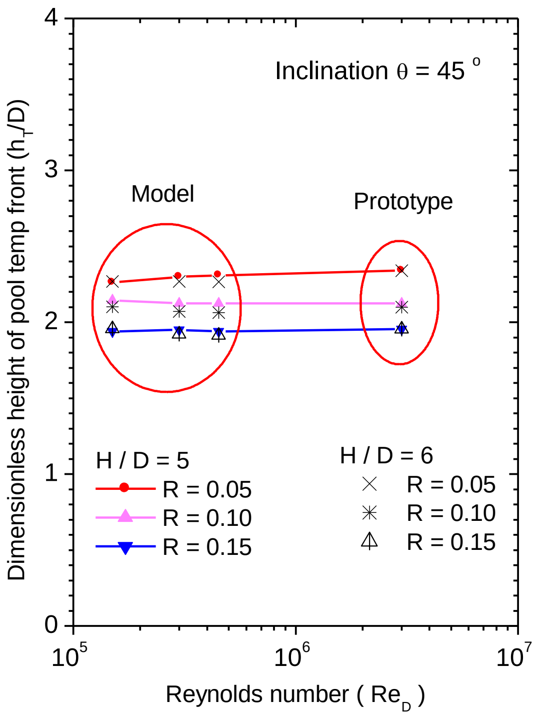


(c) $\theta = 45^o$

Fig. 5.47: Variation of dimensionless height of pool temperature front for model and prototype (θ=25°, 35°, 45°)

15% core bypass flow show that stagnation height decreases with the increase in core bypass flow. The effect of variations in core flow has also been analysed. It is observed that stagnation height as well as pool temperature front height does not change significantly with the change in core flow for the same bypass flow ratio. Non-dimensionalisation of the results shows that velocity distribution and temperature distribution inside the chimney are similar. Dimensionless stagnation height and temperature front height remains almost constant and independent of the Reynolds number of the core flow. A comparison is made with the computational results obtained for the prototype chimney after non-dimensionalisation of the results. It is observed that the dimensionless stagnation height and pool temperature front height show similar behaviour both for the prototype and the model. The numerical study described here is in Reynolds number ($Re_D$) range from $1.5\times10^5$ to $4.5\times10^5$. The prototype chimney for the reactor has Reynolds number of $3\times10^6$. The results show that in the range of the $Re_D$ studied, no significant variation of stagnation height ($h_S$) and pool temperature front height ($h_T$) is observed. This study shows that the Reynolds number range considered is turbulent enough to give results which are independent of the flow rate. Thus the reduced flow rate capability of the model is not affecting the performance and therefore the results can be extrapolated to the prototype.

It is also observed that increase in inclination causes decrease in the stagnation height as well as pool temperature front height. The study shows that for the same inclination, the stagnation height as well as pool temperature front height of the model is similar to that of the prototype if the bypass flow ratio considered is the same.

# Chapter 6

# Experimental Validation in Flow Test Facility

## 6.1 Introduction

Based on the scaling philosophy presented in chapter 5, a flow test facility is setup wherein a 2/9th scaled down model of chimney of high flux research reactor (HFRR) has been installed. The experimental set up is designed to cater for a range of dimensionless numbers

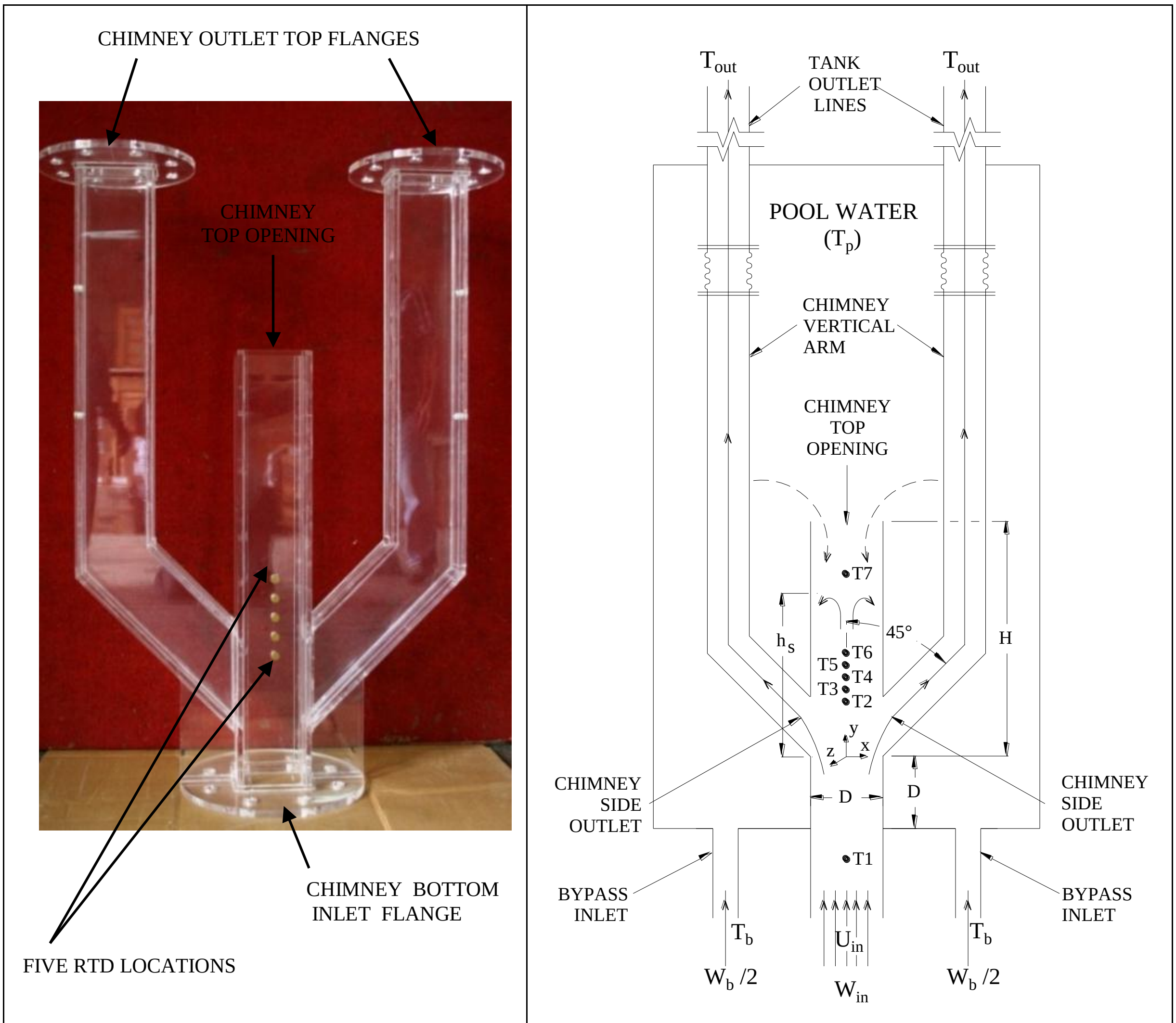

(a) Acrylic chimney model (b) Mixing inside chimney test section

Fig. 6.1: Schematic diagram of mixing behaviour inside the chimney and the tank

($Re = 1.5\times10^5 - 4.5\times10^5$; $Ri = 1.2\times10^{-3} - 5.5\times10^{-1}$; $R = 0.0 - 0.15$; $H/D = 5 - 6$). The chimney nozzle inclination ($\theta$) considered is 45º. One of the two chimney models used in the experiment is shown in Fig. 6.1a. A simplified schematic of flow mixing behaviour inside the chimney model and the tank is shown in Fig. 6.1b. The model is made of transparent acrylic material so that flow mixing inside the chimney can be visualised from outside (Fig. 6.1a). The overall height of the chimney is 1000 mm. Central chimney is of square cross section (100 mm × 100 mm) whose height is varied in the experiment (H = 500 mm, 600 mm). Locations of five nos. of Resistance Temperature Detectors (RTDs) along the height of the chimney are shown in the model. The bottom acrylic flange of chimney rests on a grid plate having central square (100 mm × 100 mm) opening inside a process water tank as shown in Fig. 6.2. Hot water is sent through this square opening of the grid plate provided above the inlet plenum at the bottom of the tank. Chimney has two vertical arms of rectangular cross section (100 mm × 50 mm). For easy connection/disconnection of acrylic chimney, an intermediate bellow is provided between the chimney outlet top flange and a steel pipe flange. The steel pipe flanges are joined with metallic pipe lines which ultimately are connected to tank outlet nozzles. These metallic pipes are larger in length and welded only at one end with the tank. Therefore a continuous support (15 mm wide × 6 mm thick plate) is welded with two sides of the tank for providing rigidity to these pipes. At the central location, a ring of 150 mm diameter is provided so that access to the chimney top opening is available for installing dye injection tube along with dye needles as shown in Fig. 6.2. Total four windows are provided from all the four sides to facilitate flow visualisation inside the tank.

The tank (size - 1100 mm diameter x 2600 mm height) is made of carbon steel. It is filled with service water up to 2400 mm.  Four window covers made of acrylic sheet are bolted securely on to these flanges to avoid any leakage through these joints (Fig. 6.2). These window flanges are suitably sized to insert the chimney model inside the tank. The bottom of the process water tank has three inlet nozzle connections. The central nozzle is made of 100 mm NB (nominal bore) pipe to provide the hot water flow into the chimney section. The other two bypass nozzles are of 50 mm NB size through which bypass flow is sent to the process water tank at lower temperature. The process water tank has two outlet nozzles

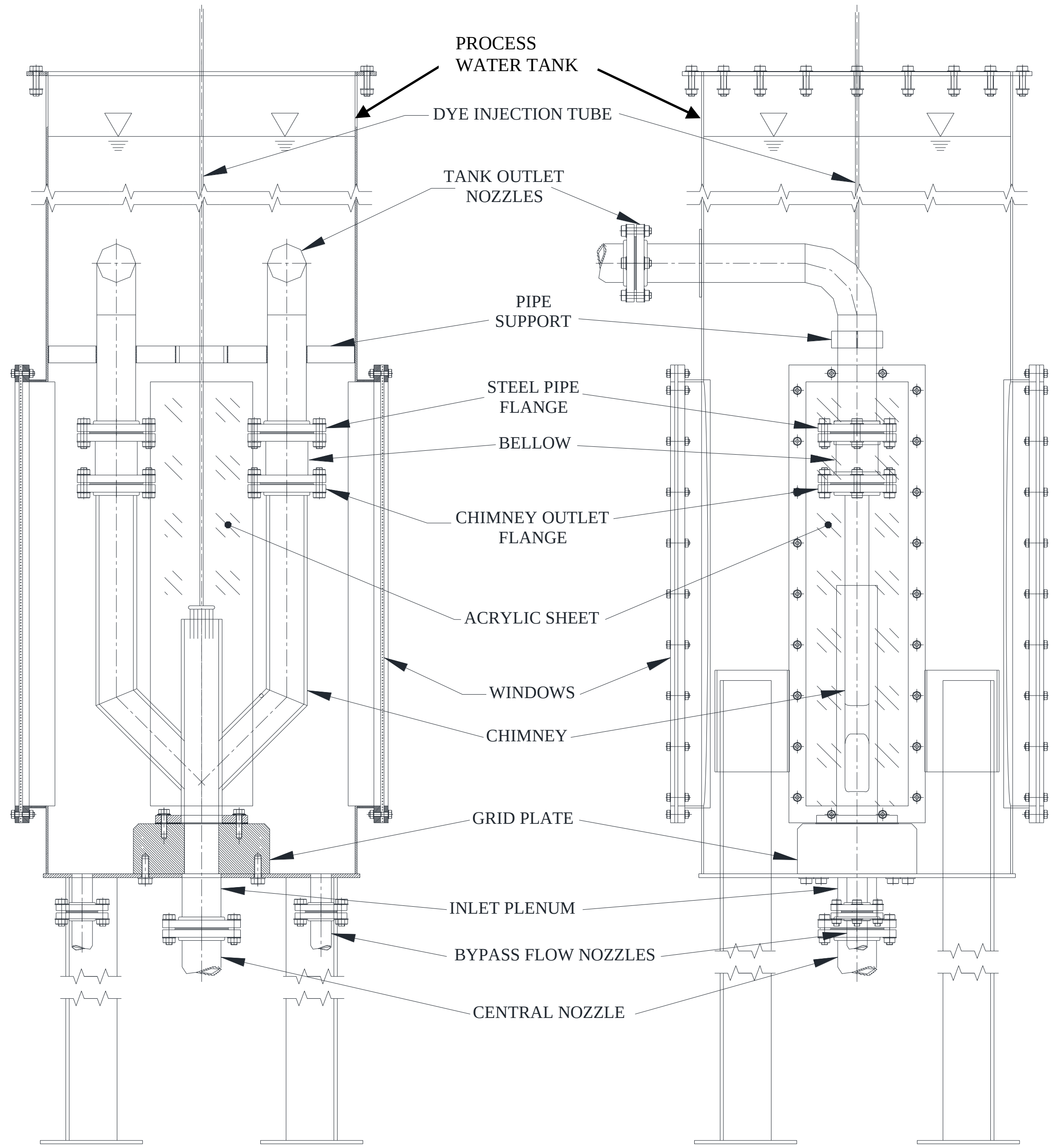


Fig. 6.2: Details of process water tank along with internals

of 100 mm NB size which is welded to the shell at a higher elevation and join to the chimney outlet nozzles through 90° bends.

As shown in Fig. 6.1b, the core outlet hot water at temperature T1 flows upward through chimney bottom inlet. The inlet cross section is a square geometry with side D. The upward flow velocity is $U_{in}$ which corresponds to a flow rate of water ($W_{in}$). Core bypass flow ($W_b$) is sent to the tank through two bypass inlet lines to compensate for the flow entering through the chimney top inlet in the downward direction. The temperature of the core bypass flow is $T_b$. Hot upward flow from the bottom and cold downward flow from the top mixes together just before the side outlets of the chimney and is sucked out of the chimney using pump through tank outlet lines of the process water system. Water temperature at tank outlet line is $T_{out}$. The core bypass flow ($W_b$) is varied to get bypass flow ratios (R) of 0.0, 0.05, 0.10 and 0.15. The effect of chimney height on the stagnation height ($h_S$) is studied using two acrylic models with (H/D) ratios of 5 and 6 in the experiments. Effect of Reynolds number ($Re_D$) and the effect of buoyancy force due to difference in temperature between the hot and cold water on the stagnation height is also tested.

## 6.2 Experimental loop

The test facility consists of two closed loop circulating water systems as detailed hereunder. Photographs of the experimental facility are shown in Fig. 6.3. For flow visualization study, a facility for injecting dye inside the chimney at y = 400 mm near the top opening of the chimney is provided as shown in Fig. 6.3b. This is used to visualise the height of the upward jet inside the chimney. Rhodamine-B is used as the dye for the experiment. For illumination under water, LED lights are attached with the wall of the tank focusing towards the region of interest of mixing inside the chimney.

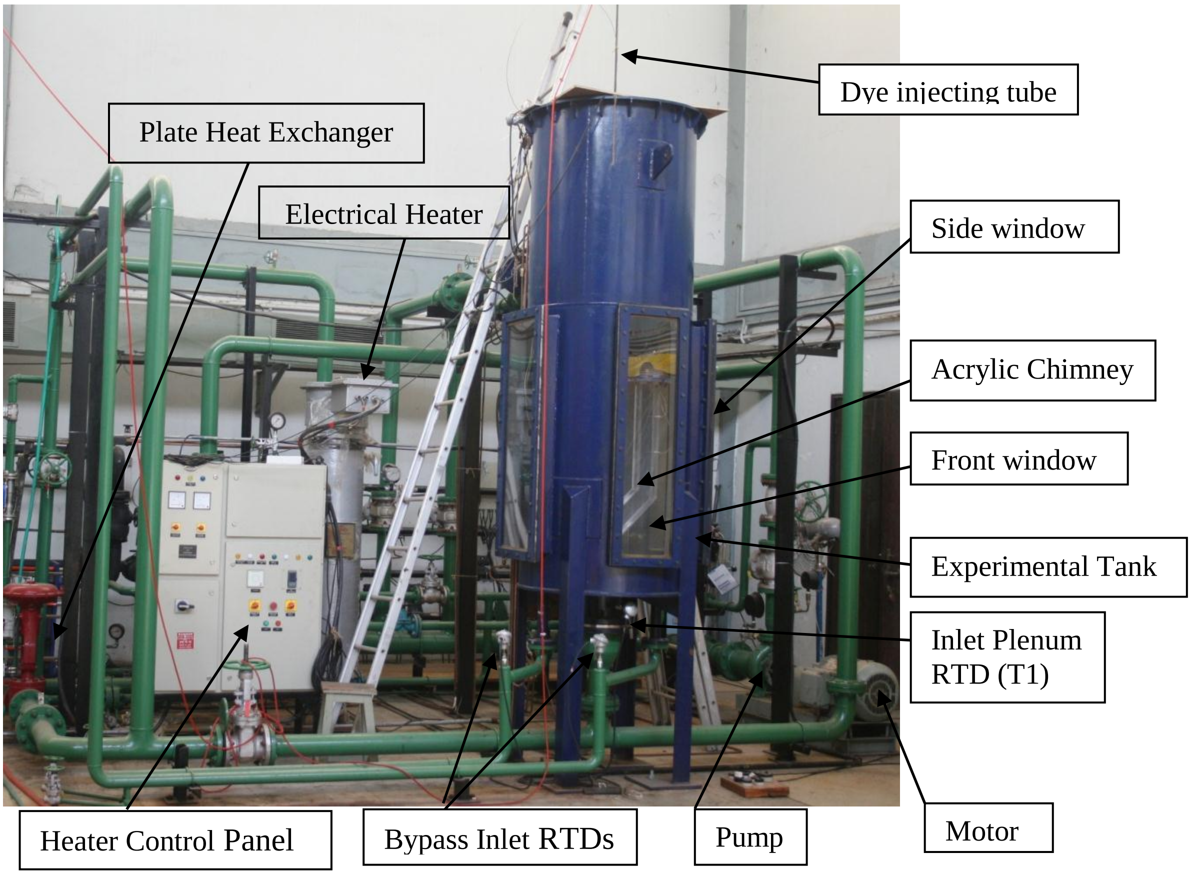


(a) Experimental setup

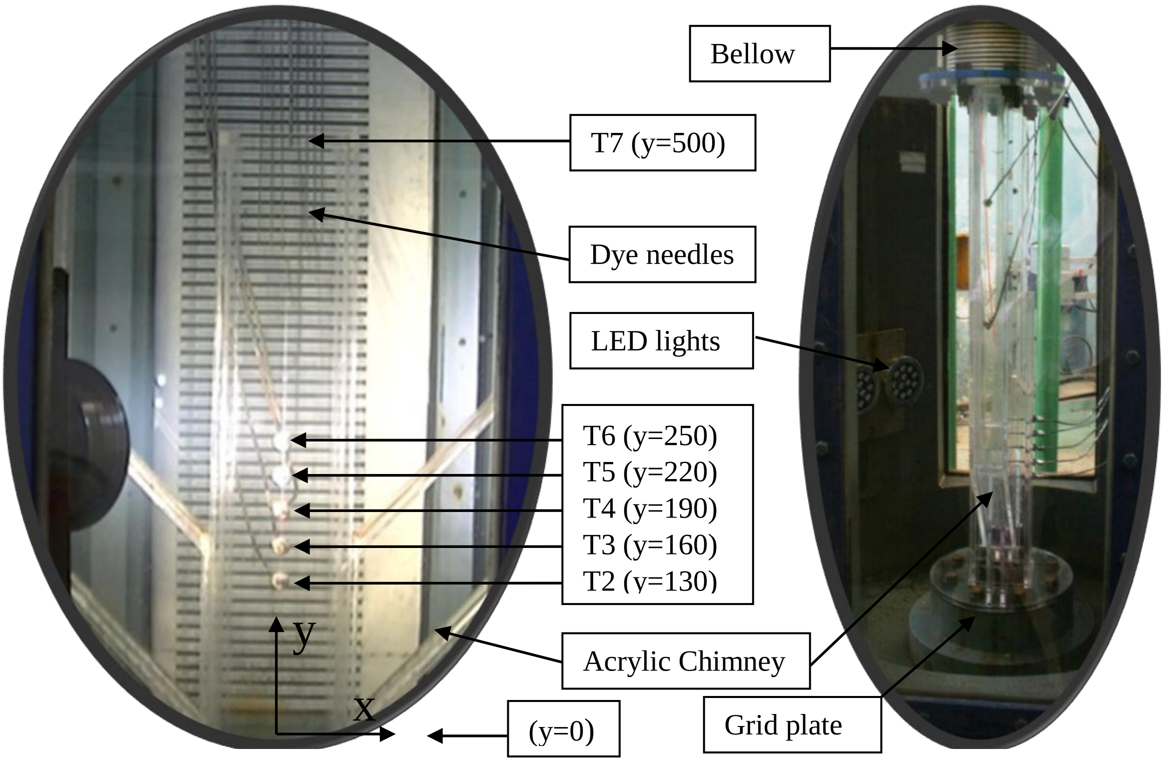


(b) View from front window
(RTD locations - dimensions in mm)

(c) View from side window

Fig. 6.3: Details of the experimental setup

*6.2.1 Process water system*

A simplified Process & Instrument diagram of the flow test facility is shown in Fig. 6.4. The process water system of the flow test facility consists of a centrifugal pump, an electric heater, a plate heat exchanger and a chimney test section immersed in a process water tank with a free level at the top. Two outlet pipe lines from the tank have individual valves to vary the resistances for keeping similar flow through each of the two lines. They form a common 150 mm NB line, which connects to the suction side of the process water pump. The rated capacity of the process water pump is 1800 liters per minute (lpm) with developed head of 30 meter of water column. The recirculation flow through the system is controlled by throttling the pump discharge valve or bypassing the flow to the pump suction through a 50 mm NB bypass line. The pump discharge line (100 mm NB) is connected to the chimney bottom inlet line. The flow rate through the chimney bottom is controlled with the help of a pneumatically operated control valve (FCV-1) installed at the upstream side of the chimney bottom inlet line. A 50 mm NB tapping is taken from the pump discharge line to send water through the thyristor controlled electrical heater to raise the temperature of water. The heater capacity is about 60 kW. Maximum flow through the heater is limited to 250 lpm to get a measurable temperature differential across the heater. This water is mixed with main flow to maintain the temperature of hot water at the bottom inlet of the chimney.

Another 50 mm NB tapping is taken from the pump discharge line to send water as bypass flow at lower temperature through a plate heat exchanger (i.e., the cooler). The flow through the cooler is varied from 0 to 180 lpm depending on the bypass flow to transfer heat to the chilled water system. Provision of bypassing the cooler is also made to operate the heat exchanger at lower heat capacity when required. The total flow through the cooler and its bypass is controlled by using a pneumatically operated control valve (FCV-2). The total core bypass flow is divided into two branches of 50 mm NB lines, which finally gets connected to the bottom 50 mm NB nozzles of the process water tank. The plate type heat exchanger is chosen as a cooler due to its compact design. The process water tank acts as the expansion tank and provides the required NPSH for the process pump.

*6.2.2. Chilled water system*

The chilled water system of the experimental facility is provided to transfer the heat from the process water system through the plate heat exchanger. The chilled water system consists of a chiller tank, a chiller pump, a chiller unit and associated piping of the system. The chiller tank of about 900 liters capacity is provided in the system and connected to the chilled water pump suction line to act as a capacitance of heat sink during tripping of compressor on low temperature. The pump is rated for 200 lpm flow and 30 meter water column head. The pump discharge line (50 mm NB) is connected to a chiller unit to supply chilled water at minimum temperature of 7°C to the secondary side of the plate heat exchanger. The chiller capacity is 22 Ton (~77 kW) consisting two sets of compressors, coolers and condensers. Provision for operating any one of the two units or both the units simultaneously is possible to take care of part load at various heat load conditions for maintaining the temperature of process water system. The chiller unit is cooled by air, which acts as the ultimate heat sink. Chilled water flow through plate heat exchanger is controlled by operating a flow control valve (FCV-3) installed at the upstream of the heat exchanger. Heat exchanger bypass provision on the chilled water side is also utilised to reduce the heat removal capability of the plate heat exchanger.

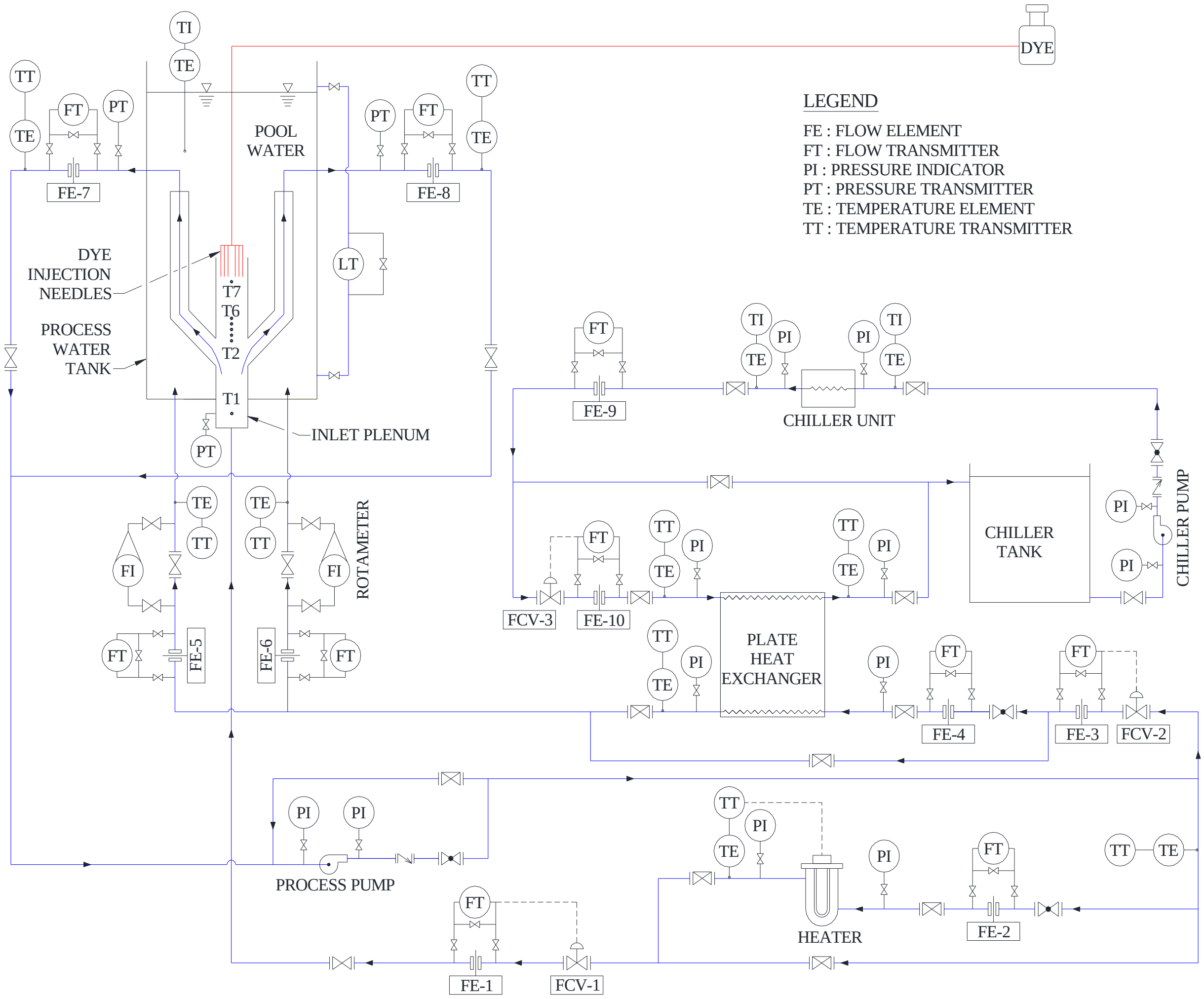


Fig.6.4: Simplified Process & Instrument diagram of experimental facility

### *6.2.3. Instrumentation*

Instruments have been provided to measure the flow rate, pressure and temperature at various locations in the process water system and also temperature profile inside the chimney. Pressure is measured at various locations using pressure gauges where local indication (PI) is required. Where recording of pressure is required, differential pressure transmitters with low pressure side open to atmosphere is used. Flow rate at various locations is measured mostly using orifice flow meters designed in accordance with the standard ISO 5167. Differential pressure transmitters connected across the orifice plates transmit the differential pressure signals. At two locations, flow rate is measured using metal tube rotameter. Temperature is measured using Pt-100 RTDs of accuracy Class A as per standard IEC 60751. Signals from all transmitters and RTDs are fed to a chartless recorder for display and recording.

The flow rate in the main supply line to the bottom inlet line (100 mm NB) of the chimney is measured using an orifice flow meter (FE-1) and can be maintained to a desired set value upto 1500 lpm by using the pneumatically operated flow control valve (FCV-1). The actuating control signal to the valve is given by a PID controller. The control signal current is converted to a pneumatic signal through an electro pneumatic valve positioner which feeds the actuator with the final actuating pressure. The feedback flow signal to the controller is derived from the orifice flow meter (FE-1). The part of the main flow which is sent through the heater is measured using another orifice flow meter (FE-2) installed in 50 mm NB heater inlet line.

The total core bypass flow rate is measured using an orifice flow meter (FE-3) and can be set to a desired value up to maximum 250 lpm. The core bypass flow is supplied through a pneumatically actuated control valve (FCV-2) installed in the plate heat exchanger inlet line prior to the tapping of the heat exchanger bypass line. Another orifice flow meter (FE-4) is installed to measure the part of the core bypass flow which is sent through the plate heat exchanger. Depending on the total core bypass flow to be sent to the process water tank through two 50 mm NB nozzles, flow through each bypass line is varied from 0 to 125 lpm. An orifice flow meter (FE-5 / FE-6) along with rotameter in parallel is provided to measure the flow rate through each bypass line. Flow rate from each vertical arm of the chimney is measured by using orifice flow meter (FE-7 / FE-8) located at the tank outlet lines.

Temperature distribution of water inside the chimney is measured using Pt100 RTDs installed directly in penetrations of the central chimney wall for faster response. Pt-100 RTDs are used for better stability, accuracy and interchangability. Five RTDs (T2 to T6) are installed along the height of the chimney at 30 mm interval starting from y=130 mm of the chimney. The RTDs are inserted perpendicular to the vertical chimney wall and protrude upto the centre of the flow channel. The compression fittings ensure that the chimney wall remains continuous, allowing no leakage. The compression fittings are also ensured to be flush with the inner face of the chimney wall to minimize flow disturbance. One RTD (T7) is provided at the centre of the top opening of the chimney (at y = 500 mm). Another RTD (T1) is located (at y = -325 mm) inside the inlet plenum to measure the upward flowing hot water temperature. To measure the temperature of water inside the process water tank, three Pt100 RTDs are located at y=1.3, 1.6, 1.9 m elevation with respect to the bottom of the tank. Water temperatures at other locations are measured using Pt100 RTDs with thermowell configuration and provided at pipe lines as detailed hereunder.

Water temperatures are measured at the 100 mm NB outlet pipe lines of the tank. Heater outlet water temperature is measured and used as the feedback signal for controlling this temperature. The mixed water temperature of main flow and flow through the heater is measured at the inlet plenum (mentioned earlier) before entering the bottom nozzle of the chimney. The heat exchanger outlet temperature and each core flow bypass temperature are also monitored.

Pressure transmitters are provided at the process water tank outlet lines as well as at the tank inlet line to monitor and record the pressure. Field mounted pressure gauges are provided at the inlet and outlet lines of all equipment. Level transmitter is provided to monitor the level of water in process water tank.

In the chilled water system, orifice flow meters are provided to measure the flow through the chiller unit (using FE-9) and also the part of the flow which is sent through the heat exchanger (using FE-10). Water temperatures are measured using Pt100 RTDs at inlet and outlet lines of the chiller unit and the heat exchanger. Pressure gauges are provided at the inlet and outlet lines of equipment such as chiller unit, secondary side of the heat exchanger and chiller pump.

The instrument details and accuracy of the measurement for various instruments used in experimental facility is given in Table-6.1.

Table-6.1: Instrument details and Accuracy of the measured values

| *Item* | *Description* | *Instrument Type* | *Max Flow (lpm)* | *DP (mmWC)* | *Accuracy* |
|---|---|---|---|---|---|
| FT-1 | Gross Inlet Flow through Chimney | Orifice Plate with DP Transmitter | 1500 | 3000 | 1.07% at full flow |
| FT-2 | Pre Heater Flow | Orifice Plate with DP Transmitter | 250 | 3000 | 0.88 % at full flow |
| FT-3 | Gross Inlet Flow to PW Tank | Orifice Plate with DP Transmitter | 250 | 3000 | 0.88% at full flow |
| FT-4 | PHE PW side Flow | Orifice Plate with DP Transmitter | 250 | 3000 | 0.88% at full flow |
| FT-5 | Flow through Bypass Line-1 | Orifice Plate with DP Transmitter | 125 | 1000 | 0.83% at full flow |
| FT-6 | Flow through Bypass line-2 | Orifice Plate with DP Transmitter | 125 | 1000 | 0.83% at full flow |
| FT-7 | Flow through Chimney outlet line-1 | Orifice Plate with DP Transmitter | 1800 | 4000 | 1.97% at full flow |
| FT-8 | Flow through Chimney outlet line-2 | Orifice Plate with DP Transmitter | 1800 | 4000 | 1.97% at full flow |
| FT-9 | Gross CW flow | Orifice Plate with DP Transmitter | 250 | 3000 | 1.05% at full flow |
| FT-10 | PHE CW side Flow | Orifice Plate with DP Transmitter | 250 | 3000 | 1.05% at full flow |
| PT-1 | Pressure in Chimney Outlet Pipe -1 | DP Transmitter (Low Side open to Atmosphere) | -- | -3000 to +2000 | 0.25% of Full scale |
| PT-2 | Pressure in Chimney Outlet Pipe -2 | DP Transmitter (Low Side open to Atmosphere) | -- | -3000 to +2000 | 0.25% of Full scale |
| PT-3 | Chimney bottom entry pressure | DP Transmitter (Low Side open to Atmosphere) | -- | 0-5000mm WC | 0.25% of Full scale |
| LT-1 | PW tank Level | DP Transmitter (Low Side open to Atmosphere) | -- | 0-2500 mm WC | 0.25% of Full scale |
| *Item* | *Description* | *Instrument Type* | *Accuracy Class* | *Accuracy Value* | |
| Temp Elem. (TE) | Chimney TEs and Loop TEs | 3 wire Pt-100 RTDs | Class A as per IEC 60751 | $\pm(0.15+0.002\|t\|)$ t is in $^{o}C$ | |

## 6.3 Experimental procedure

Different test cases considered in this experiment are listed in Table-6.2. For all the cases, the water level in the process water tank was kept at 2400 mm. The upward flow and bypass flow were adjusted to the desired values specified in the Table-6.2 with the help of flow control valves (Fig. 6.4). The upward core flow rates considered were 500, 1000 and 1500 liters per minute, which corresponds to Reynolds number of $1.5 \times 10^5$, $3.0 \times 10^5$ and $4.5 \times 10^5$ respectively. Bypass flow ratios of the downward flow and the upward flow were 0.15, 0.10, 0.05 and 0.00. Twelve sets of experiments were carried out for 500 mm chimney height. To check the effect of chimney height, another twelve sets of experiments were carried out with chimney height of 600 mm. Finally all these experiments were repeated for various temperature differentials between core flow and bypass flow to check their effects on the stagnation height and temperature profile.

Each experiment was carried out by following the steps mentioned hereunder. The primary coolant system was filled with water and system was vented to remove air pockets from the system. The process water tank was filled up to 2400 mm level and then the system was isolated from the water supply line. The chilled water system was also filled with water and kept ready for operation. Process water pump was started and the total flow rate was measured by flow element (FE-1). The flow rate was adjusted using the flow control valve (FCV-1) to get the desired core flow entering through the bottom of the chimney. Flow rate through the heater unit was measured by flow element (FE-2) to ensure that continuous flow through the electrical heater is available. Total bypass flow rate measured by flow element (FE-3) was adjusted to obtain the desired bypass flow ratio by using the flow control valve (FCV-2). Flow through each bypass line measured by flow elements (FE-5 and FE-6) was maintained equal by adjusting the resistance of valves in the bypass lines. Similarly valves are manipulated to get equal flow through the chimney outlet lines from the readings of flow elements (FE-7 and FE-8). Once these flows were established, the heater outlet temperature was set to the desired value. All the experiments were carried out by setting heater outlet temperature to either 40ºC or 45 ºC so that the acrylic windows of the process water tank did not get deformed due to higher water temperature. The thyristor controlled electrical heater was switched on and the heater outlet temperature started increasing. To reduce the water temperature of bypass flow, chilled water system pump was started. Chilled water flow through the chiller pump and the heat exchanger were monitored through flow elements FE-9 and FE-10 respectively. Both the compressors of chiller units were started to reduce the chilled water temperature at a faster rate. Due to heat transfer to chilled water by the plate heat exchanger, temperature of bypass flow started decreasing. Once the chilled water temperature reached below 8 ºC, one compressor was stopped and only one chiller unit was kept in operation. Heater outlet temperature started increasing and stabilised to the desired setting. Thyristor control system continued to operate and maintain the system at the set point till the heater current comes to zero. It was observed that the heater control system was able to maintain the temperature for a period of 20-30 minutes. During this period, dye injection was done for 20-30 seconds and dye injection was stopped. Video recording of the dye mixing was done for continuous monitoring of the mixing phenomenon inside the chimney to investigate the stagnation height. It was observed that due to highly turbulent flow, alternate vortices were created and stagnation height fluctuates. Finally snap shots were taken to predict the maximum stagnation height at the central axis of the chimney. In addition to stagnation height ($h_S$), vortex spread height ($h_V$) was also predicted from the snapshot. The stagnation height, $h_S$ and vortex spread height, $h_V$ are shown in Fig. 6.5. Vortex spread height is defined as the maximum height, the dye reached due to formation of alternate vortices created nearer to both left and right side walls ($x = \pm$ 50 mm) inside the chimney. Temperature recording was also done using chartless recorder and temperature profiles were generated for various flow conditions. Separate experiments were also done with the same flowing conditions of core flow and bypass flow without heater and chiller in operation and video recording was done by injecting dye to check the mixing behaviour without temperature differential.

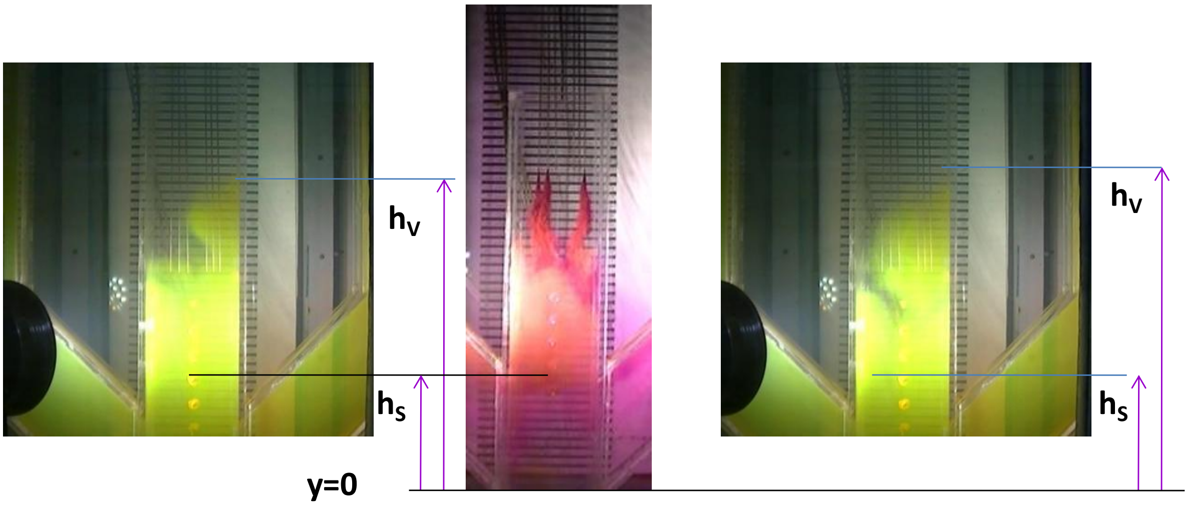


Fig. 6.5: Stagnation height ($h_S$) and Vortex spread height ($h_V$)

For various bypass flow ratios and core flow conditions, this experimental procedure was followed. Once all the experiments were completed for the chimney with 500 mm height, it was removed and the other chimney with 600 mm height was installed inside the tank. Again all these experiments with different conditions as mentioned above were repeated. Basic objectives of these experiments were to find out the stagnation height, vortex spread height and temperature profile inside the chimney for various cases of flow rates and chimney heights. Finally non-dimensionalisation of the results was done to bring them in similar platform to compare the results with respect to the numerical results.

The following sections describe the results from all these experiments.

## 6.4 Experimental results and discussion

Based on the procedure mentioned above, experiments were carried out for the cases mentioned in Table-6.2. The flow and temperature variations are described in details for the 500 mm chimney height.

Table-6.2: Test cases for the model chimney (H = 500 mm)

| Sr. No. | Upward flow through chimney (lpm) | Upward velocity ($U_{in}$ - m/s) | Reynolds number ($Re_D$) | Bypass flow ratio (R) | Downward bypass flow through top of chimney (lpm) |
|---|---|---|---|---|---|
| 1 | 500 | 0.83 | $1.5 \times 10^5$ | 0.15 | 75 |
| 2 | 500 | 0.83 | $1.5 \times 10^5$ | 0.10 | 50 |
| 3 | 500 | 0.83 | $1.5 \times 10^5$ | 0.05 | 25 |
| 4 | 500 | 0.83 | $1.5 \times 10^5$ | 0.00 | 0 |
| 5 | 1000 | 1.66 | $3.0 \times 10^5$ | 0.15 | 150 |
| 6 | 1000 | 1.66 | $3.0 \times 10^5$ | 0.10 | 100 |
| 7 | 1000 | 1.66 | $3.0 \times 10^5$ | 0.05 | 50 |
| 8 | 1000 | 1.66 | $3.0 \times 10^5$ | 0.00 | 0 |
| 9 | 1500 | 2.50 | $4.5 \times 10^5$ | 0.15 | 225 |
| 10 | 1500 | 2.50 | $4.5 \times 10^5$ | 0.10 | 150 |
| 11 | 1500 | 2.50 | $4.5 \times 10^5$ | 0.05 | 75 |
| 12 | 1500 | 2.50 | $4.5 \times 10^5$ | 0.00 | 0 |

### 6.4.1 Effect of bypass flow ratio

i) Bypass flow ratio = 0.15

Flow rate through the chimney bottom inlet representing core flow is about 500 lpm and total bypass flow is about 75 lpm as shown in Fig. 6.6a. Flow through each bypass line is about 37.5 lpm. Flow through the plate heat exchanger (PHE) is 75 lpm. Flow through the heater is about 270 lpm. Flow through each of the tank outlet line is about 287.5 lpm. All these flow rates are maintained constant during the experiment for 2200 s as shown in Fig. 6.6a. Heater outlet temperature is set to 40ºC for this experiment. Water temperatures recorded at an interval of 1 s inside the chimney (T1 to T7) is shown in Fig. 6.6b. The temperature (T1) of upward flowing hot water is maintained at about 39.6 ºC. The downward flowing cold water temperature (T7) at the top opening of the chimney is maintained at 31 ºC. The temperatures at which core bypass flows supplied are also maintained at 30.9 ºC and 31.1 ºC. Water temperatures of tank outlet-1 and tank outlet-2 are observed to be almost constant at about 38.2 and 38.4 ºC respectively. However, temperature fluctuations are observed in the region of mixing between hot and cold water (T2 to T6) as shown in Fig. 6.6b. Maximum fluctuations are observed at T3 (standard deviation of 1.17 ºC) and T4 (standard deviation of 0.92 ºC) locations. This is the region where vigorous mixing between the two opposing flows takes place inside the chimney.

The mean temperature and standard deviation of all the measured temperatures (T1 to T7) are calculated. The water temperature (T8) at the location (y = -100 mm) where acrylic chimney bottom flange starts just above the top of the grid plate is predicted from the heat balance equation considering the flow rates and corresponding temperatures at chimney top entry and tank outlet (T7 and Tout). The resulting centre line temperature profile is predicted along the height as shown in Fig. 6.6c. From the profile it is observed that the effect of upward flowing hot water completely dies down at a height of y=276 mm. At larger heights, water temperature is almost constant. Therefore, for the present case, the pool temperature front enters through the top opening of the chimney and reaches up to y = 276 mm.

The image captured using dye injection is shown in Fig. 6.6d. It is observed from the figure that maximum stagnation height (where the upward flow velocity is zero) is at y= 176 mm i.e., near to the location between temperature sensor T3 and T4. The interface of the two regions is visible from the image. However, the spread of the dye is observed up to a maximum height of y=292 mm towards the wall of chimney because of the alternate vortices created beyond the interface.

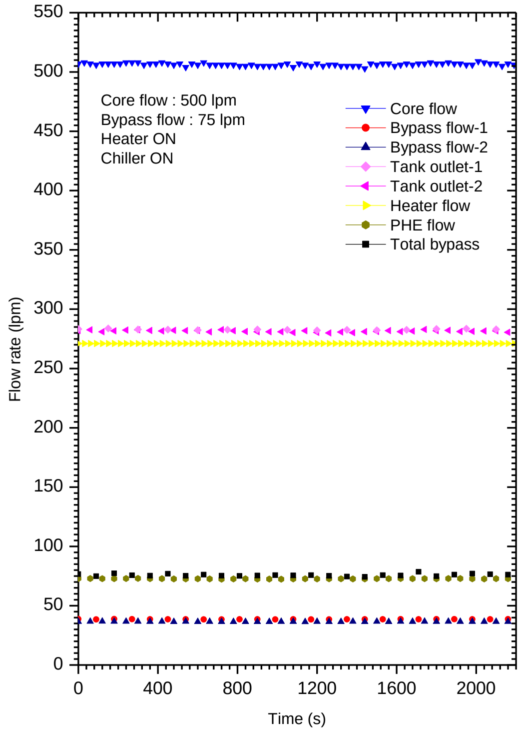


(a) Measured flow rates

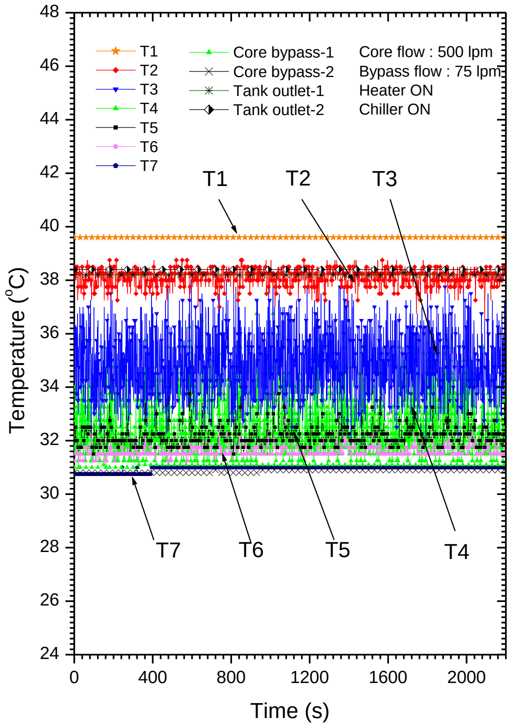


(b) Measured water temperatures

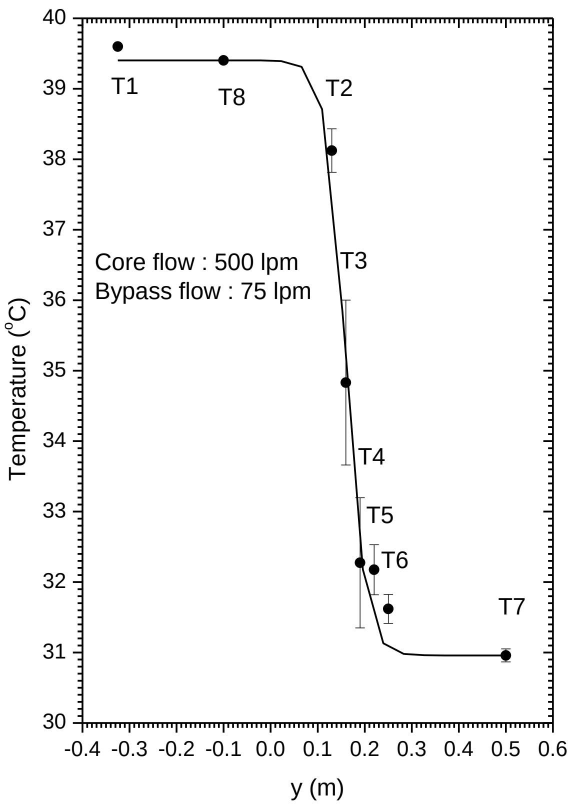


(c) Measured temperature profile

(d) Photographed image

Fig. 6.6: Experimental results ($W_{in}$=500 lpm, $W_b$=75 lpm)

ii) Bypass flow ratio = 0.10

The total bypass flow is reduced to 50 lpm and core flow is maintained at 500 lpm as shown in Fig. 6.7a. Flow through each bypass line is about 25 lpm. Flow through the plate heat exchanger and the heater is about 50 lpm. Heater flow is about 270 lpm. Flow through each of the tank outlet lines is about 275 lpm. The steady operation of the experiment is observed for a period of 2000 s. Heater outlet temperature is maintained at 40 ºC. The hot water temperature (T1) is maintained at 39.6 ºC in the experiment as shown in Fig. 6.7b. The cold water temperature (T7) at the top entry of chimney is maintained at 28 ºC. Core bypass water temperature supplied by the heat exchanger is about 27.7 ºC and 27.8 ºC. Water temperatures at the tank outlet lines are about 38.3 ºC and 38.5ºC. From the measured temperatures, temperature profile is generated as shown in Fig. 6.7c. It is observed from these results that the water temperatures in the mixing region are showing fluctuations at locations from T3 to T6. Maximum fluctuations of similar order (standard deviation of 1.5 ºC and 1.6 ºC) are observed at T3 and T4. It is observed from Fig. 6.6c that the maximum fluctuation takes place at T3 location for the case with bypass flow ratio of 0.15. With decrease in bypass flow ratio to 0.10, this point shifts up towards T4 location. This clearly shows that hot water jet effect has now moved more towards T4 location from T3. From the centre line temperature profile (Fig. 6.7c), it is observed that the zone of mixing has now moved up to a maximum height of y=382 mm beyond which water temperature is almost constant up to the top of the chimney.

The image captured using dye is shown in Fig. 6.7d. It is observed that the interface of hot water and cold water is shifted towards T4. The interface is observed to vary and the maximum stagnation height is found to be y=192 mm. Because of the alternate vortices created above this region, spreading of dye is observed upto maximum height y= 316 mm.

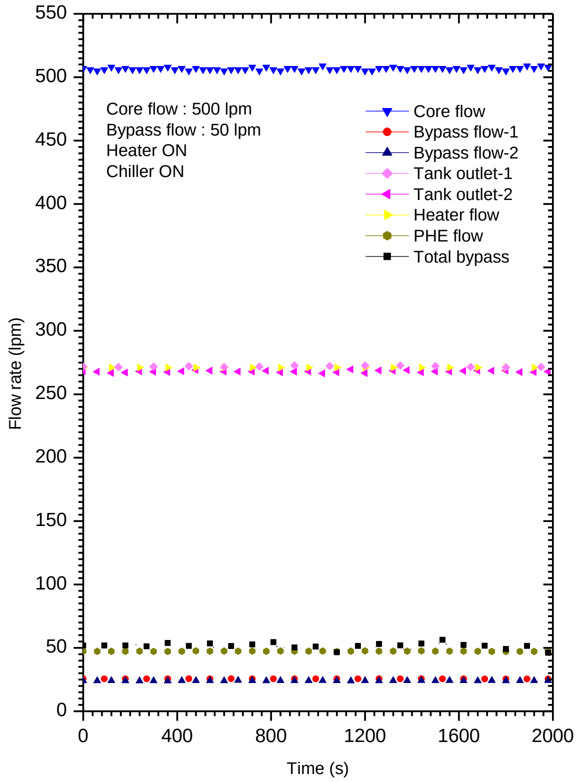


(a) Measured flow rates

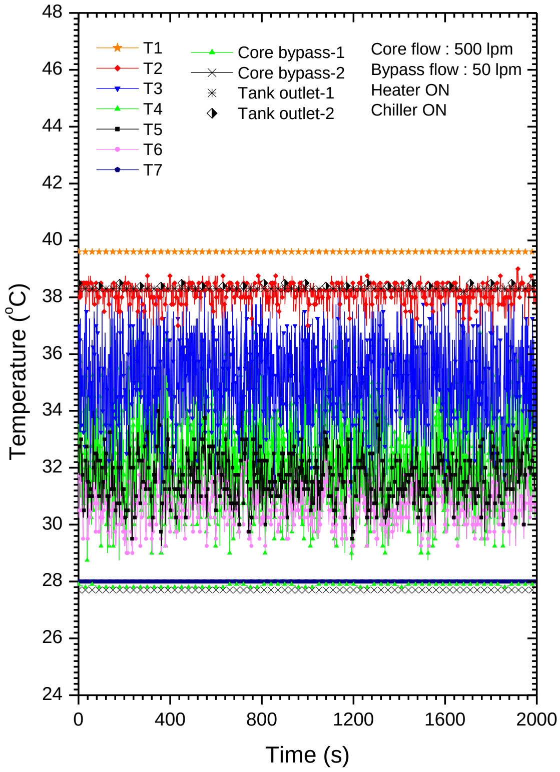


(b) Measured water temperatures

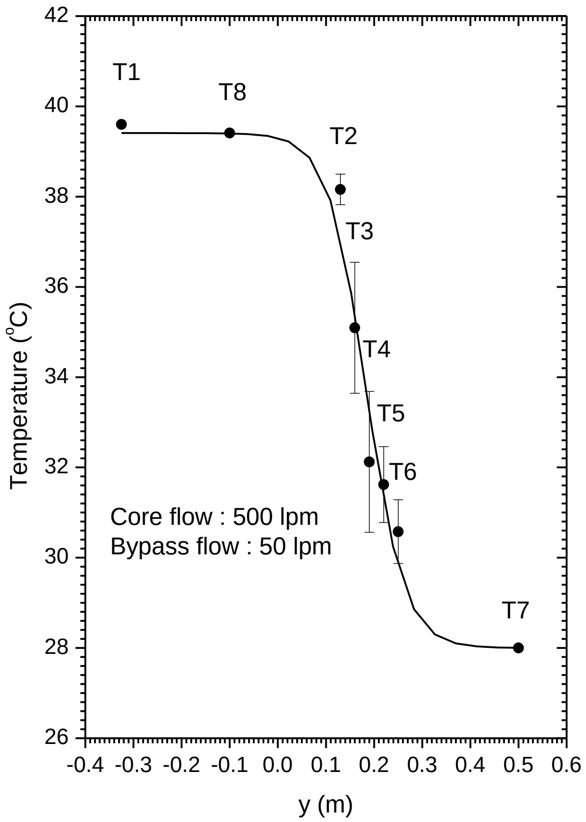


(c) Measured temperature profile

(d) Photographed image

Fig. 6.7: Experimental results ($W_{in}$=500 lpm, $W_b$=50 lpm)

iii) Bypass flow ratio = 0.05

For this case total bypass flow is further reduced to 25 lpm keeping core flow the same as 500 lpm. Figure 6.8a shows the variation of flow rates through plate heat exchanger, heater, tank outlet lines and core bypass flow lines which were maintained constant during the experiment. Figure 6.8b shows the variation of water temperature at various locations inside the chimney (T1 to T7) and also at core bypass lines and tank outlet lines. It is observed that temperature of hot water (T1) is steady for a period of 1800 s at 39.6 ºC. Core bypass temperatures is also maintained at 20.2 ºC and 20.4 ºC. Tank outlet temperatures are found to be 38.4 ºC and 38.6 ºC. From the results it is observed that though these temperatures are steady, temperature fluctuations are present inside the chimney at locations T3 to T6 as observed in the earlier cases. The maximum fluctuation is observed at T4 location (standard deviation of about 2 ºC). It is also found that temperature fluctuations at T5 and T6 locations (about 1.2 ºC) are more than 50% of that of T4 for this case. When bypass flow is 75 lpm, fluctuations at T6 location are negligible (about 0.2 ºC) as shown in Fig. 6.6c. As bypass flow is reduced to 50 lpm, fluctuations increases to be about 0.7 ºC as shown in Fig. 6.7c. It clearly shows that the mixing interface is moving up with decrease in bypass flow more and more, leading to disturbances propagating further upward. Variation of centerline water temperature with 25 lpm bypass flow is shown in Fig. 6.8c. It is found that hot water temperature effect spreads beyond the maximum chimney height (y=500 mm) and the behaviour of long column of constant cold water temperature at the top region is not observed here as against the temperature profile shown in Fig. 6.6c and Fig. 6.7c.

Photographed image with dye injection indicates the location of the interface between the upward and downward flow in Fig. 6.8d. The maximum stagnation height is found to be about 201 mm. Though the velocity of upward jet is limited up to this height, alternate vortices created above this region caused a large spread of turbulent region where circulations are present. It is observed that the dye spreads almost nearer to the top opening of the chimney.

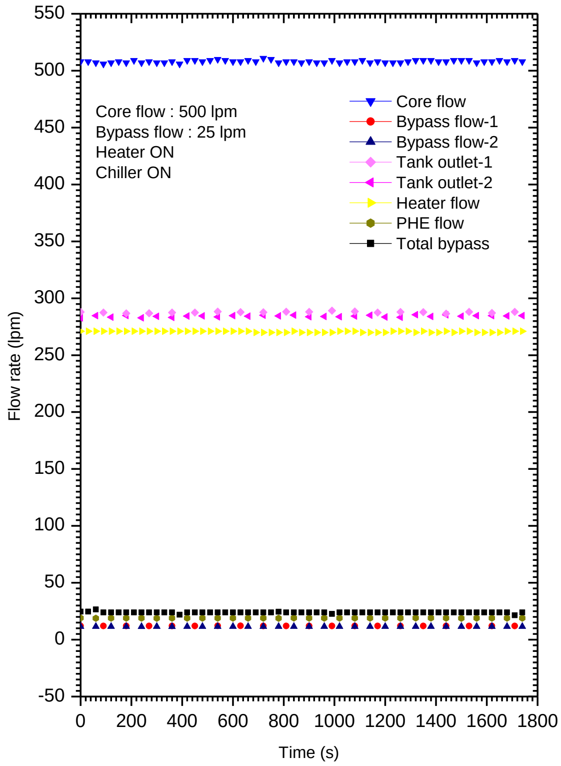


(a) Measured flow rates

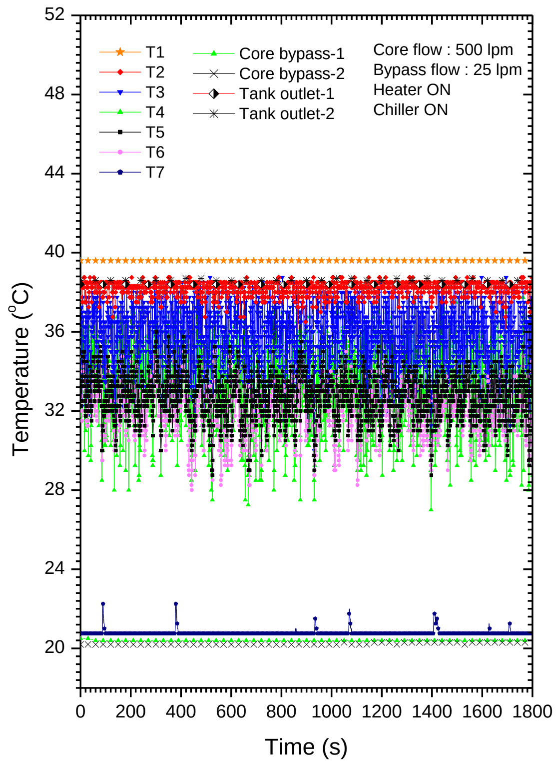


(b) Measured water temperatures

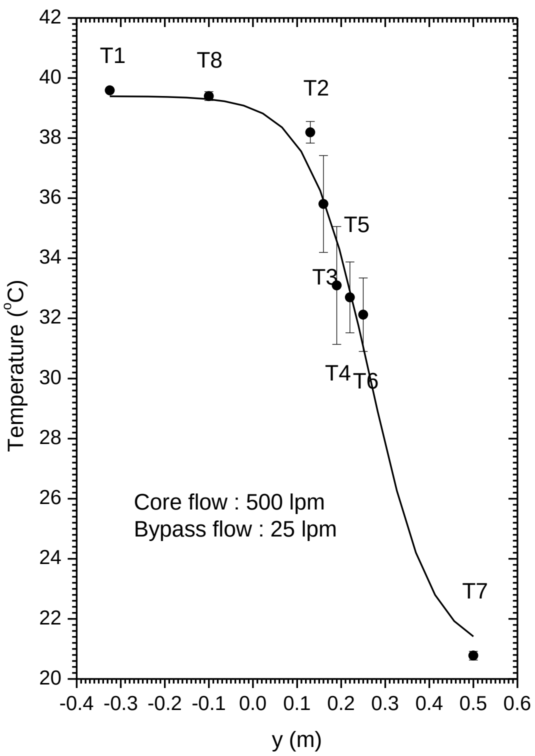


(c) Measured temperature profile

(d) Photographed image

Fig. 6.8: Experimental results ($W_{in}$=500 lpm, $W_b$=25 lpm)

iv) Bypass flow ratio = 0.00

When bypass flow is reduced to zero, the hot water supply temperature at the chimney bottom inlet is maintained by using the thysristor controlled heater. Chiller unit is not operated since bypass flow is not available. Because of this reason, steady temperature is maintained for a shorter period of time (about 1200 s) for this case as shown in Fig. 6.9b. Flow variations through heater, core, tank outlet lines are shown in Fig. 6.9a. Core flow is maintained at 500 lpm. Flow rates through each bypass line and plate heat exchanger are zero. Heater flow is about 270 lpm. Hot water temperature is maintained at about 39.8 ºC. Tank outlet temperatures are about 39.3 ºC and 39.5 ºC. It is observed from Fig. 6.9b that all temperatures from T2 to T6 reach to almost the same value (38.8 ºC to 39.3 ºC) and the fluctuations in these locations reduce to a small value (standard deviation less than 0.3 ºC). This is because the forced mixing of opposing flow near to these regions (T2 to T6) are absent for this case. Large eddies are created which cause uniform mixing and almost uniform temperature profile for all these locations from T2 to T6. However, a large fluctuation of temperature is observed at chimney top entry region (T7 location). This large fluctuation (standard deviation of 1.5 ºC) is due to the flow interactions between the pool and top region of the chimney. Here flow from the chimney reaches beyond the chimney and gets mixed with pool water.

This is clearly observed from the image captured using dye injection as shown in Fig. 6.9d. Therefore, the effect of vortices reaches beyond the chimney for zero bypass flow case. The height up to which upward velocity has reduced to zero is seen near the location of T5. Maximum stagnation height is observed to be about 225 mm.

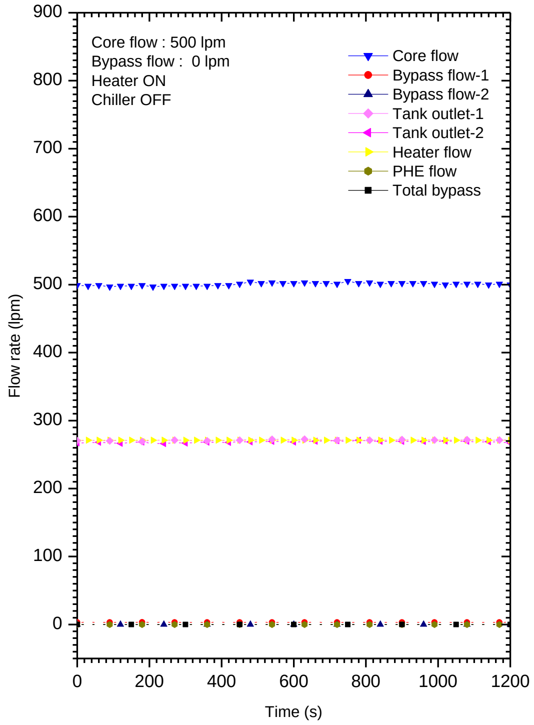


(a) Measured flow rates

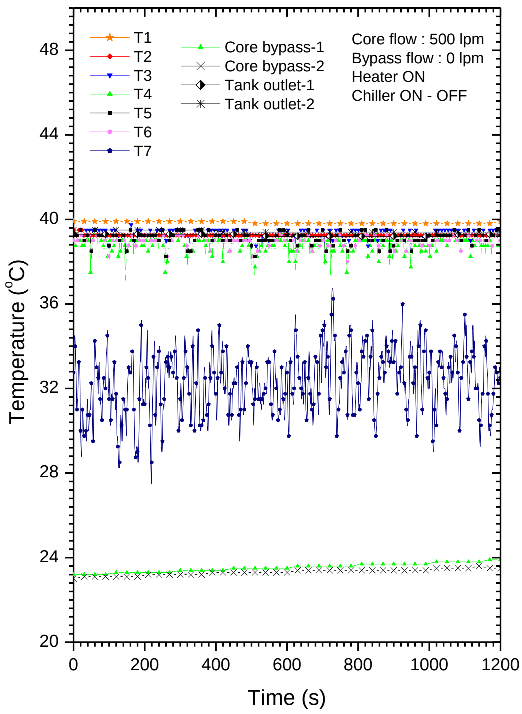


(b) Measured water temperatures

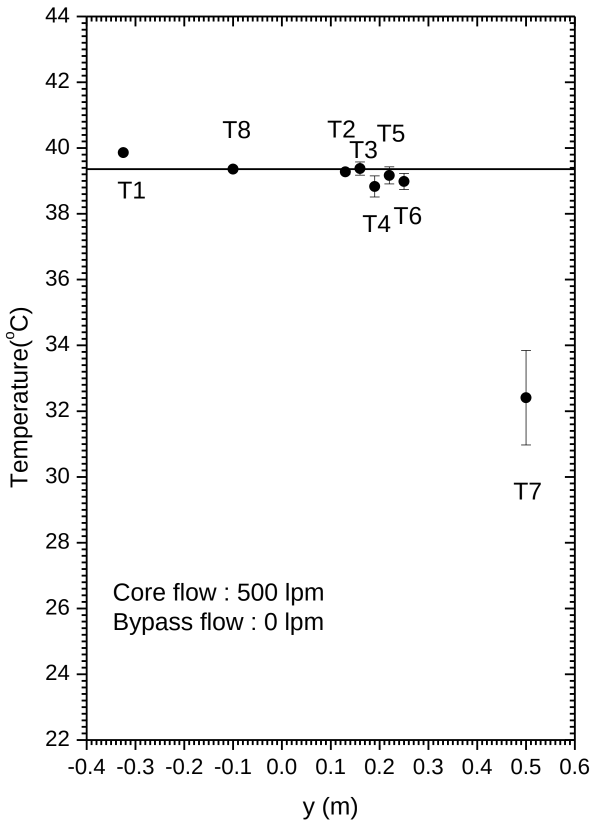


(c) Measured temperature profile

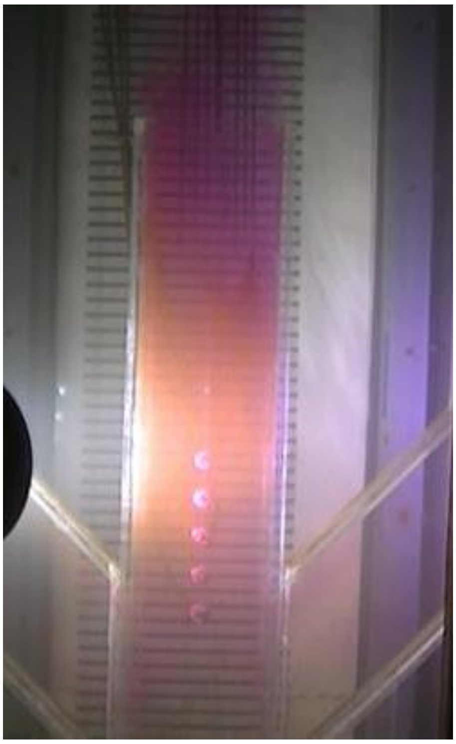

(d) Photographed image

Fig. 6.9: Experimental results ($W_{in}$=500 lpm, $W_b$=0 lpm)

### 6.4.2. Effect of Core flow

In order see the effect of increasing Reynolds number, core flow was increased to 1000 and 1500 lpm and experiments were carried out for various bypass ratios (0.15, 0.10, 0.05 and 0.00). The results of these experiments are shown in Fig. 6.10 to 6.17.

Figure 6.10 shows variation of flow rates, water temperatures at various locations, centre line temperature profile for the case with core flow of 1000 lpm and total bypass flow of 150 lpm. Flow rates through the plate heat exchanger and the heater are 150 lpm and 270 lpm respectively. Hot water temperature (T1) is maintained at 39ºC for 2000 s. Chimney top entry temperature (T7) is maintained at about 33.9ºC. Temperature fluctuations are observed at locations T3 and T4 (standard deviation about 0.5ºC). Maximum fluctuation is observed at T3. The interface between hot fluid and cold fluid occurrs between T3 and T4 locations. Image captured using dye shows that the maximum stagnation height is about 174 mm. The region of vortices created above this region is also observed which spreads the dye to a maximum height of y = 295 mm. From the centre line temperature profile (Fig. 6.10c), it is observed that water temperature is almost constant from y = 277 mm to the chimney top.

In the next case, the bypass flow is reduced to 100 lpm keeping core flow of 1000 lpm. the resulting temperature profile is shown in Fig. 6.11c. The hot water temperature is maintained at 39.1ºC. The experiment is done for a period of 2700 s. The temperature at chimney top is maintained at 32.4ºC. Temperature fluctuations are observed at locations from T3 to T6. Maximum fluctuation is observed at T4 as against T3 for the previous case of 150 lpm bypass flow indicating a higher height of interface in this case. It is observed that water temperature is almost constant in the upper part of the chimney beyond y =390 mm. Captured image of dye injection shows that maximum stagnation height reaches up to y=191 mm. Due to alternate vortices created on both the sides, the dye spreads up to a maximum height of y = 320 mm.

Bypass flow is further reduced to 50 lpm keeping the core flow same. The variations of flow rates, temperatures are shown in Fig. 6.12a and 6.12b. The hot water temperature (T1) is maintained at 39 ºC for 2500 s. Chimney top entry temperature is 27.7 ºC. Center line temperature profile along the height of the chimney is shown in Fig. 6.12c. Maximum temperature fluctuation is observed at location T4 (standard deviation 1ºC). Fluctuation is also seen to propagate to T5 and T6 (standard deviation 0.5 ºC). The hot water temperature effect has reached beyond the top of the chimney (about y = 500 mm). Maximum upward stagnation height is observed at y = 202 mm from the captured image using dye as shown in Fig. 6.12d.

When bypass flow is stopped and core flow is 1000 lpm, the experiment is continued up to 1250 s (Fig. 6.13) using the thyristor controlled heater. The hot water temperature (T1) is maintained at about 39.8 ºC. Temperatures T2 to T6 reach to almost similar value (39.2 to 39.7 ºC). Temperature fluctuations in these locations are found to be almost negligible. However, fluctuations at the chimney top entry location are increased (standard deviation 0.9 ºC). The similar phenomenon is also observed for 500 lpm core flow with zero bypass flow case. The captured image is shown in Fig. 6.13d. Maximum stagnation height is found to be y = 222 mm. The dye has reached beyond the chimney height showing activity would reach the reactor pool through the top opening of chimney in case of zero bypass flow.

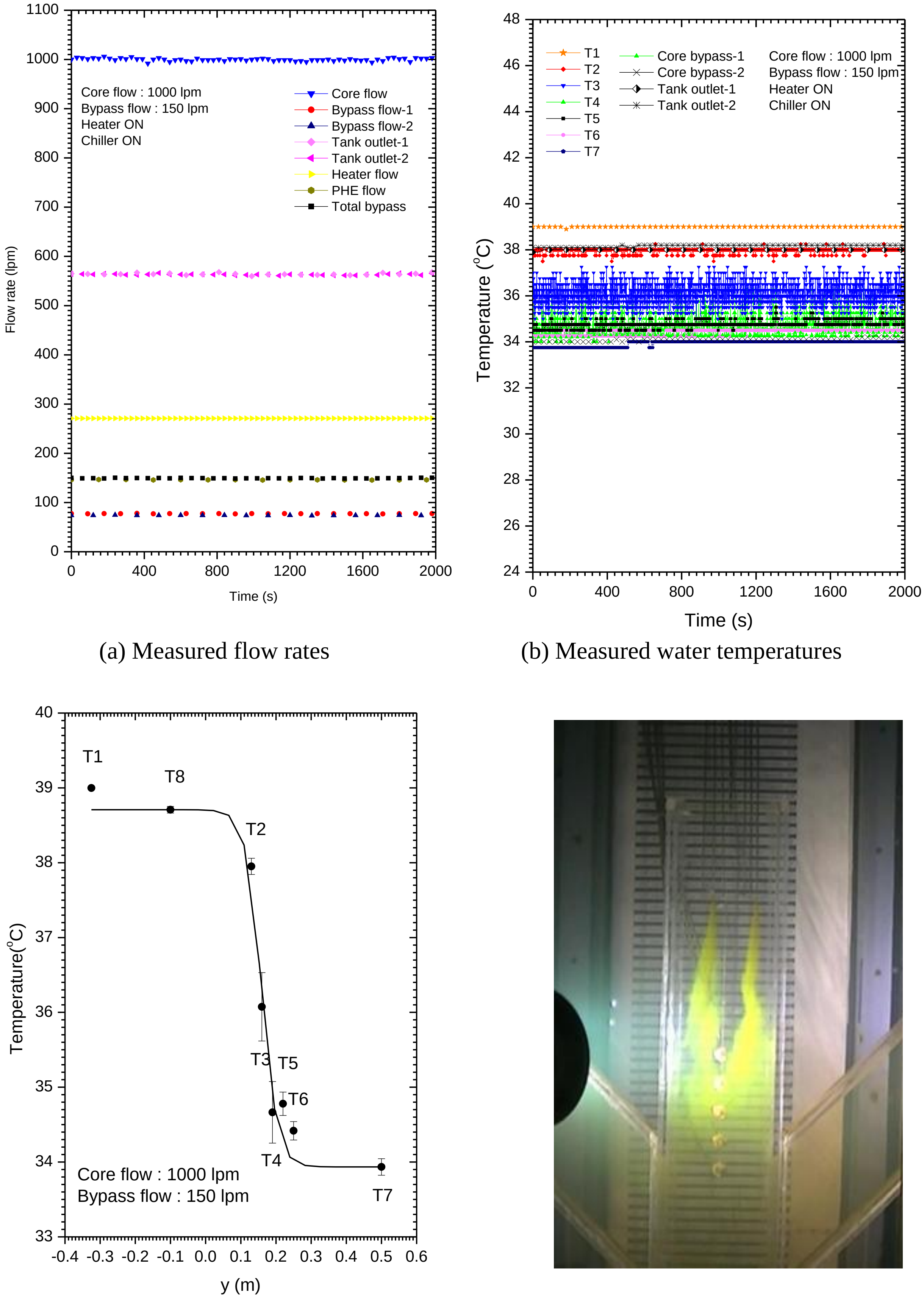


(a) Measured flow rates

(b) Measured water temperatures

(c) Measured temperature profile

(d) Photographed image

Fig. 6.10: Experimental results ($W_{in}$=1000 lpm, $W_b$=150 lpm)

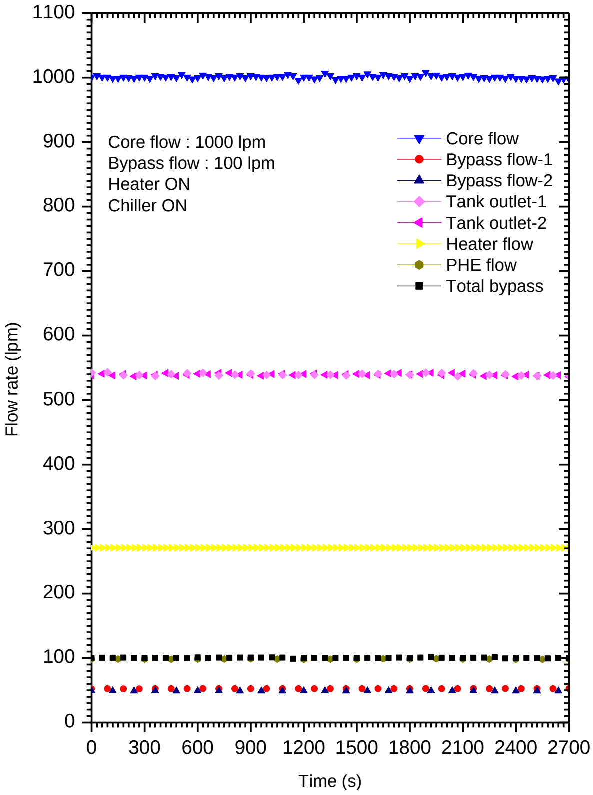


(a) Measured flow rates

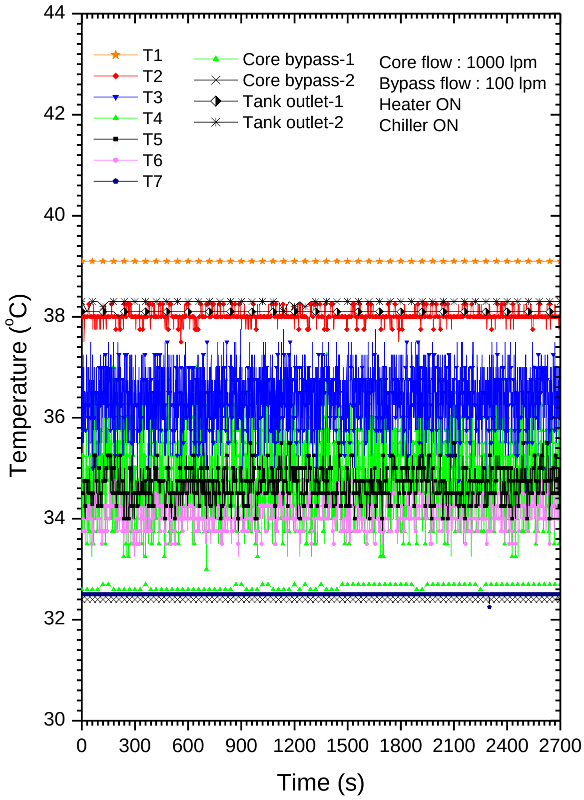


(b) Measured water temperatures

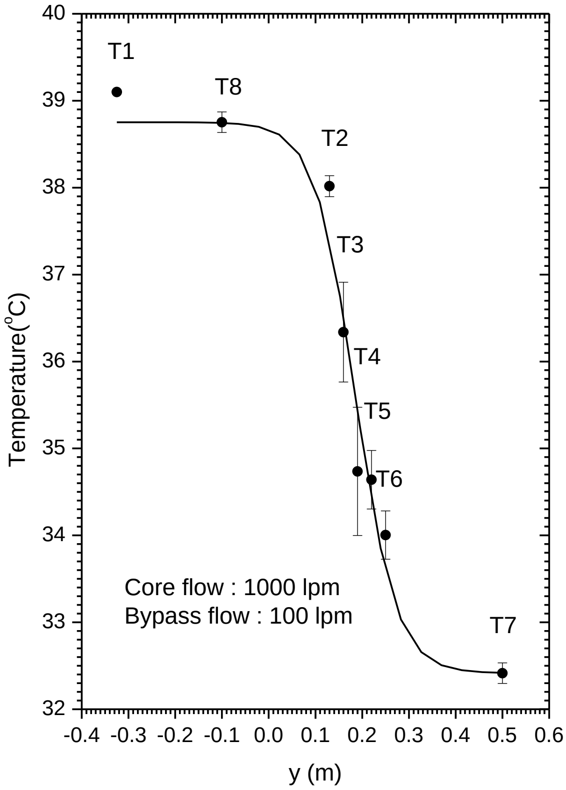


(c) Measured temperature profile

(d) Photographed image

Fig. 6.11: Experimental results ($W_{in}$=1000 lpm, $W_b$=100 lpm)

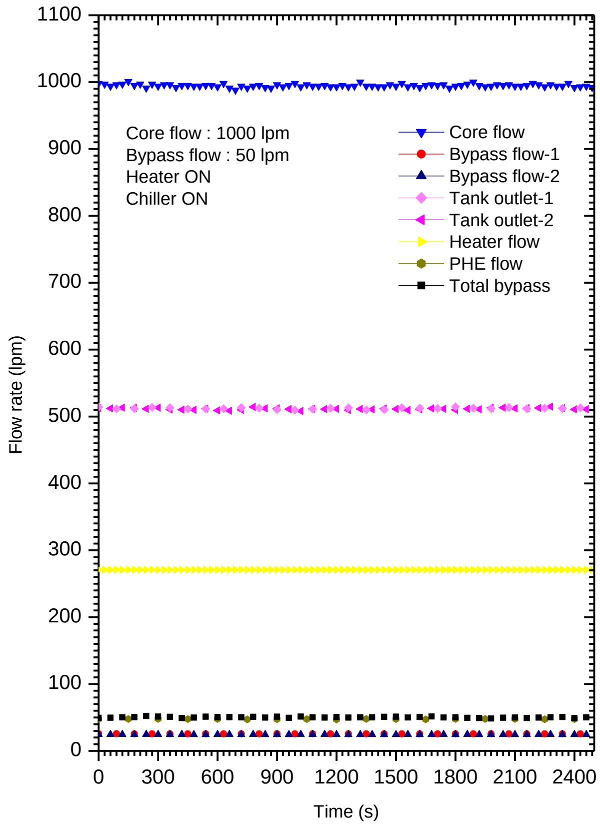


(a) Measured flow rates

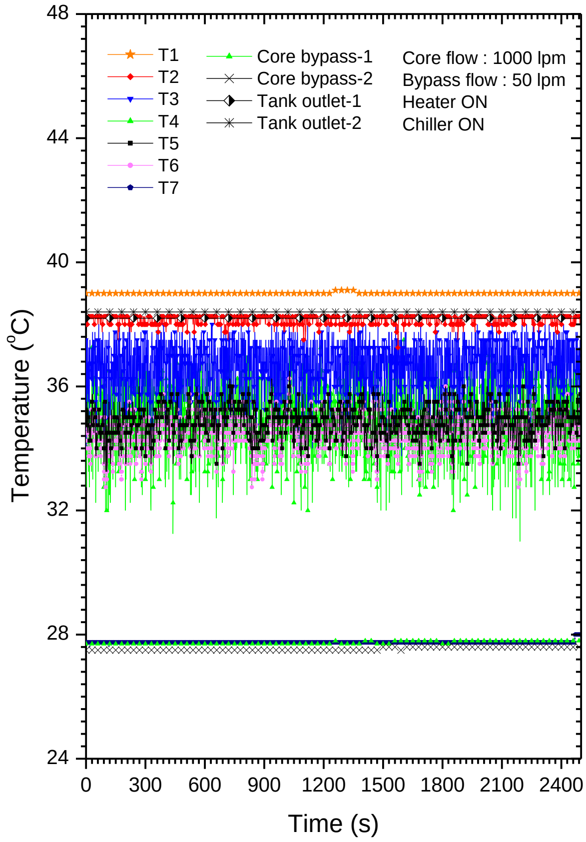


(b) Measured water temperatures

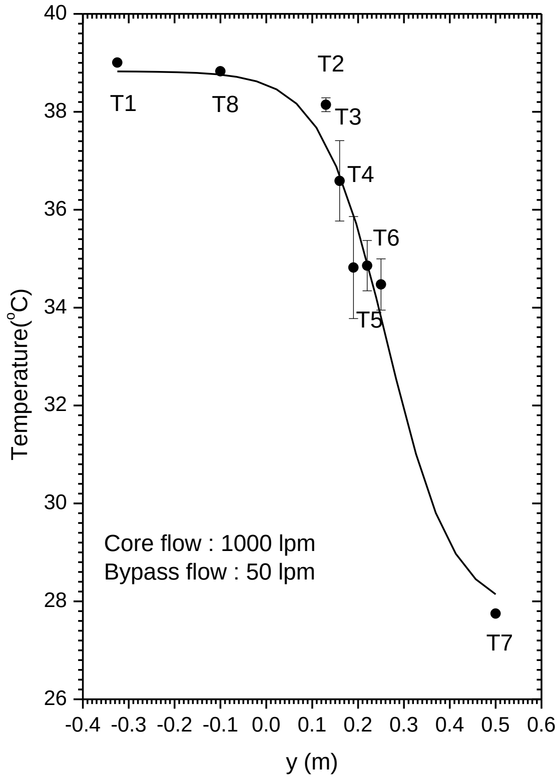


(c) Measured temperature profile

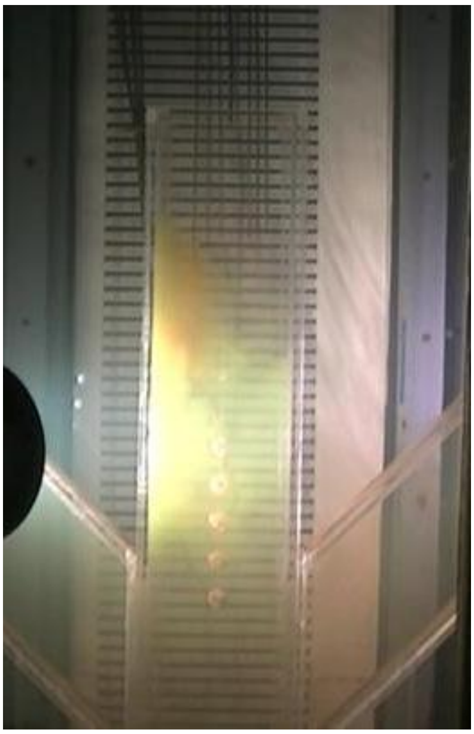

(d) Photographed image

Fig. 6.12: Experimental results ($W_{in}$=1000 lpm, $W_b$=50 lpm)

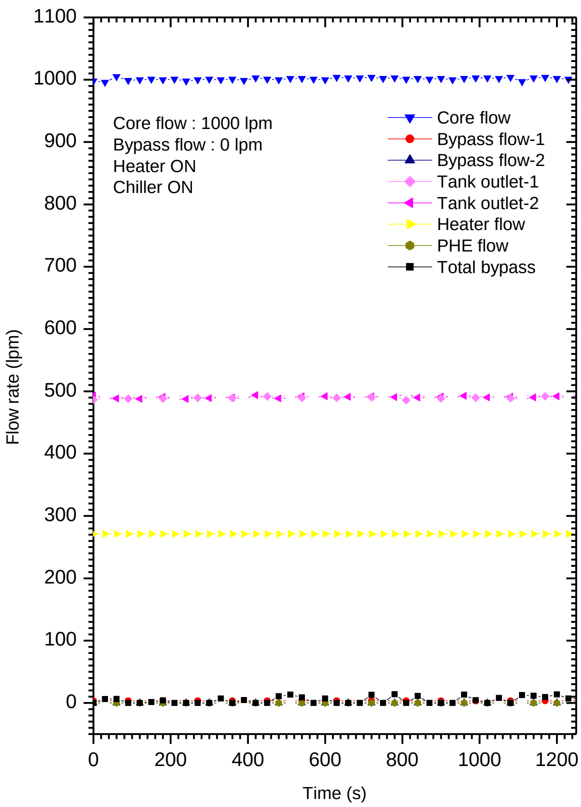


(a) Measured flow rates

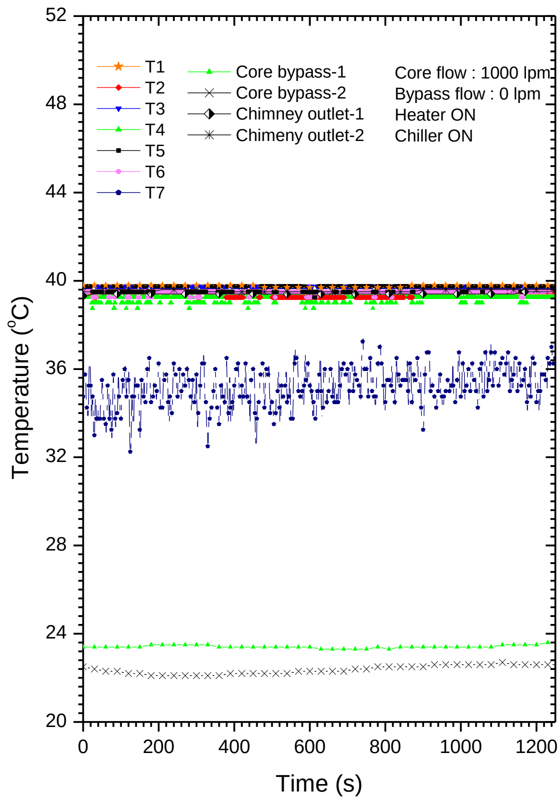


(b) Measured water temperatures

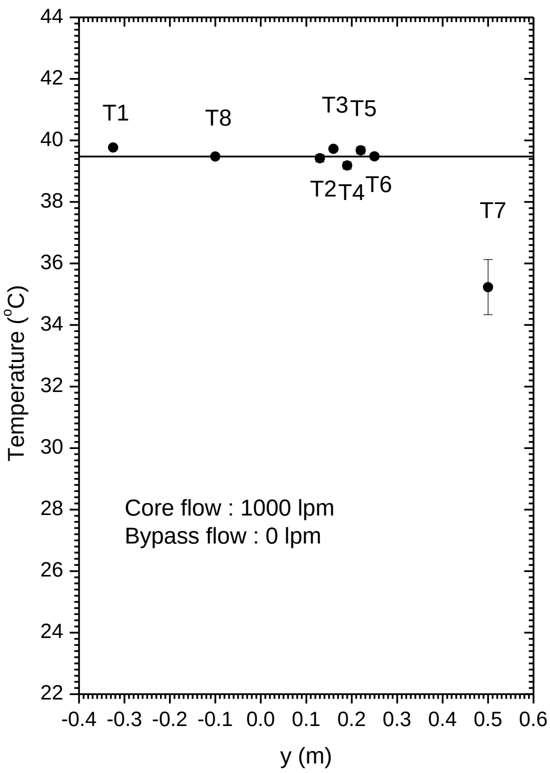


(c) Measured temperature profile

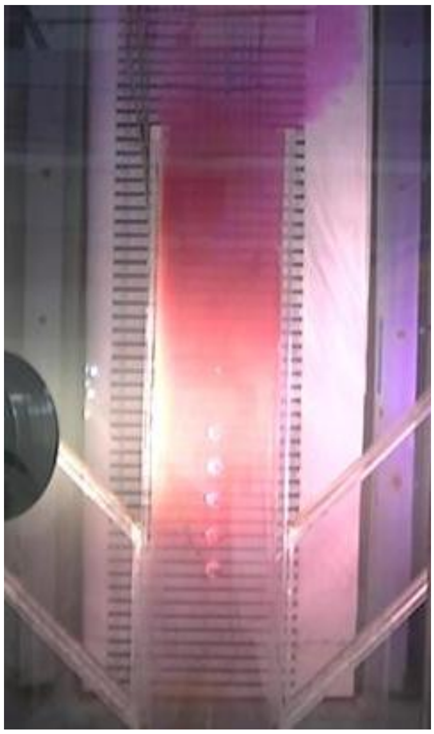

(d) Photographed image

Fig. 6.13: Experimental results ($W_{in}$=1000 lpm, $W_b$=0 lpm)

Similar to the above experiments, core flow is increased to 1500 lpm and bypass flow is varied to 225, 150, 75 and 0 lpm respectively. All the measured data of the experiments are shown in Fig. 6.14 to 6.17. In Fig. 6.14, hot water temperature (T1) and cold water temperature (T7) is maintained at 37.7 ºC and 34.2 ºC respectively for a period of about 2700 s when bypass flow is 225 lpm. The centerline temperature profile shown in Fig. 6.14c is similar to that observed in Fig. 6.6c and Fig 6.10c with bypass flow ratio of 0.15. Major temperature fluctuations are observed at T3 and T4 locations. The hot water temperature drops to the level of chimney entry temperature at y= 287 mm. The captured image using dye is shown in Fig. 6.14d. The maximum stagnation height is found to reach about y = 176 mm. The dye spreads to the maximum height of y=290 mm due to vortices created.

Figure 6.15 shows the experimental data for bypass flow of 150 lpm. The hot water temperature (T1) and cold water temperature (T7) are maintained at 38.2 ºC and 30.6 ºC respectively for 2400 s. Temperature profile shown in Fig. 6.15c is similar to that observed for Fig. 6.7c and Fig. 6.11c for bypass flow ratio of 0.10. Maximum temperature fluctuation location has moved up to T4 location due to reduction of bypass flow ratio. The centerline temperature reaches to cold temperature level at a higher height (at y = 402 mm). The photographed image with dye shows that maximum stagnation height has reached to y = 190 mm. The dye has spread to a much higher height y = 315 mm due to vortices.

When bypass flow is reduced to 75 lpm, the measured data are shown in Fig. 6.16. Steady hot water (T1) and cold water (T7) are maintained during the experiment at 38.2 ºC and 30 ºC for 1800 s. Temperature profile at the centre line of chimney is shown in Fig 6.16c. It is found that temperature fluctuation is the maximum at T4 location along with reasonable fluctuation at T5 and T6 as is observed in Fig. 6.8c and Fig. 6.12c. The effect of hot water temperature is felt up to the top of chimney as if cold water is not able to reach inside the chimney. The image photographed with dye is shown in Fig. 6.16d. The maximum stagnation height is found to be y = 203 mm. The spread of dye due to recirculation has reached to maximum height of y = 474 mm.

Figure 6.17 shows the measured data for the experiment when bypass flow is reduced to zero. The experiment is continued up to 1000 s and hot water temperature (T1) is maintained at 39.6 ºC. The measured data (Fig. 6.17b) shows that the fluctuation levels at T3 to T6 locations have reduced significantly. These temperatures have reached to almost equal (39 to 39.5 ºC). In this case, fluctuations have reached to the topmost chimney height at T7 location. Similar phenomenon is also observed in Fig. 6.9b and 6.13b. The captured image with dye is shown in Fig. 6.17d. It is observed that maximum stagnation height is about y = 220 mm at the central axis. It is also observed that due to alternate vortices created above the stagnation height towards chimney wall, the dye mixes into pool water for this case.

From all these measured results, it is found that the mixing behaviour inside chimney mainly depends on the bypass flow ratio. Effect of Reynolds number is found to be insignificant. It is also observed that temperature profile quantitatively is able to predict the maximum height the vortices have reached inside the chimney.

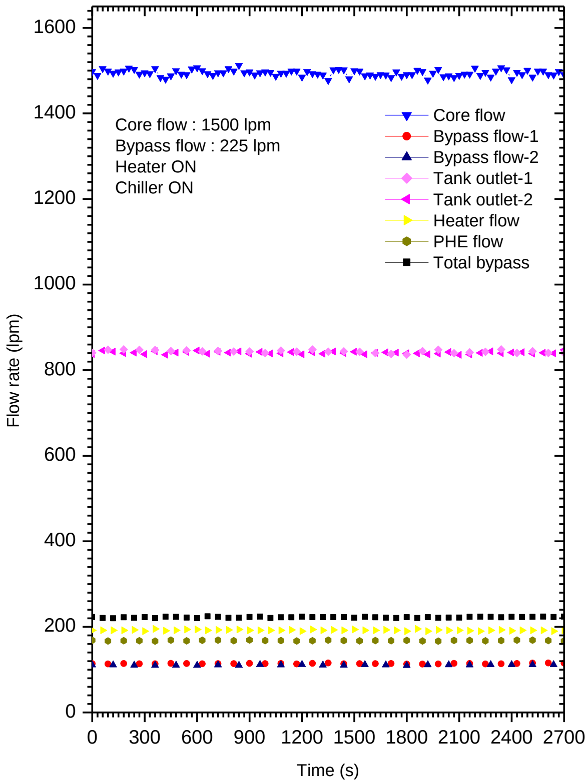


(a) Measured flow rates

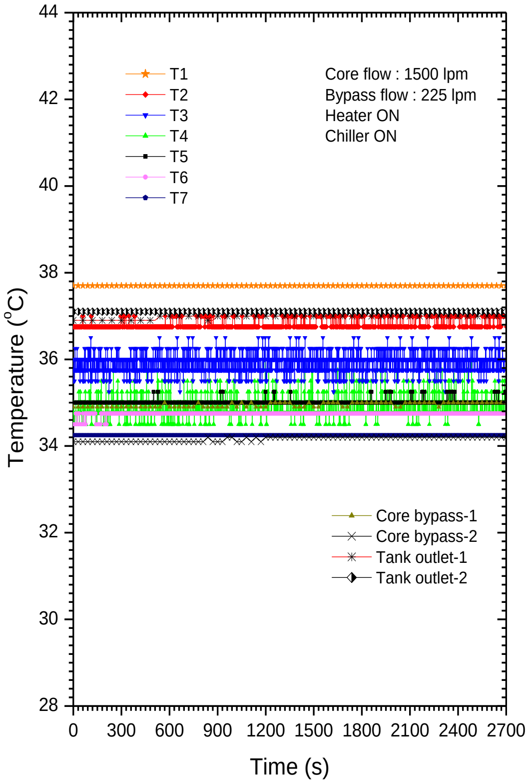


(b) Measured water temperatures

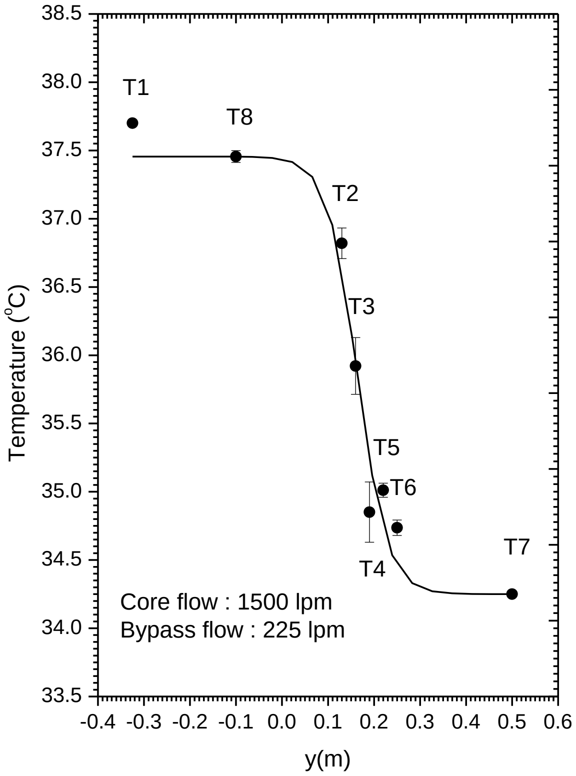


(c) Measured temperature profile

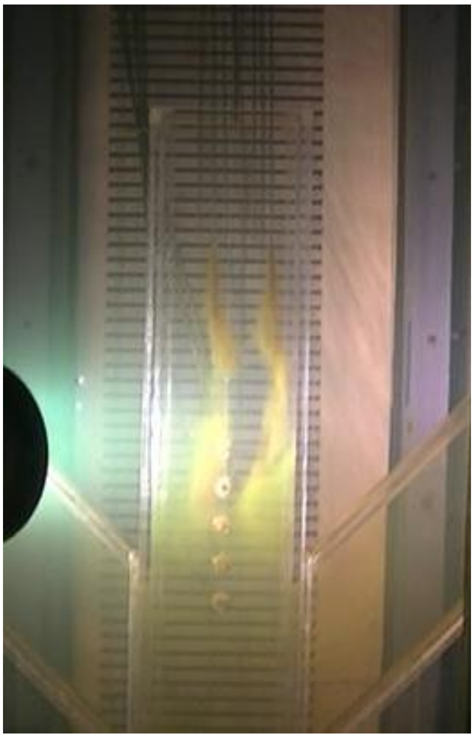

(d) Photographed image

Fig. 6.14: Experimental results ($W_{in}$=1500 lpm, $W_b$=225 lpm)

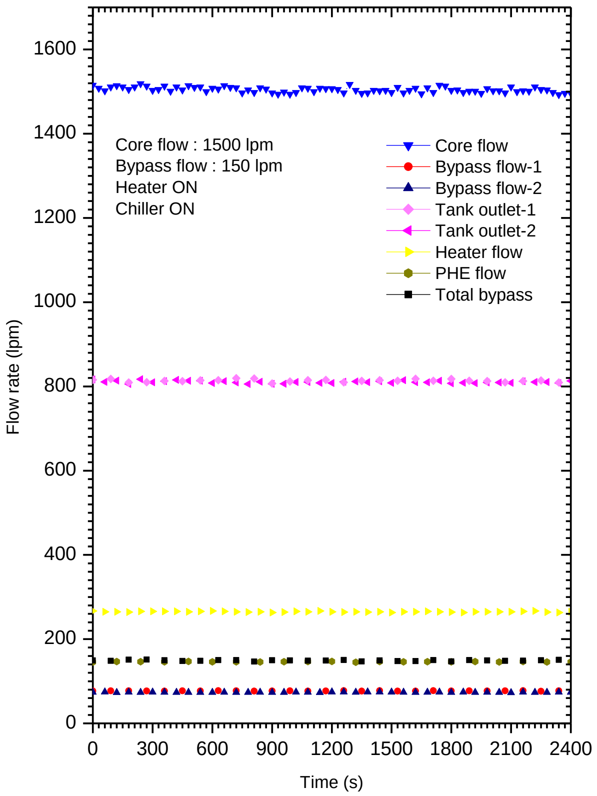


(a) Measured flow rates

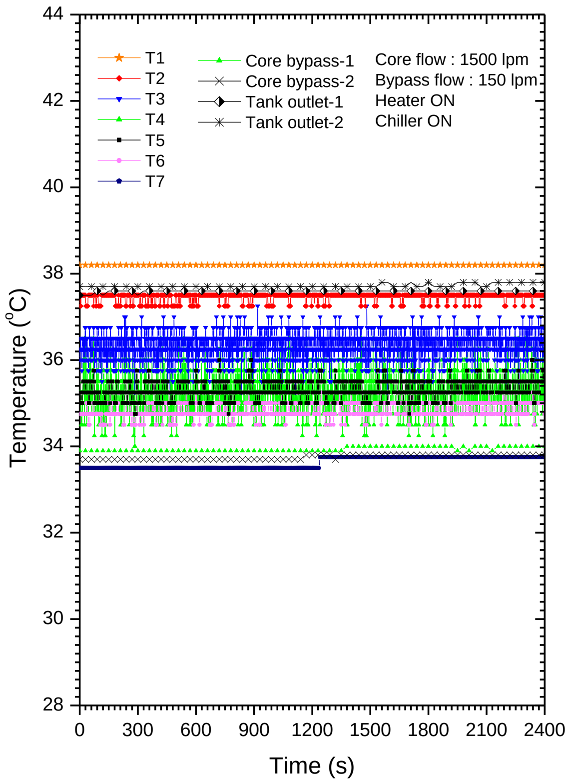


(b) Measured water temperatures

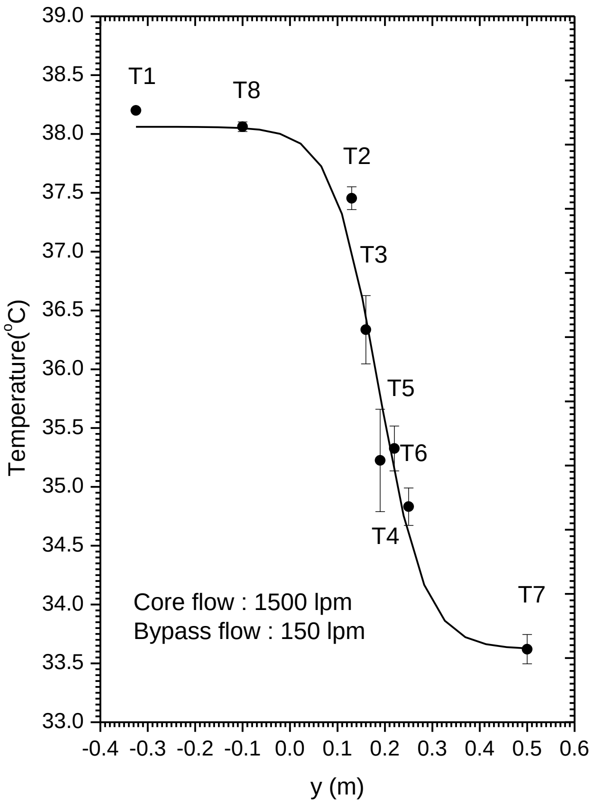


(c) Measured temperature profile

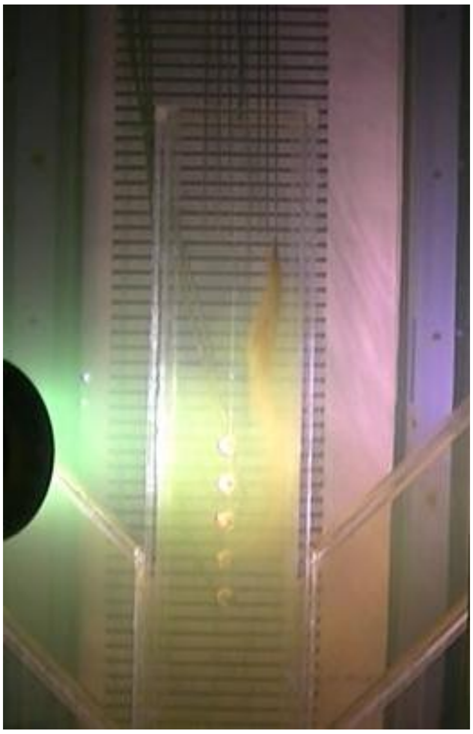

(d) Photographed image

Fig. 6.15: Experimental results ($W_{in}$=1500 lpm, $W_b$=150 lpm)

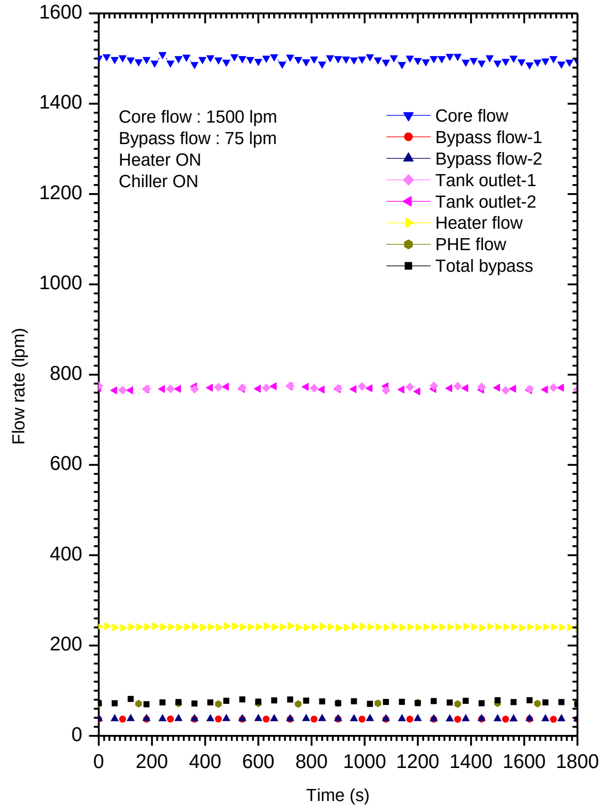


(a) Measured flow rates

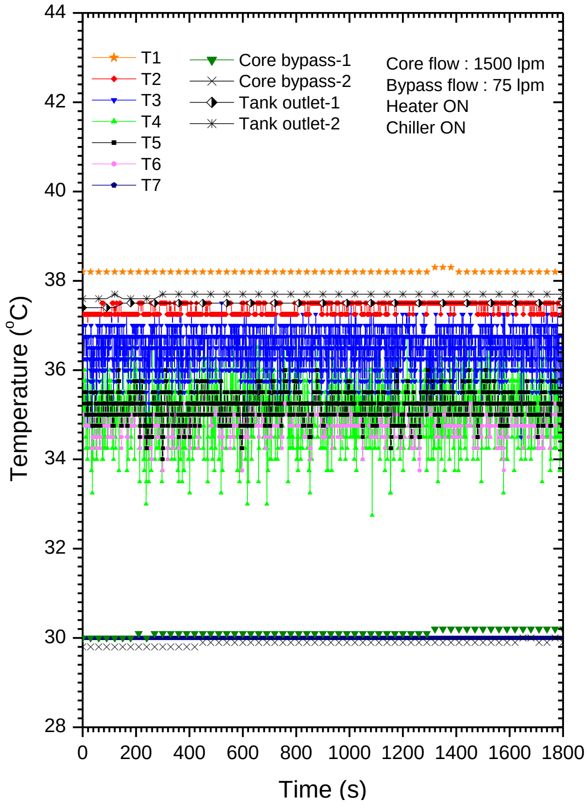


(b) Measured water temperatures

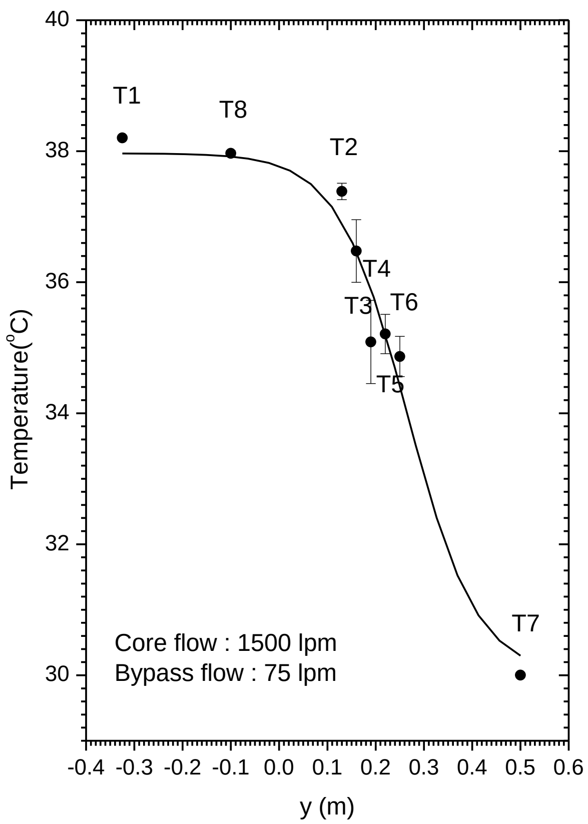


(c) Measured temperature profile

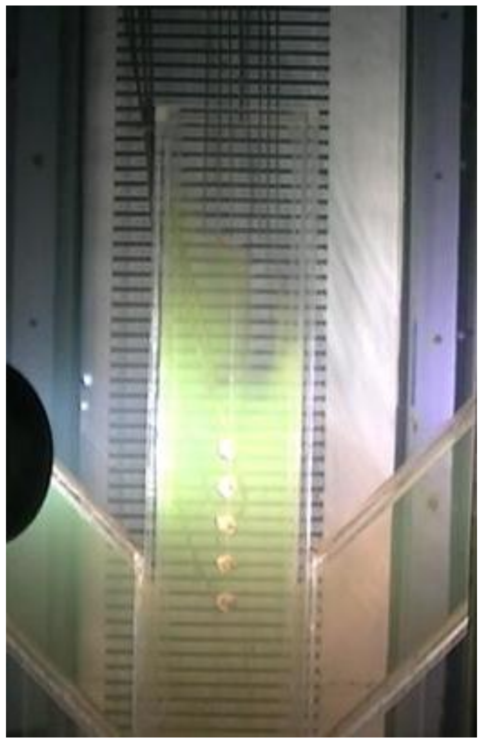

(d) Photographed image

Fig. 6.16: Experimental results ($W_{in}$=1500 lpm, $W_b$=75 lpm)

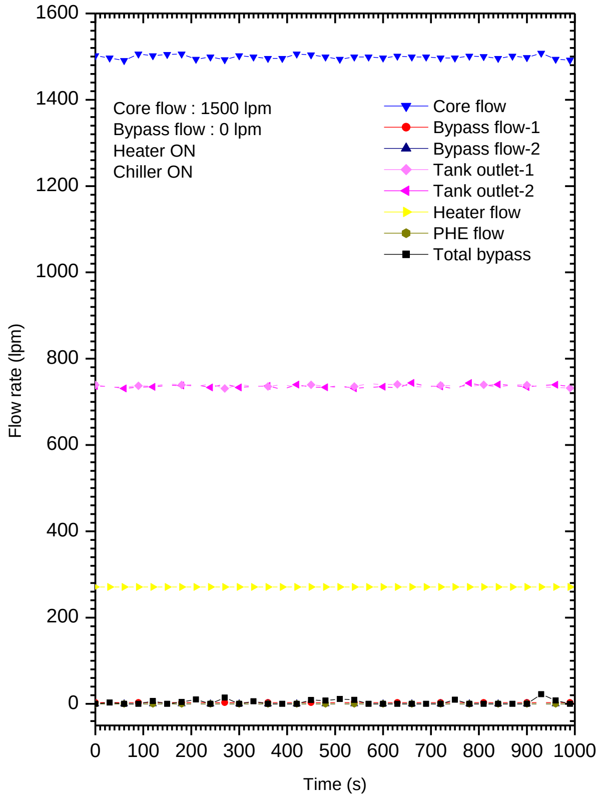


(a) Measured flow rates

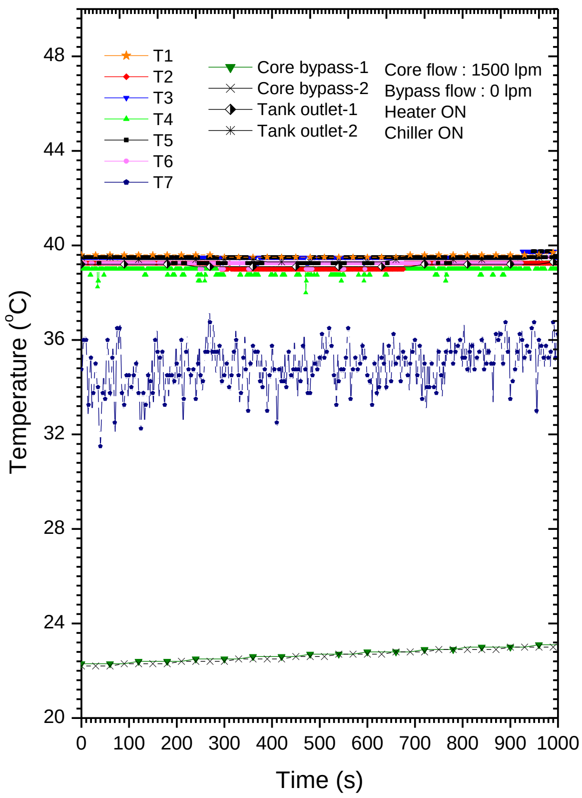


(b) Measured water temperatures

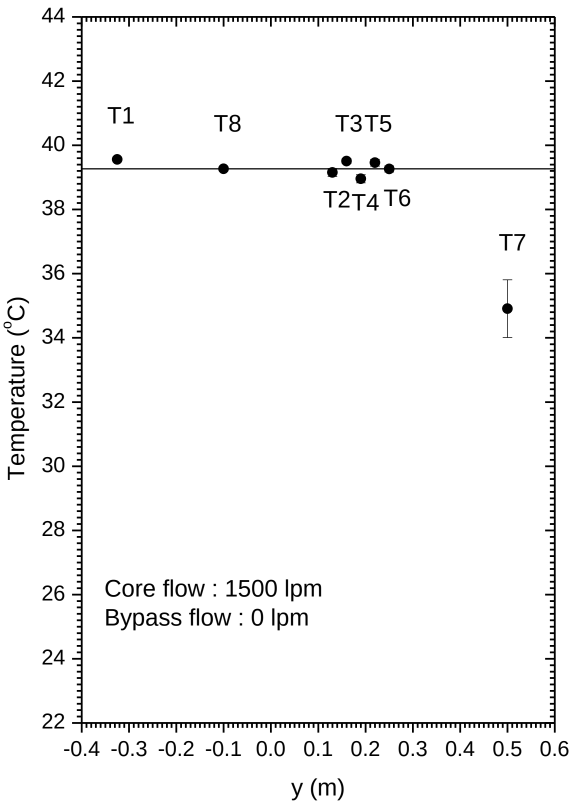


(c) Measured temperature profile

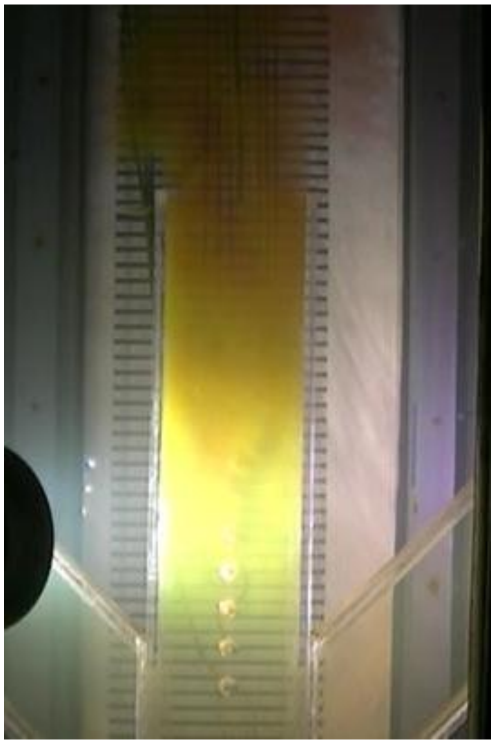

(d) Photographed image

Fig. 6.17: Experimental results ($W_{in}$=1500 lpm, $W_b$=0 lpm)

### 6.4.3 Effect of temperature

In order to assess the effect of buoyancy force at different temperatures on the mixing behaviour, a number of experiments were carried out where temperatures for the hot and the cold water were different. Figure 6.18 shows the measured temperature profiles for various cases. Since the bypass flow ratio is found to be a significant parameter, all the experiments are segregated depending on the bypass flow ratios. Figure 6.18a shows centre line temperature profiles for nine sets of experiments with bypass flow ratio of 0.15, considering three sets of data for each core flow (500, 1000 and 1500 lpm). The maximum and minimum temperature differentials between hot and cold water are 8.5 ºC and 3.2 ºC respectively. Figure 6.18c shows temperature profiles for similar nine sets of experiments with bypass flow ratio of 0.10 where the maximum temperature differential is 11.7 ºC. Minimum temperature differential is about 4.4 ºC. Similarly, measured temperature profiles along the height of chimney are shown in Fig. 6.18e and Fig. 6.18g for bypass flow ratio of 0.05 and 0.00 respectively. Maximum temperature differential for these cases are 18.9 ºC and 7.6 ºC. The minimum temperature differentials are 8ºC and 3.8ºC respectively.

The temperature profile generated for all these experiments are normalized with the difference between hot upward fluid temperature ($T_h$=T1) and cold bypass fluid temperature ($T_c$=$T_b$) sent to the pool to compare them simultaneously. Here hot fluid temperature ($T_h$) represents the water temperature ($T_{in}$) at chimney bottom inlet and cold fluid temperature ($T_c$) represents the pool water temperature ($T_p$). The dimensionless temperature profile with dimensionless chimney height (y/D) for bypass flow ratio 0.15 is shown in Fig. 6.18b. It is observed that the trend of dimensionless temperature profile for all these experiments is similar. The temperature drop up to 99% of the differential takes place at a height ranging from y/D= 2.6 to 3.2 as shown in Fig. 6.18b. Similarly, for bypass flow ratio of 0.10, dimensionless temperature profile for all the experiments shows similar trends as shown in

Fig. 6.18d. With decrease in bypass flow ratio from 0.15 to 0.10, the effect of hot water extends to a higher height (i.e., the temperature drop up to 99% of the differential takes

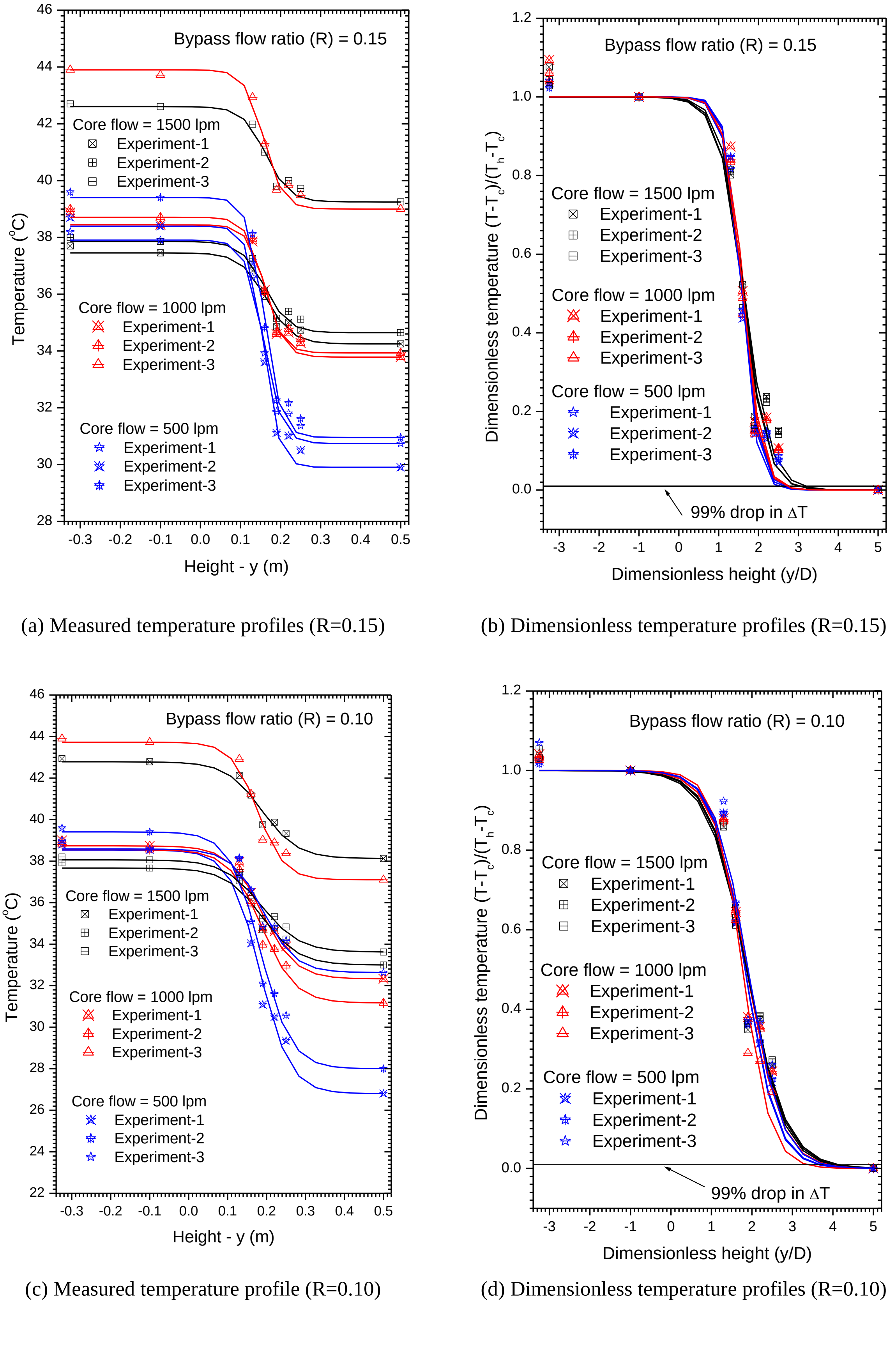


(a) Measured temperature profiles (R=0.15)

(b) Dimensionless temperature profiles (R=0.15)

(c) Measured temperature profile (R=0.10)

(d) Dimensionless temperature profiles (R=0.10)

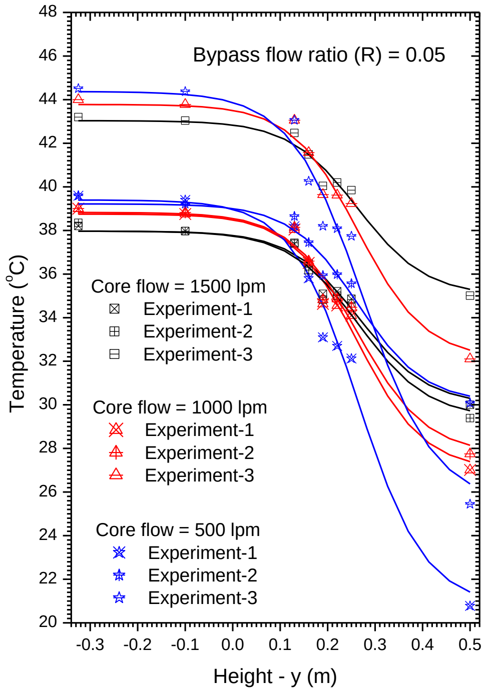


(e) Measured temperature profile (R=0.05)

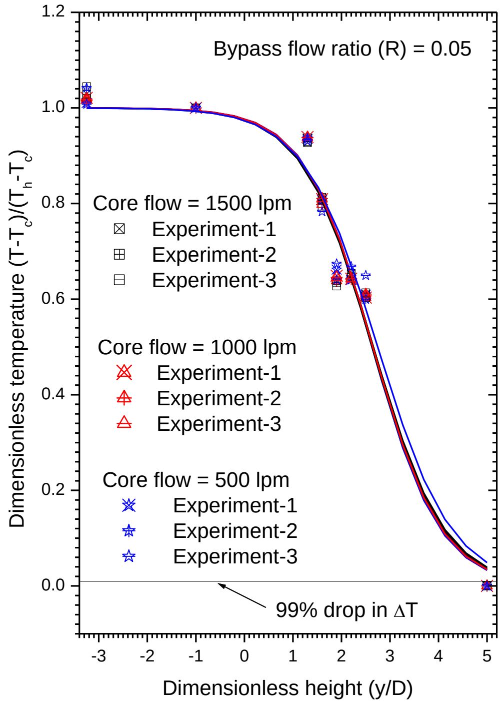


(f) Dimensionless temperature profiles (R=0.05)

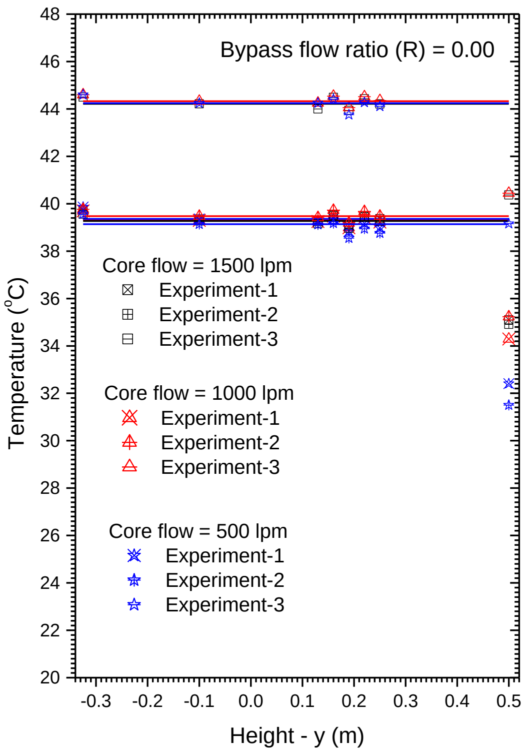


(g) Measured temperature profile (R=0.00)

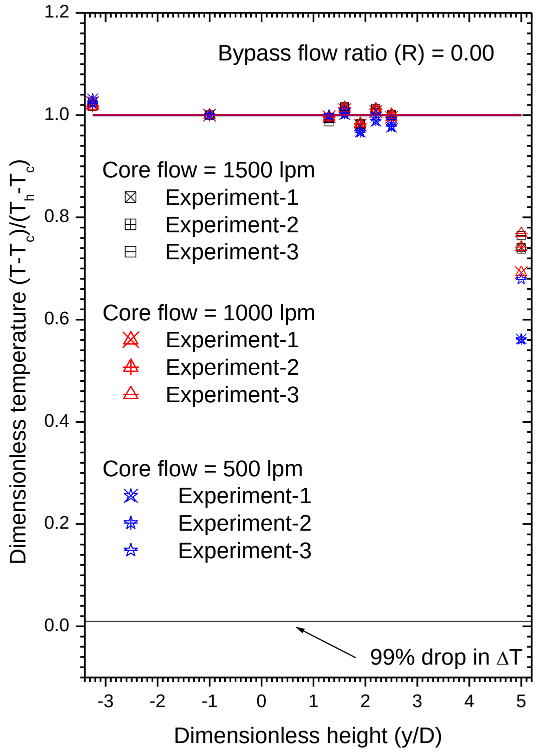


(h) Dimensionless temperature profiles (R=0.00)

Fig. 6.18: Effect of temperature and core flow on temperature profile

lager distance). For bypass ratio of 0.10, it takes place at height ranging from y/D = 3.3 to 4.1. When bypass flow ratio is reduced further to 0.05 and 0.00, hot water temperature effect extends beyond the chimney height (y = 500 mm) as shown in Fig. 6.18f and Fig. 6.18h. The dimensionless temperature profile shows similar trends also for all the experiments with bypass flow ratio of 0.05. When bypass flow ratio is 0.0, the temperature profile is almost horizontal except the top chimney temperature (T7). Since, bypass flow entering the pool is zero for this case, hot upward fluid gradually mixes with the pool after coming out through the chimney top opening and gradually the chimney top temperature (T7) will reach to the value of other temperatures (T1 to T6).

### 6.4.4 Effect of chimney height

Similar experiments are done with a separate chimney, where height (H) of the chimney is increased to 600 mm from 500 mm. Temperature profiles for core flow of 500, 1000 and 1500 lpm with 0.15 bypass ratio are shown in Fig. 6.19a. The dimensionless temperature profile with respect to difference in temperature between core flow and bypass flow is shown in Fig. 6.19b. It is observed that the trend of temperature profile is similar for this chimney also. The temperature drop up to 99% of the differential takes place at a height ranging from y/D =2.65 to 2.90. For the next case, bypass flow ratio is reduced to 0.10, the results of this experiment are shown in Fig. 6.19c and Fig. 6.19d. It is observed that the temperature drop up to 99% takes place at a larger height (y/D = 3.3 to 3.8). Figures 6.19e and 6.19f show the temperature variation and dimensionless results for the cases with bypass ratio of 0.05 respectively. Based on the trend of the result it is observed that the hot water temperature effect extends beyond the height (y/D = 5) of chimney. For bypass flow ratio of 0.0, the results indicate that all these temperatures are almost equal as shown in Figures 6.19g and 6.19h.

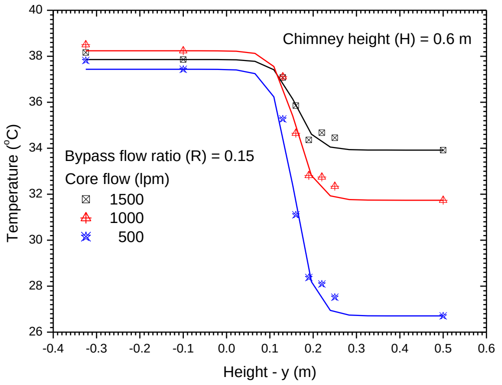


(a) Measured temperature profiles (R=0.15)

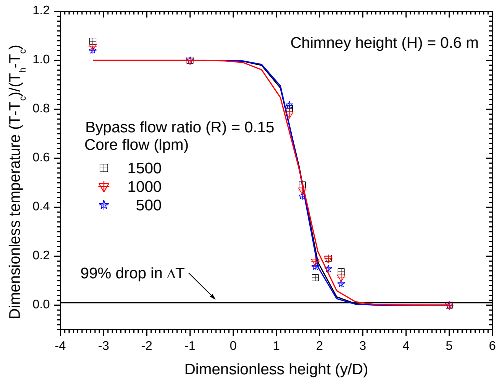


(b) Dimensionless temperature profiles (R=0.15)

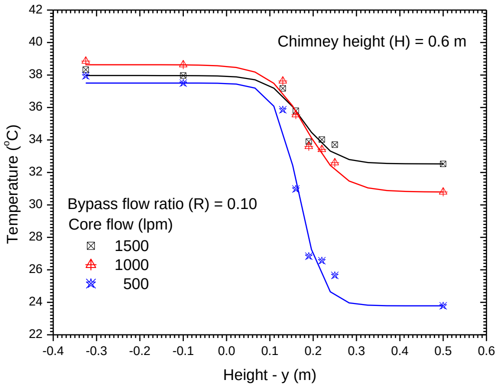


(c) Measured temperature profile (R=0.10)

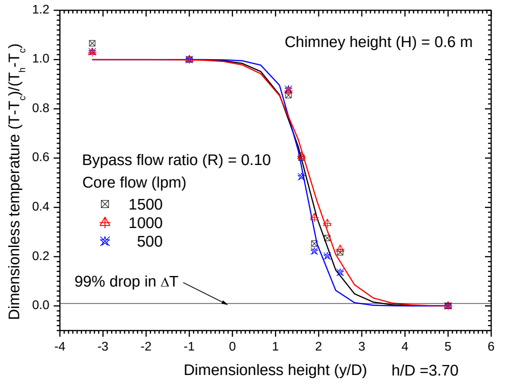


(d) Dimensionless temperature profiles (R=0.10)

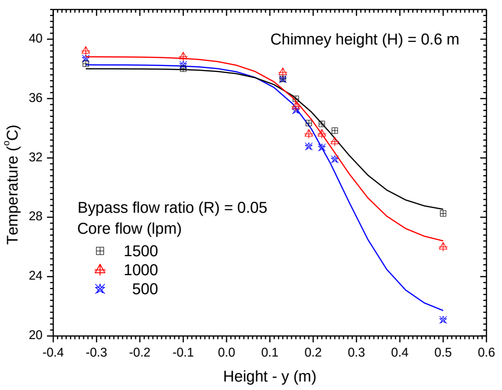


(e) Measured temperature profile (R=0.05)

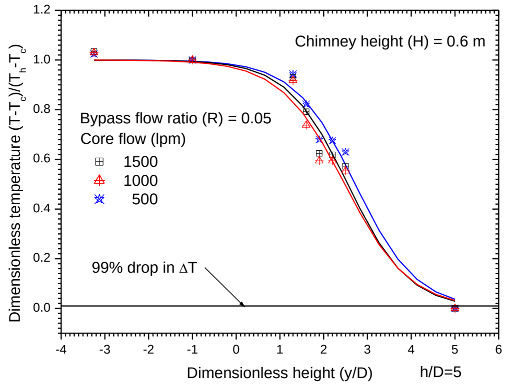


(f) Dimensionless temperature profiles (R=0.05)

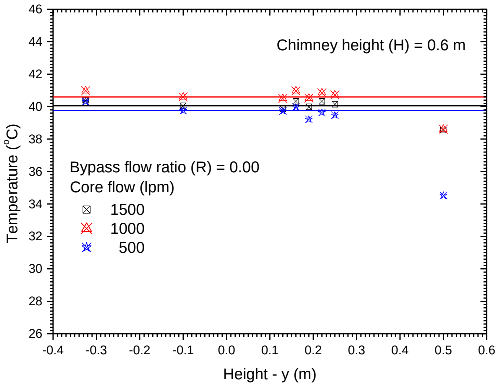


(g) Measured temperature profile (R=0.00)

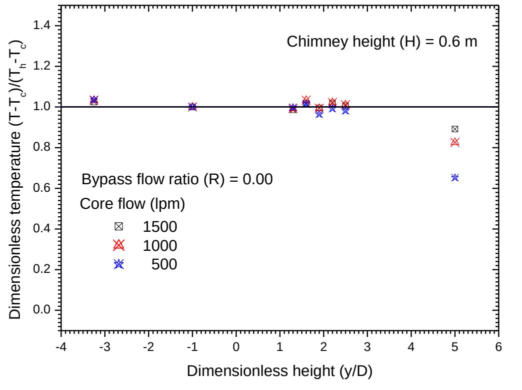


(h) Dimensionless temperature profiles (R=0.00)

Fig. 6.19: Effect of core flow on temperature profile for chimney (H=0.6 m)

These measured temperature profiles are non-dimensionalised with respect to temperature differential between the hot core flow and cold bypass flow for both the chimneys (H/D=5, 6). The dimensionless temperature profile for Reynolds number ($Re_D$) of $1.5\times10^5$, $3.0\times10^5$ and $4.5\times10^5$ are shown in figures 6.20a, 6.20b and 6.20c respectively. It is observed that dimensionless temperature profiles are similar for both the chimneys. It is also observed from the results that temperature drop takes place within a smaller distance when bypass flow ratio is increased. The height of the chimney where temperature drops to 99% is considered to be pool temperature front height. Dimensionless pool temperature front heights for these cases are compared as shown in Fig. 6.20d. It is observed that dimensionless temperature front heights ($h_T$*) can be represented using following the relationship as given Table-6.3.

Table-6.3: Dimensionless pool temperature front height ($h_T$*=$h_T$/D)

| Bypass flow ratio | Dimensionless pool temperature front height |
|---|---|
| R = 0.15 | $h_T$* = 2.9 ± 0.3 |
| R = 0.10 | $h_T$* = 3.7 ± 0.4 |
| R = 0.05 | $h_T$* = 5.5 ± 0.5 |

It is observed that bypass flow ratio (R) shall be more than 0.05, so that pool water temperature front can be inside the chimney with height to diameter ratio of 6. Reynolds number of the core flow does not significantly affect the pool temperature front height and increase in bypass flow ratio decreases the pool temperature front height. Based on these results, following generalized correlation of temperature profile is established.

$$T^* = \frac{1}{1+e^{\left(\frac{Y-a}{b}\right)}} \qquad \ldots(6.1)$$

The constants "a" and "b" are determined using regression fit of all the experimental data. Levenberg-Marquardt algorithm is used as the technique for least squares fitting of the data. Two parameters Sigmoid curve (Eqn. 6.1) with initial value of 1.0 and final value of 0.0 is used as the model to fit the data. An iterative process is used to find these parameters "a" and "b" starting with guess values. The fitting algorithm then alters each of this parameter in a set of cycles in order to determine the optimum solution of the problem. By changing these parameters, shape of the curve changes and the difference in the sum of the residuals squared is monitored. The successive iteration process is continued till the residuals are converging. The optimized values of "a" and "b" along with coefficient of determination ($R^2$) are shown in Table-6.4.

Table-6.4: Correlation for dimensionless temperature profile

| Bypass flow ratio | a | b | $R^2$ |
|---|---|---|---|
| R = 0.15 | 1.60096 | 0.23768 | 0.97497 |
| R = 0.10 | 1.84467 | 0.41644 | 0.96887 |
| R = 0.05 | 2.66404 | 0.71716 | 0.97510 |

The established correlation and the measured data for various Reynolds number ($Re_D$) with H/D ratio of 5 and 6 are shown in Fig. 6.20e. In case bypass flow ratio is 0.0 then T* = 1.0. This correlation can be used to predict temperature profile for any chimney structure with 45º nozzle outlets with the central chimney.

Captured images taken for various core flow rates with different bypass flow ratios are shown in Fig. 6.21. It is observed that for similar bypass flow ratios, the extent of maximum dye spread height is almost similar. The dye spreading beyond the stagnation height is due to the alternate vortices (near to the left wall / right wall of chimney) created during mixing between the two opposing flows. Figures 6.21a, 6.21b and 6.21c show that maximum vortex

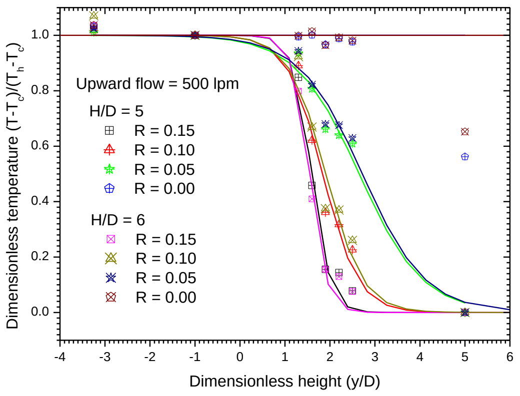


(a) Measured dimensionless temperature profile ($W_{in}$=500 lpm, $Re_D$=1.5×$10^5$)

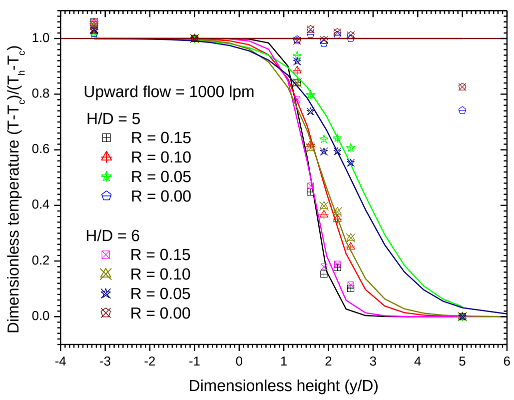


(b) Measured dimensionless temperature profile ($W_{in}$=1000 lpm, $Re_D$=3.0×$10^5$)

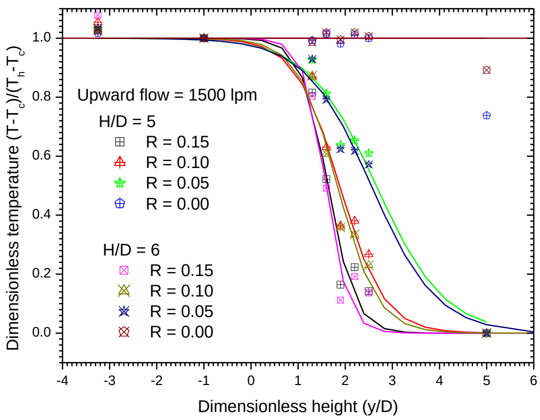


(c) Measured dimensionless temperature profile ($W_{in}$=1500 lpm, $Re_D$=4.5×$10^5$)

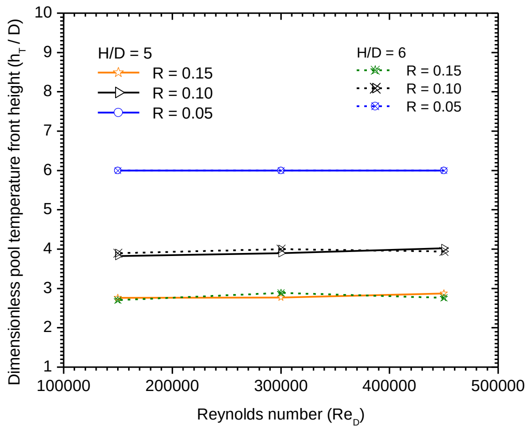


(d) Variation of measured temperature front height with Reynolds number and chimney height

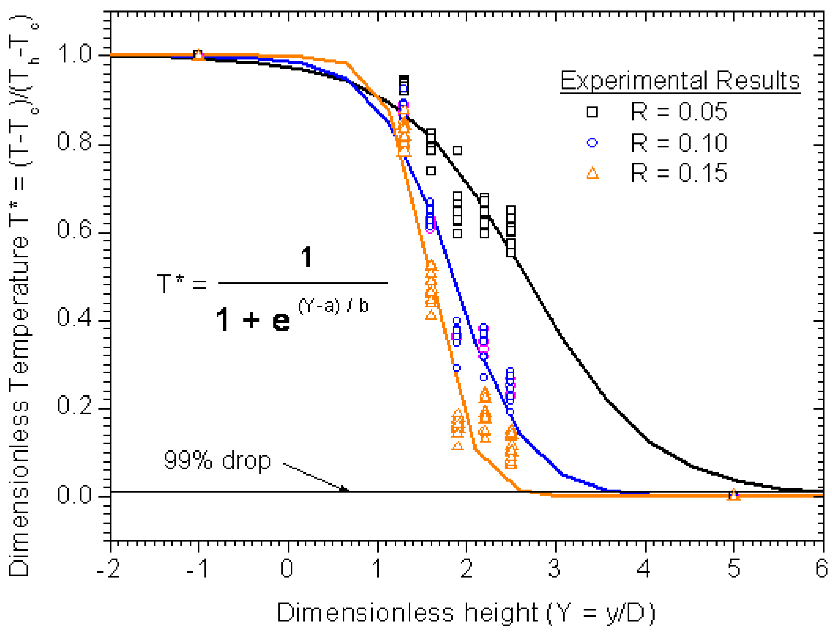


(e) Correlation of temperature profile and measured data

Fig. 6.20: Effect of chimney height and Reynolds number ($Re_D$) on temperature profile

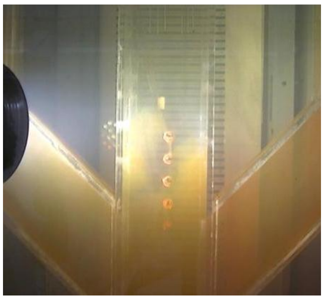

(a) $W_{in}$ = 500 lpm, R=0.15

(b) $W_{in}$ = 1000 lpm, R=0.15

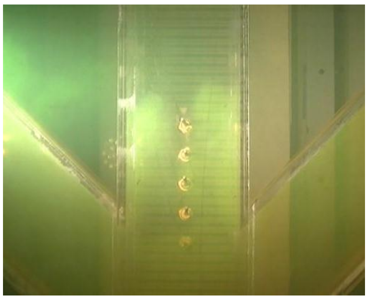

(c) $W_{in}$ = 1500 lpm, R=0.15

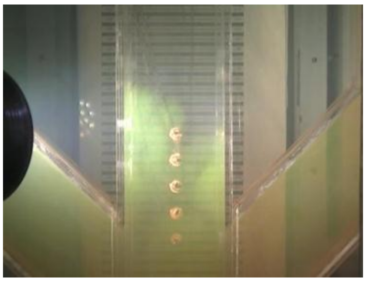

(d) $W_{in}$ = 500 lpm, R=0.10

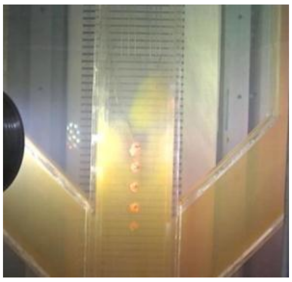

(e) $W_{in}$ = 1000 lpm, R=0.10

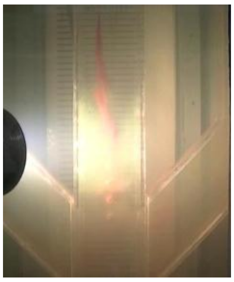

(f) $W_{in}$ = 1500 lpm, R=0.10

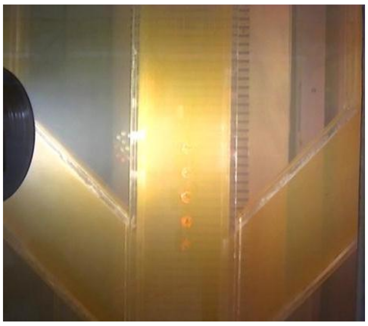

(g) $W_{in}$ = 500 lpm, R=0.05

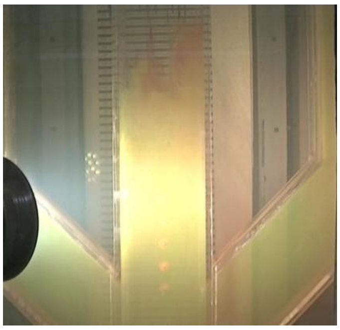

(h) $W_{in}$ = 1000 lpm, R=0.05

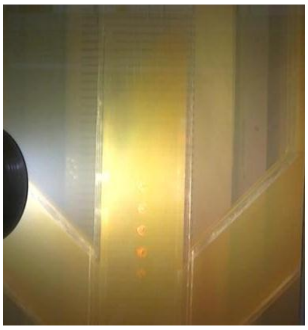

(i) $W_{in}$ = 1500 lpm, R=0.05

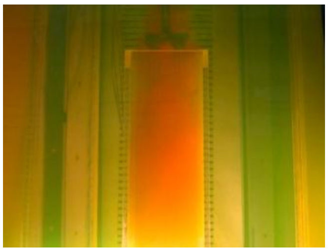

(j) $W_{in}$ = 500 lpm, R=0.00

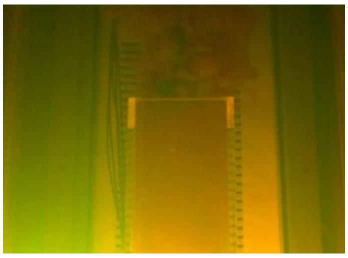

(k) $W_{in}$ = 1000 lpm, R=0.00

l) $W_{in}$ = 1500 lpm, R=0.00

Fig. 6.21: Photographed images (H = 0.6 m)

spread height for 0.15 bypass flow ratio. They are about 292, 295 and 290 mm corresponding to core flow of 500, 1000 and 1500 lpm. Maximum stagnation height is observed to be about 176, 174 and 176 mm. For bypass flow ratio of 0.10, both maximum vortex spread height and maximum stagnation height increase as shown in figures 6.21d, 6.21e and 6.21f. Maximum vortex spread height is found to be about 316, 320 and 315 mm for core flow of 500, 1000 and 1500 lpm respectively. Maximum stagnation height is observed to be about 190, 189 and 188 mm. For bypass flow ratio of 0.05, maximum vortex spread height is found to be about 496, 485 and 474 mm as shown in figures 6.21g, 6.21h and 6.21i. The maximum stagnation height is found to be about 201, 202 and 203 mm respectively. When bypass flow is stopped (R = 0.0), the dye came out of the chimney as shown in figures 6.21j, 6.21k and 6.21l. The maximum stagnation height is found to be about 225, 222, 220 mm respectively for core flow of 500, 1000 and 1500 lpm.

A comparison is made between the results obtained for the two chimneys (H = 500 mm and H = 600 mm) as shown in Fig. 6.22. It is observed that the dimensionless vortex spread height as well as dimensionless stagnation height are similar for both the chimneys and they are mainly dependent on the bypass flow ratios. Effects of core flow and chimney height are found to be not so significant.

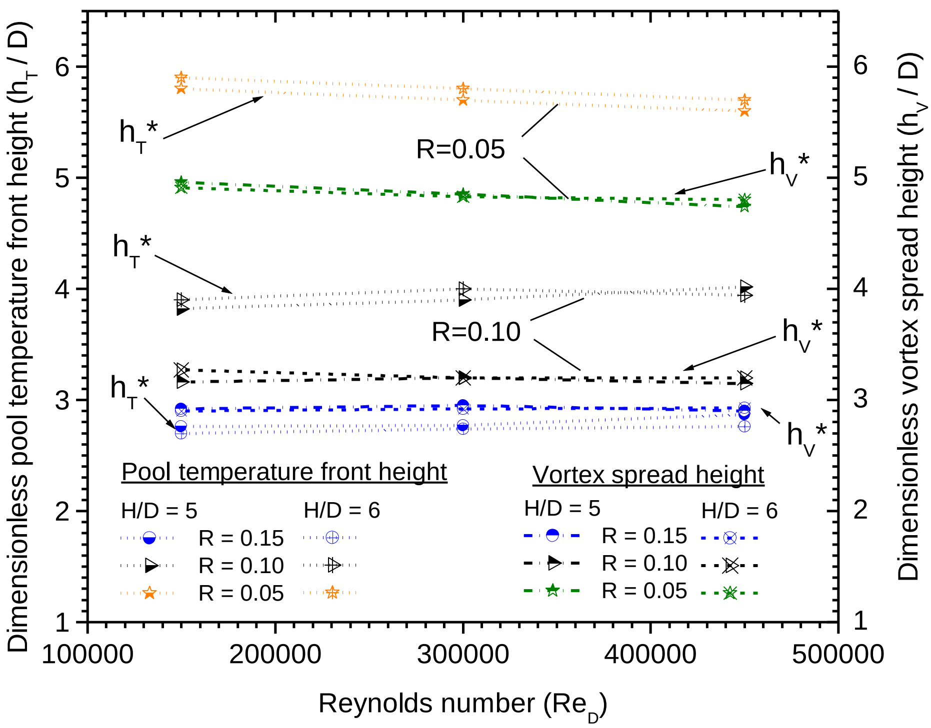


Fig. 6.22: Variation of Temperature front height and Vortex spread height with $Re_D$

Considering various cases of experiments studied, the dimensionless stagnation height ($h_S$*) and vortex spread height ($h_V$*) is expressed in terms of bypass flow ratio as given in the following Table-6.5.

Table-6.5: Dimensionless Vortex spread height ($h_V$/D) and Stagnation height ($h_S$/D)

| Bypass flow ratio | Dimensionless Vortex spread height | Dimensionless Stagnation height |
|---|---|---|
| R = 0.15 | $h_V^* = 2.9 \pm 0.2$ | $h_S^* = 1.7 \pm 0.2$ |
| R = 0.10 | $h_V^* = 3.2 \pm 0.2$ | $h_S^* = 1.8 \pm 0.2$ |
| R = 0.05 | $h_V^* = 4.9 \pm 0.2$ | $h_S^* = 2.0 \pm 0.2$ |
| R = 0.00 | Beyond chimney height | $h_S^* = 2.2 \pm 0.2$ |

### 6.5 Comparison between Experiment and Numerical results

Experimental results described above were compared with the results obtained from the numerical simulations using PHOENICS code (Ludwig, 2004). Comparison of stagnation heights for both chimneys (H/D = 5, 6) are shown in Fig. 6.23. It is observed that both the computational and experimental results are showing similar trends. When bypass flow ratios were higher (0.15, 0.10, 0.05) the numerical results are more closure to the experiment results. At bypass ratio of 0.0 experimental results predicted are less than that predicted by the numerical simulation. This was due to the reason that during low bypass flow ratios, the large vortices found in the experiment, which was not well simulated by numerical simulations.

The dimensionless temperature profiles for all the experiments carried out for the chimney with height of 500 mm are compared with the numerical results as shown in Fig. 6.24. The trends of the results are found to be similar. However, numerical simulation predicts a lower mixing zone length (the distance where the temperature drops by 99% of the temperature differential). Hence it is less conservative while predicting the upward height up to which the hot water effect could be felt due to various bypass flow ratios. The comparison for bypass flow 0.15, 0.10, 0.05 and 0.00 are shown in figures 6.24a, 6.24b, 6.24c and 6.24d respectively. Figure 6.25 shows the comparison of results for chimney height of 600 mm.

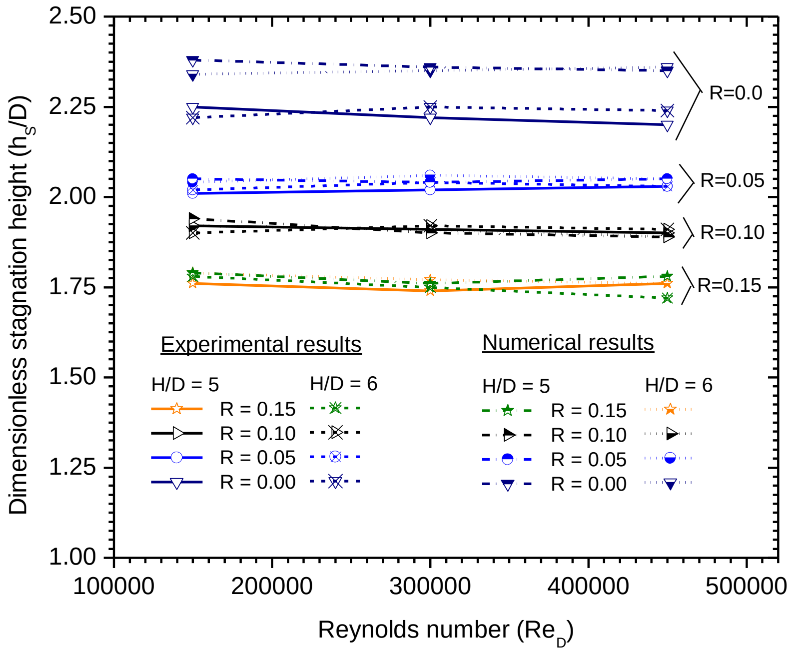


Fig. 6.23: Comparison of stagnation height - experiments and numerical simulation

Experimental results show that the water temperature drops to 99% of the differential between the hot and cold water temperature at a distance of about 3D, 4D and 5D from zero reference height for the cases with bypass flow ratio (R) of 0.15, 0.10 and 0.05 respectively. Thus mixing regions change from 3D to 5D distance depending on the amount of bypass flow ratio. With lower bypass flow ratio, mixing region is more because there exists larger difference in momentum between the two opposing flows. In numerical simulations also it is observed that mixing region increases from 1.9D to 2.1D and 2.3D as the bypass flow ratio decreases from 0.15 to 0.10 and 0.05 respectively. However, the numerical results show smaller mixing region than that observed in the experiments. This is mainly due to the turbulent mixing of the opposing fluid flows and formation of vortices during momentum transfer. In order to ascertain that temperature difference between the opposing flows does

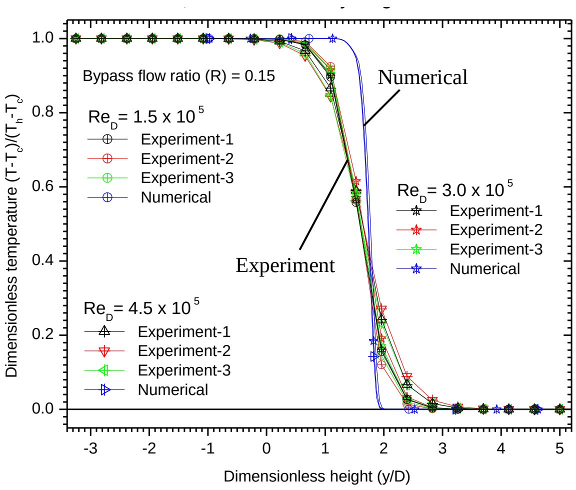


(a) R = 0.15

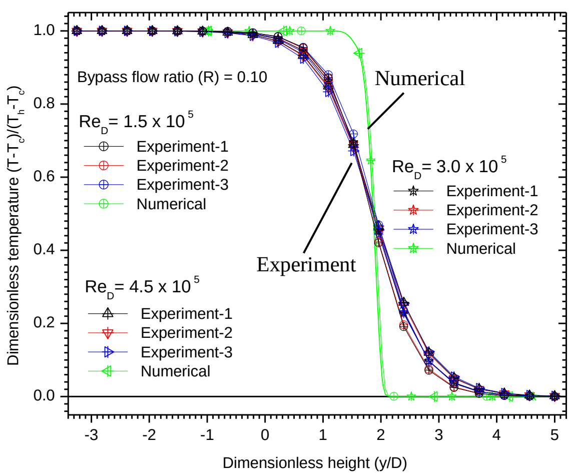


(b) R = 0.10

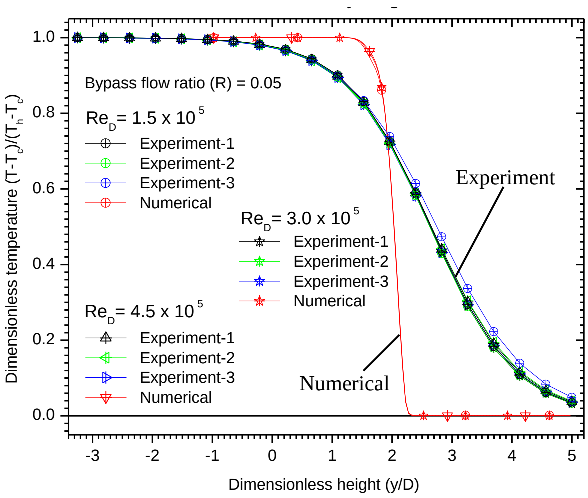


(c) R = 0.05

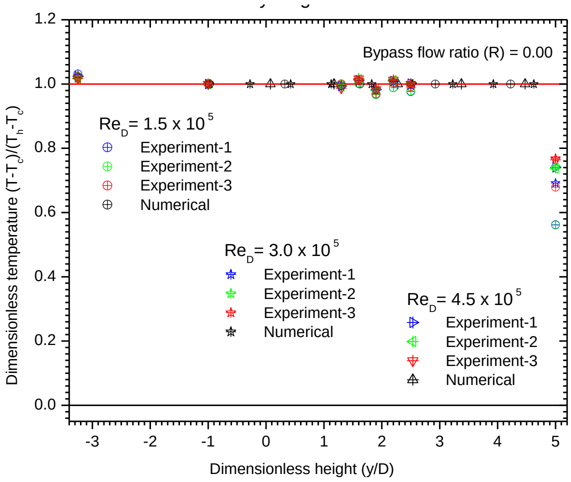


(d) R = 0.00

Fig. 6.24: Temperature profile -experiment and numerical simulations (H=0.5m)

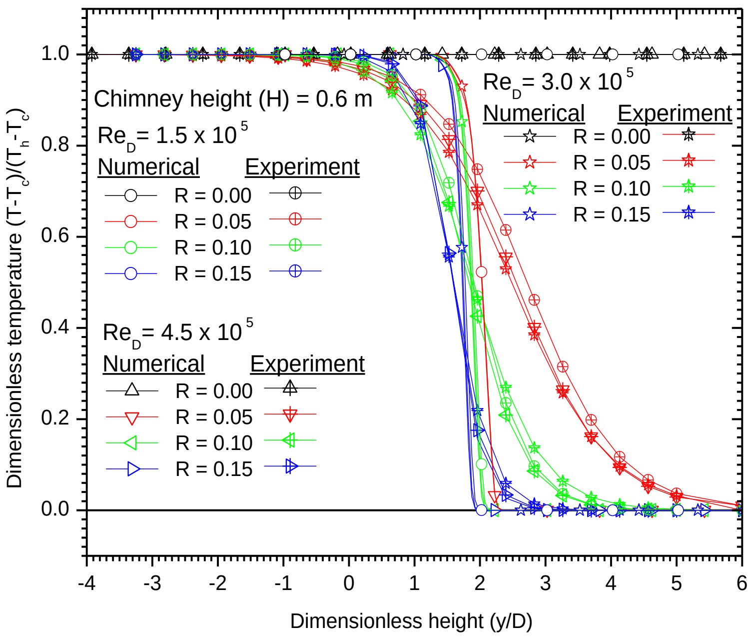


Fig. 6.25: Comparison between experiment and numerical simulations (H = 0.6 m)

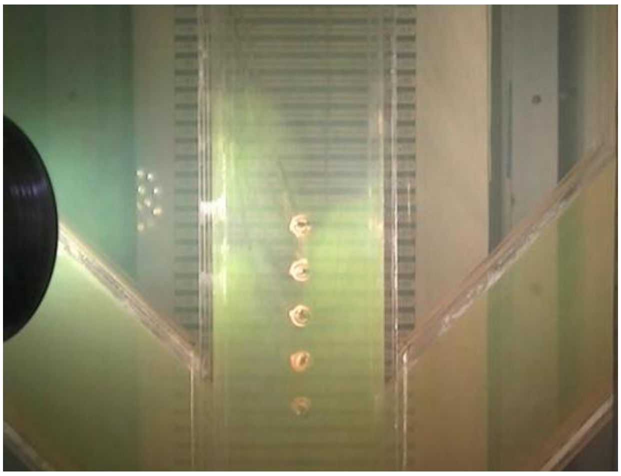

(a) $W_{in}$=1000 lpm, R=0.10, heater off

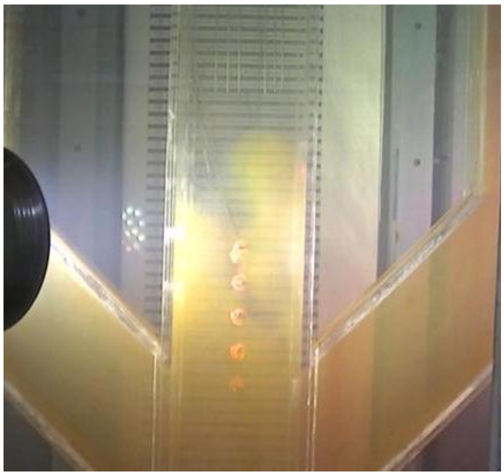

(b) $W_{in}$=1000 lpm, R=0.10, heater on

(c) $W_{in}$=1000 lpm, R=0.05, heater off

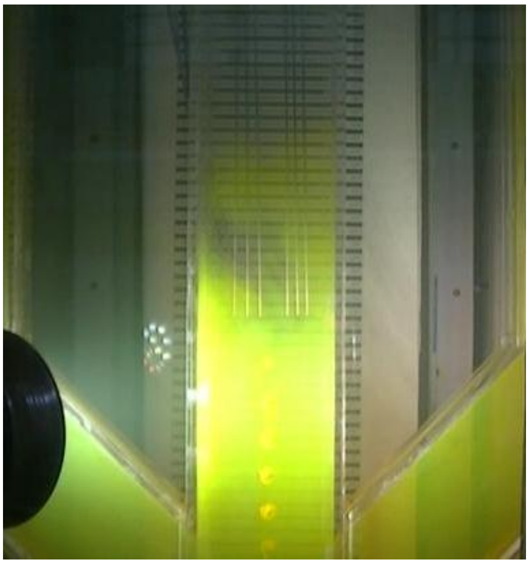

(d) $W_{in}$=1000 lpm, R=0.05, heater on

Fig. 6.26: Effect of temperature difference on mixing behaviour ($W_{in}$=1000 lpm, H/D=6)

not have significant contribution towards this extended mixing region found in the experiment and additional experiments are carried out with heater off condition. The experimental results for 1000 lpm flow with bypass flow ratios of 0.10 and 0.05 are shown in figures 6.26a and 6.26c where heater was switched off. These results are compared with heater switched on condition as shown in figures 6.26b and 6.26d. It is observed that dye spread i.e., maximum vortex spread height is similar for both heater on and off conditions when the bypass flow ratio is maintained the same.

Similar experimental results for 1500 lpm core flow with bypass ratios of 0.05, 0.10 considering heater on as well as off conditions are shown in Fig. 6.27. Here also it is observed that temperature difference did not change significantly the mixing behaviour. Figure 6.28 shows results for core flow of 500 lpm and bypass flow ratio of 0.15, 0.10 and 0.05 considering “heater off” as well as “heater on” condition. Maximum vortex spread height is found to be similar for both heater on /off conditions provided bypass flow ratio is held constant.

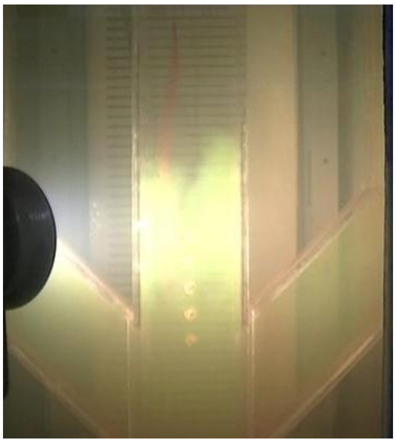

(a) $W_{in}$=1500 lpm, R=0.10, heater off

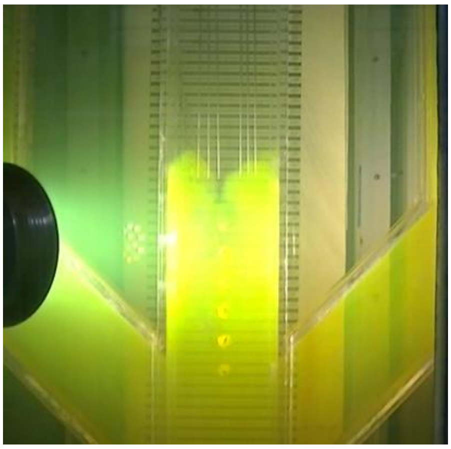

(b) $W_{in}$=1500 lpm, R=0.10, heater on

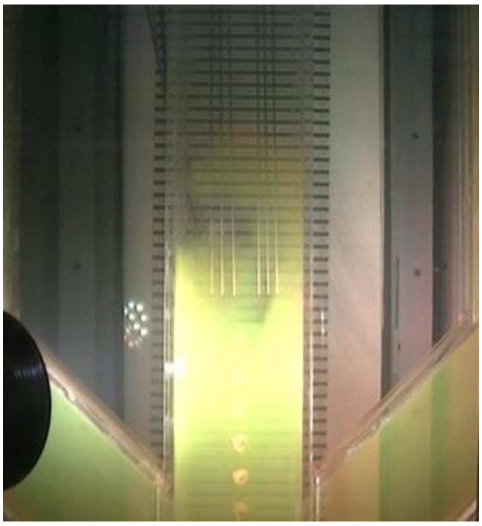

(c) $W_{in}$=1500 lpm, R=0.05, heater off

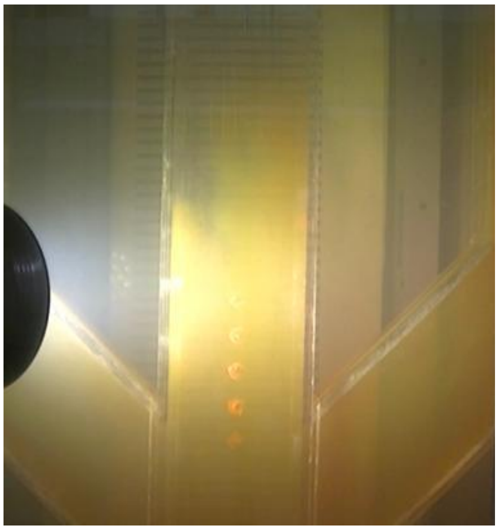

(d) $W_{in}$=1500 lpm, R=0.05, heater on

Fig. 6.27: Effect of temperature difference on mixing behaviour ($W_{in}$=1500 lpm, H/D=6)

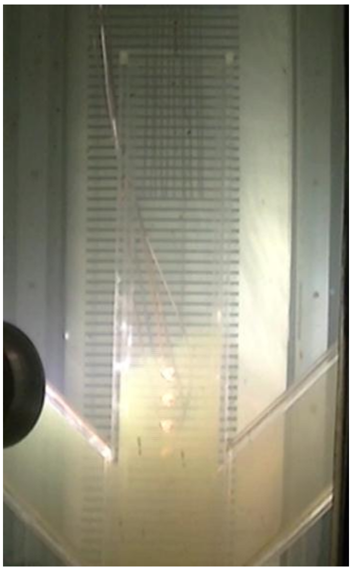

(a) $W_{in}$=500 lpm, R=0.15, heater off

(b) $W_{in}$=500 lpm, R=0.15, heater on

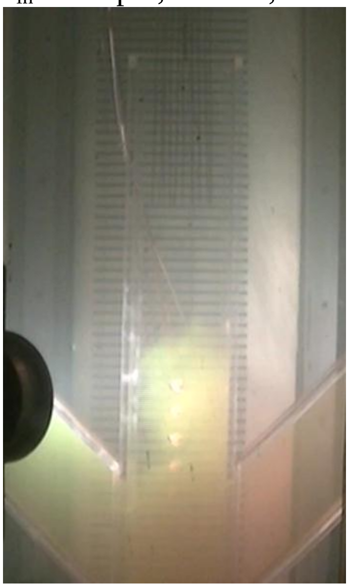

(c) $W_{in}$=500 lpm, R=0.10, heater off

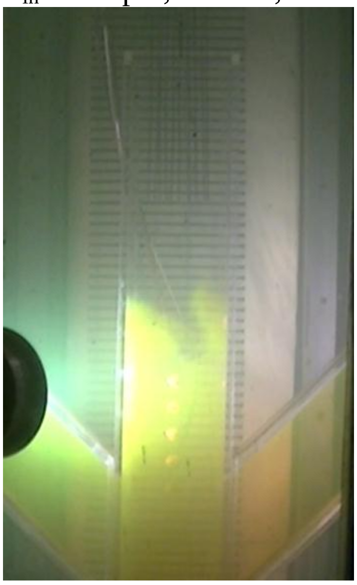

(d) $W_{in}$=500 lpm, R=0.10, heater on

(e) $W_{in}$=500 lpm, R=0.05, heater off

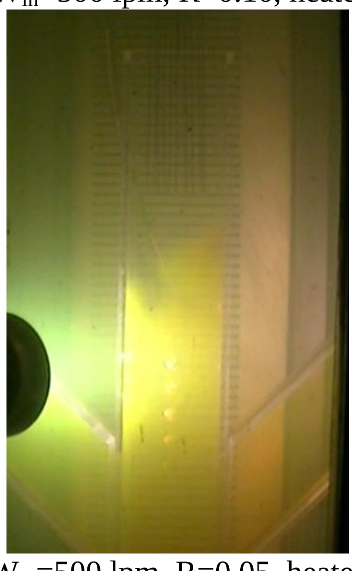

(f) $W_{in}$=500 lpm, R=0.05, heater on

Fig. 6.28: Effect of temperature difference on mixing behaviour ($W_{in}$=500 lpm, H/D=6)

## 6.6 Closure

Experimental results of the turbulent mixing studies carried out in scaled down chimney models for various cases of interest were discussed. The effects of various parameters such as height of the chimney, Reynolds number of core flow, bypass flow ratio, temperature difference between the core flow and bypass flow on the mixing behaviour were reported.

It is observed that the hot upward flow comes out of the chimney when bypass flow ratio is 0.0. With increase in bypass flow ratio, the height up to which the hot water reaches, i.e., the stagnation height decreases. The effect of increasing the Reynolds number on the stagnation height is found to be insignificant. The vortex spread height also decreases with increase in bypass flow ratio and it does not depend significantly on the Reynolds number. Because of lower temperature difference between the core flow and bypass flow, stagnation height and vortex spread height do not vary significantly due to variation in buoyancy force.

It is observed that centre line temperature distribution of the chimney indirectly is able to quantify the vortex spread height. The chimney height variation does not affect significantly the turbulent mixing behaviour when the height to diameter ratio is increased from 5 to 6. It is also observed that bypass ratio more than 0.05 is required to keep the pool temperature front within the chimney region. Flow bypass ratio of 0.10 is able to keep the maximum vortex spread as well as pool temperature front well within the chimney.

The numerical evaluations presented in the earlier chapter were compared with these experimental data. It is observed that most of the trends predicted by the code are reflected by the data. However, the mixing region is not reflective of the predictions. The core temperature is felt at the top of the chimney even for $R = 0.05$. The turbulent mixing has been grossly under estimated. The numerical spreading rate is very minimal thereby suggesting that the RANS turbulence model was not able to capture the mixing zone. In case of mixing of streams of different temperatures, in some cases it is reported that the high turbulent viscosity predicted by the RANS-based turbulence models in the mixing zone (due to the locally high shear rates) suppress any transient flow development and the CFD results tend to a steady-state solution. However, experimental observations show strong temperature fluctuations leading to larger mixing zone. This is due to the dissipative nature of k-ε type models. The advance models like SST k-ω model should be tried for comparison as future scope of work.

# Chapter 7

# Experimental Validation using PIV technique

## 7.1 Introduction

An experimental set up is made for acquiring velocity field using Particle Image Velocimetry (PIV) technique so that quantitative measurement of velocity field can be compared with the computational results. The geometry of the chimney considered in the experiment is shown in Fig. 7.1. The chimney model used in the experiment is 1/18$^{th}$ scaled down model of the prototype reactor chimney. A comparison of the prototype chimney and scaled down model is shown in Table-7.1.

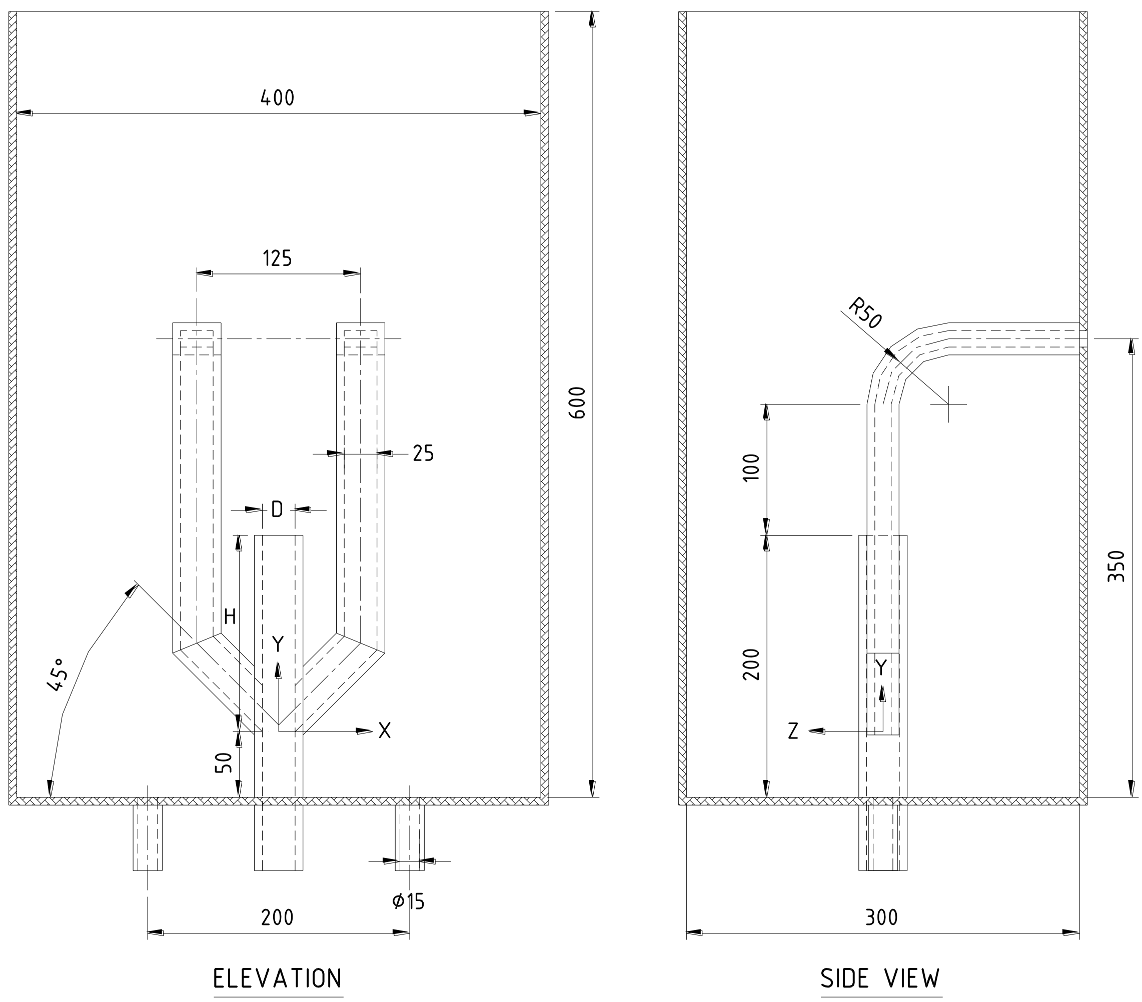


Fig. 7.1: Geometry of the chimney model

The chimney is made using 6 mm thick acrylic sheet. The tank in which chimney is immersed has dimensions 400 mm (L) × 300 mm (B) × 600 mm (H). The tank is also made of acrylic sheet and is filled with tap water up to 550 mm height. Chimney central section is a square with inner side dimension of 25 mm. The side nozzles of the chimney are at 45° with respect to the vertical central axis of the chimney. The cross section of the side outlet nozzles is rectangular (25 mm × 12.5 mm). Two bypass nozzles (each 15 mm diameter) are provided at the bottom, through which core bypass flow is sent into the water tank. By dynamic balancing this flow will be sucked inside the top opening portion of the central chimney.

Table-7.1: Comparison of prototype chimney and scaled down model

| Parameter | Prototype | Model |
|---|---|---|
| Fluid | Light water | Light water |
| Chimney square opening (D × D) | 450 mm × 450 mm | 25 mm × 25 mm |
| Side outlet nozzle area (length × breadth) | 450 mm × 225 mm | 25 mm × 12.5 mm |
| Side outlet nozzle inclination | 45° | 45° |
| Height (H) of the chimney | 2700 mm | 150 mm |

## 7.2 Experimental setup

The experimental setup consists of a centrifugal pump, a chimney test section, a water tank in which the chimney is immersed, three flow meters, associated valves and piping. A simplified process flow diagram of the experimental setup is shown in Fig. 7.2. The water tank and chimney are made of acrylic material to have a clear view of the flow through the chimney test section. The bottom of the water tank has three inlet nozzle connections. The central nozzle is 25 mm NB (nominal bore) and is connected to line-4 to supply water into the chimney representing core flow ($W_{in}$). The other two nozzles are 15 mm NB through

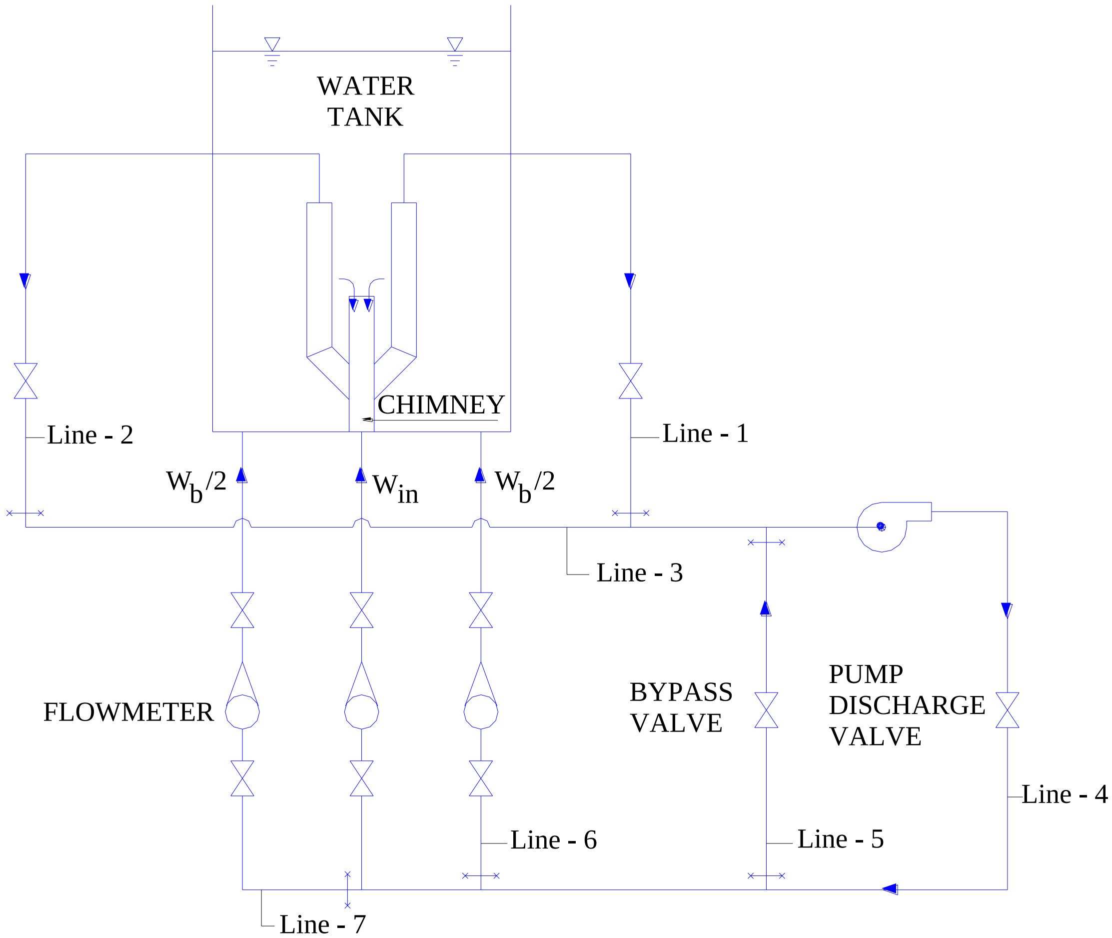

Fig. 7.2: Simplified Process flow diagram of experimental setup for PIV

which half of the total bypass flow ($W_b$) is sent to the water tank using two 15 mm NB pipes (line-6 and line-7). The tank has two outlet nozzles of 20 mm NB size, which are connected at 350 mm elevation from the bottom of the tank and join to the chimney outlet nozzles through 90° bends (Fig. 7.3). These two outlet pipe lines (line-1 and line-2) from the tank joins a common pump suction header of 40 mm NB (line-3) to draw water from the chimney. Each of these two outlet lines from the chimney has individual isolation valve for isolating any of these lines. Two vent valves are also provided in these outlet lines to facilitate venting after initial filling of the system with water. A common fill / drain valve is provided at the lowest elevation of the system which is used for filling water into the system through flexible tubing connected to a nearest water tap. Once filling is completed this valve is closed to isolate the system. After completing the experiment, the same valve is opened to drain the system to nearest drain point through flexible tubing.

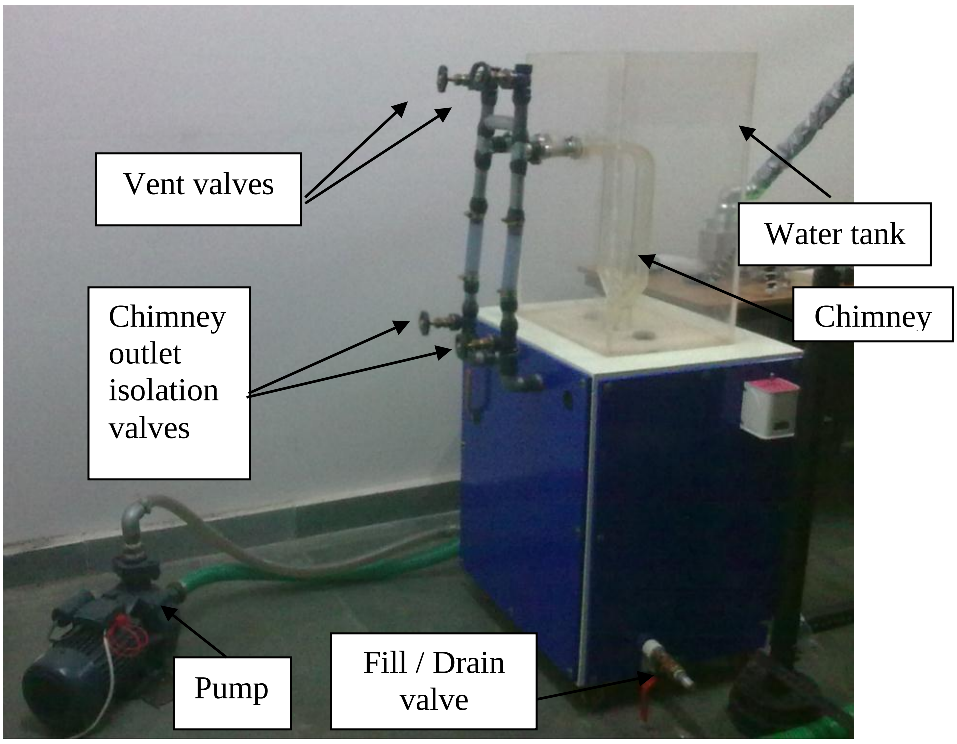


Fig. 7.3: Experimental setup

Water drawn by the pump is sent through a 25 mm NB line (line-4) provided at pump discharge to distribute water through three lines (main flow line- 25 mm NB, two bypass flow lines - 15 mm NB). Flow through each of them is measured using flow meter (rotameter). Flow through each of these lines is controlled by a regulating ball valve provided at the upstream of the rotameter as shown in Fig. 7.4. The main flow line gets connected to the central 25 mm NB nozzle provided at the bottom of the water tank. The bypass flow lines are connected to the two bypass nozzles of 15 mm NB size provided at the bottom of the tank. Total flow through the system is varied either by throttling the pump discharge valve or by opening bypass valve provided between the pump discharge and suction lines.

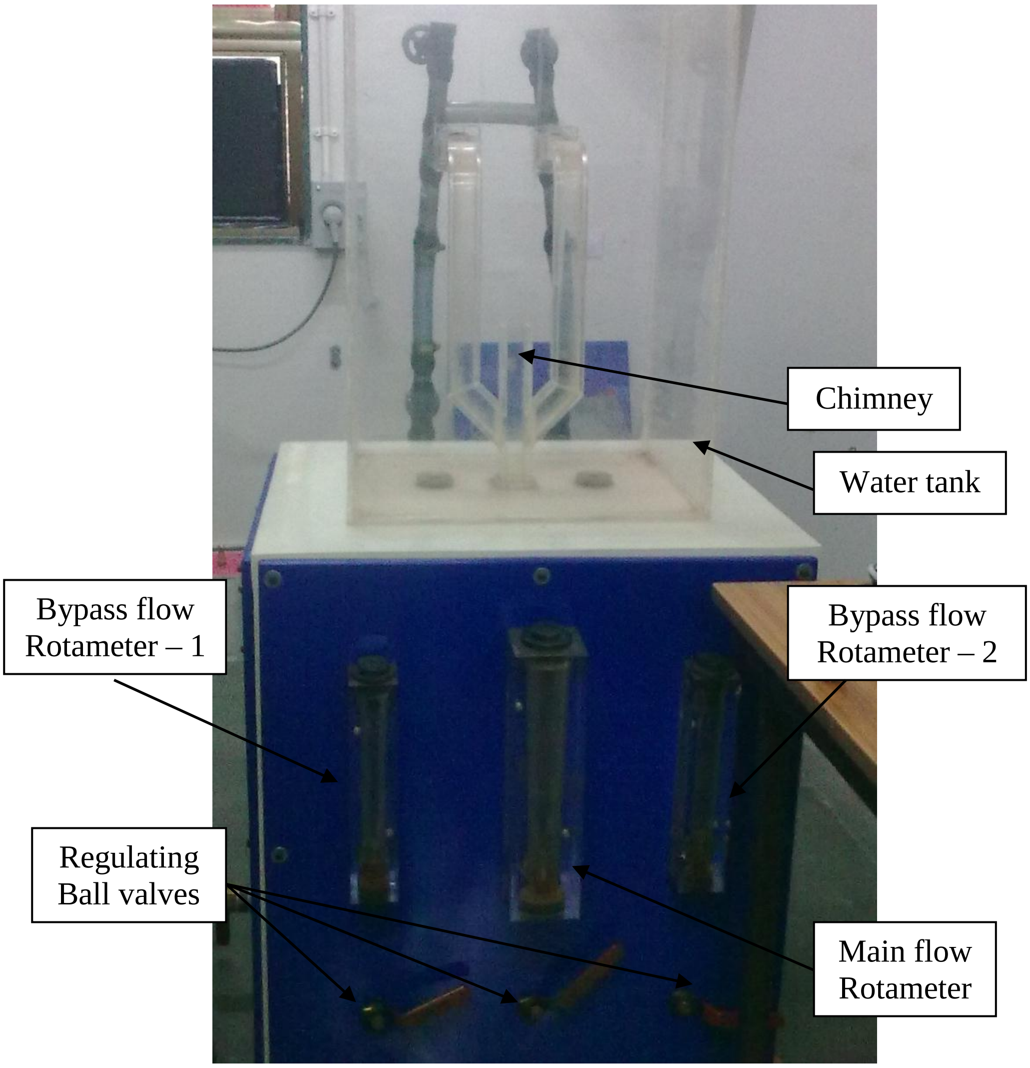


Fig. 7.4: Front view of set up showing rotameters and regulating ball valves

### 7.3 Particle Image Velocimetry system

The Particle Image Velocimetry (PIV) system used for this investigation consists of a 15 Hz pulsed laser and a camera. The double-pulsed Nd:YAG laser provides pulses of 6 ns duration with a wavelength of 532 nm and maximum energy of 350 mJ per pulse. A thin laser light sheet of 1 mm thickness is obtained using cylindrical and spherical lenses and passed through light arm to illuminate the plane of interest. Seeding particles employed are microsphere tracer particles. They are made of fused borosilicate glass (size 8-11 μm, specific density 1.1). A similar PIV system has been employed by Sewatkar et al (2012). The principles of PIV system and its components used are given in Appendix-A.

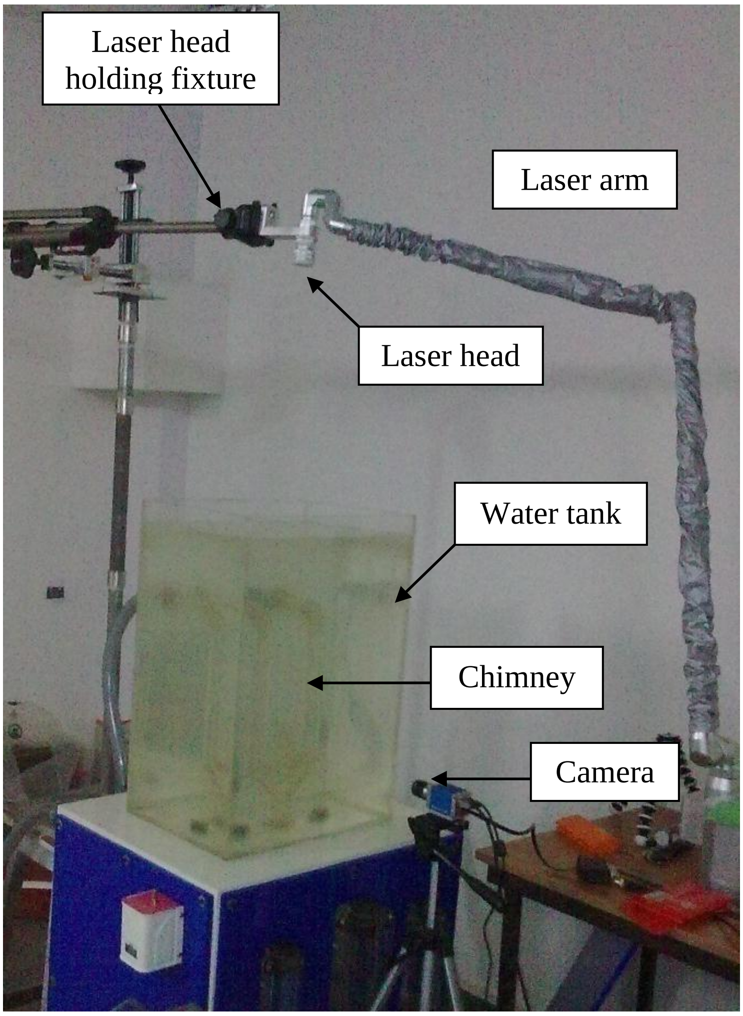


Fig. 7.5: Experimental set up showing Laser head mounted on the top and Camera from the front side of the chimney

The camera was positioned 300 mm away from the measuring plane (Fig. 7.5) and connected to a 64 bit frame grabber to capture and digitize images and to communicate with a computer. A synchronizer was used to synchronize the laser and cameras. The synchronizer delay was 540 microsecond (µs). The camera had a resolution of 1392 × 1040 pixel. It had a versatile high performance 14-bit CCD camera system with superior quantum efficiency (up to 62%). Camware, a 32-bit Windows application software was used to control the camera parameters or settings. The exposure time was adjusted to 623 µs for the camera during the experiment. Images were captured using laser A and B and the delay between them was taken 750 µs for 1800 kg/hr core flow case. The delay was decreased to 500 µs for 3600 kg/hr core flow case.

A pair of hundred images were recorded for water flowing through the chimney at position y= -10 mm to 110 mm along the vertical axis of the chimney. The software PIVlab (Thielicke, and Stamhuis, 2014) from open source was used to evaluate the recorded images via cross-correlation and the particle image was subdivided into small interrogation windows (Thielicke, 2014). For each interrogation window the average particle image separation was determined by cross-correlation and localization of the correlation peak. In this work, a multi-pass processing scheme was used; consisting of two passes with interrogation windows of 64 x 64 pixels and 50% overlap. Another pass was applied with an interrogation area of 32 x 32 pixels (3.5 mm x 3.5 mm) and 50% overlap.

Erroneous vectors were removed and replaced by a global velocity filter and local 3 x 3 median filters. Dividing with the known time between the two images captured the displacement vectors were converted into velocity vectors (Raffel, 1998) as follows:

$$\bar{u} = \frac{\Delta \bar{x}}{\Delta t}$$

where $\bar{u}$ is the velocity vector, Δx is the average displacement vector and Δt denotes the time delay between two image frames. The spacing between two vectors was about 2 mm and about thousand vectors were obtained in the zone of interest for an image. Percentage of bad vectors observed in an experiment was about 1.5%. The software PIVlab was used for analysing the results. This algorithm when used in estimating the linear displacement of 5 pixels in a pair of synthetic images gave a value of 4.99± 0.025 considering the multi-pass processing scheme used for the evaluation. The typical error in velocity measurement was estimated to be 3%. The component errors for the estimation of the PIV measurement included were the image processing uncertainty (0.5%), sampling uncertainty (1.7%) and uncertainty due to equipment (0.5%) which accounted for magnification and time.

### 7.4 Experimental Procedure

The experimental procedure which was followed for starting up the closed loop circulating system is given hereunder.

- Bring the trolley mounted experimental set up close to the laser system so that its laser head can be mounted over the top of the tank with its flexible arm
- Check the level of the top surface of the set up with spirit level
- Close two vent valves kept at the top elevation
- Open three flow controlling valves, pump discharge valve and pump bypass valve
- Connect flexible tube from nearest water tap for filling the system
- Open water tap and open filling/draining valve of the set up
- Check the level of water in the tank
- Close the filling/draining valve of the set up when water level is reached to 550 mm (i.e., 50 mm below the tank height)
- Close the water tap
- Open the two vent valves and allow air venting from the system
- Close the vent valves after air venting is completed and only water comes out from the valves
- Open water tap and open filling/draining valve
- Close the filling/draining valve when water level is reached to 550 mm
- Close water tap
- Check for any water leakage from the system

- Connect power supply to the pump and start the pump
- Check the flow through main flow rotameter and bypass flow rotameters
- Run the system till the flow stabilises
- Manipulate the three controlling valve positions to get the desired flow for the experiment
- When main flow controlling valve is fully open and desired flow is not met, gradually close the pump bypass valve to increase the flow to the desired limit
- Once the main flow and two bypass flow is set, pump is stopped for setting up the PIV system

The procedure followed in the experiment for starting the PIV system is described below.

- Mount the laser head above the tank in line with central part of the chimney
- Check the level of laser head with spirit level
- Put off the light and make the room dark
- Start the synchronizer and the computer to start the pulsed laser beam
- Check the laser sheet passing through vertical axis of the chimney and adjust accordingly till the laser sheet crosses the chimney section at the middle.
- Stop the laser beam and put on the lights
- Mount the camera on the tripod at the front side of the chimney so that it is placed perpendicular to the laser sheet
- Position the camera at the desired height to capture the image of the zone of interest
- Check the level of the camera with spirit level
- Connect the camera to computer for recording the pictures
- Put off the light and start the pulsed laser beam
- Focus the camera to the central part of the chimney

- Stop the laser beam and put on the light
- Mix few milligrams of seeding particles in a cup of water
- Take the mixture in a syringe with long needle
- Start the pump and inject the seeding particles inside the chimney into the system
- Take the remaining mixture and mix with the water in the tank
- Put off the lights and start the pulsed laser beam
- Adjust the time delay between the two laser pulse
- Check the pictures of the seeding particle and focus the camera
- Start taking photographs for 100 frames and record them
- Use PIV lab software to find the 2D velocity distribution
- Analyse and compare with numerical results

## 7.5 Experimental results

Different test cases considered in this experiment are listed in Table-7.2.

Table-7.2: Test cases for the experiments

| Sr. No. | Upward flow through chimney (kg/hr) | Upward velocity ($U_{in}$ - m/s) | Reynolds number ($Re_D$) | Bypass flow ratio (R) | Downward bypass flow through top of chimney (kg/hr) |
|---|---|---|---|---|---|
| 1 | 1800 | 0.8 | 20000 | 0.0 | 0.0 |
| 2 | 1800 | 0.8 | 20000 | 0.05 | 90 |
| 3 | 1800 | 0.8 | 20000 | 0.10 | 180 |
| 4 | 1800 | 0.8 | 20000 | 0.15 | 270 |
| 5 | 3600 | 1.6 | 40000 | 0.0 | 0.0 |
| 6 | 3600 | 1.6 | 40000 | 0.05 | 180 |
| 7 | 3600 | 1.6 | 40000 | 0.10 | 360 |
| 8 | 3600 | 1.6 | 40000 | 0.15 | 540 |

For all the cases, the water level in the tank is kept at 550 mm. The core flow and bypass flow ratio is adjusted to the desired values specified in the Table by manipulating three regulating valves provided at the upstream of the rotameters, pump discharge valve and bypass valve (Fig. 7.2). Core flow of 1800 kg/hr corresponds to Reynolds number ($Re_D$) of 20000. Four experiments are considered where bypass flow ratio is varied from 0.0 to 0.15 to understand its effect on suppressing the upward core flow through the chimney bottom central opening. Similarly, another four experiments are considered where the upward flow is increased by two times (i.e., 3600 kg/hr core flow corresponding to Reynolds number of 40000) keeping the bypass flow ratios of the same order.

### 7.5.1 Core flow – 1800 kg/hr

The velocity vectors derived using the post processing method described in section 7.3 for the cases with core flow of 1800 kg/hr are shown in Fig. 7.6.

i) Bypass flow ratio = 0.0

The velocity vector plots in the x-y plane (at z = 0) in the region from y = -10 to 110 mm is shown in Figure 7.6a. It is observed from the figure that the upward flow jet extends upto a height of $h_{S,}$ which is termed as stagnation height. At this central location, stagnation zone is created due to mixing of upward and downward flow in the central axis of the chimney. Since, no bypass flow (R=0.0) is provided in this case, to maintain the overall flow balance, upward flow is observed at the peripheral region. This clearly indicates that radioactive water from the core will reach the pool top in case no bypass is provided.

It is also observed that the velocity vectors could not be completely estimated in the region from the bottom (y= -10) to a height of about y = 35 mm due to the data loss caused

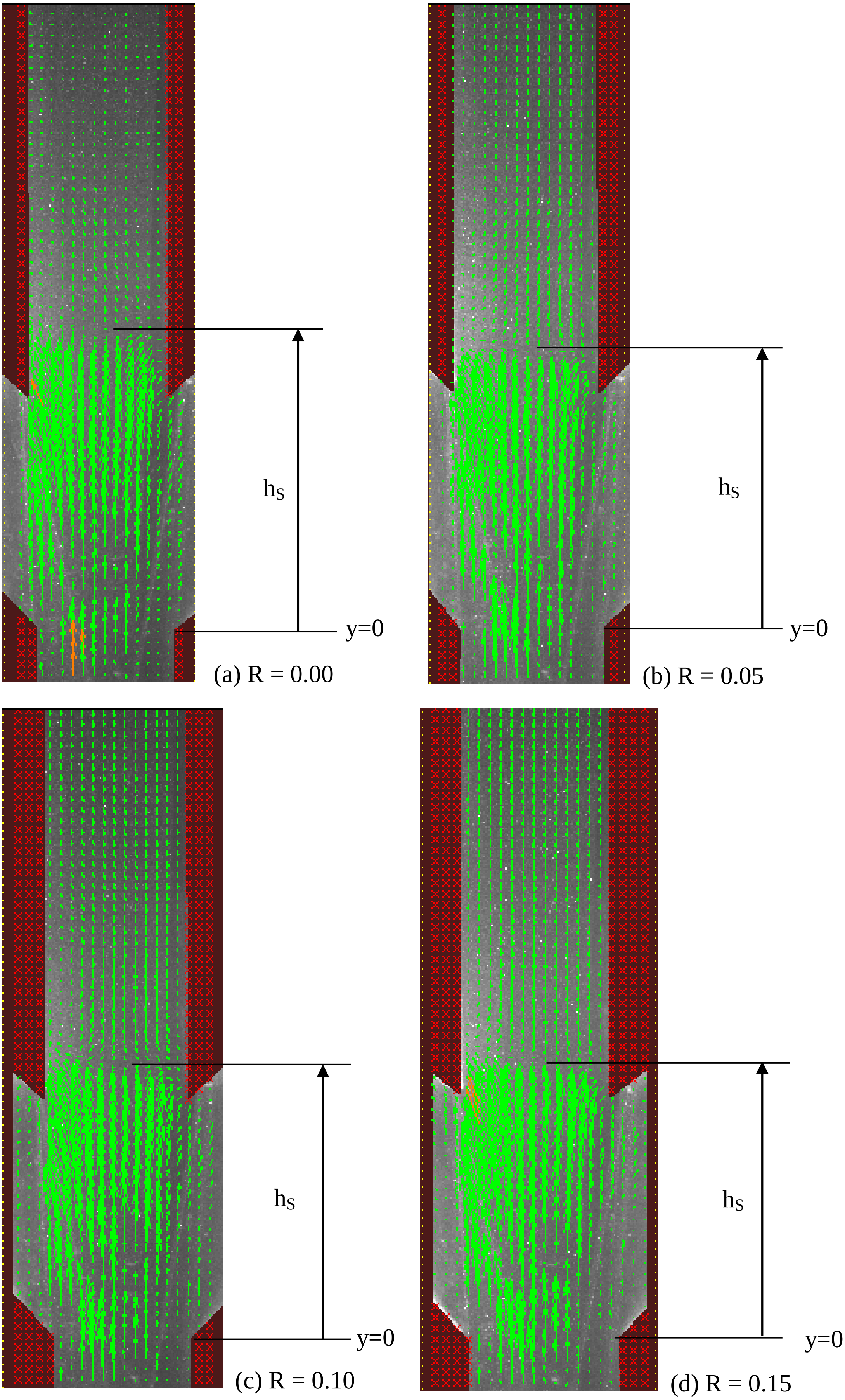


Fig. 7.6: Velocity vector plots from PIV data ($W_{in}$=1800 kg/hr, $Re_D$=20000)

by large velocity gradient present in this region and the larger distance from the laser head to this location. Due to side arms present in the chimney, the screen of light could not be created from both sides using laser source. Instead, laser head was mounted above the water tank in line with the central axis of the chimney (as shown in Fig. 7.5 ).

ii) Bypass flow ratio = 0.05

Velocity vector plots for R = 0.05 for the chimney region (y = -10 mm to 108 mm) in x-y plane are shown in Fig. 7.6b. It is observed that velocity is in the downward direction from the top of the chimney because of 5% bypass flow provided for this case. When Fig. 7.6a and Fig. 7.6b are compared, the extent of the upward velocity region is observed to be reduced indicating reduction in stagnation height ($h_S$). The downward flow velocity from the top of the chimney throughout the cross section indicates that no radioactive water is able to reach the pool top.

iii) Bypass flow ratio = 0.10, 0.15

The velocity vector plots in the x-y plane at z=0 for R = 0.10, 0.15 are shown in Fig. 7.6c and Fig. 7.6d respectively. Figure 7.6c shows the results from y = -10 mm to 105 mm and Fig. 7.6d shows the results from y= -10 mm to 100 mm. With increase in bypass flow, larger downward velocity through the top opening of the chimney is observed. This causes increase in momentum of flow in the downward direction and suppression of the upward flow. Thus reduction in the stagnation height takes place with increase in bypass flow.

In order to quantify the stagnation heights, the upward velocity along the centerline of the chimney is derived from the PIV data and plotted against the height of the chimney for various bypass flow ratios (R = 0.00, 0.05, 0.10 and 0.15) as shown in Fig. 7.7. It is observed that upward velocity ($v_y$) decreases with increase in distance (y) from the bottom of the chimney and reaches to zero value at a certain height ($h_S$). Beyond this height, upward velocity becomes negative, i.e., downward velocity is observed. From the figure it is observed that the stagnation height ($h_S$) is 0.052 m for bypass flow ratio of R =0.00. The stagnation height decreases to 0.043 m when bypass flow ratio is increased to 0.15. It is clearly observed that stagnation height decreases with increase in bypass flow ratio.

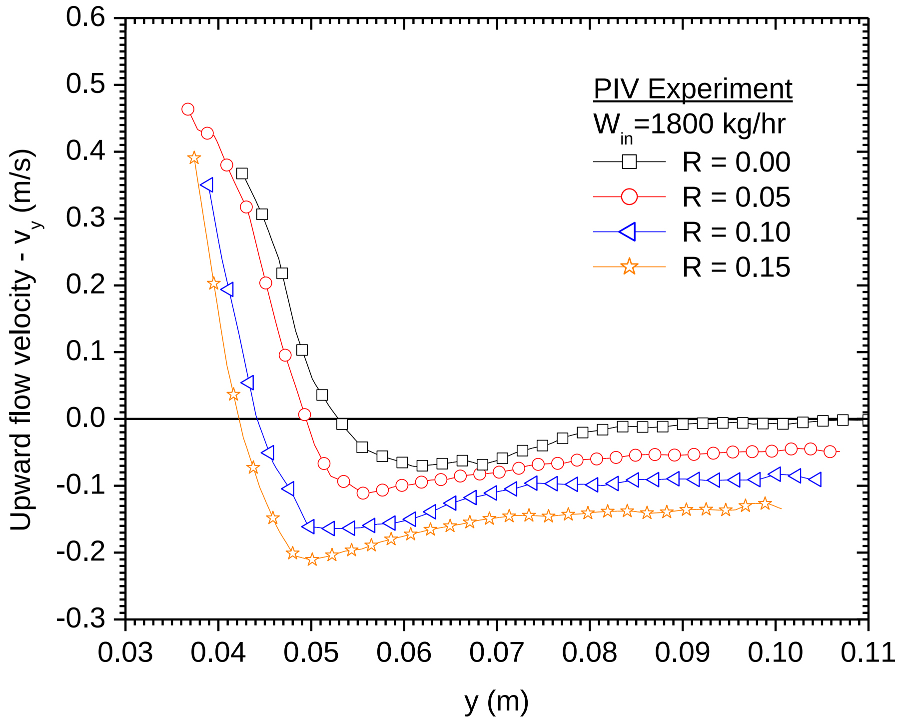


Fig. 7.7: Upward centre line velocity variation from PIV data ($W_{in}$=1800 kg/hr, $Re_D$=20000)

### 7.5.2 Core flow – 3600 kg/hr

The velocity vectors obtained from the PIV experiments with core flow of 3600 kg/hr and bypass flow ratios 0.0 to 0.15 are shown in Fig. 7.8. Velocity vector plot in x-y plane at z=0 from y = -10 mm to 110 mm for the case with bypass flow ratio of 0.0 is shown in Fig. 7.8a. The stagnation zone is observed in the figure and stagnation height ($h_S$) is marked. Velocity vector plots for bypass flow ratios of 0.05, 0.10 and 0.15 are shown upto a height of 104 mm, 100 mm and 98 mm in Fig. 7.8b, c and d respectively. Similar trends of results as explained for 1800 kg/hr core flow case are observed except the velocity here is more. From all these plots the effect of bypass flow on suppressing the upward jet is clearly observed.

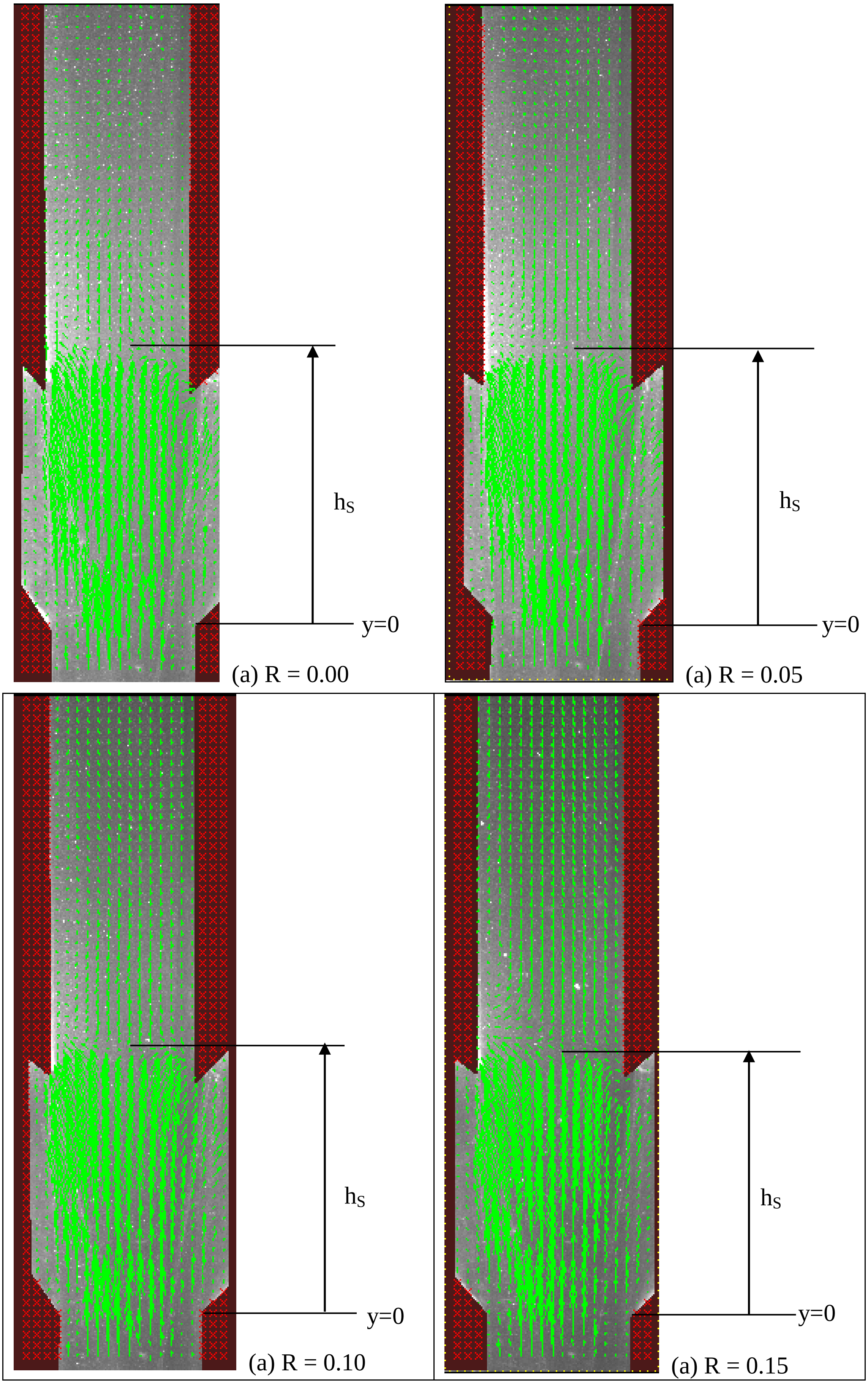


Fig. 7.8: Velocity vector plots from PIV data ($W_{in}$=3600 kg/hr, $Re_D$=40000)

For quantification of stagnation height, velocity variation with the chimney height for core flow of 3600 kg/hr is shown in Fig. 7.9. For bypass flow ratio R = 0.0 case, the velocity becomes zero at y = 0.053 m and for 0.15 bypass flow ratio, it occurs at y = 0.044 m. It is observed that the similar trends of results are observed as explained for 1800 kg/hr core flow case in Fig. 7.7.

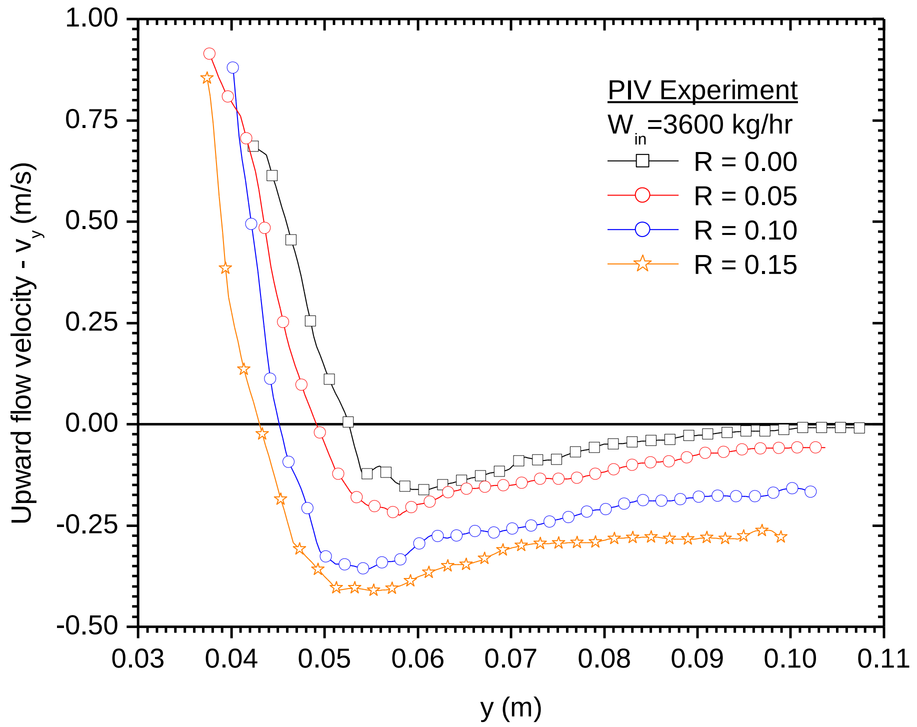


Fig. 7.9: Upward centre line velocity variation from PIV data ($W_{in}$=3600 kg/hr, $Re_D$=40000)

The velocity variation along the centre line of the axis is non-dimensionalised with respect to the inlet velocity ($U_{in}$) of water at the bottom entry of the chimney. The vertical distance (y) is non-dimensionalised with respect to the side (D) of the chimney. Results for both the core flows (1800 kg/hr and 3600 kg/hr) for various bypass ratios (R = 0.0, 0.05, 0.10 and 0.15) are shown in Fig. 7.10. It is observed that the results are similar for the cases with similar bypass ratios. It is also found that the dependence of the velocity variation on Reynolds number is not significant.

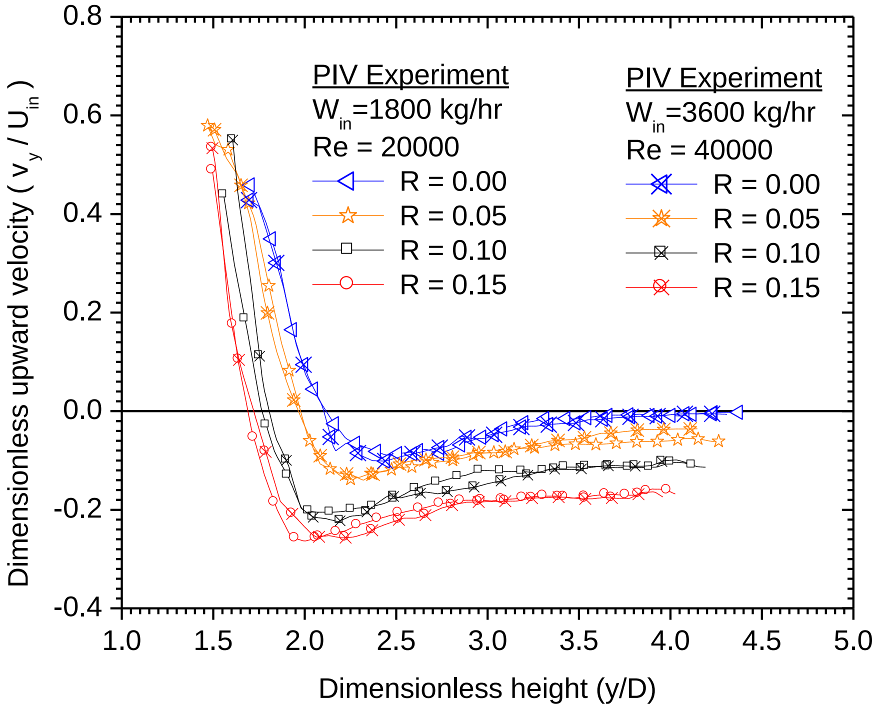


Fig. 7.10: Dimensionless centre line velocity variation from PIV data ($Re_D$=20000, 40000)

### 7.6 Comparison with Numerical results

In order to compare the experimental data of velocity distribution with the numerical results obtained for the prototype as well as chimney model, the results were plotted in the dimensionless form. The velocity is non-dimensionalised with the reference inlet velocity ($U_{in}$) at the bottom inlet of the chimney and the chimney distance is non-dimensionalised with respect to the side (D) of square chimney as explained in the scaling philosophy.

The dimensionless velocity variation along the central axis of the chimney with dimensionless chimney height for the prototype ($Re_D=3\times10^6$), chimney model ($Re_D=1.5\times10^5$ to $4.5\times10^5$) and PIV experiment ($Re_D$=20000, 40000) was compared for various cases of bypass ratios (R=0.0, 0.05, 0.10 and 0.15) as shown in Fig. 7.11, 7.12, 7.13 and 7.14 respectively.

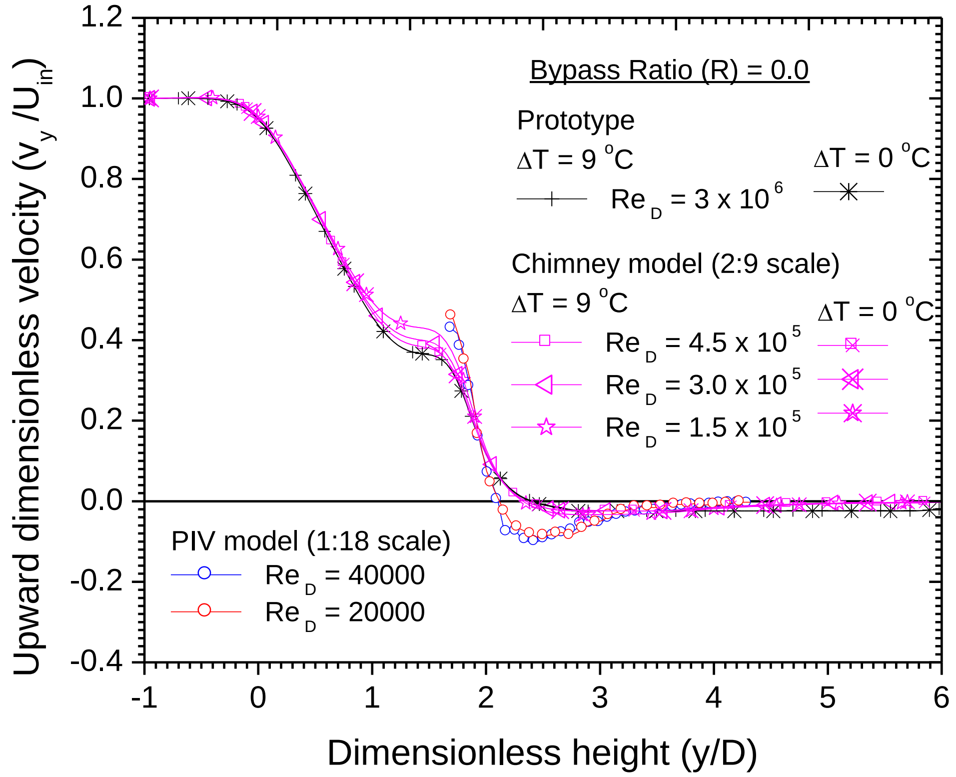


Fig. 7.11: Experimental data Vs. Computation results (R=0.0)

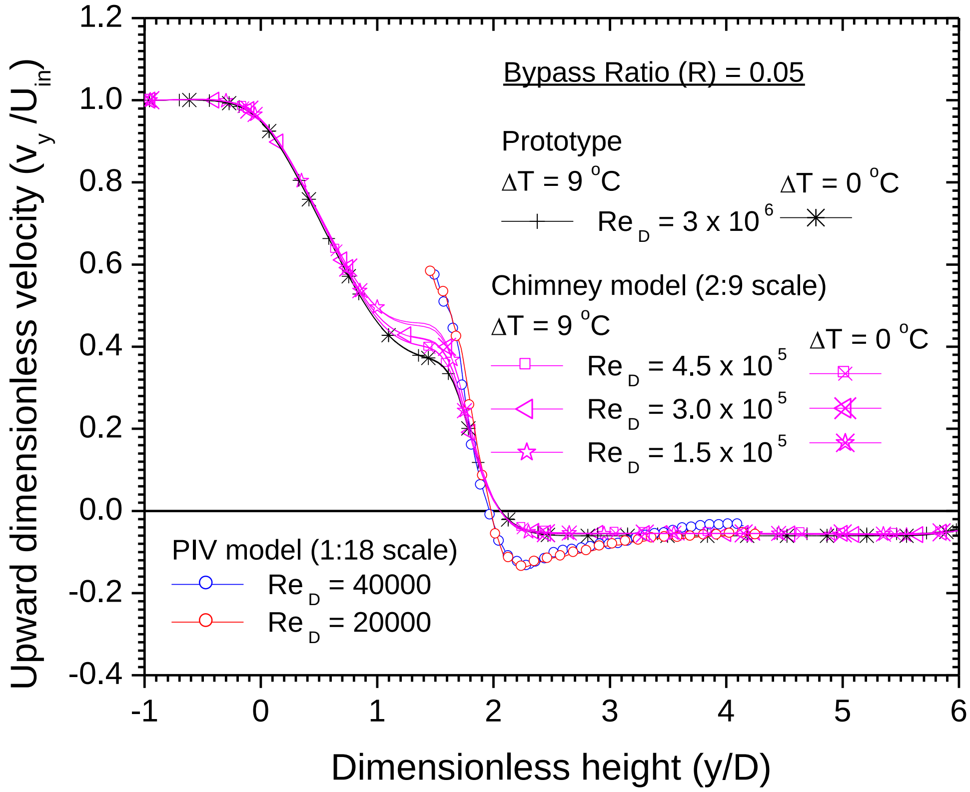


Fig. 7.12: Experimental data Vs. Computation results (R=0.05)

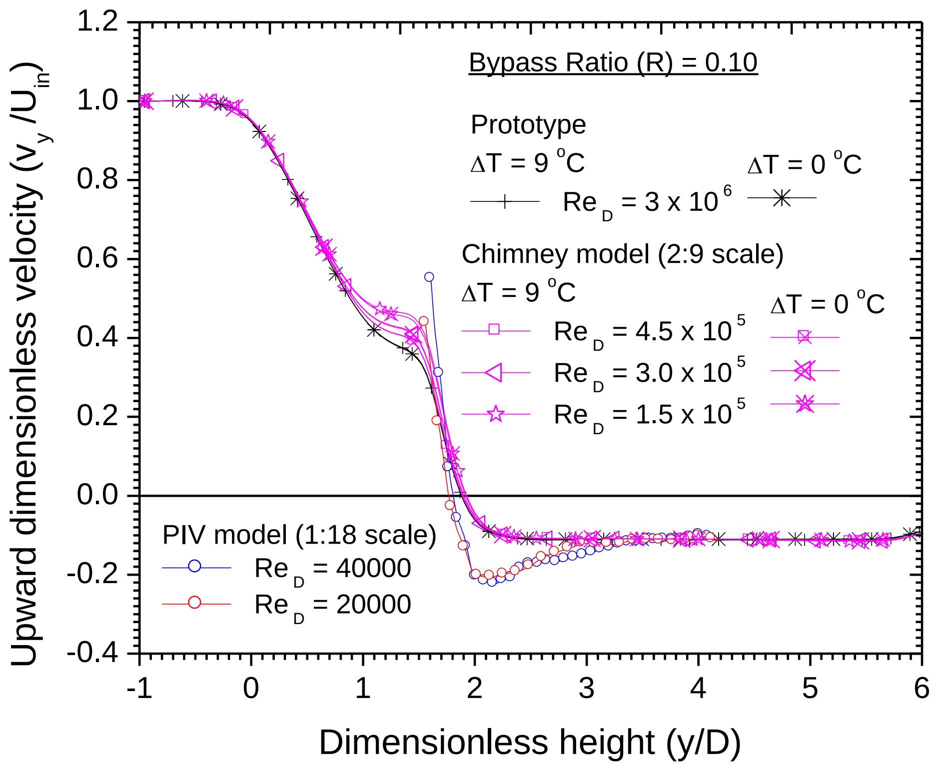


Fig. 7.13: Experimental data Vs. Computation results (R=0.10)

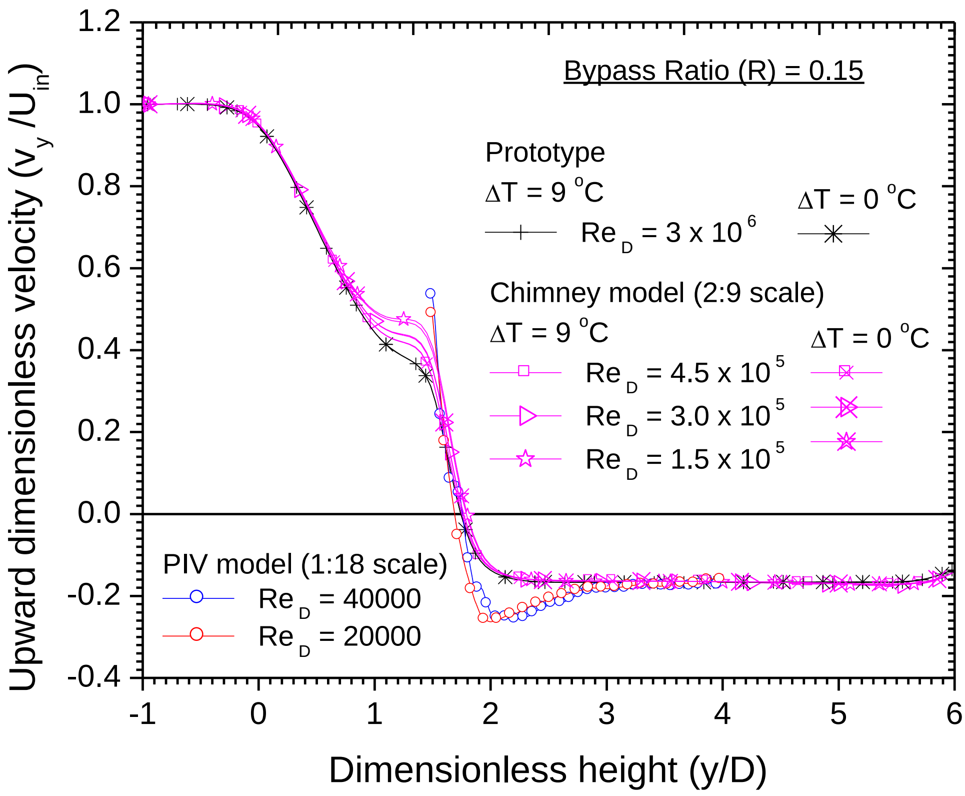


Fig. 7.14: Experimental data Vs. Computation results (R=0.15)

It is observed that the numerical results for the prototype (1:1 scale) and model (2:9 scale) as well as experimental results of the model (1:18 scale) show similar trends. This clearly shows the applicability of the scaling philosophy adopted here for prediction of mixing bhaviour inside the chimney structure.

It is also found that the results do not vary significantly for the cases with or without temperature differential between the upward hot water and downward cold water for the prototype, models and they match well with the PIV experimental data.

The effect of Reynolds number on the velocity distribution along the central axis is found to be insignificant. As bypass flow ratio is increased the dimensionless stagnation height is decreased which is seen both in the experiment and in the numerical results.

It is observed that a maximum velocity (- ve) is reached while changing the direction of flow velocity from upward to downward with increase in y value, and subsequently its magnitude decreases and attains a value which remains almost constant throughout the rest of the chimney height. However in numerical results, this trend is not observed except for the cases with bypass flow ratio R =0. With zero bypass flow ratio (Fig. 3.10b, Fig. 5.3d), two vortices are observed, where flow moves upward from the peripheral side and circulates back downward through the central region. This causes higher velocity in the centre up to the height where circulation of vortices is available. The extent of vortices predicted by numerical simulations is less than that observed in the experiment (Fig. 7.6a, Fig 7.8a). For other bypass flow ratios (R=0.05, 0.10 and 0.15), these vortices are observed in the experiment (Fig. 7.6b-d and Fig. 7.8b-d). However, the extent observed in the numerical results is relatively less (Fig. 3.12b, Fig. 3.14b, Fig 5.4d, Fig. 5.5d and Fig 5.6d). Hence, decrease in magnitude of downward velocity is not observed in the numerical results shown in Fig. 7.11 to Fig. 7.14.

The dimensionless stagnation height obtained for various cases in the experimental and numerical studies are plotted in Fig. 7.15. The predicted stagnation height in the computational studies is found to be similar to that obtained from the experiment. It is observed that stagnation height is dependent mainly on the bypass flow ratio.

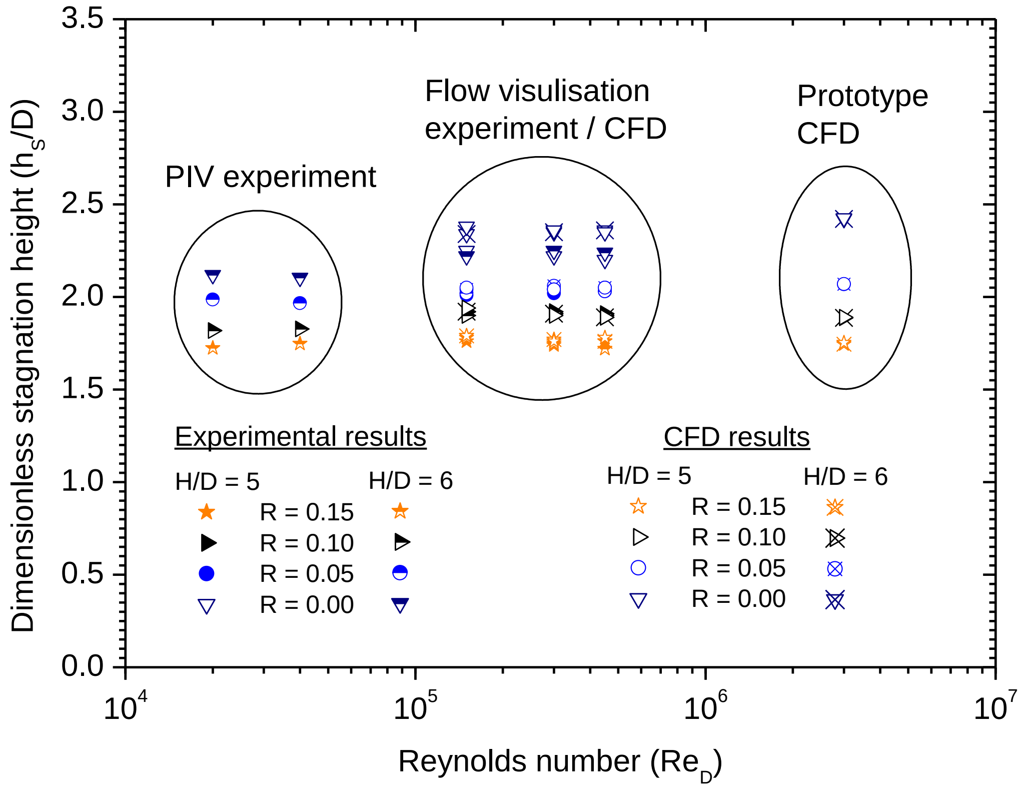


Fig. 7.15: Dimensionless stagnation height - Experimental data Vs. Computation results

## 7.7 Closure

The experimental study of turbulent mixing behaviour of two opposing flows inside the 1:18 scaled model of chimney using PIV technique is described. The experimental results for Reynolds number 20000 and 40000 for various bypass flow ratios (R=0.0, 0.05, 0.10, 0.15) are compared after non-dimensionalisation. It is observed that dimensionless velocity distribution is almost independent of Reynolds number. These experimental dimensionless velocity distributions are also compared with numerical results obtained for the prototype (1:1) and the scaled model (2:9) after non-dimensionalisation and found in good agreement.

The flow mixing study shows the effect of downward flow in suppressing the upward flow jet inside the chimney structure at different velocity conditions starting from a low Reynolds number ($2\times10^4$) of the PIV experiment to a high Reynolds number ($3\times10^6$) for the prototype. It is observed that velocity distribution does not vary significantly due to change in Reynolds number as long the flow is highly turbulent. Similar observation was also found in the experiments carried out in 2:9 scaled model of the experimental facility while predicting the stagnation height using flow visualization technique. The effect of change in temperature difference is also observed to be not so significant while comparing the results in the experiments as well as models due to dominating inertia force over the buoyancy force in the present problem. Therefore, the major parameter which decides the mixing behaviour inside the chimney is the bypass flow ratio. The scaled model design and the data generated hence are justified and numerically validated. Thus the results for prototype are applicable for the research reactor application.

# Chapter 8

# Conclusions and Suggestions for Future work

### 8.1 Contribution and Research findings

The major contribution of this work is to understand the turbulent mixing behaviour of opposing flows inside the chimney structures which are typically found in pool type nuclear research reactors to avoid radioactive water from the reactor core outlet reaching the reactor pool top. Thus pool top radiation field can be eliminated and thereby reactor pool top can be accessible to the researchers for carrying out irradiation experiments. The present work is carried out to establish that the core bypass flow sent to the pool is drawn in the downward direction inside chimney to suppress the upward flow (i.e., core outlet radioactive water) by dynamic balancing. Numerical simulations performed for the prototype as well as models using CFD code are presented in chapter 3 and 5 respectively. The velocity vector plots inside the chimney region for the prototype (Fig. 3.12b, 3.14b, 3.34, 3.35) and the models (Fig.5.4, 5.5, 5.6, 5.23, 5.25, 5.27) show the suppression of upward flow caused by the core bypass flow sent to the pool. With increase in core bypass flow, the downward flow through chimney increases causing more suppression of upward hot water. Experiments were performed and flow visualisation was done on 2:9 scale model which establishes the same (Fig. 6.6d, 6.7d, 6.10d, 6.11d, 6.14d, 6.15d, 6.21a-f, 6.26a-b, 6.27a-b, 6.28a-d). Quantitative measurement of velocity field was also done in experiments with 1:18 scaled down model. The suppression of upward flow by the bypass flow is observed in the velocity vector plots obtained from the experiments (Fig. 7.6, 7.8). This work also specifies the minimum core bypass flow required to be sent to the reactor pool so that the radioactive water will not come out of the chimney. The results with 10% core bypass flow clearly show that upward core flow is suppressed well within the chimney region in the numerical simulations for prototypes & models as well as in flow visualisation experiments & PIV experiments. Regarding the geometrical structure of the chimney, the minimum height of the chimney is specified and also the angle between the central chimney and the side arm which gives better suppression is indicated. It is shown from the numerical results of the prototype that dimensionless stagnation height ($h_S/D$) and dimensionless pool temperature front height ($h_T/D$) do not improve much by increasing chimney height from 5D to 6D (Fig. 3.44 - 3.46). Therefore, further increase in height is not found beneficial and chimney height is specified to be 6D. Similar results are observed from the flow visualisation experiments where chimney heights of 5D and 6D are reported (Fig. 6.10-17, 6.21). It is observed that chimney height 6D is adequate to suppress the radioactive water considering 10% bypass flow. A scaling philosophy is developed and methodology for prediction of mixing behaviour in a scaled down chimney model is reported. It is observed that prototype and models show similar behaviour once the results are non-dimensionalised based on the scaling philosophy explained in chapter 4. It is observed that dimensionless centerline velocity distribution of the prototype and the models shows similar profile for all the cases of nozzle inclination (Fig. 5.44). Similarly dimensionless temperature distribution of the prototype and the models shows similar profile for all the cases of nozzle inclination (Fig. 5.45). Dimensionless stagnation height and pool temperature front height for the prototype and the models show similar results for a range of Reynolds number (Fig. 5.46, 5.47). Major parameters which affect the mixing behaviour are identified to be the nozzle inclination and the bypass flow ratio from the numerical simulation results (Fig. 5.44-5.47). Experiments are carried out on chimney models with 45° nozzle inclination and reported in chapter 6. The effect of core flow and bypass flow ratio on vortex spread height and temperature profile are established (Fig. 6.6 to 6.18) for the chimney model with H/D=5. Effect of chimney height is experimentally established using another chimney model with H/D=6 (Fig. 6.19, 6.20). The effect of buoyancy due to temperature difference between core outlet water and the pool water is established experimentally (Fig. 6.26-6.28). Experimental validation of the numerical simulation is done on the scale down model (Fig. 6.23-6.24) by comparing stagnation height and temperature profile. Experimental validation of the scaling philosophy is established by comparing the dimensionless velocity distribution obtained from numerical simulations of the prototype, 2:9 scale model and experimental results of 1:18 scale PIV model (Fig. 7.11 -7.14). Finally relationship between the major parameters affecting the flow mixing behaviour inside the chimney for 45° nozzle inclination is developed (Fig. 6.20) for various bypass flow ratios.

## 8.2 Conclusions

- It is established by analyses and experiments that core bypass flow sent to the pool is drawn in the downward direction inside the chimney which is able to suppress the upward flow.
- The effects of Reynolds number, height of chimney, inclination of chimney, core flow, bypass flow ratio and temperature difference is studied through CFD analyses and experiments.
- It is observed that changes in inclination angles vary the height up to which effect of upward flow is felt. The higher is the angle, the lower is the stagnation height of the upward jet.
- Change in height of the chimney does not have significant effect on the stagnation height.
- Experimental investigations for Reynolds number ($1.5x10^5$ to $4.5x10^5$) simulating temperature difference between the opposing flows are studied in a scale down (2:9)

flow test facility. Richardson number (Ri) range simulated in the experiments is from $1.2\times10^{-3}$ to $5.5\times10^{-1}$ to cover Prototype Ri of $7.5\times10^{-3}$.

- Centre line temperature profiles obtained from the measurements carried out for various bypass flow ratios and core upward flow combinations. The results are non-dimensionalised and a generalized correlation is established.
- Experiments validate the observations from CFD simulations that (i) the temperature profile is mainly affected by the bypass flow ratio (ii) increasing bypass flow ratio decreases the pool temperature front height (iii) effects of Reynolds number, chimney height is found to be insignificant on the pool temperature front height.
- However temperature profiles from experiments show larger mixing region. This is due to alternate vortices created during mixing as observed in experiments and not found in CFD results.
- From experiments it is observed that (i) Vortex spread height decreases with increase in bypass flow ratio (ii) Effect of Reynolds number on vortex spread height is insignificant.
- Experiments validate the results of numerical simulations that (i) the hot upward flow comes out of the chimney when bypass flow ratio is 0.0 (ii) with increase in bypass flow ratio, stagnation height decreases (iii) effect of Reynolds number on stagnation height is insignificant (iv) low temperature difference (low Ri) between the core flow and bypass flow shows insignificant effect on the stagnation height (v) chimney height variation does not affect significantly the turbulent mixing behaviour.
- The minimum bypass flow required to be sent to the pool is about 10% of the core flow so that the effect of radioactive water will be within a height ($h_T$) of 4 times the

side (D) of square chimney. The minimum height (H) of the chimney required is 6 times the side of the square chimney.

- PIV investigations on a scaled (1:18) model establish the velocity field inside the chimney for Reynolds number-20000 and 40000. The stagnation height is found to be independent of the Reynolds number.
- Non-dimensionalised velocity distribution obtained from PIV experiment is compared with that of the numerical results obtained for the prototype chimney as well as for scaled model (2:9) and good agreement is found. It is found that bypass flow ratio is the major parameter which decides the mixing behaviour inside the chimney.

## 8.3 Scope for future work

The computational and experimental simulations established the effects of various parameters on the turbulent mixing behaviour considering core flow moving out of the core through both the side arms of the chimney. The behaviour will be different in case core flow takes place through one of the side arms which may be of interest as future scope of study. This can result in asymmetric mixing behavior in the chimney leading to larger stagnation height. However, this operation is expected when only one loop of the primary coolant system is available for core cooling during reactor shutdown condition. Hence pool top radiation field is not expected to be high. Additional work related to vibration of the chimney structure due to turning of the flow in the arm region will also be an important aspect which can be taken up as future scope of study related to the design of the chimney structure.

# Appendix - A

## Particle Image Velocimetry

Particle image velocimetry (PIV) is an optical method of flow visualization used in education and research to obtain instantaneous velocity measurements. It is a modern and powerful method for investigating fluid flowing system. Using a standard PIV system, two dimensional flow velocity data can be obtained for a specified cross section inside the system. The first requirement for using PIV is a transparent experimental system. Once the experiment is ready, several components are necessary to apply the PIV: A sketch of typical PIV system is presented in Fig. A.1.

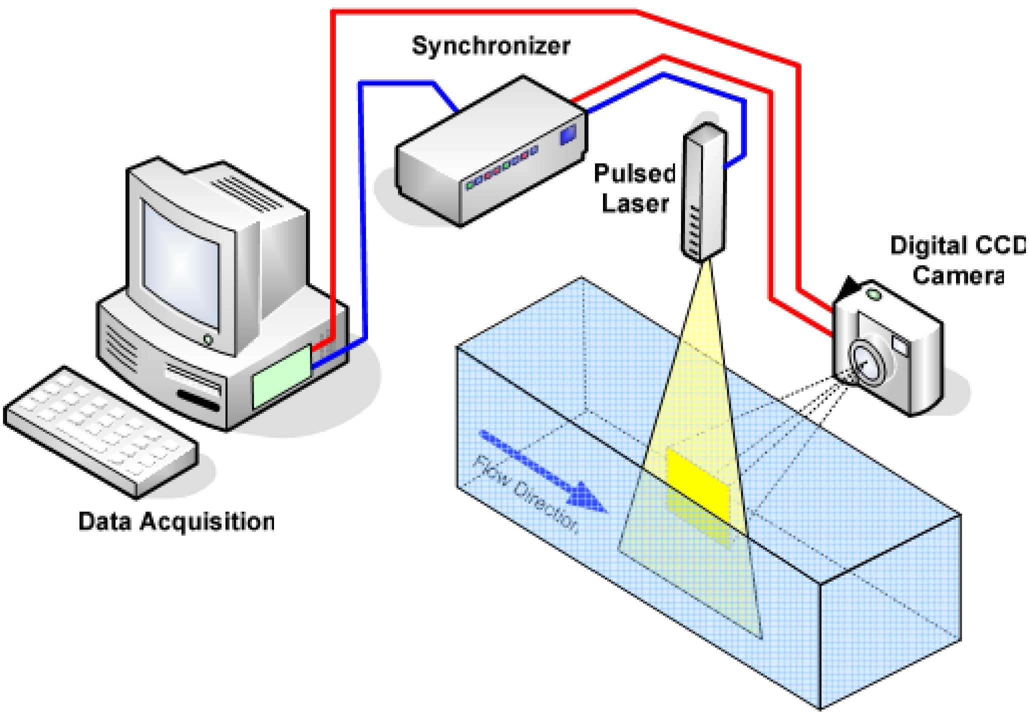


Fig. A.1: Sketch of a typical PIV system

The following are the major components of a PIV system.

1. A pulsed laser for illuminating the interested cross section in the fluid flow
2. A cylindrical lens for transforming the laser beam into a laser sheet
3. Particle tracers seeded in the fluid for illustrating the motion of fluid particles
4. A charged coupled device (CCD) camera for recording pictures
5. A synchronizer for controlling the time scale of recording image and laser pulses
6. A computer with grabber for collecting pictures from CCD
7. A software program for post-processing image analysis and velocity measurement

### A.1 Principles of PIV Technique

Particle image velocimetry is based on the average velocity measurement of the particle tracers (displacement measurement during a short period of time). The acquisition method relies on image analysis. To obtain spatial information about the displacement of particle tracers, a synchronizer simultaneously controls the laser pulse time and the recording separation time of the CCD camera. The laser source generates a pulsed sheet, which illuminates a cross section of the fluid flow. The fluid contains seeded tracers which diffuse the laser light in all directions. The CCD camera, placed perpendicularly to the laser sheet, records one image. This process is repeated a second time. The separation time "t" is defined as the time between two recorded images for the CCD camera and the two laser pulses. The exposure laser pulse time "$t_s$" represents the life time of one laser pulse. Finally, the synchronizer controls the triggering time in order to record several pairs of images (a minimum of 100 couples of images are required).

Once images are recorded, post-processing PIV software is used to calculate the statistical displacement of particle tracers between a pair of recorded images. Each image is divided into small sections called interrogation areas. For each section a statistical average displacement of particles is calculated using a correlation function. Each section is also compared with neighboring zones to obtain a coherent displacement field. The software uses the separation time “t” and displacement of particles “x” between two images for calculating an average velocity for each small region of image. Figure A.2 represents the successive processes for obtaining valid results from a PIV system.

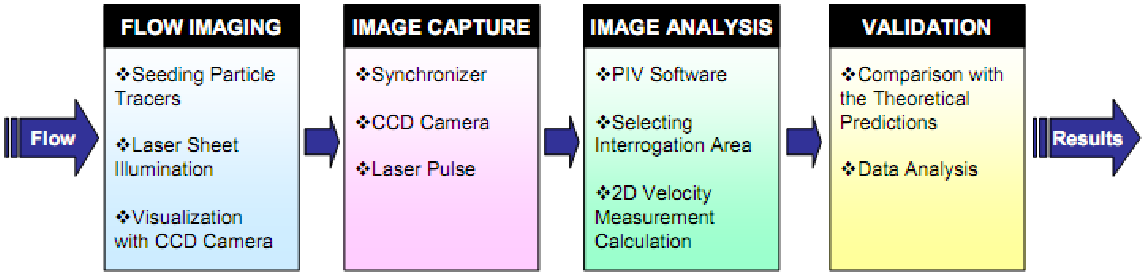


Fig. A.2: Sketch of successive processes of the PIV system

Two fundamental criteria are required to obtain physical results from a PIV system. The direction of the particle tracers must be identical and the distribution of the particle tracers must be homogeneous. The detection of the particles depends on the separation time (t) between images. If “t” is very small, the camera cannot see a displacement of the particle tracers between the two images. Conversely, if “t” is very large, the camera loses the trajectory of particles. Thus it is very important to adjust “t” according to the actual velocity of the particles inside the flow. The second criterion depends on the density and the concentration of particles tracers inside the fluid flow. Finally, external illumination and any perturbation effects may adversely influence the results. It is advisable to run the experiment in dark laboratory. The theoretical background of the post-processing image and velocity measurement is explained in detail by Raffel et al. (1998).

The life time of the laser pulse ($t_s$) is another important control parameter. The laser should pulse for a very short period in order to create an image with small bright tracers inside the images. If the laser pulse time is too long, a series of stream lines instead of particles will appear in the images.

Once the velocity is calculated, the physical meaning of the results can be focused. In practice, every pair of recorded images gives a velocity field, and subsequently the results can be analyzed.

## A.2 Components of PIV system

### Laser and lens

The integral part of a PIV system is the laser pulse and its corresponding lens. Finally the thickness of the laser sheet ($\delta z_o$) is an important parameter in a PIV system. The Thickness $\delta z_o$ should be as small as possible (preferably less than 1 mm). A small laser sheet thickness prevents the CCD camera from recording particle tracers from several slides into one image. For PIV measurement a high intensity light source is required for efficient scattering of light from tracer particles. Light sheet is generated from a collimating laser beam using cylindrical lens and spherical lens. The effective intensity of a light sheet can be increased by sweeping a light beam to form sheet thereby concentrating the energy by a factor equal to the height of the light sheet divided by the height of the beam. Figure A.3 shows the schematic of a light sheet formation. A combination of cylindrical and spherical lens is used. A negative focal length lens is first used to avoid focal line. The cylindrical lens causes the laser beam to expand in one direction only, i.e. it "fans" the beam out. The position of the minimum thickness is determined by the focal length of the cylindrical lens.

The spherical lens causes the expanding beam to focus along the perpendicular direction, at a distance of one focal length downstream to the beam waist.

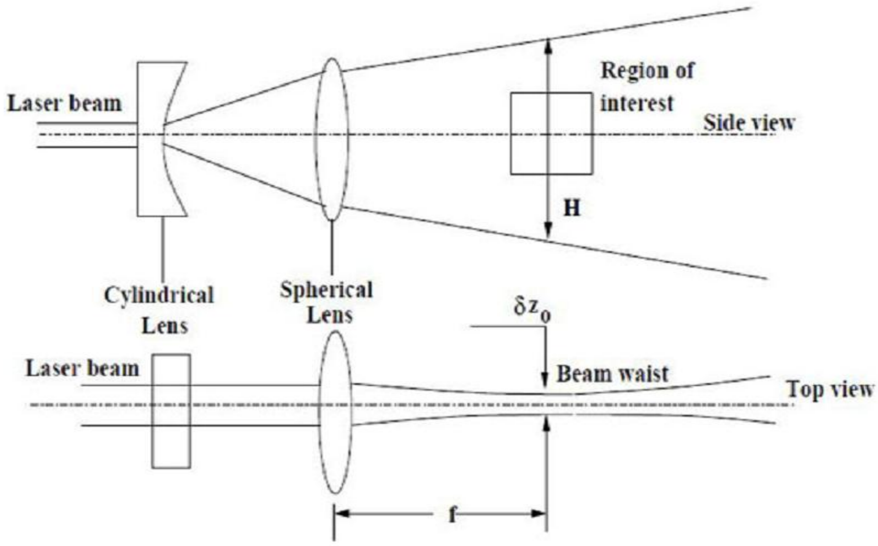


Fig. A.3: Light sheet formation using cylindrical and spherical lens for PIV

**Synchronizer**

The synchronizer represents the heart of the PIV system and should control four fundamental time dependent parameters in a PIV system:

- The exposure laser pulse time $t_s$ (microseconds)
- The separation time between two images t (the separation times depend on the flow rate and the velocity of particles inside the flow)
- The frame time of the CCD camera
- The triggering time for recording several pairs of images

**CCD Camera**

A high speed CCD camera is required for generating appropriate pair of PIV images. The CCD camera represents the most expensive part of the system. Selection of the resolution of the camera depends on the size of the illuminated section in the system. For instance a CCD camera with 1024 by 1024 pixels is suitable for 2 cm by 2 cm measuring area in the experiment.

**Software**

A wide range of suitable PIV software is available with various options and tools available for data analysis. Basic software contains the mathematical correlation transformation for calculating the velocity. Finally a computer is needed for transferring images from the camera and running the PIV software.

**Fluid and Tracers Particles**

The most common fluid used for this class of experiments is distilled water. The transparent oils can also used if it is necessary to study the effect of the viscosity in the system. As previously mentioned, the density of the fluid and particle tracers must be the same to prevent the particles from sinking and forming sedimentation during the experiment. For water, white polymer powder is available in the cosmetic industry (for instance Polyamide tracers). The shape of tracers must be spherical, and the diameter depends on the size of the cross section of the flow (around 40 to 100µm for a 2 cm by 2 cm illuminated area).

## A.3 PIV Images

As typical PIV images, the recorded images for the case of water flowing through the chimney is shown in Fig. A.4. Three sets of captured images generated using laser A and laser B for 30 lpm core flow and bypass flow ratio 0.0 are shown in Fig. A.4. The delay between laser A and Laser B is taken 750 microseconds (µs) for this case. A typical captured image showing the seeding particles in the laser illuminated zone is shown in Fig. A.5.

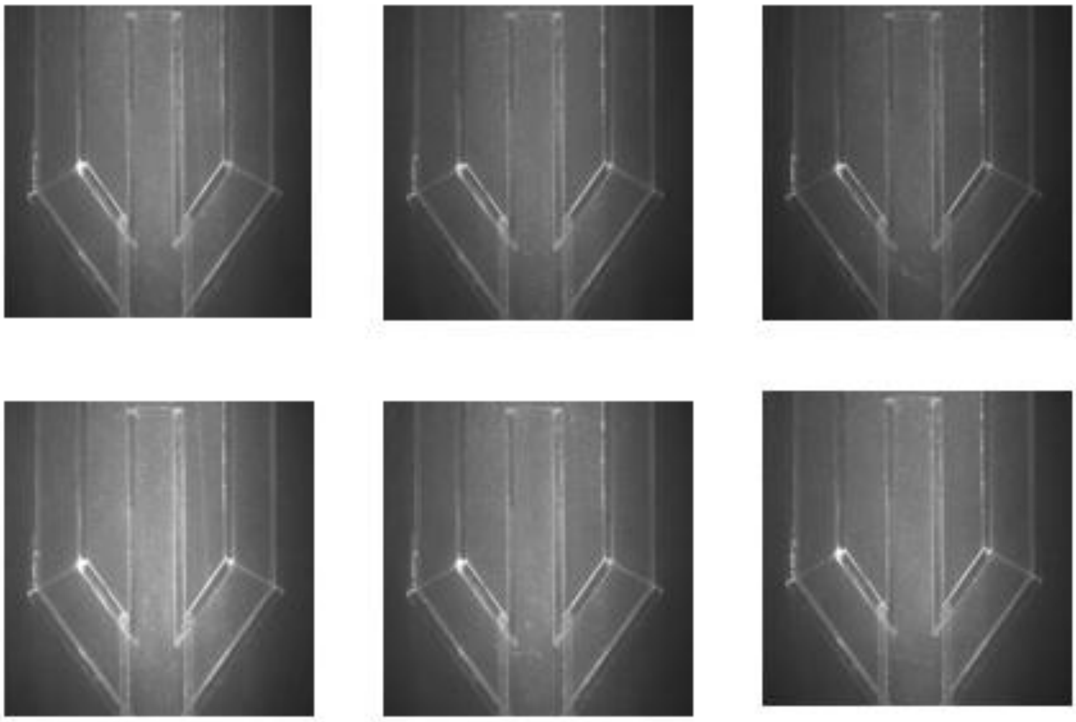

Fig. A.4: Captured images (Top images – Laser A, Bottom images – Laser B)

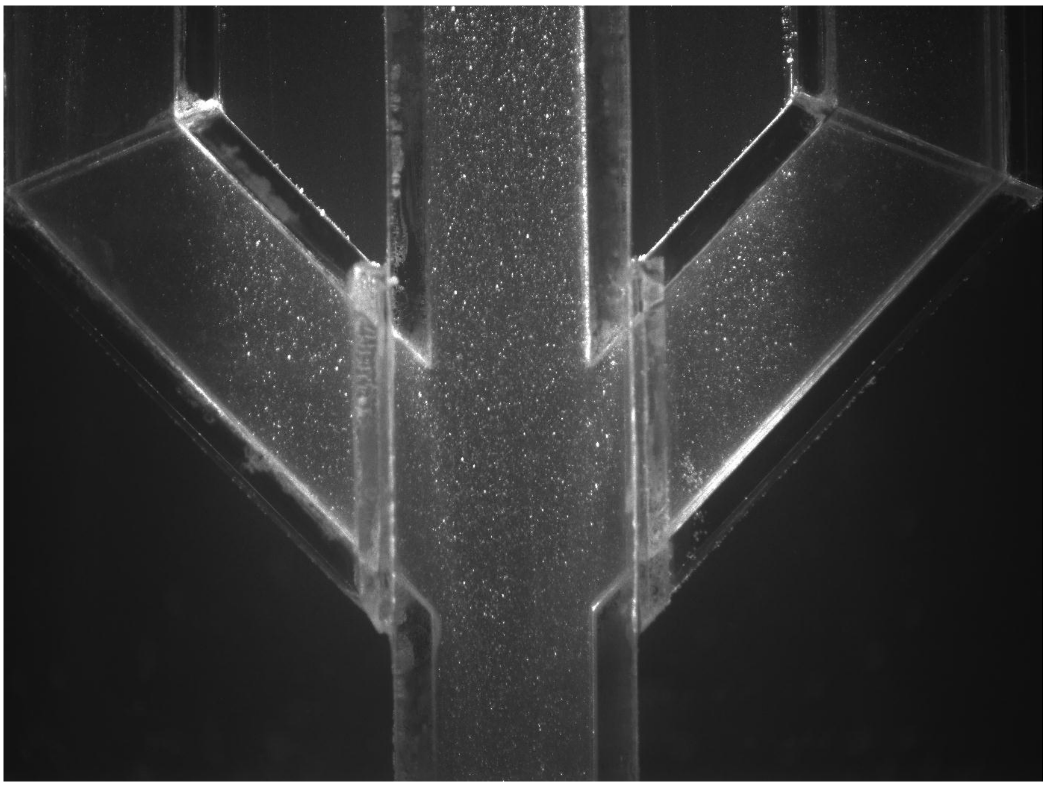

Fig. A.5: Image captured showing seeding particles

# References

*Abou Mandour, M. A.; Megahid, R. M.; Hassan, M. H.; Abd El Salam, T. M.:* Characterization and Application of the Thermal Neutron Radiography Beam in the Egyptian Second Experimental and Training Research Reactor (ETRR-2*),* Science and Technology of Nuclear Installations, 2007, doi :10.1155/2007/24180.

*ANSYS, 2006.* ANSYS CFX User Manual, ANSYS-CFX-10.

*Boussinesq, J.:* Mem. Presentes par Divers Savants Acad. Sci. Inst. Fr., 1887, Vol 23, p. 46

*Chafle, S. B.; Sengupta, S.; Mukherjee, P.; Sasidharan, K.; Raina, V. K.:* High Flux Research Reactor. Peacefulatom 2009, Thematic volume – Reactor Systems & Applications, 2011, p. 195

*Chen, S. H.; Ou, J. J.; Dukat, A. J.; Murthy, J. Y.* : Dynamics of Fluid Mixing at a T-junction with Implications on Natural Gas Processing, Ind. Eng. Chem. Res., 1990, Vol. 29, pp. 1690–1695.

*Chen, S. H.; Ou, J. J.; Dukat, A. J.* : Dynamics of fluid mixing induced at a T-junction. An Evaluation of a Mathematical Model with Existing Experimental Observations, Ind. Eng. Chem. Res., 1991, Vol. 30, pp. 1646–1651.

*Dang, G.; Luo; Y.; Wang, H.; Chen, T.; Mao, Q.; Zhang, Y.*: Experimental investigation on heat transfer characteristics in a safety injection nozzle component in PWR, Nuclear Engineering and Design, 2008, Vol. 238 pp. 1828–1837.

*Devahastin, S.; Mujumdar, A. S.* : A numerical study of flow and mixing characteristics of laminar confined impinging streams, Chemical Engg. Journal, 2002, Vol. 85 pp. 215–223.

*Doval A. S.; Mazufri, C. M.* : Relevant Thermal-hydraulic aspects in the design of the RRR, Institute of Nuclear and Energy Research, XIII ENFIR, Brazil, 2002.

*El-Morshdy, S. El-Din :* Analytical study of the closure flow inside the ETRR-2 core chimney, Ann. Nucl. Energy, 2007, Vol. 34, pp. 228 – 232.

*FLUENT* 6.1.18. User's guide, Vols. 1-5, Fluent Inc., 2002.

*Forney, L. J.; Kwon, T. C.* : Efficient Single-Jet Mixing in Turbulent Tube Flow. AIChE J., 1979, Vol. 25, pp. 623.

*Forney, L. J.; Lee, H. C.* : Optimum Dimensions for Pipeline Mixing at a T-junction. AIChE J., 1982, Vol. 28, pp. 980.

*Frank, Th.; Lifante, C.; Prasser, H. M.; Menter, F.* : Simulation of turbulent and thermal mixing in T-junctions using URANS and scale-resolving turbulence models. Nuclear Engineering and Design, 2010, Vol 240, pp. 2313-2328.

Fric, T. F.; Rosko, A. : Vortical structure in the wake of a transverse jet. Journal of Fluid Mechanics, 1994, Vol. 279, pp. 1-47

*Fureby, C.; Grinstein, F. F.*: Monotonically Integrated large eddy simulation of free shear flows, AIAA journal, 1999, 37 (5).

*Gang Pang; Hui Meng:* Experimental study of turbulent mixing in a tee mixer using PIV and PLIF. AIChE Journal, 2001, 47(12), pp. 2653-2665.

*Grinstein, F. F.; Fureby, C.*: Recent Progress on MILES for high Reynolds Number flows, Journal of Fluid Engineering, 124 :848861, 2002.

*Guobing Kang:* Numerical simulation of jet and cross flow mixing in Tee pipe, Advanced Materials Research, 2014, Vol 960-961, pp. 523-527.

*Harlow, F. H.; Nakyama, P. I.:* Transport of turbulent energy decay rate, LA-3854, 1968.

Hirota, M.; Asano, H.; Nakayama, H.; Asano, T.; Hirayama, S. : Three dimensional structure of turbulent flow in mixing T-junction, 2006, JSME International Journal, Series B, Vol. 49, No. 4, pp. 1070-1077.

*Hirota, M.; Mohri, E.; Asano, H.; Goto, H.:* Experimental study on turbulent mixing process in cross-flow type T-junction, 2010, International journal of Heat and Fluid Flow, Vol. 31, pp. 776-784.

*Ho, C. K.; O'Rear, L.; Wright, J. L.; McKenna, S. A.* : Cotaminant Mixing at Pipe Joints – Comparison between Experiments and Computational Fluid Dynamics Models, 2006, 8th Annual Water Distribution System Analysis Symposium, OhiO, USA

*Hosseini, S. M.; Yuki, k.; Hashizume H.:* Classification of turbulent jets in a T-junction area with a 90-deg bend upstream, Int. Journal of Heat and Mass Transfer, 2008, Vol. 51, p. 2444

*Hosseinalipour, S. M.; Mujumdar A. S.*: Flow, heat transfer and particle drying characteristics in confined opposing turbulent jets: a numerical study, Drying Technology, 1995, Vol. 13, pp. 753–781.

*Hosseinalipour, S. M.; Mujumdar A. S.*: Flow and thermal characteristics of steady two-dimensional confined laminar opposing jets: Part I. Equal jets, Int. Comm. Heat Mass Transfer, 1997, Vol. 24, pp. 27–38.

*Hosseinalipour, S. M.; Mujumdar A. S.*: Flow and thermal characteristics of steady two-dimensional confined laminar opposing jets: Part II. Unequal jets, Int. Comm. Heat Mass Transfer, 1997, Vol. 24, pp. 39–50.

*IEC 60751 :* Industrial platinum resistance thermometers and platinum temperature sensors, Edition 2.0 2008-07

*Igarashi, M.; Tanaka, M.; Kawashima, S.; Kamide, H.* : Experimental study on Fluid Mixing for Evaluation of Thermal stripping in T-pipe junction, 2002, ICONE10-22255.

*Igarashi, M.; Tanaka, M.; Kimura, N.; Kamide, H.* : Study on Fluid Mixing Phenomena for Evaluation of Thermal stripping in a Mixing Tee, 2003, NURETH10-A00512.

*ISO 5167 -1 :2003(E)* -Measurement of fluid flow by means of pressure differential devices inserted in circular- cross section conduits running full Part-1 : General Principles and Requirements

*ISO 5167 -2 :2003(E)* -Measurement of fluid flow by means of pressure differential devices inserted in circular- cross section conduits running full Part-2 : Orifice Plates

*Jaroslav Stigler; Roman Klas; Michal Kotekc; Vaclav Kopeckyd* :The Fluid Flow in the T-Junction. The Comparison of the Numerical Modeling and PIV Measurement, Procedia Engineering, 2012, Vol 39, pp. 19 – 27

*Johnson D.A. and Wood, P. E.*: Self-sustaining oscillations in opposed impinging jets in an enclosure, Canadian J. Chem. Eng., 2000, Vol. 78, pp. 867–875.

*Kamide, H.; Igarashi, M.; Kawashima, S.; Kimura, N.; Hayashi K. :* Study on mixing behavior in a tee piping and numerical analyses for evaluation of thermal striping, Nuclear Engineering and Design, 2009, Vol 239, p. 58

*Karwat, H.* : Principal characteristics of experimental simulators suitable for SBLOCA events of LWRs and scaling principles adopted in their design, Proc. Spec. Meet. on Small Break LOCA Analyses in LWRs, Pisa, Italy, 23-27 June 1985, Vol. 1, pp. 399-433.

*Kim, J. H.* : An analytical mixing model for Buoyant jet injected into pipe flow, Journal of Heat Transfer, 1985, Vol. 107, pp. 630.

*Kim, H.; Kim, H. R.; Lee, K. H.; Lee, J. B.* : Design Characteristics and Startup Test of HANARO – The Newly In-service Korean Research Reactor, Journal of Nuclear Science and Technology, 1996, Vol. 33, No. 7, pp. 527-538.

*Kok, J. B. W.; Van der Wal, S.* : Mixing in T-junctions, Appl. Math. Modelling 1996, Vol. 20, pp. 232 – 243.

*Launder, B. E.; Spalding, D. B.*, 1972: Lectures in Mathematical Models of Turbulence, Academic Press, 1972, London, England.

*Launder, B. E.; Spalding, D. B.:* The numerical computation of turbulent flows, Computer Methods in Applied Mechanics and Engineering, 1974, Vol. 3, p. 269-289.

*Li, Wei-Feng; Yao, Tian-Liang; Wang, Fu-Chen* : Study on factors influencing stagnation point offset of turbulent opposed jets, AIChE Journal, 2010, Vol. 56, No. 10, pp. 2513 – 2522.

*Li, Wei-Feng; Du, Ke-Jiang; Yu, Guang-Suo; Liu, Hai-Feng; Wang, Fu-Chen* : Experimental study of Flow regimes in three-dimensional Confined Impinging Jet Reactors, AIChE Journal, 2014, Vol. 60, No. 8, pp. 3033-3045.

*Ludwig, J. C.:* Concentration, Heat and Momentum Limited (CHAM), POLIS: Phoenics On-line Information System. 2004, London.

*Maekawa, I.*: Numerical diffusion in single phase multi-dimensional thermal hydraulic analysis. Nuclear Engineering Design, 1990, Vol. 120, pp. 323-339.

*Manhart, M.; Tremblay, F.; Friedrich, R.* : MGLET- A parallel code for efficient DNS and LES of complex geometries, 2001, Parallel Computational Fluid Dynamics. Elsevier Science BV, Amsterdam, pp. 449-456.

*Maruyama, T.; Suzuki S.; Mizushina, T.* : Pipeline mixing between two fluid streams meeting at a T-junction, Int. Chem. Eng. 1981, vol. 21, pp. 205

*McGuirk, J. J.; Rodi, W.:* The calculation of three dimensional turbulent free jets, Turbulent Shear Flows I, Springer Verlag, Heidelberg, 1979

*Menter, F. R.:* Two-equation Eddy-viscosity turbulence models for engineering applications, AIAA J, Vol. 32 (8), 1994.

*Nahavandi, A. N.; Castellana, F. S.; Moradkhanian, E.N.* : Scaling laws for modeling nuclear reactor systems, Nucl. Sci. Eng. 72, 1979, pp. 75-83.

*Naik-Nimbalkar, V. S.; Patwardhan, A. W.; Banerjee, I.; Padmakumar, G.; Vaidyanathan, G.:* Thermal mixing in T- junctions, Chem. Eng. Sci., 2010, Vol. 65, pp. 5901 – 5911.

*Peller, N.; Le Duc, A.; Tremblay, F.; Manhart, M.* : High-order stable interpolations for immersed boundary methods, Int. J. Numer. Meth. Fluids., 2006, Vol. 52(11), 1175-1193.

*Ogawa, H.; Igarashi, M.; Kimura N.; Kamide, H.* : Experimental study on fluid mixing phenomena in T-pipe junction with upstream elbow, 11$^{th}$ International Topical meeting on Nuclear Reactor Thermal-Hydraulics (NURETH-11), France, Oct 2005

OSIRIS Reactor, Nuclear Reactors Services Department, Nuclear Energy Directorate Division, French Atomic Energy Commission (CEA), Saclay, 2002

*Patankar, S. V.:* Numerical heat transfer and fluid flow, Hemisphere Publication, 1980

*Raffel M.; Willert C.; Kompenhaus J.* : Particle Image Velocimetry. Springer Verlag. 1998.

*Rastogi, A. K.; Rodi, W.:* Calculation of general three dimensional turbulent boundary layers, AIAA Journal, 1978, Vol. 16, p. 151

*Reynolds, A. J.* : The prediction of turbulent Prandtl and Schmidt number, Int. J. Heat Mass Transfer, 1975, Vol 18 (9), pp 1055 – 1069.

*Rodi, Wolfgang :* Turbulence models and their application in hydraulics, A state of the art review, Third edition, 1993. A. A. Balkema, Rotterdam,Netherlands.

*Roy, J.C.; Bertrand C.; Palec, G. L.*: Numerical and experimental study of mixed and forced convection in a junction, Int. J. Heat and Mass Transfer, 1994, Vol. 37, pp. 1985–2006.

*Schwertfirm, F.; Gradl, J.; Schwarzer, H. C.; Peukert, W.; Manhart M.* : The low Reynolds number turbulent flow and mixing in a confined impinging jet reactor. International Journal of Heat and Fluid Flow, 2007, Vol. 28 pp. 1429–1442.

*Sewatkar, C.M.; Patel, R.; Sharma, A; Agrawal, A.* : Flow around six in-line square cylinders, Journal of Fluid Mechanics, 2012, Vol. 710, pp. 195-233.

*Sharma, D. :* Turbulent convective phenomena in straight rectangular sectioned diffusers, Ph. D. Thesis, University of London, 1974

*Smith, S. H.; Mungal, M. G.* : Mixing structure and scaling of the jet in crossflow, Journal of Fluid Mechanics, 1998, Vol. 357, pp. 83-212.

*Stroka, L. M.; Forney, L. J.* : Fluid Mixing with a Pipeline Tee - Theory and Experiment. AIChE J. 1989, Vol 35, pp. 406.

*Tang, D. Y.; Ou, J. J.; Heist, R. H.; Chen, S. H.; Dukat, A. J.; Eberle A. C.* : Dynamics of Fluid Mixing induced at a T-junction. Experimental Characterization and Fluid Dynamic Computation of Temperature Distribution in Space, Ind. Eng. Chem. Res., 1993, Vol. 32, pp. 1727–1733.

*Tosun, G.* : A study of micromixing in Tee mixers, Ind. Eng. Chem. Res. 1987, Vol. 26, pp. 1184.

*Thielicke, W.; Stamhuis. E. J.* : PIVlab – Time-Resolved Digital Particle. Image Velocimetry Tool for MATLAB, 2014. (version: 1.31), http://dx.doi.org/10.6084 /m9.figshare.1092508.

*Thielicke, W.:* The Flapping Flight of Birds - Analysis and Application. Phd thesis, Rijksuniversiteit Groningen. 2014.

*Unger, D. R.; Muzzio, F. J.; Brodkey R. S.* : Experimental and Numerical characterization of Viscous flow and Mixing in an Impinging Jet Contactor, Canadian J. Chem. Eng., 1998, Vol.76, pp. 546–555.

*Van Doormal, J. P.; Raithby, G. D.*: Enhancements of the SIMPLE Method for Predicting Incompressible Fluid Flows, Numerical heat transfer, 1984 Vol. 7, pp. 147 – 163.

*Vicente, W.; Salinaas-Vazquez, M.; Chavez, C.; Carrizosa, E.:* Different numerical methods in the study of passive scalar transport in a pipeline x-junction, Applied Mathematical Modelling. 2008

*Walker, C.; Simiano, M.; Zboray, R.; Prasser, H.-M. :* Investigations on mixing phenomena in single phase flow in a T-junction geometry, 2009, Nuclear Engineering and Design, Vol. 239, pp. 116-126.

*Walker, C.; Manera, A.; Niceno, B.; Simiano, M.; Prasser, H.-M. :* Steady-state RANS-simulations of the mixing in T-junction, Nuclear Engineering and Design, 2010, Vol. 240, pp. 2107-2115.

*Wang, S. J.; Devahastin S.; Mujumdar A. S.* : A numerical investigation of some approaches to improve mixing in laminar confined impinging streams, Applied Thermal Engineering, 2005, Vol. 25, pp. 253–269.

*Wang, S. J.; Mujumdar, A. S. :* A numerical study of flow and mixing characteristics of three dimensional confined turbulent opposing jets : Unequal jets, Chemical Engineering and Processing, 2005, Vol. 44, p. 1068 – 1074.

*Wang, S. J.; Mujumdar A.S. :* Flow and mixing characteristics of multiple and multi-set opposing jets, Chemical Engineering and Processing, 2007, Vol. 46, p. 703 – 712.

*Webb, Stephen W.; Waanders, Bart G. van Bloemen :* High fidelity computational fluid dynamics for mixing in water distribution systems, 8th Annual Water Distribution Systems Analysis Symposium, Cincinnati, Ohio, USA. 2006

*Wood P.; Hrymak, A.; Yeo: R.; Johnson, D.; Tyagi, A.*: Experimental and computational studies of the fluid mechanics in an opposed jet mixing head, Phys. Fluids A 3, 1991 pp. 1362–1368.

*Zuber, N.* : Problems in modeling of small break LOCA, Rep. NUREG-0724, 1980.